High-precision Versatile Ultrasonic Flow Meters Based on Matrix Transducer Arrays

Massaad Mouawad, J.M.

Citation (APA)
Massaad Mouawad, J. M. (2021). *High-precision Versatile Ultrasonic Flow Meters Based on Matrix Transducer Arrays*. [Dissertation (TU Delft), Delft University of Technology]. https://doi.org/10.4233/uuid:e930dace-0655-4b4c-9b4b-f5d846414fe7

Important note
To cite this publication, please use the final published version (if applicable).
Please check the document version above.

High-precision Versatile Ultrasonic Flow Meters Based on Matrix Transducer Arrays

High-precision Versatile Ultrasonic Flow Meters Based on Matrix Transducer Arrays

Dissertation

for the purpose of obtaining the degree of doctor
at Delft University of Technology
by the authority of the Rector Magnificus, Prof. dr. ir. T. H. J. J. van der Hagen,
chair of the Board for Doctorates
to be defended publicly on
Wednesday 3 March 2021 at 10:00 o'clock

by

Jack Mitchell MASSAAD MOUAWAD

Master of Science, Norges Teknisk-naturvitenskapelige Universitet, Norway
born in Caracas, Venezuela

This dissertation has been approved by the promotors:

Prof. dr. ir. N. de Jong
Dr. ir. M. D. Verweij

Composition of the doctoral committee:

Rector Magnificus,	chairperson
Prof. dr. ir. N. de Jong	Delft University of Technology, promotor
Dr. ir. M. D. Verweij	Delft University of Technology, promotor

Independent members:

Prof. dr. ir. R. Benedictus	Delft University of Technology
Prof. dr. S. Kenjereš	Delft University of Technology
Prof. dr. ing. M. Vogt	Ruhr-Universität Bochum
Dr. ir. J. Hogendoorn	KROHNE New Technologies BV

Other members:

Dr. ir. M. A. P. Pertijs	Delft University of Technology
Dr. ir. P. L. M. J. van Neer	TNO

Listen, to yourself and to those with whom you are speaking.
Your wisdom then consists not of the knowledge you already have,
but the continual search for knowledge,
which is the highest form of wisdom.

Jordan B. Peterson

Contents

Contents

Contents

1

Introduction

1

1.1. Flow sensors

Flow metering in many industrial settings is desired and often legally required for monitoring, in real time, the performance of complex industrial processes. Reliable flow meters are therefore essential. Several physical phenomena are exploited to design and build different kinds of flow metering sensors, each with its advantages and disadvantages. An overview of common flow meters is given below.

1.1.1. Variable area flow meters

These are one of the first flow metering technologies ever developed. However, due to their operational principle, these sensors can only be installed in straight upwards pipelines. They consist of a conically-shaped pipe (i.e. variable diameter) section, within which a special floater material, which also has a conical shape, is placed. During flow, this floater moves upwards and downwards freely until equilibrium of all forces acting on it (i.e. gravity, buoyancy and drag) is reached. Finally, the orifice area that is created between the inner diameter of the pipe and the outer diameter of the floater material is a proportional indicative of the desired flow speed [1].

Variable area flow meters may be used to measure flow speed of liquids and gases. They report an accuracy that is usually between $1 - 4\,\%$. Moreover, their operation is entirely mechanical and thus does not require external power supplies.

However, this sensor also has certain disadvantages. Its design, i.e. pipe dimensions and floater material are fluid (density, viscosity), pressure and temperature dependent. Changes in fluid pressure and temperature relative to design conditions, which are very typical to occur, always require to apply a correction factor on the reported values. On the other hand, flow speeds below $10\,\%$ of the flow measurement range report very high uncertainties, and highest measurement accuracy is only achieved when measuring flow speeds above $50\,\%$ of the full measurement range. Furthermore, due to its mechanical operation principle, the sensor does not perform correctly in pulsating or fluctuating flows, or when there are solid particles on the pipe line.

1.1.2. Electromagnetic flow meters

This kind of sensor makes use of Faraday's law of electromagnetic induction, which states that a conductive material, of length L, moving with a certain speed v, through a magnetic field with a magnetic flux density B, produces a voltage difference U, which is proportional to these parameters:

$$U = B.L.v. \tag{1.1}$$

In essence, an electromagnetic flow meter consists of usually two coils wrapped around a custom-made non-conductive tube (or liner). These coils produce a magnetic field with a flux density across the pipeline. Two electrodes are used to measure the voltage difference U generated by the electrically conductive liquid flowing through the pipeline and therefore through the magnetic field. Then, Eq. 1.1 is used to estimate the desired flow speed v of the liquid [2].

This kind of sensors is usually very reliable, and has a high measurement accuracy (between $0.2 - 0.3\,\%$) and a high repeatability. Furthermore, flow measurements may be performed bi-directionally, with a partially-filled pipe section, and they are independent of the flow profile and the fluid viscosity. They also report good performance at low flow speed conditions. Moreover, the sensor design is simple and consists of no moving parts. Therefore, its installation is straightforward. Also, it can operate in a wide range of pipe sizes, as well as in a wide range of liquid temperature and pressure.

However, this sensor also has some disadvantages. It operates based on electromagnetism, thus it is limited to measure the flow speed of conductive liquids only. Therefore, it cannot be used to measure flow speeds of liquids such as hydrocarbons or gases. Moreover, pipe (or liner) properties may affect the accuracy and repeatability of the measurements: at high temperatures, usually used plastic liners may expand, which modifies the pipe cross-section and therefore introduce measurement errors. On the other hand, gas bubbles introduce a significant effect on the measurements. Since the sensor reports a total volume flow, which may consist of gas and liquid, it cannot distinguish them separately, which usually leads to an overestimation of the flow speed. Furthermore, the accuracy of the sensor decreases drastically towards low flow speeds, and their installation near other electromagnetic devices may cause interference with the flow measurements.

1.1.3. Coriolis mass flow meters

As the name suggests, these sensors exploit the Coriolis effect to measure mass flow rate. The sensor consists of a pipe section with two straight tubes inside. The inertia of the fluid moving through these tubes causes them to deflect from their straight position due to the Coriolis effect. This deflection is measured by placing a sensor at the beginning of the system, and another one at the end. During flow, the two measured signals have a phase shift relative to each other, which is proportional to the mass flow rate [3].

For liquids and special gases, the accuracy of these sensors is usually reported to be $\approx 0.1\,\%$ and $0.35\,\%$, respectively. Due to the nature of the physical principle, bi-directional measurements are possible. Furthermore, with this sensor is also possible to measure other factors such as density and temperature. Moreover, they are independent of the electrical conductivity of the liquid.

Nevertheless, the measurement is dependent on the Reynolds number (Re), and the sensor presents high instabilities at zero-flow conditions. Its operation is limited only to a range of gases, and it is not entirely suitable to work within large pipe diameters.

1.1.4. Vortex flow meters

This sensor makes use of the Kármán vortex street principle to measure flow speed. It consists of a pipe section with a bluff body (i.e. a square-shaped rod) along the cross-section of the pipe. During flow, this piece induces vortex shedding. A sensor placed behind the bluff body records the frequency f at which these vortexes are induced. This frequency is then proportional to the desired flow speed v [4]:

1

$$v \approx f. \tag{1.2}$$

Vortex flow meters are able to measure flow speeds of conductive and non-conductive liquids, including gases. Their measurement accuracy usually ranges between $0.75 - 2\,\%$. However, they do not operate properly on liquids with a viscosity larger than $10\,\mathrm{cP}$. Also, their performance depends on the Reynolds number since they can operate properly only in turbulent flow regimes ($Re > 20000$). Moreover, their design is fluid, pressure and temperature dependent. They are also not suitable to operate in partially-filled pipes or to measure multi-phase flows. Furthermore, measurements should be performed in sections of the pipe line where no sludge/sediments are accumulated, and where other components, such as valves or pumps, may induce extra vortexes. These factors finally limit the sections of the pipeline where the sensors could be installed.

1.2. Ultrasonic flow meters

Ultrasound is the area of physics that implements mechanical waves with a frequency content beyond $20\,\mathrm{kHz}$ (i.e. inaudible to humans) in order to measure mechanical properties of the medium in which they propagate. Its applications span from medical imaging of the (human) body, to non-destructive evaluation (NDE) of solid structures. One relevant application of ultrasound is the industrial monitoring of liquid and/or gas flow through pipelines.

There are many reasons why ultrasonic flow meters are the common choice in many industrial processes. These sensor are relatively cheap and their footprint on the pipeline is much smaller compared to other flow sensor technologies. Also, they are able to perform measurements without disturbing the flow and over a wide range of pipe sizes, liquids and gases. They are used in different industries, i.e. oil & gas, power generation, water & wastewater, chemical, food & beverages, pharmaceuticals, paper & pulp and semiconductor. Therefore, there is a logic interest in improving and developing better ultrasonic flow sensors.

Current sensors consist of single-element transducers which generate acoustic waves that propagate in both directions of the flow, i.e. upstream and downstream. The transit time difference between these two waves is then proportional to the flow speed [5].

The world-wide flow meter market totalled M€ 7300 in 2018 and is projected to reach M€ 11900 by 2026, having a compound annual growth rate of $6.3\,\%$ from 2019 to 2026. The ultrasonic flow meter market makes up about $10\,\%$ of this. There are two main configurations of ultrasonic flow meters: in-line and clamp-on. In-line ultrasonic meters account for two-thirds of revenues, with the remainder divided between clamp-on and insertion meters. The growth in this market is driven by the use of ultrasonic flow meters for custody transfer applications and the resulting product development of accurate multi-path meters [6].

1.2.1. In-line flow meters

Considering a pipe with an inner diameter ID, filled with a liquid with a sound speed c_l, and a pair of single-element transducers oriented under an angle θ relative to the flow direction (i.e. the pipe axis), as shown in Fig. 1.1, the acoustic wave propagating downstream the flow would be detected by the other transducer after a transit time given by:

$$T_d = \frac{ID}{sin(\theta)} \frac{1}{c_l + v_m.cos(\theta)}, \tag{1.3}$$

where v_m is the desired flow speed. Similarly, the acoustic wave propagating upstream would be detected by the other transducer after a transit time given by:

$$T_u = \frac{ID}{sin(\theta)} \frac{1}{c_l - v_m.cos(\theta)}. \tag{1.4}$$

From Eqs. 1.3 and 1.4, it is possible to compute the flow speed v_m from the measured transit times:

$$v_m = \frac{ID}{sin(2\theta)} \frac{T_u - T_d}{T_u.T_d}. \tag{1.5}$$

To improve measurement accuracy, in-line flow meters might have more than one pair of transducers placed around the spool piece section that conforms the sensor. The accuracy of this type of sensor usually ranges between $0.15 - 0.5\,\%$. To align the different transducer pairs, the manufacturer needs to know the size of the pipeline in which the sensor will be installed, as well as the range of liquids (i.e.
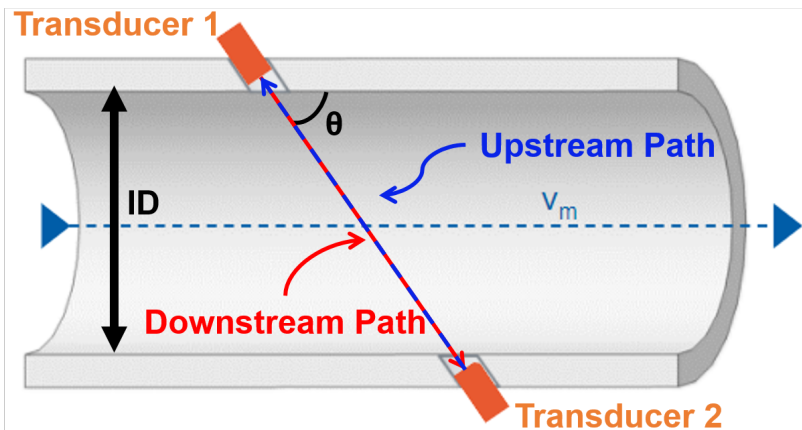
Figure 1.1: Cross-section of an ultrasonic in-line flow meter arranged in a pipe with an inner diameter ID. The single-element transducers are oriented under an angle θ relative to the pipe axis. The fluid moves towards the right with a speed v_m. Modified from [7].

sound speeds) that will be flowing through the pipeline. Nevertheless, these parameters are not always known in practice. Furthermore, to install these sensors, it is necessary to temporarily interrupt the fluid flow, which might introduce leakage, fouling, pressure drops or energy losses in the pipeline [8]. Therefore, their installation might compromise safety. Also, for economical reasons, interrupting the flow is something not desirable in many industries. Thus, clamp-on flow meters become a more viable option.

1.2.2. Clamp-on flow meters

Current sensors consist of one pair of single-element transducer placed along the outside of a pipe wall, as seen in Fig. 1.2, which avoids contamination, leakage, fouling, pressure drops or energy losses within the pipeline. They are usually cheaper and more flexible than their in-line flow counterparts, and their installation can be permanent or not. Most of them also operate on the same transit time difference principle of Eq. 1.5.

However, their accuracy is usually no better than 2.5 % [5, 8, 9]. Furthermore, several complex factors need to be carefully considered and taken into account for proper operation. These are explained in more detail below.

1.3. Challenges of ultrasonic clamp-on flow metering

Even though the flow measurement concept of ultrasonic clamp-on flow meters is relatively straightforward, different complex and physical phenomena occur, which
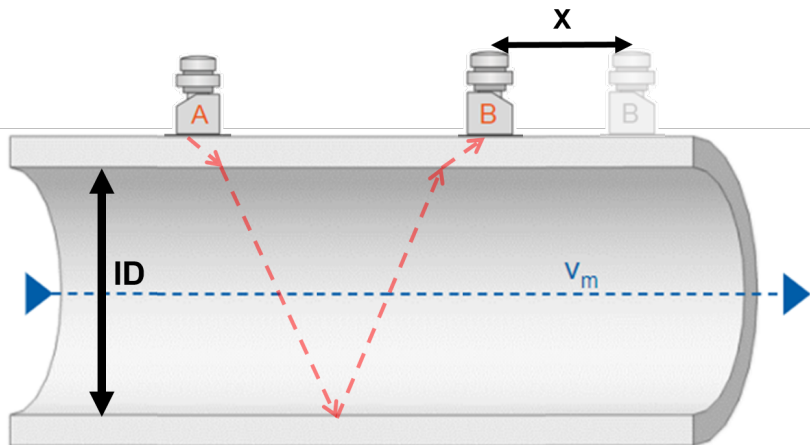
Figure 1.2: Cross-section of a current ultrasonic clamp-on flow meter arranged on a pipe wall along the pipe axis. The fluid moves towards the right with a speed v_m. Prior to metering, the single-element transducers are calibrated by fixing one of them and manually moving the other one along the pipe until there is no offset distance X and the acoustic beam (in red) gets recorded at the right position. Modified from [7].

complicate the measurement process at a relatively early stage.

1.3.1. Elastic wave propagation
In contrast to ultrasonic in-line flow meters, clamp-ons are not in direct contact with the liquid. Instead, they are mechanically coupled to the outer surface of the pipe wall. Thus, acoustic (longitudinal) waves generated by the transducers will induce elastic wave propagation in the pipe wall, where not only wave mode conversion occurs (i.e. bulk longitudinal and shear waves get excited), but also dispersive guided waves get excited. All theses kinds of waves propagate with different sound speeds, and may also refract into the liquid under different angles, creating a very intricate and complex interference pattern, from which it becomes very challenging to identify the flow-sensitive information.

1.3.2. Acoustic signal
The efficiency of ultrasonic clamp-on flow meters is relatively low compared to their in-line counterparts. The main reason for this is the very abrupt acoustic impedance (Z) boundary between the metal pipe wall ($Z \approx 50\,\text{MRayl}$) and the liquid ($Z < 3\,\text{MRayl}$), from which up to $90\,\%$ of the impinging acoustic energy may be reflected back into the pipe wall and the transducer, and not refract into the liquid. This results in measured signals with very low signal-to-noise ratio (SNR). Therefore, it is very challenging for the same ultrasonic clamp-on flow meter to operate properly in a wide range of situations, especially those involving highly attenuating liquids.

1.3.3. Guided waves in the pipe wall
As mentioned earlier, in an ultrasonic clamp-on flow meter configuration, the pipe wall is inevitably coupled to the resonance system, and when excited mechanically by the transducers, it acts as a waveguide. The waves generated in a waveguide are usually known in literature as Lamb waves [10], and they have a dispersive behavior, i.e. their wavelength (sound speed) is frequency dependent. For a pipe geometry, three types of guided wave modes exist: longitudinal, flexural and torsional. Each type of wave mode propagate within the pipe wall with both in-plane and out-of-plane particle motion.

   These waves represent the main source of measurement error of ultrasonic clamp-on flow meters. They may interfere with the longitudinal wave that refracts from the liquid and carries information about the flow, and introduce and absolute errors in the transit time difference between the upstream and downstream time signals (see Fig. 1.3), and because they are coherent, they cannot be averaged-out during measurements. Furthermore, the amount of possible Lamb wave modes that can be excited is proportional to the thickness of the pipe wall and to the excitation frequency of the transducers, which also increases the probability of interference (see Fig. 1.4).

   For a certain transducer excitation frequency f, the generation of a particular Lamb wave mode, with a particular sound speed $c(f)$, is maximized when the incidence angle of the acoustic beam impinging from the liquid and into the pipe
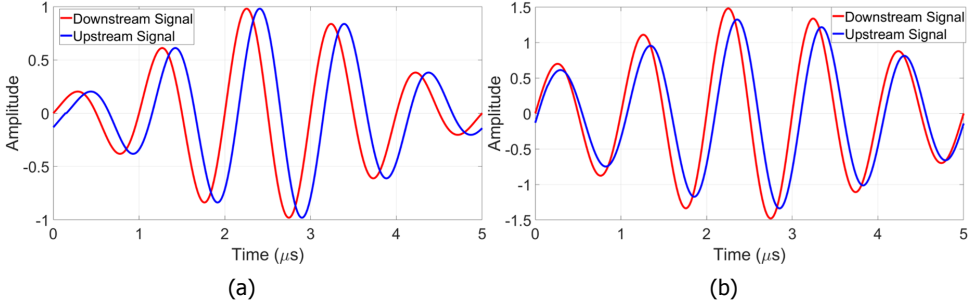
Figure 1.3: Upstream and downstream signals for an ultrasonic clamp-on flow measurement (a) without (b) with the interference of dispersive guided waves from the pipe wall. The phase shift between each pair of signals has been exaggerated to highlight the absolute error in transit time difference introduced by the guided waves.

wall is larger than the critical angle of the wave mode, as given by Snell's law:

$$\theta_{\text{crit}} = \arcsin \frac{c_{\text{liquid}}}{c(f)}. \tag{1.6}$$

In Eq. 1.6, c_{liquid} represents the sound speed of the liquid. As a consequence of Eq. 1.6, the practical range of incidence angles of acoustic beams is limited during ultrasonic clamp-on flow metering, which directly restricts the sensitivity of the acoustic beam, and therefore the sensor, to the flow.

1.3.4. Calibration

Prior to operation, the transducers in Fig. 1.2 need to be manually placed at the right position along the pipe wall (i.e. calibrated). This calibration distance depends on the mechanical properties of the pipe, such as diameter, sound speeds and wall thickness, as well as on the sound speed of the liquid. All these parameters need to be used as input by the operator, and in most practical cases they are
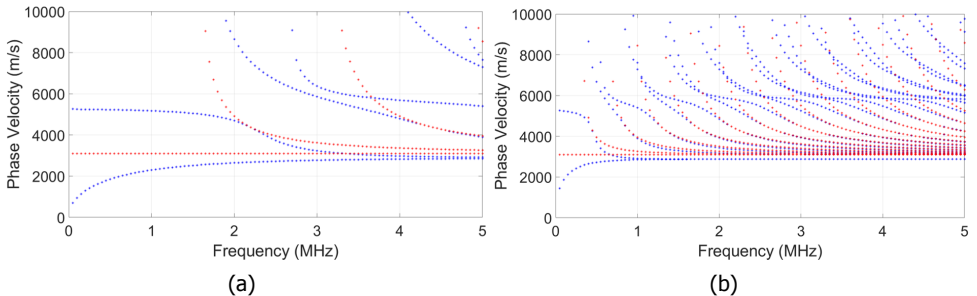
Figure 1.4: Longitudinal (blue) and torsional (red) Lamb wave modes corresponding to a (a) 1 mm-thick and (b) 5 mm-thick stainless steel pipe wall.

known with limited accuracy, which results in beam misalignment. Furthermore, temperature changes of the pipe and/or the liquid also modify their properties. These are not accounted for during calibration and are therefore another cause of beam misalignment.

The combination of all these factors make the design of ultrasonic clamp-on flow meters very hard.

1.4. More challenges of ultrasonic flow metering

Next to the challenging issues described in the previous section, other factors should be taken into account in the design of ultrasonic flow meters.

Ultrasonic flow sensors are designed based on the principle of reciprocity. This means that all of its components (transducers, mechanical parts, electronics), with the exception of the flow, should report the same response during upstream and downstream measurements. Therefore, in principle, at zero-flow conditions, the measured upstream and downstream time signals should overlap completely and report no relative phase shift. However, in practice, some delay between both signals is always measured. This value is referred to as the zero-flow error of the sensor. It is very challenging to control the magnitude of the zero-flow error as it depends on very complex factors such as the piezo-elements themselves and on the electronic components of the system. Also, solid particles and gas bubbles present in the flow scatter the acoustic energy, which affect, in a nonlinear way [11], the zero-flow error of the sensor.

In practice, very small transit time differences between upstream and downstream signals is always measured. At medium flow speeds, this value is usually in the order of nanoseconds. Nevertheless, it could be as low as a few picoseconds when measuring very low flow speeds. High sampling rates are necessary to be able to measure these very small transit time differences, which is expensive and requires more computer memory.

Moreover, it is also very difficult for current ultrasonic clamp-on flow meters to operate properly for a wide range of liquids. Because of the large span of sound speeds of liquids, the sensor (the acoustic beam) should be manually aligned for every new liquid and/or for changes in pressure or temperature. On top of this, SNR may be seriously affected by highly attenuating liquids.

Flow turbulence may also decrease SNR by reducing the effective available bandwidth of the system, especially if the frequency content associated to the flow itself lays within the bandwidth of the metering system.

System nonlinearities may also affect the accuracy of ultrasonic flow meters. For instance, ultrasonic flow meters of gases usually implement high input voltages to counteract the poor acoustical impedance matching between the transducer and the flowing gas. This may induce nonlinear wave propagation, and Eq. 1.5 may no be entirely valid, especially for measurements of high flow speeds.

1.5. Matrix transducers as ultrasonic clamp-on flow meters

A series of piezo-electric elements arranged next to each other along one axis may form a linear/phased ultrasonic transducer array. In contrast to single-element transducers, with an array configuration, the phase and amplitude of the input signals on the individual piezo-elements may be manipulated to optimize the acoustic loading and beam-form and steer the acoustic beams [12]. Their versatility makes them present in a very wide range of medical and industrial applications. Furthermore, the arrangement of the piezo-elements may also be performed along two axles to achieve a matrix transducer array, which offers one more degree of freedom.

Matrix transducer arrays may be exploited to tackle the limitations of current ultrasonic clamp-on flow meters. They may unlock the potential of a completely new technological portfolio to achieve high-precision self-calibrated ultrasonic clamp-on flow metering, where not only flow may be measured but also pipe and liquid properties, which might render manual calibration of the sensor unnecessary in the future. This technology would make the performance of ultrasonic clamp-on sensors more comparable to that of in-line sensors, and considerably expand their range of applicability.

As the name suggests, a matrix transducer array consists of a series of piezo-elements arranged in two directions (azimuth and elevation), and with a constant inter-element separation (pitch). Each individual element may be controlled separately, which allows to control the amplitude and phase of the input signals. Usually, the phases are manipulated to steer the acoustic beams, while the amplitudes are manipulated to shape them. This is not possible with single-element transducers. However, the demand on the electronic driving components is much higher. Matrix transducer arrays have shown great performance in different areas of ultrasound, especially in medical imaging [13, 14]. As an ultrasonic clamp-on flow sensor, a matrix transducer may be designed to operate with a high-enough SNR with the purpose of measuring the flow speed of a wide range of liquids [15].

Furthermore, spatial placement of transducer elements on the pipe wall allows to exploit Lamb waves for estimating its mechanical properties. Exciting guided waves with one matrix array, and measuring them with the other one allows to analyze the recorded spatio-temporal $(t - x)$ data in the frequency - horizontal wavenumber (i.e. $f - k_x$) domain. Here, the measured wave modes may be compared with analytical expressions of Lamb waves, and the theoretical trends that optimally match the measured ones would therefore provide the mechanical properties of the pipe wall. Moreover, excitation and measurement of guided waves around the circumferential direction of the pipe may be implemented to extract its inner and outer diameter [16]. With these procedures, the pipe is completely characterized. Then, considering the round shape of the pipe and the transducer elements along its circumferential direction, it may also be possible to excite a plane wave and implement a pulse-echo approach to estimate the sound speed of the liquid.

Provided these measured properties of the pipe and the liquid, the travel path

of the acoustic beams is completely known. Therefore, beam steering capabilities of matrix arrays [17] can be exploited to achieve automatic beam alignment and therefore maximum signal level. Moreover, this alignment can be kept under changing pressure and/or temperature conditions, flow speeds and/or flow composition. Also, this feature allows to account for pipe imperfections (i.e. wall thickness variance along the pipe, corrosion, roundness, etc.). On the other hand, by steering the ultrasound beams at different angles, multiple paths along the flow profile can be realized (Fig. 1.5), which extends the ability of ultrasonic clamp-on flow sensors towards flow profile measurements, which are until now only achievable by means of multiple in-line transducer pairs [18].

In addition, with transducer arrays, smart excitation schemes may be implemented during flow measurements to suppress, in transmission, problematic guided waves in the pipe wall that may overlap in time with the longitudinal wave refracting from the liquid and carrying information about the flow [19]. Moreover, filtering guided wave modes in reception also becomes available, and the absolute errors introduced by them may be reduced.

Until now, flow profile measurements have only been possible by placing multiple single-element transducers, in an in-line configuration around two pipe cross-sections, and using one plane of transducers as transmitters, and the other one as receivers. This way, the flow speed is measured from several directions/angles. Then, flow profiles are usually reconstructed by implementing a tomographic reconstruction algorithm [18]. However, the installation of many single-element transducers invasively around a pipe section requires a lot of mechanical precision, making the sensor more prone to human error and compromising pipeline safety. The multi-path measurement capabilities of matrix transducer arrays as ultrasonic clamp-on flow meters would make it possible to measure flow profiles in a non-invasive manner. These measurements are largely useful in industries such as the Oil & Gas, to accurately measure the amount of product distributed. They are also important for custody transfer and/or monitoring of different industrial processes.
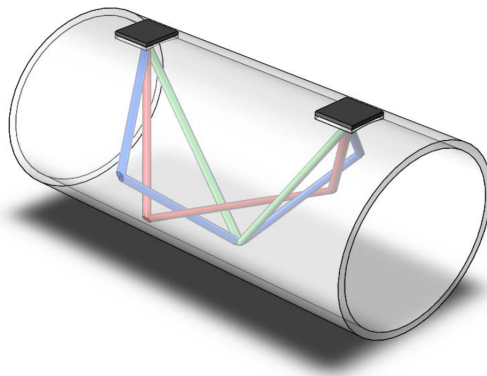
Figure 1.5: Multi-path ultrasonic clamp-on flow measurement concept with two matrix transducers. From the different measurement paths, a flow profile may be reconstructed.

1

Nevertheless, a properly designed sensor is needed first, and the ideas to achieve it are outlined next.

1.6. Thesis outline

Provided the clear benefits of matrix transducers in revolutionizing ultrasonic clamp-on flow metering, the following chapters of this book describe and discuss the steps for designing, manufacturing and characterizing the sensor, as well as the techniques to achieve a self-calibrated ultrasonic clamp-on flow meter.

Chapter 2 describes in detail the acoustic requirements of the desired flow sensor, i.e. its measurement accuracy and operational range (pipe dimensions and range of liquids). Based on these, the matrix array requirements, i.e. aperture, number of elements, pitch, operational frequency range, acoustic stack, are also defined [15]. The effect of guided Lamb waves in the pipe wall and the need to suppress them is also taken into account in the design. Furthermore, in this chapter is described the electronic design of an application-specific integrated circuit (ASIC) mounted on PCB to drive the designed transducer array and to read-out its output.

Chapter 3 describes a developed method for clever transducer array excitation with the purpose of selectively suppressing the generation of guided waves in solid geometries, such as plates and pipes [19]. Based on the manipulation of the amplitude and phase of each individual array element, the method operates as a transmission filter in the Fourier domain taking into account the fastest expected guided wave mode. This method has a direct application provided the absolute error that guided waves introduce in ultrasonic clamp-on flow measurements.

Chapter 4 describes in detail three proposed measurements to characterize properties of the pipe and the liquid, and therefore achieve automatic calibration of the sensor prior to initiating flow measurements.

The first measurement consists in exciting guided waves in the pipe wall with one of the arrays, and recording them with the other array. The recorded time-space ($t - x$) data is translated into the $f - k_x$ domain, where the dispersion curves of the propagating wave modes are observed. These dispersive trends are intrinsically related to three pipe wall parameters: bulk longitudinal and transversal wave speed, c_L and c_T, respectively, and wall thickness, h. Theoretical dispersion curves are compared with the measured dispersive trends, and a fitting error is defined to identify the dispersion curve, and therefore the pipe parameters, that best match the measured trends. The second measurement consists in exciting a guided wave around the pipe wall, and measuring its transit time after propagating a full circumference. Given the parameters estimated from the first auto-calibration measurement, the sound speed of the recorded guided wave mode is known. Therefore, after performing dispersion correction on the recorded signal, the inner and outer diameter of the pipe are estimated. The third measurement consists in performing a pulse-echo measurement considering array elements in the circumferential direction of the pipe. Provided that all travel paths are known at this point, the sound speed of the liquid can be estimated by measuring the transit time of the echo. Simulation and measurement results of the implementation of these auto-calibration procedures are also presented in this chapter [16].

1

In Chapter 5 is presented a new method to estimate flow speed by combining the advantages of zero-crossing and cross-correlation algorithm approaches. This clever combination manages to reduce both the offset and random errors usually present during ultrasonic flow metering.

Chapter 6 describes flow measurements performed with a first prototype consisting of two 36-element linear arrays clamped on top of a stainless steel pipe wall. The fabrication of these arrays was based on the design presented in Chapter 2. Furthermore, the acquisition and signal processing steps performed to achieve a highly reciprocal system are shown in detail. Moreover, flow measurement results are presented for two scenarios: longitudinal and shear waves in the pipe wall. These results are regarded as another key proof of the potential of transducer arrays to perform self-calibrated ultrasonic clamp-on flow measurements.

In Chapter 7, the idea of exploiting nonlinear wave propagation for the improvement of ultrasonic flow measurements is presented and developed. Provided a high-enough input voltage on the transducers, nonlinear wave propagation effects become significant. Furthermore, from flow measurements and simulations it was found that the transit time differences computed from the fundamental and the 2nd harmonic bandwidths are very similar. Therefore, with the combination of both of them, a more precise estimate of transit time difference, and therefore flow speed, was achieved [20]. Moreover, the applicability and practicality of the method is also discussed in detail.

Chapter 8 presents a method to simultaneously extract the bulk wave sound speeds and thickness of a waveguide from the measured (or simulated) dispersion curves. Furthermore, error functions are defined to carefully visualize and evaluate the sensitivity of a particular wave mode to each of the parameters, which ultimately provide a more quantitative sense of (un)certainty about them.

Chapter 9 summarizes the achievements of the performed research, including its future impact and suggestions for future and related work.

References

[1] S. Brauers, *Variable area flowmeters,* KROHNE Academy Online (2012).

[2] S. Brauers, *Electromagnetic flowmeters,* KROHNE Academy Online (2012).

[3] S. Brauers, *Coriolis mass flowmeters,* KROHNE Academy Online (2012).

[4] S. Brauers, *Vortex flowmeters,* KROHNE Academy Online (2012).

[5] R. C. Baker, *Flow measurement handbook: industrial designs, operating principles, performance, and applications* (Cambridge University Press, 2005).

[6] K. Yeware and E. Prasad, *Global flow meter market outlook – 2026,* https://www.alliedmarketresearch.com/flow-meter-market (2019).

[7] S. Brauers, *Ultrasonic flow meters - liquids,* KROHNE Academy Online (2012).

[8] M. Sanderson and H. Yeung, *Guidelines for the use of ultrasonic non-invasive metering techniques,* Flow. Meas. Instrum. **13**, 125 (2002).

[9] D. V. Mahadeva, R. C. Baker, and J. Woodhouse, *Further studies of the accuracy of clamp-on transit-time ultrasonic flowmeters for liquids,* IEEE Trans. Instrum. Meas. **58**, 1602 (2009).

[10] J. L. Rose, *Ultrasonic guided waves in solid media* (Cambridge University Press, 2014).

[11] R. Thuraisingham, *Sound speed in bubbly water at megahertz frequencies,* Ultrasonics **36**, 767 (1998).

[12] C. H. Sherman and J. L. Butler, *Transducers and Arrays for Underwater Sound*, Vol. 4 (Springer, 2007).

[13] Z. Yu, S. Blaak, Z.-Y. Chang, J. Yao, J. G. Bosch, C. Prins, C. T. Lancee, N. De Jong, M. A. P. Pertijs, and G. C. M. Meijer, *Front-end receiver electronics for a matrix transducer for 3-d transesophageal echocardiography,* IEEE Trans. Ultrason. Ferroelectr. Freq. Control **59**, 1500 (2012).

[14] C. Chen, S. B. Raghunathan, Z. Yu, M. Shabanimotlagh, Z. Chen, Z.-y. Chang, S. Blaak, C. Prins, J. Ponte, E. Noothout, H. J. Vos, J. G. Bosch, M. D. Verweij, N. de Jong, and M. A. P. Pertijs, *A prototype pzt matrix transducer with low-power integrated receive asic for 3-d transesophageal echocardiography,* IEEE Trans. Ultrason. Ferroelectr. Freq. Control **63**, 47 (2015).

[15] J. Massaad, D. van Willigen, P. van Neer, N. de Jong, M. Pertijs, and M. Verweij, *Acoustic design of a transducer array for ultrasonic clamp-on flow metering,* IEEE Int. Ultrason. Symp. , 1133 (2019).

[16] J. Massaad, P. L. M. J. van Neer, D. M. van Willigen, M. A. P. Pertijs, N. de Jong, and M. D. Verweij, *Towards a calibration-free ultrasonic clamp-on flow meter: Pipe geometry measurements using matrix arrays,* Proc. Meet. Acoust. **39**, 1 (2019).

[17] D. H. Turnbull and F. S. Foster, *Beam steering with pulsed two-dimensional transducer arrays,* IEEE Trans. Ultrason. Ferroelectr. Freq. Control **38**, 320 (1991).

[18] D. Kurniadi and A. Trisnobudi, *A multi-path ultrasonic transit time flow meter using a tomography method for gas flow velocity profile measurement,* Part. Part. Syst. Charact. **23**, 330 (2006).

[19] J. Massaad, P. L. M. J. van Neer, D. M. van Willigen, M. A. P. Pertijs, N. de Jong, and M. D. Verweij, *Suppression of Lamb wave excitation via aperture control of a transducer array for ultrasonic clamp-on flow metering,* J. Acoust. Soc. Am. **147**, 2670 (2020).

[20] J. Massaad, P. van Neer, D. van Willigen, N. de Jong, M. Pertijs, and M. Verweij, *Feasibility of ultrasonic flow measurements via non-linear wave propagation,* IEEE Int. Ultrason. Symp. , 1 (2018).

2

Design of a matrix transducer array for self-calibrated ultrasonic clamp-on flow measurements

Common ultrasonic clamp-on flow meters consist of two single-element trans-ducers placed on the pipe wall. Flow speed is measured non-invasively, i.e. without interrupting the flow and without perforating the pipe wall, which also minimizes safety risks and avoids pressure drops inside the pipe. How-ever, before metering, the transducers have to be carefully positioned along the pipe axis to correctly align the acoustic beams and obtain a well-calibrated flow meter. This process is done manually, is dependent on the properties of the pipe and the liquid, does not account for pipe imperfections, and becomes troublesome on pipelines with an intricate shape. Matrix transducer arrays are suitable to realize self-alignment and perform self-calibrated ultrasonic clamp-on flow measurements over a wide range of liquids and pipe sizes. The large number of matrix elements allows for advanced features such as two-dimensional beam steering, spatial filtering, and dedicated measurements of the mechanical properties of the pipe and liquid. Here is presented the acous-tic design of such a matrix array, including the required number of transducer elements in the axial and circumferential directions, and the layering of the acoustic stack and its dimensions. Furthermore, based on the proposed de-sign, a linear array was fabricated and acoustically characterized to prove its suitability for ultrasonic clamp-on flow metering.

2.1. Introduction

Ultrasonic flow meters are used in a wide range of industrial applications [3–5], and can be divided in two categories: in-line and clamp-on flow meters. The latter consist of two single-element transducers fixed along the outside of a pipe wall. Alternatingly, one transducer emits an ultrasound wave which is transmitted through the pipe wall and refracted into the liquid, where it can bounce one or more times before refracting back into the pipe wall and being received by the other transducer. The transit time difference between the signals recorded upstream and downstream is proportional to the flow speed [6], at least for small flow velocities.

Clamp-on flow meters have advantages compared to their in-line counterparts with transducers fixed inside the pipe wall. They can be installed without interruption of the flow and without the addition of extra pipe sections or making cuts through existing ones. Nevertheless, clamp-on flow meters also have disadvantages. For alignment of the transducers and calibration of the flow meter, a priori knowledge of the properties and geometry of the pipe, as well as the speed of sound in the liquid is needed. In practice, these values are uncertain and therefore limit the accuracy of the calibration and, consequently, the measurements. Alternatively, the transducers can be aligned using a manual calibration procedure, which is cumbersome, labour intensive and operator dependent.

Common clamp-on flow meters use a specific wave type in the pipe wall (typically a bulk shear wave, but in principle this may also be a bulk compressional wave). This wave will refract into the fluid to obtain information about the flow speed. However, it also excites Lamb waves in the pipe wall. These Lamb waves interfere with the compressional wave refracting back from the liquid and introduce an offset error in the transit time differences and hence in the measurement of the corresponding flow speed. To tackle this issue, current clamp-on flow meters may incorporate an absorbing layer placed around the pipe wall and in-between both transducers with the purpose of attenuating these interfering Lamb waves [7]. Unfortunately, this solution is not always practical, as access to the pipe is often limited, and/or the pipe is covered by material with other purposes, e.g. heat isolation.

A pair of matrix transducer arrays has the potential to tackle the current problems and limitations of clamp-on flow meters. Prior to flow measurements, the properties of the pipe and the liquid can be obtained using dedicated measurements. The measured parameters can be combined with electronic beam steering capabilities to create a self-calibrated flow sensor [8]. Furthermore, the transducer arrays can be cleverly excited to suppress, in transmission, the spurious Lamb waves in the pipe wall while maintaining a beam shape in the liquid with a clearly defined flat wavefront [9].

Here, the design of a matrix transducer array for ultrasonic clamp-on flow metering within a wide range of liquid and pipe parameters is presented. The design is supported by simulations and measurements.

2.2. Conventional and matrix ultrasonic clamp-on flow meters

Consider two single-element transducers with a certain axial separation x on the outer pipe wall, as shown in Fig. 2.1. Between each transducer and the pipe wall there is an angled wedge, which allows the compressional wave generated by the transducers to impinge the pipe wall under a certain angle with respect to the normal of the pipe surface. At the interface between the wedge and the pipe wall, wave mode conversion occurs, i.e. a compressional and a shear wave get excited in the pipe wall. Then, at the interface between the pipe wall and the liquid, wave mode conversion takes places again. Here, both waves in the pipe wall refract into the liquid as compressional waves. Given the sound speeds of common metal pipe walls and of common liquids, Snell's law predicts that shear waves in the pipe wall refract under higher angles into the liquid compared to the compressional waves in the pipe wall. For this reason, common ultrasonic clamp-on flow meters use wedges with sufficiently-high angles to only excite shear waves in the pipe wall (the compressional waves will be evanescent), so that the longest horizontal path in the fluid is obtained and the highest possible sensitivity of the acoustic wave to the flow is achieved. However, during propagation through such long travel paths, the beam also experiences more attenuation compared to shorter travel paths. The compressional wave propagating in the liquid may reflect a few times within the pipe before finally refracting back into the pipe wall and towards the other transducer. This procedure occurs both upstream and downstream, and given that the flow velocity adds-up vectorially to the velocity of the wave in the liquid, both signals will be recorded with a transit time difference that will finally be proportional to the desired flow speed, at least for flow speeds well below the wave speed in the fluid.

From Fig. 2.1 it can be understood that, to make an accurate flow measurement, the axial transducer separation x must be adjusted correctly. This parameter de-
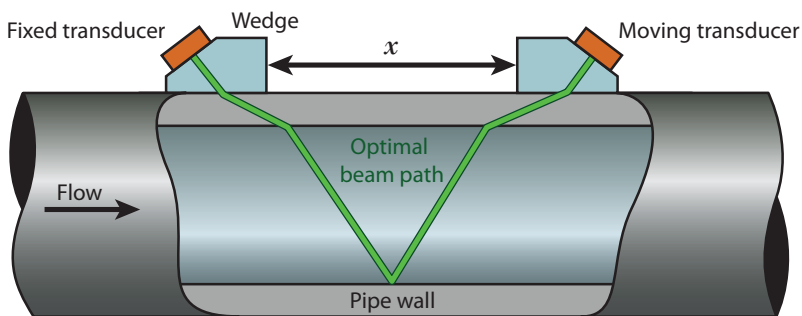
Figure 2.1: Sketch of a conventional ultrasonic clamp-on flow meter. Upon installation, one single-element transducer is manually moved along the pipe wall to find the optimal axial transducer separation x, which ultimately depends on the properties and geometry of the pipe wall, and on the sound speed of the liquid. The green line represents the acoustic beam path in the flow sensor. Here the beam bounces only once inside the pipe.

pends on the bulk wave sound speeds of the pipe wall, the pipe wall thickness, the pipe diameter, the sound speed of the liquid, and also on the number of bounces inside the pipe. Upon installation, the axial transducer separation x is found by fixing one of the transducers and manually moving the other one along the pipe wall until a peak amplitude is detected. In practice, this results in a cumbersome and time-consuming process for the operator, especially in hardly accessible places. Moreover, most of the parameters required for calibration are not exactly known and the procedure doesn't account for pipe imperfections (e.g. variations of pipe wall thickness and diameter, effects of corrosion). An ultrasonic clamp-on flow meter based on two matrix arrays could be used to measure the required parameters of the pipe and the liquid [8], and its beam steering capabilities can be applied to achieve correct alignment of the transducers without the need to manually move the transducers.

2.3. Basic requirements

2.3.1. Measurement accuracy

Currently available ultrasonic clamp-on flow meters are able to measure flow within an inaccuracy below $2\,\%$ [10]. It is reasonable to attempt to improve this value by designing a better sensor. Therefore, it is aimed to measure flow speeds above $1\,\mathrm{m/s}$ with an inaccuracy below $1\,\%$.

2.3.2. Parameter ranges of liquid and pipe

Because of the wide range of liquids used in practice, the sensor should be able to measure the flow of liquids with sounds speed ranging from $1000 - 2000\,\mathrm{m/s}$, and attenuation coefficients $\alpha \leq 1\,\mathrm{dB/MHz.cm}$ [11].

The pipelines of most industrial processes consist of metallic pipes, which was also assumed here. The sensor should operate on pipes with inner diameters ranging from $25 - 100\,\mathrm{mm}$. Next to that, a wide range of pipe wall thicknesses occurs in practice, therefore the sensor should be able to deal with pipe wall thicknesses ranging from $1 - 5\,\mathrm{mm}$.

2.3.3. Measurement of elastic parameters

Before performing flow measurements, the matrix array-based sensor should be able to estimate the elastic properties of the pipe and the liquid. These measured properties are then used as input to estimate the flow speed. As reported in [8], guided waves in the pipe wall would be very useful to measure the required parameters.

2.4. Derived requirements

2.4.1. Operational frequency range

Currently, clamp-on flow meters operate at central frequencies that may range between $0.2\,\mathrm{MHz}$ and $2\,\mathrm{MHz}$. This depends on the property range of the liquid (notably the sound speed and attenuation) and the pipe wall diameter (determining

the length of the beams). Hence, the bandwidth of the flow meter design is aimed at $0.2 - 2\,\text{MHz}$.

2.4.2. Pitch

To enable spatial filtering, beam steering, and the required calibration measurements, the matrix array should be properly spatially sampled, i.e. have a sufficiently small pitch. To ensure this, Lamb wave modes of the thickest considered stainless steel pipe wall ($5\,\text{mm}$) were analyzed. From this study, the pitch was set to $0.72\,\text{mm}$, which is half the wavelength of the slowest propagating Lamb wave mode at a frequency of $2\,\text{MHz}$ ($c_{\text{low}} = 2900\,\text{m/s}$).

2.4.3. Suppression level of the Lamb waves

To achieve the required accuracy of the flow measurements, it is necessary to suppress the amplitude of the spurious Lamb waves in the pipe wall down to a particular level relative to that of the wave refracting from the liquid.

A frequency independent study was performed, in which two 'clean' waveforms (5-cycle Gaussian-modulated sine waves with a center frequency of $f_c = 1\,\text{MHz}$), representing upstream and downstream signals in a flow measurement, were used. These were phase-shifted by a known amount that was also reconstructed by a cross-correlation algorithm. A linear relationship was obtained between the imposed phase-shift and the one computed by cross-correlation, as expected. However, when a spurious signal (a continuous sine wave with a center frequency of $f_c = 1\,\text{MHz}$) is added to the 'clean' waveforms, this relation is not linear anymore since the spurious signals introduce an offset error in the relative phase-shift between upstream and downstream signals. A slightly nonlinear relation between the amplitude of the spurious wave and the induced phase shift error was obtained. As Fig. 2.2a shows, the induced error is directly proportional to the amplitude of the
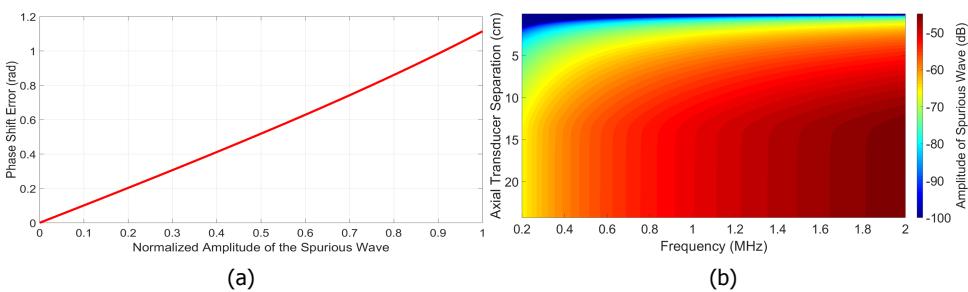
Figure 2.2: (a) Phase-shift error induced by spurious signals, versus the normalized amplitudes of these spurious signals. Normalization is performed with respect to the maximum amplitude of the 'clean' upstream and downstream signals. (b) Required amount of suppression of the spurious waves, versus frequency and axial transducer separation. The suppression is relative to the compressional wave refracting from the liquid, and indicates what is needed for measuring flow speeds above $1\,\text{m/s}$ within an inaccuracy of $1\,\%$.

spurious wave.

Next, it was needed to obtain the required amount of suppression for achieving a measurement inaccuracy of 1%. This made it necessary to estimate the phase-shift error that corresponds to the change in transit time difference when a flow speed of $1\,m/s$ changes by 1%. This was done for different frequencies and axial transducer separations. The obtained phase shift error estimations, in combination with the information in Fig. 2.2a, resulted in Fig. 2.2b, from which it can be seen that, at $1\,MHz$ and for axial transducer separations $\geq 5\,cm$, the amplitude of the Lamb waves needs to be $55\,dB$ below the amplitude of the compressional wave refracting from the liquid.

2.4.4. Signal-to-noise ratio
Current ultrasonic clamp-on flow meters perform flow measurements with a signal-to-noise ratio (SNR) as low as $20\,dB$. Therefore, it is desired aim to obtain a flow meter design that produces this minimum value of SNR within the desired frequency range and for all considered liquids.

2.5. Array aperture, coupling piece, and axial positioning on a pipe wall

2.5.1. Center frequency
We choose the center frequency of the array at $1\,MHz$, which is almost in the middle of the required frequency band of $0.2 - 2\,MHz$. This should be the frequency of the main thickness resonance mode. Moreover, the frequencies of all modes with lateral vibrations should have at least, three times this frequency [12].

2.5.2. Transducer array aperture: axial direction
Finite Element simulations using the software package PZFlex (Onscale, Redwood City, CA, USA) were performed for a clamp-on flow measurement setting with standard beam steering and focusing, see Fig. 2.3a, and a liquid with the highest considered attenuation ($\alpha = 1\,dB/MHz.cm$). For this case it was found that Lamb waves have amplitude levels that are $20\,dB$ below the amplitude of the compressional wave that refracts from the liquid (Fig. 2.3b). According to Section 2.4.3, it was therefore necessary to further suppress the Lamb waves by $35\,dB$ to achieve the desired flow measurement inaccuracy of 1%.

Because the flow sensor consists of transducer arrays, several signal processing techniques based on phase-shift and amplitude manipulation of the element signals could be exploited to suppress the generated Lamb waves in transmission [13–16]. Unfortunately, the element phases required for this suppression would add to the element phases required for beam steering, which would result in a significantly deformed acoustic beam. Therefore, it was decided to manipulate the element amplitudes, i.e. apply apodization, for Lamb wave suppression and use the element phase shifts for beam steering and focusing. This method was described in [9], where it was concluded that, for an array satisfying the given requirements, 37 piezo-elements are enough to generate an acoustic wave with a sufficiently smooth
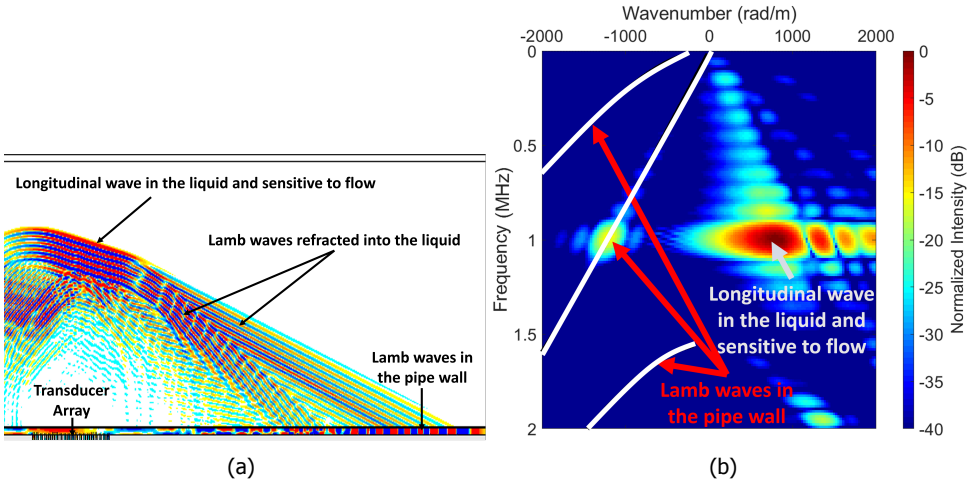
Figure 2.3: (a) Finite Element simulation of a transducer array with standard beam steering and focusing, on the bottom side of a 1 mm-thick stainless steel pipe for clamp-on flow measurements. (b) Magnitude in the wavenumber-frequency domain of the narrow-banded time signals recorded along the bottom pipe wall (i.e. along the same surface on which the array is located) of the geometry in (a). The Lamb waves have approximately 20 dB lower amplitude relative to the compressional wave that is refracted from the flow. The white lines represent the theoretical Lamb wave dispersion curves.

beam profile to achieve 35 dB suppression of the Lamb waves along the axial direction. At the same time, upon reception a beam having the same width as the receiving array aperture is obtained, which maximizes SNR during flow measurements (see more details in Chapter 3).

2.5.3. Transducer array aperture: circumferential direction

To calculate the pipe diameter, it is very important to accurately estimate the sound speeds in the pipe wall. In the design, an inaccuracy in sound speed of 1 m/s was aimed for. Assessing the situation in which two waves with propagation speeds of $c_{low} = 2900$ m/s and $c = 2901$ m/s would travel around a pipe with an inner diameter of 40 mm, an arrival time difference of 29 ns was obtained. Based on the relation in Fig. 2.2a, this translated into a relative amplitude level of around 0.08, i.e. a 22 dB lower amplitude of the Lamb waves. Next, the method described in [9] predicted that 17 elements are enough to achieve the desired suppression of the Lamb waves along the circumferential direction of the pipe.

2.5.4. Coupling piece

Current ultrasonic clamp-on flow meters excite shear waves in the pipe wall to achieve higher refraction angles in the liquids, and therefore improve beam sensitivity to the flow. The way to excite such waves is by impinging a compressional wave on the pipe wall beyond the critical angle for the refracted compressional wave. Without a coupling layer between the transducer and the pipe wall, such an

2

angle would be impractically high, and therefore difficult to achieve, due to similar compressional sound speed values of the transducer's piezoelectric material (PZT) and the metal pipe wall. To obtain shear waves in the pipe wall at much lower incidence angles, plastic wedges with a much lower compressional sound speed are commonly placed between the transducer and the pipe wall.

Nevertheless, the acoustic impedance of plastic ($Z_{\text{wedge}} \approx 2.5\,\text{MRayl}$) relative to that of the metal pipe wall ($Z_{wall} \approx 47\,\text{MRayl}$) might not guarantee the right performance for all required angles, since most of the impinging energy gets reflected back into the wedge. Therefore, it was necessary to consider a coupling material that had roughly the same compressional sound speed as plastic ($c_{\text{plastic}} = 2290\,\text{m/s}$) to achieve wave mode conversion at reasonably low incidence angles, but a much higher density than plastic ($\rho_{\text{plastic}} = 1.24\,\text{kg/m}^3$) to get sufficient energy into the pipe wall. Therefore, lead ($c_L = 2200\,\text{m/s}$, $\rho = 11200\,\text{kg/m}^3$) was chosen as the appropriate coupling material between the transducer array and the pipe wall.

2.5.5. Axial positioning

To measure flow for liquids with $c_{\text{liquid}} = 1000 - 2000\,\text{m/s}$ and $\alpha \leq 1\,\text{dB/MHz.cm}$, it was necessary to determine the appropriate axial separation between both transducer arrays. This value was found via ray tracing. Assuming compressional waves in the pipe wall and six bounces (v-shapes) of the beam in the liquid (Fig. 2.4a), and assuming shear waves in the pipe wall and two bounces of the beam in the liquid (Fig. 2.4b), it was found that an axial transducer separation of $80\,\text{mm}$ makes it possible to measure flow in both scenarios for the entire range of liquids considered, avoiding at the same time the critical angles for which this value goes to infinity (see Fig. 2.4c). Moreover, at this axial transducer separation, the acoustic beam width at the $-3\,\text{dB}$ level ($26.1\,\text{mm}$) is almost the same as the array aperture along the axial direction of the pipe ($26.6\,\text{mm}$) [9].

2.6. Acoustic stack design of the array

In this section, the design process of the acoustic stack of the transducer arrays for ultrasonic clamp-on flow metering is explained. This process has been partially described in [2].

2.6.1. Signal level

An important check of the suitability of the transducer array are the achievable SNR levels. With the acoustic path shown in Fig. 2.4a (or in Fig. 2.4b), the expected SNR levels can be determined via the sonar equation

$$V_{\text{open}} = V_{\text{in}} T_t T_r T (RW)^{2b-1} W. \tag{2.1}$$

Here, V_{open} is the open-clamp voltage measured at the receiving transducer, V_{in} is the input voltage on the transmitting transducer (in this case $V_{\text{in}} = 5\,\text{V}$), T_t and T_r are the transmit and receive transfer functions of the transducer array, respectively, T is the product of the transmission coefficients at all interfaces in Fig. 2.4a (or in
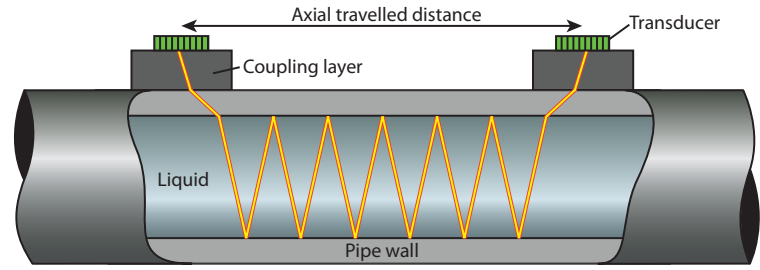
(a)
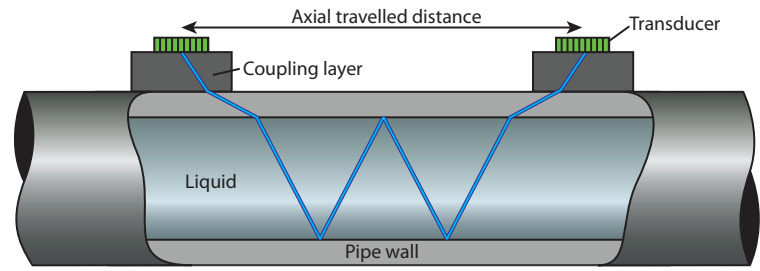
(b)
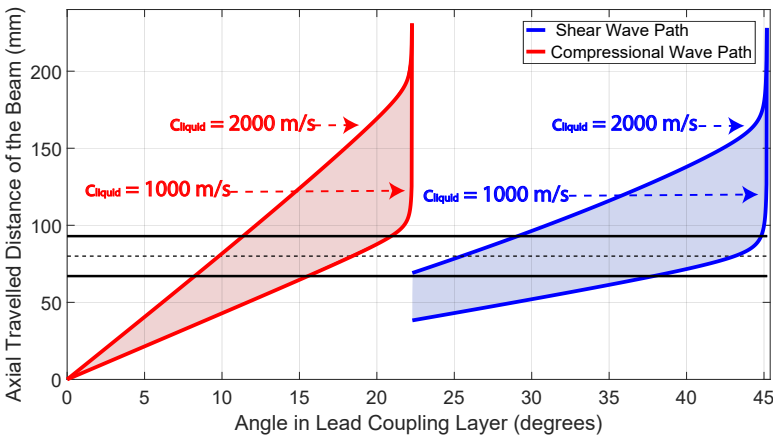
(c)

Figure 2.4: Travel path of an acoustic beam during ultrasonic clamp-on flow measurements using (a) compressional, and (b) shear waves in the pipe wall. (c) Axial travelled distance of the beam (equal to the axial transducer separation) versus the beam angle in the coupling layer, for a pipe with an inner diameter of 40 mm. The black dashed line represents the physical location of the center of the receiver transducer array (80 mm), and the black solid lines give the boundaries of its aperture in the axial direction.

2

Fig. 2.4b) through which the acoustic wave propagates, R is the reflection coefficient of the liquid-pipe interface, b is the number of bounces (v-shapes) of the acoustic wave within the pipe, and $W = e^{\alpha L} G D$, where α is the attenuation coefficient of the liquid and L is the total length of the acoustic travel path in the fluid, G is the focusing gain factor, and D accounts for the diffraction of the propagating wave through the liquid. Here, G is set equal to 1 because the width of the transmitted beam and the received beam are both approximately equal to the aperture of the transducers, and D is approximated using the expression given in [17].

2.6.2. Finite Element model

The software package PZFlex was used to simulate the waves in the various materials of the configuration. In PZFlex, the linear wave equation is solved. Linear isotropic elasticity was assumed for the pipe wall and the coupling piece. The anisotropic piezo-electric constitutive equations were solved for the piezo-materials. Damping was considered to be visco-elastic and to be present in all materials, and its effects on wave propagation were mainly noticed in the backing material behind the transducer, and in the liquid. Moreover, to ensure proper spatial sampling, the lowest expected wavelength at $1\,\mathrm{MHz}$ was estimated, and the mesh grid consisted of square elements with side length of $1/30^{\mathrm{th}}$ of this minimum wavelength.

2.6.3. Piezo layer

In most ultrasonic clamp-on flow metering settings, there is a large difference between the acoustic impedance of the liquid and that of the pipe wall. Therefore, most of the acoustic energy produced by the transmitting transducer reflects back into the pipe wall, resulting in signals with low amplitude from the receiver transducer. One way to increase this amplitude is to use a PZT piezo material that gives the most efficient conversion of electric energy into mechanical energy. This convergence efficiency is proportional to the dielectric constant ϵ_{33}^{S} and the coupling factor k_{33} of the material.

There is a wide spectrum of PZT materials, typically, with values of $\epsilon_{33}^{S} = 100 - 7000$ and $k_{33} = 0.70 - 0.80$. In different medical and industrial applications, materials such as PZT5A ($\epsilon_{33}^{S} = 1800$, $k_{33} = 0.72$) and PZT5H ($\epsilon_{33}^{S} = 3800$, $k_{33} = 0.75$) are used. On the other hand, when SNR is a critical issue, single crystals are used because of their higher efficiency ($\epsilon_{33}^{S} = 4000 - 7500$, $k_{33} = 0.89 - 0.95$) relative to typical PZTs. However, matrix arrays are typically made from sub-diced plates, and single crystals do not usually behave as expected after being sub-diced. Therefore, the logical choice for the application was a PZT with the highest possible dielectric constant and coupling factor. The material of choice was HK1HD ($\epsilon_{33}^{S} = 6800$, $k_{33} = 0.72$, TRS Technologies, Inc., State College, PA).

A HK1HD PZT element on top of a steel half-space was simulated, and resonance modes were determined by computing the transmit transfer function at the interface between the piezo-element and the steel half space. The dimensions of the piezo-element were optimized to achieve a thickness resonance mode with a center frequency of $1\,\mathrm{MHz}$ and modes with lateral vibrations occurring at frequencies of at least $3\,\mathrm{MHz}$.

The initial thickness and width of a transducer element were $h_{\text{PZT}} = \lambda_{\text{PZT}}/4 = 1.0\,\text{mm}$ ($\lambda_{\text{PZT}} = 4.1\,\text{mm}$ at 1 MHz,), and $w = 0.72\,\text{mm}$, but these values were optimized at a later stage.

2.6.4. Printed Circuit Board layer
On the backside of the PZT, a printed Circuit Board (PCB) (modelled as FR4 material with a standard thickness of $1.6\,\text{mm}$) was placed. The PCB is used to wire out the electric signals from all the PZT elements of the matrix transducer array ($37 \times 17 = 629$ elements in total).

2.6.5. Backing layer
Reflections from the back side of the PCB layer are unwanted because these can be recorded by the other transducer elements and induce errors in the measurements. Therefore, it is necessary to reduce these reflections. For this purpose, an absorbing backing material was placed behind the PCB layer. To ensure maximum transmission from the PCB into the backing and to minimize reflection back into the PCB layer, the impedance of the backing material was chosen to be the same as that of the PCB layer ($Z = 6.7\,\text{MRayl}$). This is a relatively soft backing material, and its attenuation coefficient was set to $5\,\text{dB/MHz.cm}$ based on practical experience with these kinds of materials. Other ultrasound applications, such as medical imaging, aim to attenuate the waves that return from the backing after a two-way travel path by $\approx 40\,\text{dB}$. Based on this, the same level of damping is aimed for. Hence, the thickness of the backing layer was set to $40\,\text{mm}$.

2.6.6. Coupling layer
The upper surface of our coupling piece runs parallel to the pipe wall in the axial direction, i.e. the coupling piece is not an angled wedge, and the lower surface conforms to the pipe wall. The bandwidth of the designed acoustic stack placed on a lead half space generated a time pulse with a length of $\approx 2.5\,\mu s$ (equivalent to $\approx 5.5\,\text{mm}$ in lead). To be able to properly window-out in time this pulse, and also to avoid interference with its reflection from the lead - pipe wall interface, the thickness of the lead piece was set to $11\,\text{mm}$ at the center (i.e. 2x the pulse length), and thicker towards the edges in the circumferential direction. The addition of both PCB, backing, and coupling layers added losses and shifted the resonance frequency of the acoustic stack. Therefore, PZT thickness had to be optimized to $h_{\text{PZT}} = 0.35\,\lambda_{\text{PZT}} = 1.4\,\text{mm}$ to shift the thickness resonance mode back to 1 MHz. To achieve the desired resonance profile, the width of the elements was optimized to $w = 0.42\,\text{mm}$, respectively.

2.6.7. Lateral width of the piezo-elements
Now, all 37 PZT elements along the axial direction of the matrix array were considered in the simulations. The PCB and backing materials had a width equal to the array aperture. The width of the lead coupling piece was large enough to be able to steer the acoustic beam up to $45\,^\circ$ without hitting the edges, which is enough to achieve all the desired angles for wave mode conversion in the pipe wall (see

Fig. 2.4c). The performance of the 37 PZT elements showed an interference effect of a propagating Rayleigh wave on the surface of the coupling layer, which was avoided by optimizing the width of the elements to $w = 0.62\,\text{mm}$ (see Fig. 2.5).

The location of the lateral mode on the red curve of Fig. 2.5 moved very close to the frequency band of interest. To shift it back to a frequency of at least $3\,\text{MHz}$, the PZT elements were sub-diced. The width of the sub-dicing kerf was $50\,\mu\text{m}$, which is the same as for the kerfs of the array, to preserve the required array pitch of $0.72\,\text{mm}$. A sub-dicing depth of $95\,\%$ of the thickness of the PZT element was sufficient to shift the peak of the lateral mode to the right position.

2.6.8. Vias in the PCB

So far, the PCB layer has been modeled as a single solid material. In practice, PCB layers are manufactured with metallized holes, called vias, to make vertical connections, e.g. to the elements. Here, these vias have a diameter of $200\,\mu\text{m}$ across and their walls are covered by a $20\,\mu\text{m}$ copper layer.

To study the effect of vias on the acoustic response of the transducer, the vias were included in the FEM simulations. The center of each via was aligned with the center of the electrode of each PZT element (see Fig. 2.6a). The transmit transfer function was computed at the interface between the piezo-elements and the lead coupling piece. It turned out that the thickness resonance mode of the acoustic stack shifted away from $1\,\text{MHz}$ due to the presence of the vias. Therefore, the thickness of the PZT elements had to be optimized once again to $h_{\text{PZT}} = 0.30\lambda_{\text{PZT}} = 1.2\,\text{mm}$ to achieve the desired resonance profile given in Fig. 2.6b. Further it was computed that the designed stack will have a transmit
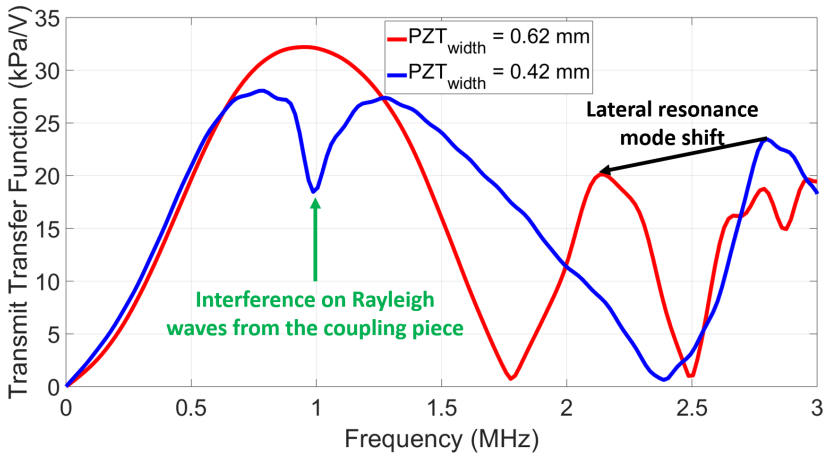
Figure 2.5: Transmit transfer functions obtained from Finite Element simulations of a 37-element HK1HD PZT transducer array with $h_{\text{PZT}} = 0.35\lambda_{\text{PZT}}$ on top of a lead coupling piece and with PCB and backing layers on the back side. The transmit transfer function was computed at the interface between the piezo-elements and the lead. The black arrow indicates the shift of the mode with lateral vibrations towards a lower frequency that is achieved by increasing the width of the piezo-elements.
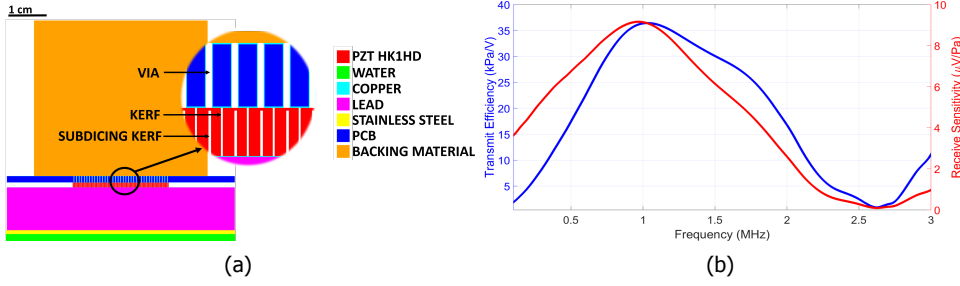
Figure 2.6: (a) Acoustic stack of the designed transducer array. The sub-dices of the PZT elements run up to 95 % of the element thickness. The vias in the PCB layer are 200 μm across and their walls are covered by a 20 μm thin copper layer. (b) Expected performance of the designed transducer array. There are no modes with lateral vibrations within the frequency band of interest (0.2 − 2 MHz). Both the transmit efficiency and the receive sensitivity were computed at the interface between the piezo-elements and the lead.

efficiency of $T_t = 36.4\,\text{kPa/V}$ and a receive sensitivity of $T_r = 9.2\,\mu\text{V/Pa}$, both at resonance.

2.6.9. Signal-to-Noise ratio

To compute the noise produced by one of the sub-diced PZT elements in receive, thermal noise at room temperature was assumed, and the Johnson-Nyquist equation was used

$$v_n = \sqrt{4k_b TR\Delta f}. \tag{2.2}$$

Here, v_n represents the root-mean-square (RMS) noise voltage produced by the PZT element, k_b represents Boltzmann's constant, T is the absolute temperature, R is the real component of the electrical impedance of the PZT element, and Δf represents the frequency bandwidth over which the noise is computed.

The real part of the electrical impedance of the PZT elements was extracted from FEM simulations on the acoustic stack in Fig. 2.6a, and within the bandwidth of interest it was estimated that the average noise produced by the element would be in the order of $1.1\,\mu\text{V}_{\text{RMS}}$. This implies that the required $20\,\text{dB}$ SNR translates into a minimum required value of $11\,\mu\text{V}_{\text{RMS}}$ for V_{open} in Eq. 2.1 to perform a useful flow measurement.

SNR levels should be $\geq 20\,\text{dB}$ for the entire range of liquids involved. Using the obtained performances from Fig. 2.6b, SNR estimates were computed with Eq. 2.1 for the acoustic travel paths shown in Fig. 2.4a and Fig. 2.4b. Fig. 2.7 shows the expected SNR levels for the designed transducer array. From the figure it can be concluded that, at resonance (1 MHz), SNR $\geq 20\,\text{dB}$ for all considered liquids.
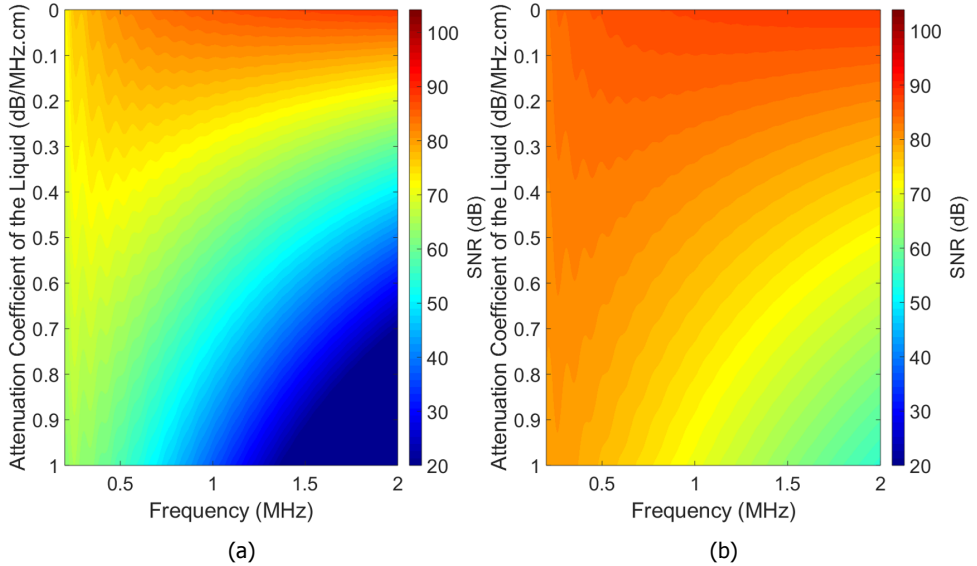
Figure 2.7: Computed SNR of the designed transducer array, versus frequency and attenuation coefficient of the liquid. (a) Compressional waves in the pipe wall and six bounces within the pipe. (b) Shear waves in the pipe wall and two bounces within the pipe.

2.7. Acoustic characterization of a linear array prototype

Based on the proposed transducer design, a 36-element linear array was fabricated and acoustically characterized to test its potential and suitability for self-calibrated ultrasonic clamp-on flow metering in the wide range of scenarios defined previously.

2.7.1. Fabrication

Off-the-shelf plates of PZ26 (Meggit A/S, Kvistgård, DK), with a thickness of $1.67\,$mm, were diced with a $0.1\,$mm thick diamond saw to produce linear arrays of 36 elements. In the azimuth direction, each array element had a width of $0.62\,$mm, and a kerf of $0.1\,$mm. In the elevation direction, each element has a height of $12\,$mm (i.e. ≈ 17x$0.72\,$mm). Although the dielectric constant of PZ26 is approximately half of that of HK1HD, the estimated SNR levels for flow measurements of water, computed via Eq. 2.1, are still significantly above the $20\,$dB level requirement.

In addition, a backing material was also fabricated. It consisted of a mix of epoxy and tungsten particles of different sizes. The backing had an acoustic impedance of $Z \approx 6.7\,$MRayl, and an attenuation coefficient at $1\,$MHz of $\alpha \approx 15\,$dB/MHz.cm. Therefore, a $13\,$mm-thick backing was sufficient to achieve the required $40\,$dB attenuation of the waves reflecting at the backside of this layer.

Molten lead was poured into custom-made molds to fabricate the desired coupling pieces. To characterize the array, a flat $11\,$mm thick lead piece was cast (see

Fig. 2.8). For performing the flow measurements, pieces with a concave shape were made that would fit on top of a stainless steel pipe with an outer diameter of $42\,\mathrm{mm}$. This piece had a minimum thickness of $11\,\mathrm{mm}$ in its center. Figure 2.9 shows the fabricated linear array prototype, including the array after the dicing process.

2.7.2. Beam profile

The fabricated acoustic stack was place on top of a $1\,\mathrm{mm}$-thick stainless steel plate, and finally on a water surface (see Fig. 2.10a). The transducer array was excited via a Verasonics V1 system (Verasonics Inc., Kirkland, WA, USA), with a 1-cycle square wave pulse with a center frequency of $1\,\mathrm{MHz}$ and a peak voltage amplitude of $5\,\mathrm{V}$. $107\,\mathrm{mm}$ below the water column, measurements of the acoustic wavefield were performed in a plane parallel to the surface of the transducer array using a $0.2\,\mathrm{mm}$-diameter hydrophone (Precision Acoustics Ltd., Dorchester, UK), and amplified by $60\,\mathrm{dB}$ (AU-1519, L3Harris Technologies, Inc. - Narda-MITEQ, Hauppauge, NY, US) before being finally recorded.

Peak amplitudes of the envelopes of the measured signals show a relatively symmetric pattern (Fig. 2.10b), although the imperfect shape may be caused by the slight inter-element efficiency variation, and/or by a slight relative inclination between the plane that defines the surface of the transducer array and the measurement plane.

2.7.3. Efficiency

As shown in Fig. 2.6, FEM simulations of the designed array reported an efficiency, in lead, of $\approx 36.4\,\mathrm{kPa/V}$. However, in practice, transducer efficiency is usually measured in water, where an efficiency of $\approx 1.95\,\mathrm{kPa/V}$ was reported for the same array. In contrast, for the fabricated linear array prototype shown in Fig. 2.8 and 2.9, FEM simulations reported an efficiency, in water of $\approx 0.88\,\mathrm{kPa/V}$.

Considering the measured time signal, $V_{out}(t)$, associated to the coordinate of maximum amplitude in Fig. 2.10b, the transmit transfer function of the fabricated
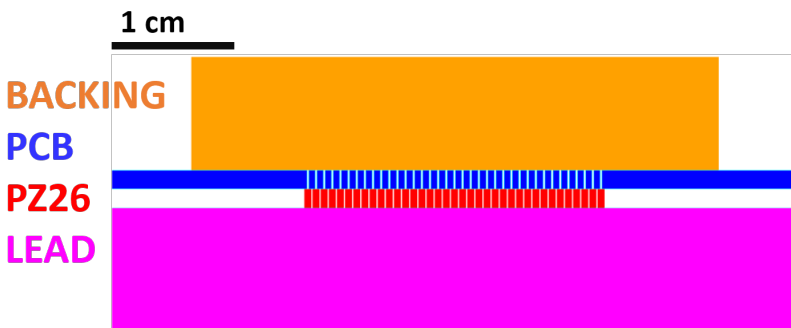
Figure 2.8: Geometry of the fabricated linear transducer array prototype. The PCB included air-filled vias with a thickness of $200\,\mathrm{\mu m}$ and a $20\,\mathrm{\mu m}$-thick copper layers on the sides.

(a)   (b)   (c)
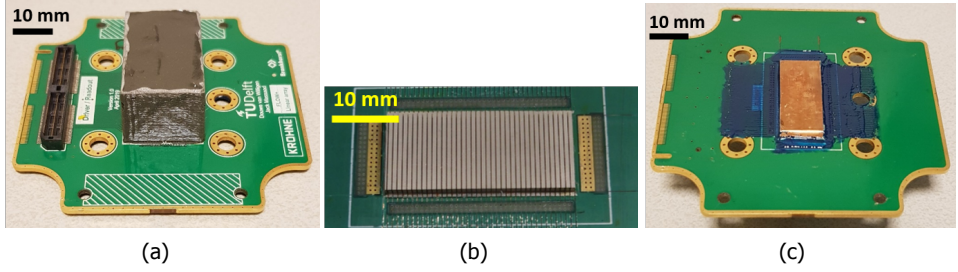
Figure 2.9: Fabricated prototype of one of the linear arrays. (a) Backing poored on top of the custom-made PCB. (b) Array obtained after dicing the PZ26 plate on top of the PCB and before applying a copper ground foil. (c) PZT array with a $20\,\mu m$ thick copper ground foil layer.

linear transducer array, $T_t(\omega)$, was estimated via the method of [18] as

$$T_t(\omega) = \frac{V_{tr}(\omega)}{V_{rc}(\omega)D(\omega)T_{amp}(\omega)T_{hyd}(\omega)}, \qquad (2.3)$$

where ω represents the angular frequency, $V_{tr}(\omega)$ represents the Fourier transform of the transmitted time signal, and $V_{rc}(\omega)$ represents the Fourier transform of the signal measured by the hydrophone. $T_{amp}(\omega)$ and $T_{hyd}(\omega)$ represent the transfer functions of the amplifier and hydrophone, respectively. The symbol $D(\omega)$ represents the diffraction correction of the acoustic wavefield. Simulations of the acoustic wavefield produced by the fabricated array aperture were performed using Field II [19, 20] to obtain the diffraction correction term, which was computed as

$$D(\omega) = \frac{p_{z0}(\omega)}{p_0(\omega)}, \qquad (2.4)$$

where $p_{z_0}(\omega)$ represents the FFT of the on-axis acoustic pressure signal at $z_0 = 113.5\,mm$, and $p_0(\omega)$ represents the FFT of the averaged acoustic pressure signal

(a)   (b)
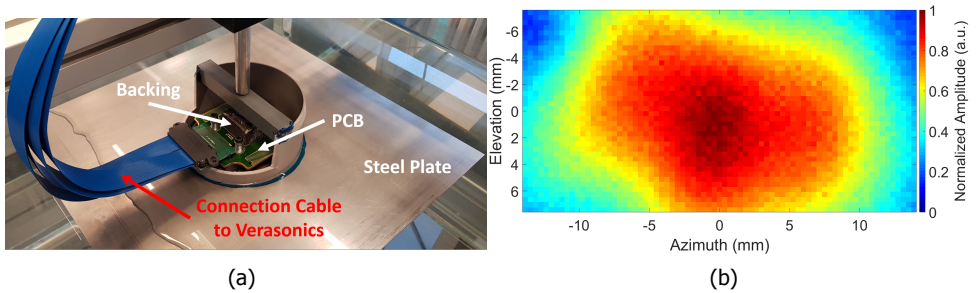
Figure 2.10: (a) Experimental setting to characterize the fabricated linear transducer array prototype shown in Fig. 2.9. The Backing and PCB layers are shown. The linear array (not shown here) is located below the PCB. (b) Beam profile hydrophone measurements of the fabricated linear transducer array prototype. The time signals were recorded at an axial distance of $107\,mm$ with respect to the array.
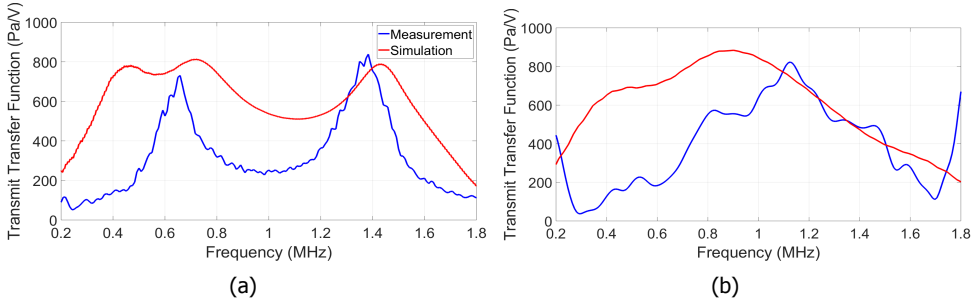
Figure 2.11: Measured and simulated transmit transfer function, in water, of the prototype linear transducer array of Fig. 2.9.

located along the surface of the transducer array but also in the far field of the mathematical elements simulated by Field II.

Figure 2.11 shows the measured and simulated efficiencies with and without the lead coupling piece. Fig. 2.11a shows two distinctive resonance peaks: one at $\approx 1.5\,\mathrm{MHz}$ and another one at $\approx 0.6\,\mathrm{MHz}$, which correspond to the PZT and the coupled PCB-PZT resonance, respectively. Moreover, the PZT and the steel layer destructively interfered at $\approx 1\,\mathrm{MHz}$. On the other hand, Fig. 2.11b shows the matching effect of the lead, where only one resonance frequency was observed. Although the measured and simulated magnitudes of the efficiencies shown in Fig. 2.11 correspond reasonably well, they also show some distinct differences in their shape, which are mainly due to practical limitations during the measurements. First, due to the relatively low operation frequency of the array, in combination with space constrains in the water tank, the wavefield used to compute efficiencies was not measure in the far field as it is usually done, but just near the natural focus of the azimuth aperture (focus $\approx 113.5\,\mathrm{mm}$). Second, PZTs are complex materials, and it is not uncommon for some of their nominal properties, which were used in simulations, to have fabrication uncertainties of up to $10\,\%$. The combination of these two likely factors may be the cause for the measured sharper resonance peaks in Fig. 2.11a and the $\approx 10\,\%$ in peak resonance shift observed in Fig.2.11b. Furthermore, since the diffraction correction term was also computed near the natural focus and not in the far field as usual, the resultant correction presented a ripple-like shape along the bandwidth of interest, which directly caused the ripple-like behavior around the measured resonance frequency of Fig. 2.11b and to report a lower bandwidth relative to the simulation. However, at a measured resonance frequency of $1.12\,\mathrm{MHz}$, Fig. 2.11b reports a measured efficiency of the fabricated linear array of $\approx 0.82\,\mathrm{kPa/V}$, which is reasonably close to the $0.88\,\mathrm{kPa/V}$ reported by FEM simulations. Furthermore, the measured efficiency reported a $-20\,\mathrm{dB}$ bandwidth between $0.38 - 1.70\,\mathrm{MHz}$.

2.7.4. Beam steering and wave mode conversion

It was important to also investigate the ability of the fabricated array to achieve wave mode conversion in the pipe wall and measure flow speed in the scenarios of Fig. 2.4a and Fig. 2.4b. In the experimental setup, time delays were applied to the array elements to steer an acoustic beam through the lead coupling piece, the metal layer, and finally into the water, where a linear scan of the wavefield was performed in the water, at a depth of $z_0 = 113.5\,\text{mm}$ and along the azimuthal direction of the array.

Three steering angles were tested: $\theta_{\text{lead}} = 0°$, $\theta_{\text{lead}} = 20°$ and $\theta_{\text{lead}} = 40°$. Given the compressional bulk wave sound speed of lead ($c_L = 2200\,\text{m/s}$) and stainless steel ($c_L = 5800\,\text{m/s}$), Snell's law predicts a critical angle of $22°$, beyond which only shear waves will propagate in the pipe wall. Therefore, for the steering angle of $40°$, the shear bulk wave speed of stainless steel ($c_T = 3100\,\text{m/s}$), was used. Fig. 2.12 shows the measured linear scans. As expected, the peak pressure shifts as a function of the steering angle. Furthermore, given the azimuthal location x_{max} of the main peak of a linear scan profile and the associated time signal from which the transit time t_w of the acoustic beam can be extracted, the measured steering angle of the acoustic beam in water ($c_w = 1500\,\text{m/s}$) was determined as

$$\theta_w = \arcsin\left(\frac{x_{\text{max}}}{c_w t_w}\right). \tag{2.5}$$

For the considered angles $\theta_{\text{lead}} = 20°$ and $\theta_{\text{lead}} = 40°$ beams steered in lead, the measured angles in water were $\theta_w = 15.8°$, and $\theta_w = 30.6°$, respectively. These were comparable to the theoretical values of $\theta_w = 13.2°$, and $\theta_w = 25.4°$. The

(a)
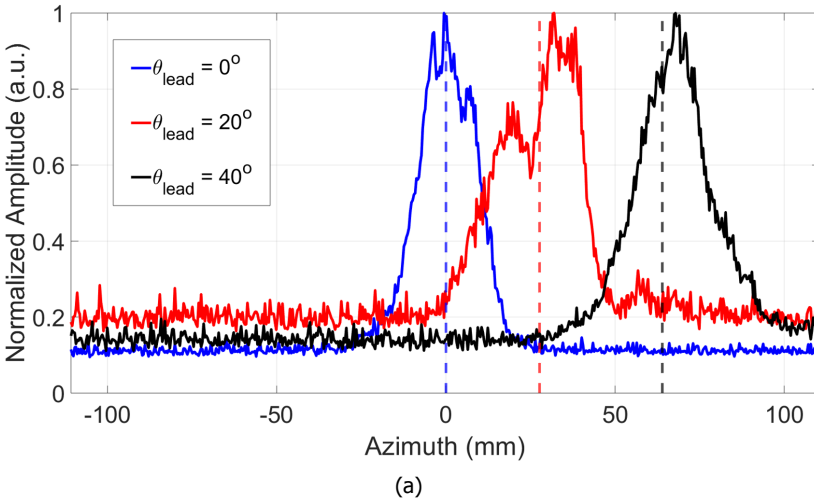
Figure 2.12: Measured linear scans of the amplitude of the acoustic wavefield in water, generated by the transducer array of Fig. 2.9 for three different beam steering angles. The dashed vertical lines indicate the theoretical expected position of the peak pressures for the theoretical sounds speeds involved.

discrepancies are most likely due to the sound speeds considered in the theoretical calculations. Other evidence was the constant offset between the theoretical and measured peak locations for each considered angle. At $\theta_{\text{lead}} = 20\,°$, an interference effect was observed between the bulk compressional and shear waves in the steel, which refracted into the water with a similar angle and produced the dip in the amplitude measured in the azimuthal range between $20 - 30\,\text{mm}$. The results of Fig. 2.12 confirmed that, with the fabricated array, it is possible to also excite shear waves in the pipe wall and measure flow with either scenario Fig. 2.4a or scenario Fig. 2.4b.

Noise floor levels are slightly different for each scan in Fig. 2.12 because, in each case, particular wave interferences were occurring, which lead to measurement of a slightly different peak amplitude for normalization.

2.8. Electronics design

Here, the application-specific integrated circuit (ASIC) design for a matrix transducer aimed at ultrasonic clamp-on flow measurements is described. An ASIC is the preferred solution since the matrix consists of 629 elements, making it impossible to implement a driver and read-out circuit with discrete components. As discussed previously in this chapter, several functions have to be implemented on the ASIC to perform accurate flow measurements. The following sections will discuss the implementation of apodization, beam steering and arbitrary waveform generators to produce the intended acoustic beams. Furthermore, a low-noise receive amplifier design, implemented to recover the acoustic signals with the best SNR possible, will be discussed.

2.8.1. Apodization

Amplitude apodization can help to suppress the transmission of spurious waves (see Chapter 3), hence it is important to include this feature in the driver electronics. Ideally, one would want to be able to create any apodization amplitude, however, as the functionality has to be implemented on an ASIC and be programmable as well, the apodization levels have to be quantized. To investigate the minimum quantization resolution required, a simulation in MATLAB was performed. The aim of the simulation was to create a beam profile that has no side lobes with a magnitude higher than $35\,\text{dB}$ below the main beam, as posed by the acoustic requirements. Figure 2.13 shows that with a 3-bit (8-level) quantization, some of the side lobe peaks do not satisfy the requirement. With 4 bits, the requirement is just barely met. Therefore, an implementation with a 5-bit quantization was chosen.

Apodization has to be realized in both column and row direction to optimally suppress the spurious waves in the pipe wall. A column-and-row approach was chosen to reduce the circuit complexity in the channel circuit and because it is not necessary to program each element amplitude individually. To create a smooth apodization in both directions, the amplitude levels for the column and for the row of the matrix have to be multiplied on channel level.

The amplitudes of the individual transducer elements have to be a multiplication

of the column-level and row-level apodization. Multiplication of the two settings is done by pulse-width modulating (PWM) a column level amplitude with a row level PWM signal inside each channel circuit.

Amplitudes for the column level setting are generated using 5-bit digital-to-analog converters (DACs). A common DAC implementation, called the R2R DAC, was used on the ASIC as it is compact, and a relatively slow speed is acceptable as the apodization settings is only planned to be updated when changing settings in the flow meter. The R2R-DAC implemented on the ASIC is depicted in Fig. 2.14. The output voltage V_{out} is a fraction of the reference voltage V_{ref}, set by the configuration bits b1 to b5.

Multiplying the two settings is done in a calibration phase that precedes the transmit phase (the one in which the acoustic waves are generated). The circuit responsible for the multiplication operation is shown in Fig. 2.15. In the calibration phase, V_{pwm} is set to the maximum pulse length. After a reset, the current source M1 charges capacitor C1 for the duration set by V_{pwm}. After the pulse, the voltage on the capacitor (V_{apod}) is compared to the column amplitude setting (V_{column}). The current source M1 is increased if V_{apod} is smaller, whereas the current is decreased in case the voltage is higher than V_{column}. This is repeated until a steady situation is reached. Finally, a single PWM pulse of the configured duration results in a fraction of the column voltage. The voltage is kept on the capacitor until the next calibration phase.

In normal operation, the calibration phase can be very short (a few microseconds) as it only has to compensate for voltage drop on the capacitor resulting from leakage currents. Only when changes to the apodization setting are made, a longer calibration phase is required. The amplitude setting of the individual channels after column and row apodization is depicted in Fig. 2.16, which shows a smooth amplitude apodization in all directions.
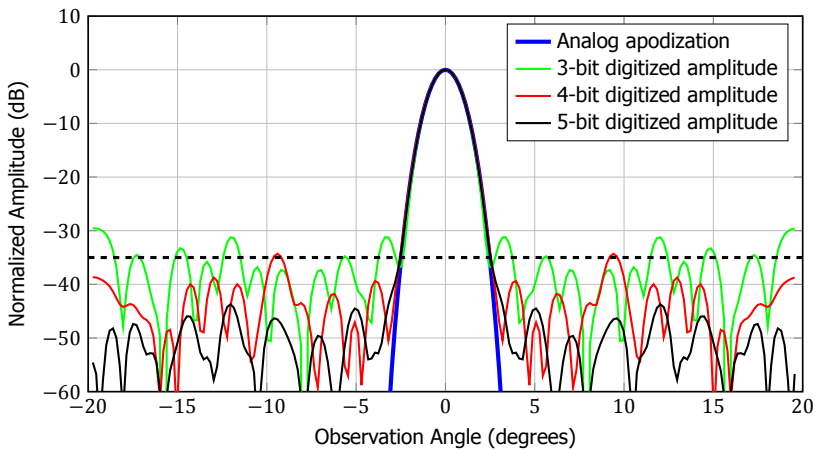
Figure 2.13: Quantization levels and their resulting unwanted peaks in the beam profile.

2
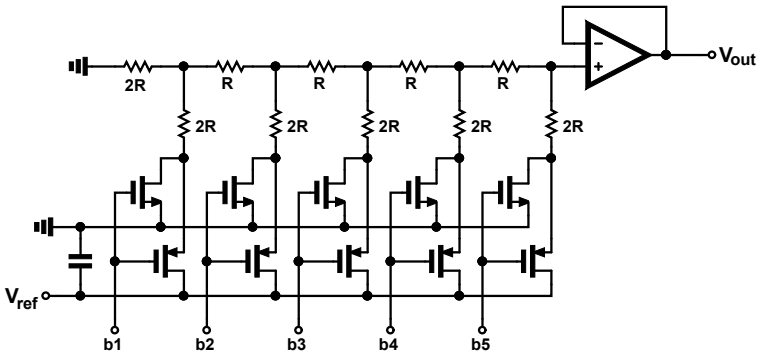
Figure 2.14: Column level apodization circuit.

2.8.2. Beam steering

Steering, and preferably with an accurate angle, is required to be able to aim the acoustic beams at the center of the receive transducer array. Two measurement configurations are considered. In the first configuration, longitudinal waves are excited in the pipe wall, and the refracting acoustic beam into the liquid bounces six times (v-shapes) within the pipe before arriving at the other transducer array. In the second configuration, shear waves are excited in the pipe wall, and the longitudinal wave that refracts into the liquid does so at a sharper angle compared to the first configuration, requiring it to only bounce two times within the pipe wall before being recorded (refer again to Fig. 2.4).

As pointed in Fig. 2.4c, the distance between the two transducer arrays is spec-
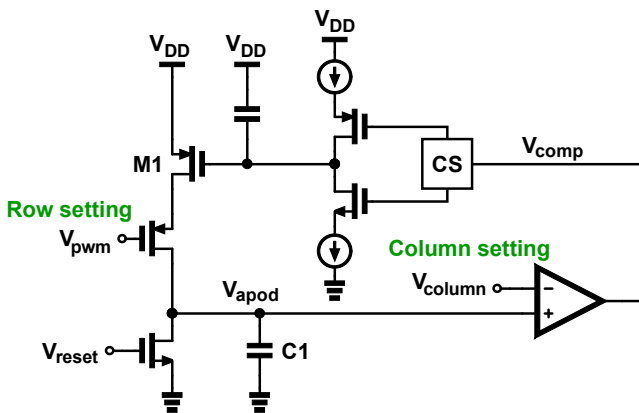
Figure 2.15: The apodization circuit, multiplying the PWM signal with the R2R dac value.

2
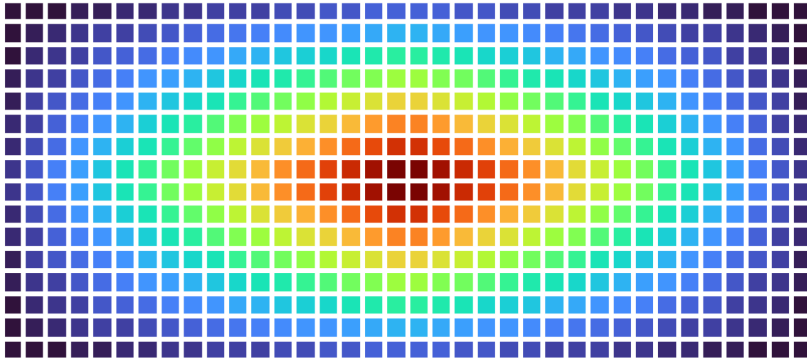
Figure 2.16: Apodization levels resulting from column and row-level settings.
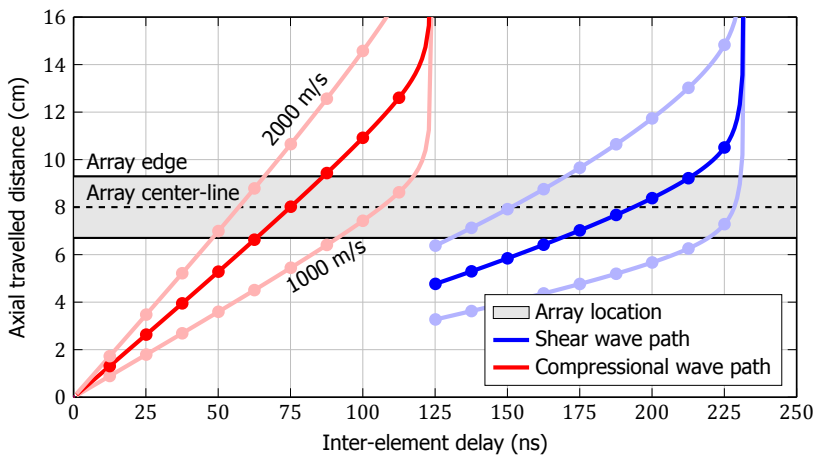
Figure 2.17: Possible delay settings (markers), allowing beam steering in all fluids with sound speeds between $1000 - 2000\,\mathrm{m/s}$.

ified to be $80\,\mathrm{mm}$. A simulation was performed to find the required delays to steer the acoustic beam towards the receive array, as shown in Fig. 2.17. The horizontal axis shows the inter-element delay settings. For liquids with a slow speed of sound, the shear wave path is too short to reach the receive transducer after two bounces within the pipe wall. In such cases, extra bounces of the beam can be introduced so that the in-coming acoustic wave hits the receive transducer array.

To delay the transmit waveform, the bitstream that represents the waveform is fed through a shift register with a programmable length. The shift register delays the bitstream with an integer number of clock cycles. A multiplexer in front of the shift register sets the direction from which to use the bitstream: either the previous channel or the next channel. In Fig. 2.18, a block diagram is shown, with the *dt*-block representing the variable-length shift register. One could say that the bitstream ripples over the array, starting in one or in multiple corners, adding a

2

delay for each consecutive channel.

For precise beam alignment, the circuit is designed such that the clock frequency can be tuned, which directly affects the delay step. A $\pm 10\%$ deviation from the designed frequency allows tuning the beam angle to cover the required range shown in Fig. 2.4c.

2.8.3. Curvature compensation

In the circumferential direction, the pipe has a curved shape, while the transducer array depicts a flat surface. In between the array and the pipe wall, a coupling piece is used to transition from the flat surface to the pipe curvature. The curvature must therefore be corrected such that a plane wave can be generated in the liquid. The delays caused by the coupling piece and pipe wall are shown in Fig. 2.19.

These delays are also quantized since the ASIC uses fixed delay steps. Contrary to the axial direction, it is not helpful to use the clock frequency for fine-tuning the delay, since it would only change the magnitude of all the delays. Figure 2.20 shows the required delay profile and the delays generated using the quantized delay step.

2.8.4. Waveform generation

An arbitrary waveform generator is required to be able to keep flexibility as well as to create the preferred smooth transmit waveforms, such as Gaussian-apodized sine waveforms. Arbitrary waveforms also allow for additional tricks in noise reduction, such as coded excitation.

Inside each channel circuit, a 3-level PWM signal is generated, with peak amplitudes defined by the column and row apodization amplitude. The PWM signal has to be amplified to drive the piezo element. A maximum apodization level of $\pm 500\,\mathrm{mV}$, in combination with a $10\times$ amplification, allows for a maximum of $5\,\mathrm{V}$ transmit am-
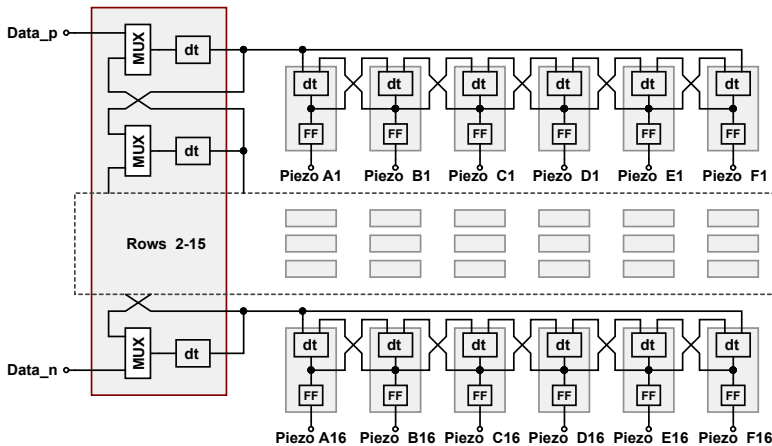
Figure 2.18: Circuit used to implement phase shift for beam steering.

plitude. The transmit amplifier is not able to drive voltages to the maximum power supply levels, therefore in practice, the reference voltage of the R2R-DAC (column level) can be adjusted to make optimal use of the dynamic range.

The block diagram of the channel circuitry is shown in Fig. 2.21. Apodization, as discussed in Section 2.8.1 is shown as a block here, of which the output is assumed to equal the multiplication of the column and row setting. Two buffer amplifiers with a gain of 1 and -1 are used to create an equal positive and negative voltage that are used to generate the waveform using the PWM bitstream inputs. The PWM switches are shown with their junction diodes, to indicate the requirement for two transistors to ground. With only one transistor, the junction diode would forward bias and not allow a positive or negative pulse, depending on its orientation.

The waveform signal consists of two data streams, as shown in Fig. 2.22. One data stream represents the positive values (red), and the other one represents the negative values (green) to make a 3-level PWM signal that is symmetric around $0\,V$. The low-pass filter and limited bandwidth of the HV amplifier will smoothen the waveform, but some saw-tooths will be visible on the output (seen in purple and blue in Fig. 2.22, with different apodization levels). Finally, after the filtering caused by the piezo transducer itself, a smooth transmit waveform will be created, as shown in orange and red in Fig. 2.22, with a high and a low apodization level, respectively.

2.8.5. Receive amplification

The received acoustic signals have to be amplified to achieve a good SNR. Since wiring the individual channels would create too many of them to connect to a Verasonics acquisition machine (which would provide a maximum of 256 channels available) when the full array is used, the channels are multiplexed in groups of 8,
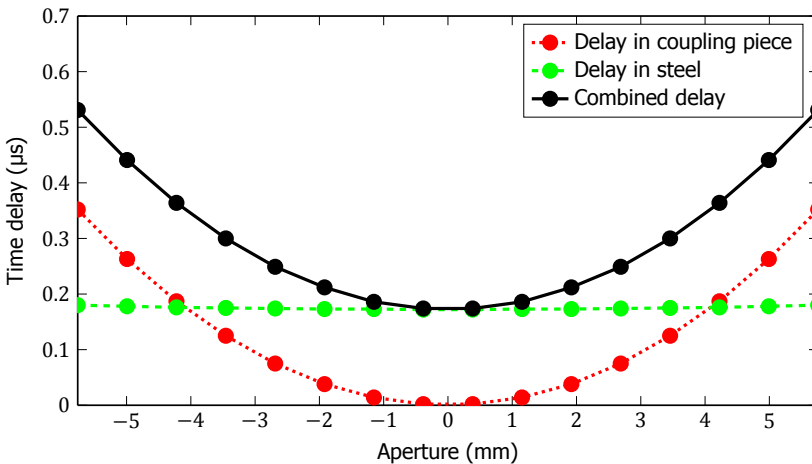
Figure 2.19: Time delays inside the coupling piece and steel pipe wall until the wave refracts into the liquid (water in this case). Compensation is required for the flat matrix transducer on a curved pipe wall.
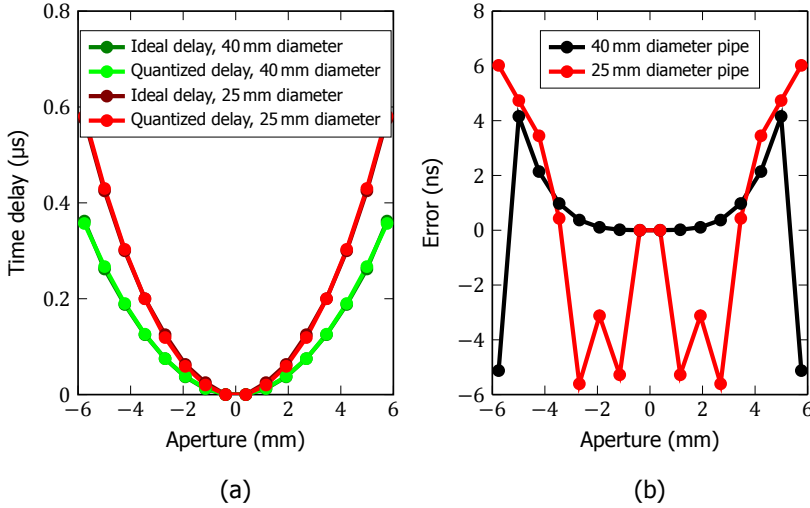
Figure 2.20: (a) Global quantized circumferential delay. (b) Quantization error compared to ideal delay profile.
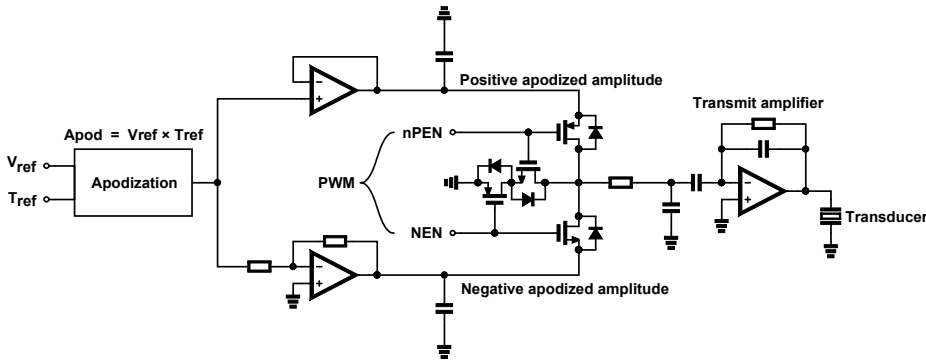
Figure 2.21: Circuit diagram of the channel circuitry, including PWM and HV amplifier.

resulting in 12 analog outputs. The multiplexers are wired such that symmetrical groups around the pipe axis can be read-out at the same time. Since per ASIC a sub-array of 6×16 elements is addressed, groups of 6 elements on either side of the pipe axis are read out. The elements and their corresponding analog output channel are shown in Fig. 2.23.

A large dynamic range of signals is expected in the acoustic domain, with high amplitude Lamb waves coming in, potentially valuable for calibration measurements (see Chapter 4), and at the same time the low amplitude longitudinal wave refracting from the liquid containing the flow information. To cope with the range of amplitudes, the LNA has a programmable gain of $40\,\mathrm{dB}$ in steps of $8\,\mathrm{dB}$. Since

calibration and flow measurements happen consecutively, no continuous change in the gain is required. A topology is therefore chosen that uses switches in the feedback network to change the gain setting. The implemented LNA circuit is shown in Fig. 2.24.

2.9. Discussion

The region of low SNR predicted in Fig. 2.7a for relatively high-damping liquids may be narrowed-down in two simple ways: The beam steering angle could be decreased and the acoustic beam could bounce fewer of times within the pipe, therefore increasing SNR, or the beam steering angle could be increased enough to operate the sensor in the shear wave mode shown in Fig. 2.4b. On the other hand, the input voltage may be increased to also achieve higher SNRs, however, this value is usually limited in practical applications to $5\,\mathrm{V}$ for intrinsic safety, especially when measuring flow speed of liquids in an industrial setting.

Good confidence was built around the simulation tool for the design of a matrix array for ultrasonic clamp-on flow measurements. Based on the fabrication of a linear array prototype, and the results of its acoustic characterization, its potential for the desired application was demonstrated. These results motivate the fabrication of a first prototype ultrasonic clamp-on flow meter consisting of two of these linear arrays. More details about this are presented in Chapter 6.
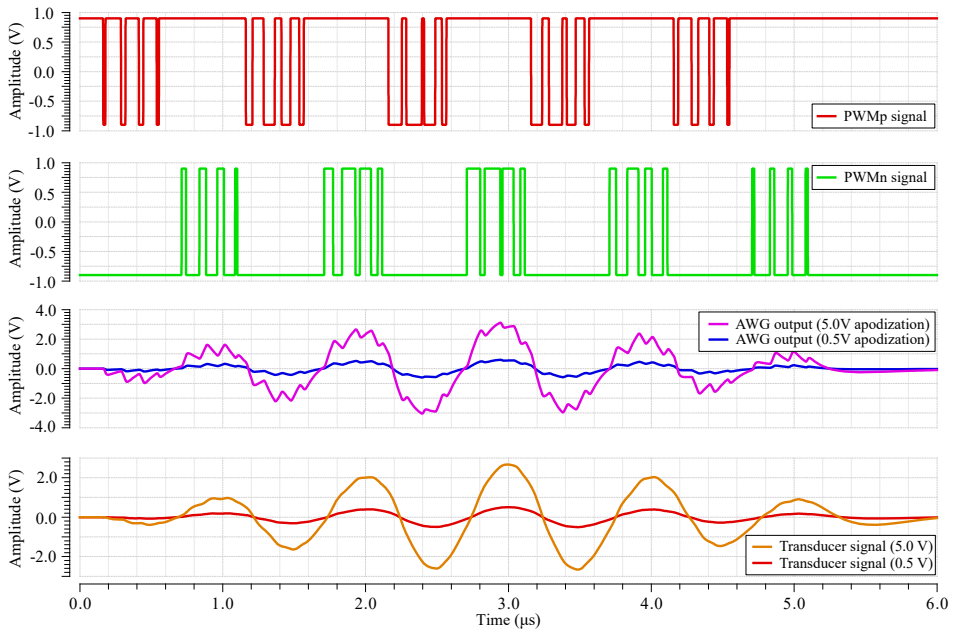
Figure 2.22: Transmit waveform and corresponding driving PWM signals.

	1	2	3	4	5	6	7	8	9	10	11	12	13	14	15	16
F	6	12	6	12	6	12	6	12	9	3	9	3	9	3	9	3
E	5	11	5	11	5	11	5	11	8	2	8	2	8	2	8	2
D	4	10	4	10	4	10	4	10	7	1	7	1	7	1	7	1
C	12	6	12	6	12	6	12	6	3	9	3	9	3	9	3	9
B	11	5	11	5	11	5	11	5	2	8	2	8	2	8	2	8
A	10	4	10	4	10	4	10	4	1	7	1	7	1	7	1	7

Figure 2.23: The piezo elements and corresponding multiplexer channel connections.

2.10. Conclusions

Here, the design of an ultrasonic clamp-on flow meter based on matrix transducers has been presented. A proof-of-concept linear array prototype has been fabricated based on the proposed design. The prototype was characterized acoustically and it showed good agreement with FEM simulations. Its measured efficiency and beam steering capabilities demonstrated its ability to achieve wave mode conversion in metal pipes and its suitability for ultrasonic clamp-on flow metering of a wide range of liquids.

Moreover, a circuit capable of generating arbitrary waveforms for ultrasonic clamp-on flow measurements with matrix transducer arrays has been designed. The built-in apodization function is able to apodize the amplitude while maintaining a constant waveform shape on all the piezo-elements. In receive, outputs of the individual piezo-elements can be amplified in a $40\,\mathrm{dB}$ gain range making the total dynamic range $100\,\mathrm{dB}$. This allows to measure the large-amplitude guided waves for calibration of the pipe and the liquid, as well as faint waves arriving from the liquid containing the flow information.
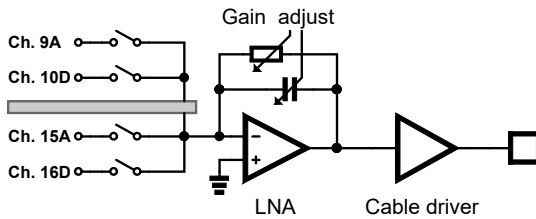
Figure 2.24: Block diagram of the LNA.

References

[1] J. Massaad, P. L. M. J. van Neer, D. M. van Willigen, E. C. Noothout, N. de Jong, M. A. P. Pertijs, and M. D. Verweij, *Design of a matrix transducer array for self-calibrated ultrasonic clamp-on flow measurements,* IEEE Trans. Ultrason. Ferroelectr. Freq. Control (submitted).

[2] J. Massaad, D. van Willigen, P. van Neer, N. de Jong, M. Pertijs, and M. Verweij, *Acoustic design of a transducer array for ultrasonic clamp-on flow metering,* IEEE Int. Ultrason. Symp. , 1133 (2019).

[3] R. C. Baker, *Flow measurement handbook: industrial designs, operating principles, performance, and applications* (Cambridge University Press, 2005).

[4] W.-S. Cheung, H.-S. Kwon, K.-A. Park, and J.-S. Paik, *Acoustic flowmeter for the measurement of the mean flow velocity in pipes,* J. Acoust. Soc. Am. **110**, 2308 (2001).

[5] J. C. Wendoloski, *On the theory of acoustic flow measurement,* J. Acoust. Soc. Am. **110**, 724 (2001).

[6] D. Kurniadi and A. Trisnobudi, *A multi-path ultrasonic transit time flow meter using a tomography method for gas flow velocity profile measurement,* Part. Part. Syst. Charact. **23**, 330 (2006).

[7] M. Sanderson and H. Yeung, *Guidelines for the use of ultrasonic non-invasive metering techniques,* Flow. Meas. Instrum. **13**, 125 (2002).

[8] J. Massaad, P. L. M. J. van Neer, D. M. van Willigen, M. A. P. Pertijs, N. de Jong, and M. D. Verweij, *Towards a calibration-free ultrasonic clamp-on flow meter: Pipe geometry measurements using matrix arrays,* Proc. Meet. Acoust. **39**, 1 (2019).

[9] J. Massaad, P. L. M. J. van Neer, D. M. van Willigen, M. A. P. Pertijs, N. de Jong, and M. D. Verweij, *Suppression of Lamb wave excitation via aperture control of a transducer array for ultrasonic clamp-on flow metering,* J. Acoust. Soc. Am. **147**, 2670 (2020).

[10] F. Hofmann, *Fundamentals of ultrasonic-flow measurement for industrial applications,* KROHNE Messtechnik GmbH & Co. KG, Duisburg , 1 (2000).

[11] A. S. Dukhin and P. J. Goetz, *Characterization of liquids, dispersions, emulsions, and porous materials using ultrasound* (Elsevier, 2017).

[12] P. L. M. J. van Neer, S. Blaak, J. G. Bosch, C. T. Lancée, C. Prins, A. F. W. van der Steen, and N. de Jong, *Mode vibrations of a matrix transducer for three-dimensional second harmonic transesophageal echocardiography,* Ultrasound Med. Biol. **38**, 1820 (2012).

[13] C. Adams, S. Harput, D. Cowell, T. M. Carpenter, D. M. Charutz, and S. Freear, *An adaptive array excitation scheme for the unidirectional enhancement of guided waves,* IEEE Trans. Ultrason. Ferroelectr. Freq. Control **64**, 441 (2016).

[14] J. Li and J. L. Rose, *Implementing guided wave mode control by use of a phased transducer array,* IEEE Trans. Ultrason. Ferroelectr. Freq. Control **48**, 761 (2001).

[15] K.-C. T. Nguyen, L. H. Le, T. N. H. T. Tran, M. D. Sacchi, and E. H. Lou, *Excitation of ultrasonic Lamb waves using a phased array system with two array probes: Phantom and in vitro bone studies,* Ultrasonics **54**, 1178 (2014).

[16] W. Zhu and J. L. Rose, *Lamb wave generation and reception with time-delay periodic linear arrays: A bem simulation and experimental study,* IEEE Trans. Ultrason. Ferroelectr. Freq. Control **46**, 654 (1999).

[17] P. H. Rogers and A. L. Van Buren, *An exact expression for the lommel-diffraction correction integral,* J. Acoust. Soc. Am. **55**, 724 (1974).

[18] P. L. M. J. van Neer, G. Matte, J. Sijl, J. M. G. Borsboom, and N. de Jong, *Transfer functions of US transducers for harmonic imaging and bubble responses,* Ultrasonics **46**, 336 (2007).

[19] J. A. Jensen and N. B. Svendsen, *Calculation of pressure fields from arbitrarily shaped, apodized, and excited ultrasound transducers,* IEEE Trans. Ultrason. Ferroelectr. Freq. Control **39**, 262 (1992).

[20] J. A. Jensen, *Field: A program for simulating ultrasound systems,* 10th Nordic-Baltic Conference on Biomedical Imaging, Vol. 4, Supplement 1, Part 1, **34**, 351 (1996b).

2

3

Suppression of Lamb wave excitation via aperture control of a transducer array for ultrasonic clamp-on flow metering

During ultrasonic clamp-on flow metering, Lamb waves propagating in the pipe wall may limit the measurement accuracy by introducing absolute errors in the flow estimates. Upon reception, these waves can interfere with the up and downstream waves refracting from the liquid, and disturb the measurement of the transit time difference that is used to obtain the flow speed. Thus suppression of the generation of Lamb waves might directly increase the accuracy of a clamp-on flow meter. Existing techniques apply to flow meters with single element transducers. This work considers the application of transducer arrays and presents a method to achieve a predefined amount of suppression of these spurious Lamb waves based on appropriate amplitude weightings of the transducer elements. Finite element simulations of an ultrasonic clamp-on flow measurement setting will be presented to show the effect of array aperture control on the suppression of the Lamb waves in a 1 mm-thick stainless steel pipe wall. Furthermore, a proof-of-principle experiment will be shown that demonstrates a good agreement with the simulations.

3.1. Introduction

Acoustic waves are widely used to measure flow [2–4]. The most basic ultrasonic flow meters consist of two single-element transducers, located a certain distance apart along a pipe wall. Both transducers can be used to excite and record acoustic waves, which enables point-to-point transmission of waves that propagate upstream or downstream relative to the direction of the flow. The transit time difference between these two waves, in combination with the acoustic length of the travel paths and the wave speeds, can be used to obtain a flow speed estimate [5]. The transducers of a flow meter can be in contact with the liquid in an in-line fashion, or be mounted on the outside of the pipe wall in a clamp-on fashion. In the latter case, the acoustic waves will make one or more bounces at the opposite pipe wall. The advantage of the clamp-on type is that they can be installed without interruption of the flow in the pipe and without affecting the mechanical strength of the pipe wall.

Unfortunately, clamp-on flow meters generate multiple wave modes, such as Lamb waves, in the pipe wall. These are mainly caused when the acoustic waves in the fluid reflect at the pipe wall. At the receiving transducer, these modes can interfere with the longitudinal acoustic waves refracting from the liquid. This will disturb the measurement of the transit time difference between up-and down-going waves in the fluid, thus cause an absolute error in the estimation of the flow speed. Current solutions to this problem are: use of a specific incidence angle of the acoustic waves when these hit the pipe wall to minimize the excitation of the Lamb waves; liquid-dependent transmitter-receiver placement along the pipe to enable proper time-windowing of the Lamb waves; and placement of absorbing layers around the pipe wall to reduce propagation of Lamb waves [6]. In view of Snell's law, a fixed angle of the acoustic beam in the pipe wall (e.g. defined by an angled wedge) results in a wave speed-dependent refraction angle of the beam in the liquid. This means that the travel path of the acoustic beam is liquid-dependent, and the distance between transmitter and receiver has to be modified (i.e. calibrated) accordingly for every fluid. Therefore, the dependence on the liquid prohibits a calibration-free flow meter.

Time-windowing of the longitudinal wave is not possible for all cases, since for pipe walls with a large thickness to wavelength ratio, a considerable amount of Lamb wave modes can be excited, and the probability of overlapping in time with the longitudinal wave refracting from the liquid increases. This problem is even more serious because Lamb waves are dispersive and the different Lamb wave modes have different group speeds. Moreover, the installation of absorbing layers around intricate pipe lines is difficult to perform in practice and sometimes not possible, especially in confined spaces. This motivates the development of an ultrasonic flow meter solution that provides Lamb suppression without compromising measurement precision, is independent of the specific liquid, and is calibration-free.

Selectivity of wave mode excitation with single-element transducers via angled wedges is described in literature [7]. However, by exploiting the wedge angle for Lamb wave suppression, this degree of freedom is lost for simultaneously steering the angle of the beam that will refract into the fluid. With transducer arrays and their capabilities for element-wise phase and amplitude control, considerably more

control can be achieved.

There are a number of articles on suppression of transmitted Lamb waves [8–16]. These methods are based on phase manipulation of the time domain signals for the suppression of one specific Lamb wave mode. On the other hand, methods for boosting the generation of Lamb waves in a plate via an ultrasonic array have been previously described as well [17–21]. These are also based on phase manipulation of the time domain signals. Apart from suppression of specific Lamb wave modes in the pipe wall, during flow metering it is desired to have an acoustic beam with a very well-defined wave front and propagation direction. Although both individual goals can be achieved with manipulation of the phase, it is not possible to reach both goals simultaneously. This is because the phase appears in the exponent of the complex representation of a signal, so the addition of two phases has the effect of one overall time delay. This is appropriate for concatenated time delay effects like beam steering and beam focusing. However, phase addition does not work for effects that require two separate time delays, like simultaneously generating two beams in different directions. Because Lamb wave suppression and acoustic beam generation are effects involving two different directions, these also cannot be achieved by the addition of phases.

Separating the aperture function of a transducer array by splitting it into its amplitude and phase behavior has been used in medical imaging [22–24]. Here is described a method that uses the amplitude of the transmitting elements of an array transducer to suppress Lamb waves, while the phase of the elements is used to control the direction and shape of the acoustic beam.

3.2. Theory

In this section, the relevant equations for Lamb wave propagation are described, as well as how their excitation can be controlled by means of the apodization of a transducer array.

3.2.1. Lamb waves

Lamb waves are plane elastic waves that propagate in a flat plate with traction free surfaces [25, 26]. In a cylindrical geometry (like a pipe), the mathematical treatment is analogous, using the boundary value problem for a hollow elastic cylinder [19, 27, 28]. Here, it is assumed that the considered pipe has a sufficiently large diameter, therefore the approximation of a flat plate can be made [29]. Furthermore, forward models of dispersion curves of flat plates and hollow cylinders of the same thickness (comparable to its radius) show discrepancies at frequencies that are very low to make a practical flow measurement anyway.

Lamb waves exist in the form of symmetric and anti-symmetric vibration modes, which can be further specified by their mode number. As mentioned earlier, Lamb waves are dispersive, see Fig. 3.1b. Both vibration modes produce in-plane and out-of-plane particle displacement. For symmetric modes, the main motion is in-plane, while for anti-symmetric modes it is out-of-plane, as depicted in Fig. 3.1a.

For an infinite plate of thickness *2h*, the Lamb modes are mathematically de-

(a)

(b)
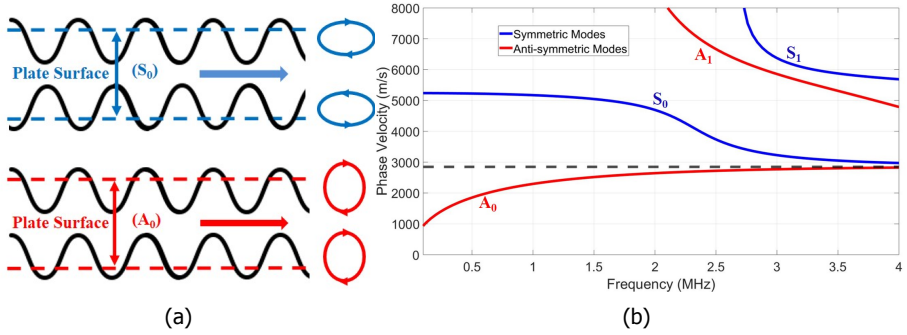
Figure 3.1: (a) Retrograde surface motion of symmetric (S) and anti-symmetric (A) Lamb wave modes in a plate. The blue and red ellipses indicate the trajectory of particle motion at each surface of the plate. The arrows indicate the propagation direction of the wave modes. (b) Phase velocity dispersion curves of the zero and first order Lamb wave modes that can propagate along a stainless steel plate with a thickness of $1\,\text{mm}$ ($c_L = 5800\,\text{m/s}$, $c_L = 3100\,\text{m/s}$). The dashed line indicates the Rayleigh wave speed c_R at a single free surface.

scribed by the Rayleigh-Lamb dispersion relations for symmetric modes

$$\frac{\tan(qh)}{\tan(ph)} = -\frac{4k^2 pq}{(q^2 - k^2)^2},\tag{3.1}$$

and for anti-symmetric modes

$$\frac{\tan(qh)}{\tan(ph)} = -\frac{(q^2 - k^2)^2}{4k^2 pq}.\tag{3.2}$$

In Eqs. 3.1 and 3.2, p and q are defined as

$$p^2 = \left(\frac{\omega^2}{c_L^2}\right)^2 - k^2,$$

$$q^2 = \left(\frac{\omega^2}{c_T^2}\right)^2 - k^2.\tag{3.3}$$

In Eq. 3.3, ω represents the angular frequency; k represents the wavenumber; c_L and c_T the longitudinal (compressional) and transversal (shear) wave speed in the material, respectively. The solutions to the dispersion equations can be found numerically [19].

The total wave field propagating in a solid slab can be expressed as the sum of symmetric and anti-symmetric mode functions for both in-plane, and out-of-plane particle motion. Considering x as the coordinate in the thickness direction, and z as the coordinate in the propagation direction, in-plane particle displacement can be mathematically expressed as

$$u(\omega, x, z) = \sum_{n=0}^{\infty} A_n(\omega)\, \Phi_{s,n}(\omega, x) e^{ikz} + B_n(\omega)\, \Phi_{a,n}(\omega, x) e^{ikz}, \qquad (3.4)$$

where $\Phi_{s,n}(\omega, x)$ and $\Phi_{a,n}(\omega, x)$ represent the symmetric and anti-symmetric in-plane mode functions, respectively, and $A_n(\omega)$ and $B_n(\omega)$ represent the expansion coefficients of both modes.

Correspondingly, out-of-plane particle displacement can be expressed as

$$w(\omega, x, z) = \sum_{n=0}^{\infty} A_n(\omega)\, \Psi_{s,n}(\omega, x) e^{ikz} + B_n(\omega)\, \Psi_{a,n}(\omega, x) e^{ikz}, \qquad (3.5)$$

where $\Psi_{s,n}(\omega, x)$ and $\Psi_{a,n}(\omega, x)$ represent the symmetric and anti-symmetric out-of-plane mode functions.

Mode functions $\Phi_{s,n}(\omega, x)$ and $\Phi_{a,n}(\omega, x)$ are orthogonal in x. This property allows to compute an expression for the expansion coefficients $A_n(\omega)$ and $B_n(\omega)$, at some location $z = z_0$

$$A_n(\omega) = \frac{\int_a^b u(\omega, x, z_0)\Phi_{s,n}^*(\omega, x) e^{-ikz_0}\, dx}{\int_a^b \Phi_{s,n}(\omega, x)\Phi_{s,n}^*(\omega, x)\, dx}, \qquad (3.6)$$

$$B_n(\omega) = \frac{\int_a^b u(\omega, x, z_0)\Phi_{a,n}^*(\omega, x) e^{-ikz_0}\, dx}{\int_a^b \Phi_{a,n}(\omega, x)\Phi_{a,n}^*(\omega, x)\, dx}. \qquad (3.7)$$

The limits of the integrals in Eqs. 3.6, 3.7 comprise the thickness of the solid slab being examined, and * indicates the complex conjugate. For each frequency, the expansion coefficients indicate the importance of the contribution of a particular mode to the total field distribution. The location z_0 should be outside the area where the modes are generated, i.e. outside the transducer range.

Frequency dependence of the amplitudes of the zero-order Lamb wave modes for a $5\,\text{mm}$-thick stainless steel plate is shown in Fig. 3.2. Even though an appropriate excitation frequency can help with the suppression of Lamb waves by a factor of 2, it is often not enough to achieve the needed accuracy for clamp-on flow metering.

3.2.2. Beam transmission with transducer arrays

Ultrasonic arrays have been designed and used for different purposes including medical imaging and NDE [30]. The far field directivity pattern of the acoustic beam produced by a transducer array consisting of rectangular elements radiating into a half-space can be described by the directivity function[24]

$$D(\theta) = d\left(-\frac{d}{\lambda}\sin\theta\right) \sum_{n=-\frac{N-1}{2}}^{\frac{N-1}{2}} F_n e^{jn(\Delta\phi_n + kd\sin\theta)}, \qquad (3.8)$$

3
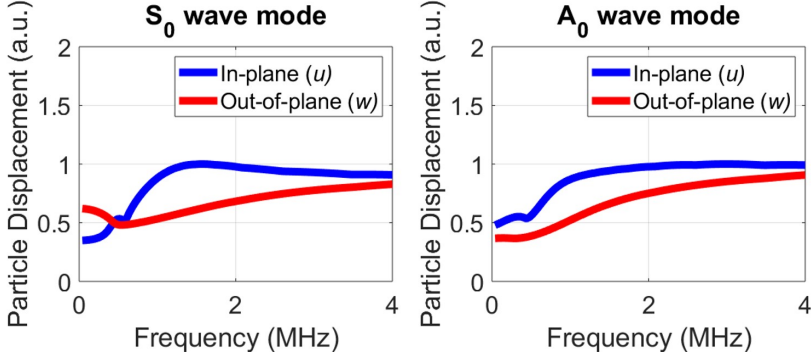
Figure 3.2: Amplitudes of the particle displacement of the zero-order Lamb waves in a 5 mm-thick stainless steel plate, loaded by water on one side, and by vacuum on the other side. A transducer array, placed on the vacuum-loaded surface of the plate, was used to excite an acoustic beam that impinged the steel-water interface with an angle of $45°$. The displacements $u(\omega, x, z_0)$ and $w(\omega, x, z_0)$ were computed across the thickness of the pipe wall ($-h \leq x \leq h$), at a propagation distance (z_0) located at the edge of the transducer array.

in which the amplitude F_n and phase $\Delta\phi_n$ of each element are parts of the complex apodization or aperture function $F_n \exp(i\Delta\phi_n)$ in the Fourier domain. Moreover, d is the pitch of the array; θ is the observation angle relative to the normal on the transducer surface, and N is the total number of elements of the array. In a clamp-on flow measurement setting, λ is the wavelength in the liquid.

Considering Eq. 3.8 in an ultrasonic clamp-on flow measurement setting, the
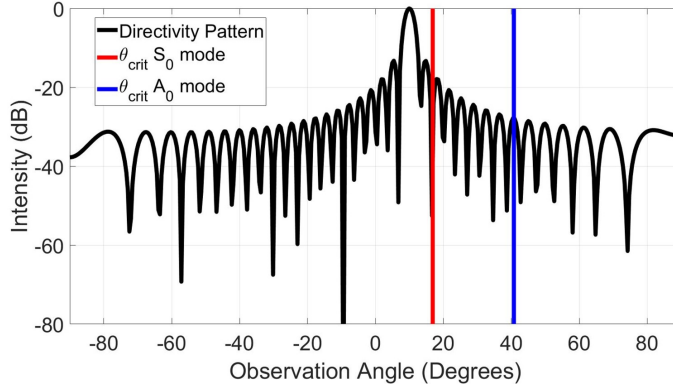
Figure 3.3: Directivity pattern (black curve) of a $\Psi = 10°$-steered acoustic beam in water ($c_m = 1500 m/s$) produced by a 37-element transducer array with a pitch of 0.72 mm excited at 1 MHz. To compute it, Eq. 3.8 was implemented, where $F_n = 1$, and $\Delta\phi_n = nkd \sin(\Psi)/c_m$, with k being the wavenumber of the acoustic beam in water at 1 MHz. The vertical red and blue lines indicate the critical angles beyond which only the zero-order Lamb wave modes propagate when such a beam impinges on a 1 mm-thick stainless-steel pipe wall. Due to the presence of side lobes, some energy from the beam may leak into these Lamb modes.

transducer array is virtually placed in the pipe wall - liquid interface. Furthermore, the effect of the pipe wall on Eq. 3.8 is directly observed in Fig. 3.3, by the amount of energy located beyond the critical angles of the Lamb wave modes. These angles depend on Snell's law through the sound speed of each mode at a particular frequency (1 MHz in case of Fig. 3.3) and the sound speed of the liquid.

During flow metering, significant Lamb wave modes are excited each time the acoustic beam impinges from the liquid onto the pipe wall. Such wave modes are excited even more efficiently when the incidence angle is close to their critical angle [31] (Fig. 3.3). Therefore, it may be necessary to suppress the amount of energy leaking into Lamb wave excitation at each beam reflection. Proper phase control of the transmitting array may result in steering the incidence angle as to avoid excitation of Lamb waves [21]. In contrast to previous work, in this research the phase shifts $\Delta\phi_n$ are reserved to steer and shape the beam, and the amplitude factors F_n are manipulated to suppress, the generation of undesired Lamb waves at each reflection of the acoustic beam.

3.3. Algorithm

The beam spot width W of an acoustic beam that hits the pipe wall with an incident angle θ relative to the normal of the pipe wall, can be computed as

$$W = \frac{2L \tan(\alpha/2)}{\cos \theta}. \tag{3.9}$$

Here, α is the opening angle of the beam at the -3 dB power level, and L is the distance travelled by the acoustic beam, i.e. the total length of the beam path from transmitter to receiver.

In clamp-on flow metering, the best accuracy is achieved when a maximum signal-to-noise ratio (SNR) is reached. This occurs when the entire aperture of the array is insonified by the entire in-coming beam. Therefore, it is desired to have an array aperture of N array elements that allows to generate a narrow acoustic beam on the transmission side and also to record this beam on all N elements on the receiving side. In receive, this will average out the noise by a factor of $\sqrt{N}$ compared to a single element.

However, such beams require small opening angles, and therefore demand a considerable number of elements. Cost and complexity of application-specific integrated circuits (ASICs) are proportional to the number of elements needed to drive a transducer array, and may become prohibitive for the number of elements that are needed to produce theoretically ideal beams. In practice, only a limited number of elements will be available, which will have an impact on the beam. Therefore, it is necessary to find a way to reduce the number of elements while retaining a good signal-to-noise ratio and a sufficient suppression of Lamb waves.

A flowchart of the algorithm to achieve this is shown in Fig. 3.4, and will be described in detail below.

3
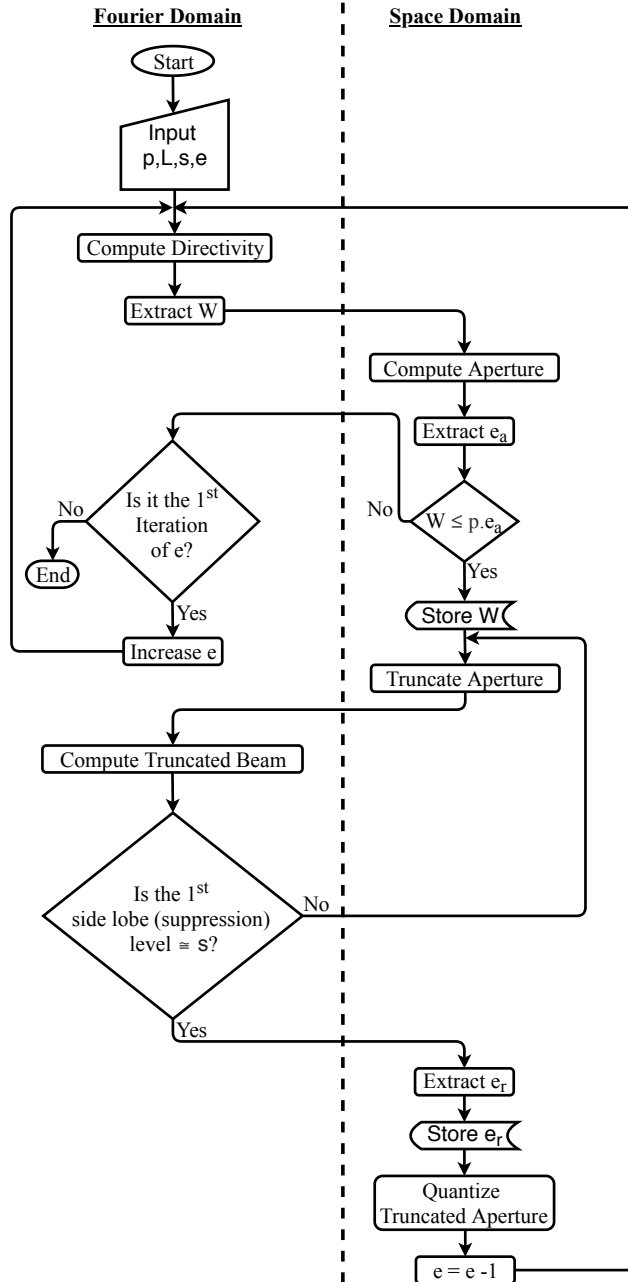
Figure 3.4: Flowchart of the proposed algorithm to obtain a transducer array aperture giving a good signal-to-noise ratio and sufficient suppression of Lamb waves. The ideal transmit beam yields a receive beam spot width that is equal to the recording array aperture.

3.3.1. Step 1: Define known parameters for beam and trans- ducer

First, the known parameters for the beam and the transducer are set. These are: the length L of the travel path of the beam, the level s of the first side lobe relative to the level of the main beam, and the pitch p of the array. These parameters are application dependent. Moreover, an initial number of e array elements is set. As an example, a transducer array with a center frequency of $1\,\text{MHz}$ will be designed. Moreover, a pipe inner diameter of $40\,\text{mm}$ and a beam propagating in water under an angle of $\theta = 10°$ with the normal of the pipe wall and making six bounces (v-shapes) within the pipe will be considered. For this geometry, a travel path length $L = 488\,\text{mm}$ can be determined.

Moreover, it will be assumed, as an external demand, that a suppression $s = 35\,\text{dB}$ of the spurious Lamb waves is needed. As a worst case scenario, it is assumed that all side lobes of the acoustic beam are converted into spurious Lamb modes, and that side lobe and Lamb mode amplitude are equivalent.

For a frequency band up to $2\,\text{MHz}$, a pitch $p = 0.72\,\text{mm}$ was considered to properly sample all possible propagating Lamb wave modes in stainless steel pipes with wall thicknesses between $1\,\text{mm}$ and $5\,\text{mm}$.

A relatively large number of array elements e is recommended to produce a narrow beam in reception and to ensure that all of its energy gets recorded. As an example, the algorithm is explained by showing the results with $e = 152$ initial array elements.

3.3.2. Step 2: Compute desired beam

To achieve the desired suppression level, the element amplitudes F_n in Eq. 3.8 were set to form a Blackman window. Figure 3.5a shows that the first side lobe is conveniently below the required $35\,\text{dB}$ level. Furthermore, at the $-3\,\text{dB}$ level, the beam has an opening angle $\alpha = 3°$ in water, which according to Eq. 3.9, produces a beam spot width $W = 25.1\,\text{mm}$ upon reception.

3.3.3. Step 3: Compute desired aperture

The aperture to produce the beam shown in Fig. 3.5a is computed via the Inverse Fast Fourier Transform (IFFT) of Eq. 3.8. The obtained aperture in Fig. 3.5b suggests that $e_a = 50$ active elements are sufficient to produce such a beam. The corresponding effective aperture of $36\,\text{mm}$ ensures that the whole beam width gets recorded upon reception. Otherwise, the algorithm would ask for a higher initial number of array elements e to produce a narrower beam.

3.3.4. Step 4: Truncate aperture and extract residual active elements

The challenge is to reduce the number of elements e below the obtained number of active elements e_a. Aperture truncation in the space domain is performed by multiplying the function in Fig. 3.5b with a rectangular window. This has the physical meaning of reducing the total number of elements of the array (red curve

3
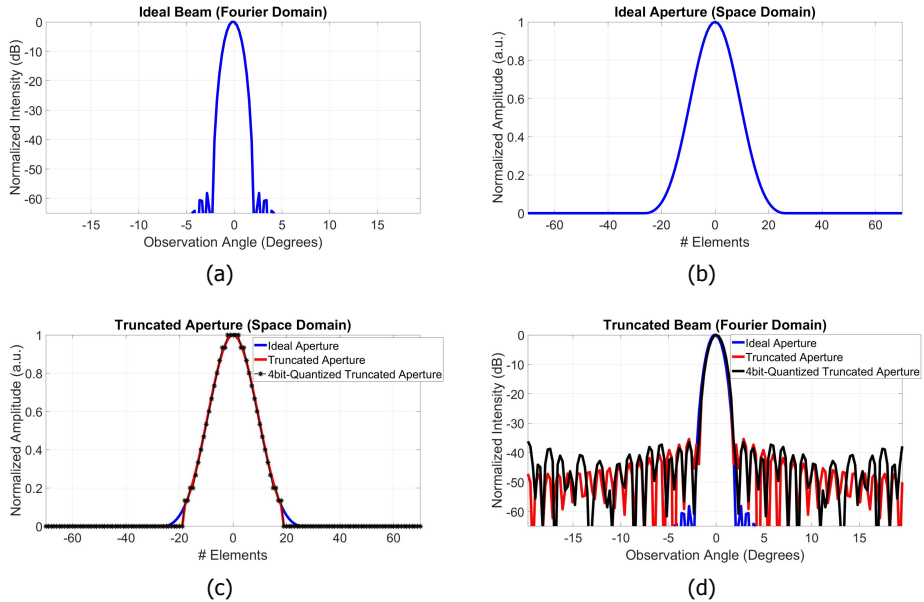
Figure 3.5: Beams and apertures involved in the design of a $1\,\mathrm{MHz}$-transducer array with a $0.72\,\mathrm{mm}$ pitch for ultrasonic clamp-on flow measurements, capable of suppressing Lamb waves of a $1\,\mathrm{mm}$-thick stainless steel wall by $35\,\mathrm{dB}$ during transmission. (a) Ideally desired beam: small opening angle and low side lobe levels. (b) Aperture function that shows an unpractical number of active elements needed to produce the ideal beam. (c) Truncated aperture function obtained with a rectangular window (red curve). After truncation, the aperture region with non-zero amplitudes is quantized (black curve). (d) Effect of truncation: rise of the side lobes relative to the ideal beam (red curve), and of quantization: small variation in side lobe levels (black curve).

in Fig. 3.5c), at the cost of increasing the side lobe levels compared to the initial beam. In this case, truncation is performed until the amplitude of the first side lobe reaches 35 dB (red curve in Fig. 3.5d). This resulted in $e_r = 37$ residual active elements, which cover an aperture of $26.6\,\mathrm{mm}$.

3.3.5. Step 5: Quantize the truncated aperture

In practical electronic transmit circuits, the amplitudes F_n of the elements will be quantized, and the aperture will have a step-like shape. In the current case, a 4 bit-quantization of the aperture has been applied (black curve in Fig. 3.5c). This further modifies the shape of the resultant beam.

3.3.6. Step 6: Compute practical beam

By again invoking Eq. 3.8, the beam resulting from the truncated and quantized aperture can be obtained. At this stage it is possible to see whether the quantization still leads to an acceptable performance. For the described 4-bit case, the beam has a very similar width as the non-quantized one and keeps the side lobe levels
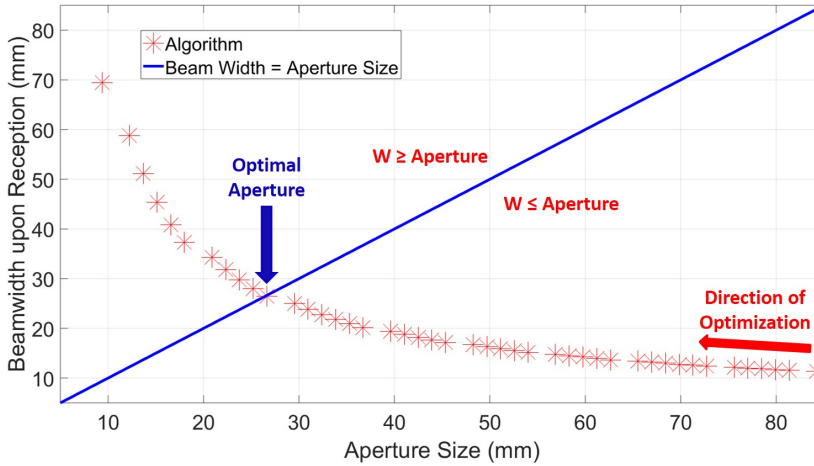
Figure 3.6: Beam spot width upon reception as a function of aperture size, as computed by the algorithm, for a 1 MHz transducer array with a 0.72 mm pitch and 35 dB suppression of Lamb waves. The optimal aperture size of 26.6 mm corresponds to 37 array elements.

below 35 dB (black curve in Fig. 3.5d). Higher quantization levels would produce a smoother aperture, but the complexity of the electronics would increase proportionally. Lastly, the -3 dB opening angle α can be extracted and the spot width W of the quantized beam can be computed. In this case, the beam has an opening angle $\alpha = 3.1°$ and produces a beam spot width $W = 26.1$ mm upon reception, which is close to the 26.6 mm size of the array aperture.

The algorithm will loop steps 2-6 with a smaller initial number of array elements e. This happens until the beam spot width becomes larger than the residual active array aperture. Figure 3.6 shows the beam spot size upon reception, as a function of the aperture size. From this figure it is possible to graphically find the optimal number of array elements for the ultrasonic clamp-on flow metering application: the one whose aperture has the same (or very similar) length as the produced beam spot width upon reception.

3.4. Simulation study

In this Section, 2D simulations are presented for a water-filled stainless steel pipe with 40 mm inner diameter and 1 mm wall thickness, in combination with a transducer array with a pitch of 0.72 mm clamped outside the pipe wall. Furthermore, two different center frequencies will be considered in two separate scenarios: 1 MHz and 1.5 MHz. The first one will be the center frequency of a sensor under development, and the second one is the center frequency used in experimental studies presented in the next section.

3.4.1. Simulation settings

At $1\,\mathrm{MHz}$, the fastest Lamb wave mode that can propagate in a $1\,\mathrm{mm}$-thick stainless steel pipe wall is the zero-order symmetric (S_0) mode ($c_{S_0} = 5173\,\mathrm{m/s}$, see Fig. 3.1b). It was found in the previous section that 37 elements are enough to produce a $35\,\mathrm{dB}$ suppression of this mode. In this case, a beam steered at $45°$ through the pipe wall would refract into water at $10°$ with an opening angle of $3.1°$, which is below the critical angle for the S_0 mode, being $16.9°$.

On the other hand, to suppress the S_0 wave mode at $1.5\,\mathrm{MHz}$, the implementation of the algorithm proposed in the previous section would report an optimal $e_r = 25$ residual active elements (aperture of $18\,\mathrm{mm}$) with a beam spot width of $W = 18.64\,\mathrm{mm}$ upon reception. Considering the dispersion curves of Fig. 3.1b, and the same $10°$ angle of refraction of the acoustic beam into the water, it is expected to suppress the S_0 wave mode, and also to have some leakage towards the excitation of the A_1 wave mode since this last one has a faster sound speed, relative to the S_0 wave mode, that is not accounted by the beam direction.

Two-dimensional Finite Element Modeling (FEM) was used to simulate the effect of controlling the amplitudes of the elements of a transducer array for the suppression of Lamb waves. The software package PZFlex (Onscale, Redwood City, CA, USA) was used. A 2D longitudinal cross section of a water-filled pipe was defined (Fig. 3.7a), including an array consisting of lead-zirconate-titanate (PZT) elements made of HK1HD (TRS Technologies, Inc., State College, PA, USA).

For each scenario (i.e. center frequency), two simulations were carried out. In both, the driving function on the PZT elements consisted of a 2-cycle sine wave, and the acoustic beam was steered $45°$ by means of phase shifting. For the first simulation, a uniform amplitude function was applied to the driving signals of the elements. For the second simulation, a tapered amplitude function obtained by the previously described algorithm was applied (Fig. 3.7b). Virtual receivers were placed along the steel-air interface to record the total perpendicular stress compo-
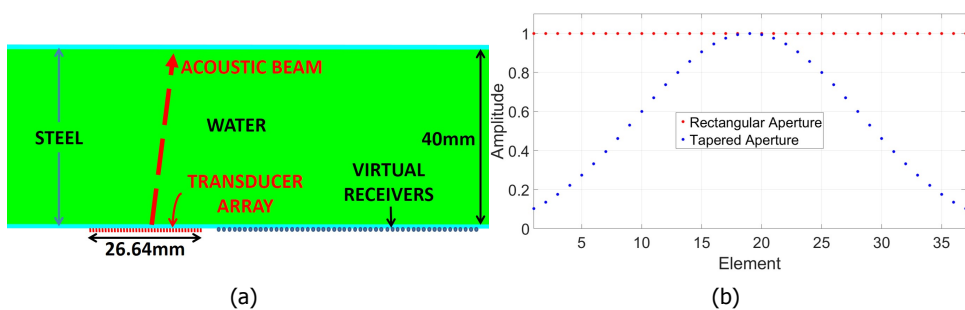
Figure 3.7: (a) Cross-section of the pipe used in 2D FEM simulations of a 37-element transducer array with a center frequency of $1\,\mathrm{MHz}$. The acoustic beam was steered $45°$ through the $1\,\mathrm{mm}$-thick pipe wall, traveling to the right. Stress perpendicular to the steel surface was recorded by the virtual receivers to identify propagating waves in post-processing. (b) Amplitude function (F_n) applied to the driving signals of the elements.

nent from all waves in the pipe wall, including the longitudinal wave refracting from the liquid. These waves were subsequently identified in the Fourier domain. The simulations were run until the beams had bounced six times (v-shapes) within the pipe.

3.4.2. Results for 1 MHz

For the applied uniform and tapered amplitudes, the stress component perpendicular to the steel surface is shown in Fig. 3.8a and Fig. 3.8b. In Fig. 3.8a the excitation of Lamb waves at each bounce of the beam is visible, and in Fig. 3.8b it is shown that these waves are highly suppressed. To demonstrate the working of the algorithm, the geometry in Fig. 3.7a was chosen such that the longitudinal wave and the Lamb waves are independently visible in the time domain.

The magnitude of the 2D Fast Fourier Transform (FFT) of the time signals in Fig. 3.8 was computed to quantitatively get the amount of Lamb wave suppression achieved in each case. Fig. 3.8c and Fig. 3.8d show the independently normalized magnitudes with a dynamic range of $35\,\mathrm{dB}$. It can be noticed that, after the implementation of a tapered amplitude function (Fig. 3.8d), the S_0 Lamb wave mode was suppressed below $35\,\mathrm{dB}$, as desired.

The striped nature of the information in Fig. 3.8c and Fig. 3.8d is a result of applying an FFT to the entire time-space domain of Fig. 3.8a and Fig. 3.8b, respectively, rather than to individual echoes. Furthermore, the side lobes located around $0.25\,\mathrm{MHz}$ and $1.7\,\mathrm{MHz}$ are the result of space-time windowing effects of the signal.

3.4.3. Results for 1.5 MHz

The time signals in Fig. 3.9a and Fig. 3.9b show the effect of a suppression of the Lamb wave modes when a tapered aperture of the transducer array is implemented. Moreover, the 2D FFTs shown in Fig. 3.9c and Fig. 3.9d quantitatively indicate a suppression of the amplitude of the problematic S_0 Lamb wave mode by $35\,\mathrm{dB}$ relative to the longitudinal wave refracting from the liquid, as designed and expected from the algorithm described here.

In view of the previously described points, the transducer array apertures leading to the signals of Fig. 3.8b and Fig. 3.9b will make a more accurate estimate of flow relative to those of Fig. 3.8a and Fig. 3.9a, since the disturbing Lamb wave mode (in particular the one closest to the longitudinal wave carrying information from the water) has been suppressed below the required level. If necessary, other types of methods (e.g. filtering, time windowing) can be applied afterwards to suppress less problematic spurious Lamb waves.

3.5. Experimental validation of the method

3.5.1. Measurement description

For a proof of principle, the experimental setup of Fig. 3.10 was built. It consisted of two $1\,\mathrm{mm}$-thick parallel stainless-steel plates separated by a $40\,\mathrm{mm}$ column of water. Two ATL P4-1 phased array probes (Philips, Bothell, WA, USA) were horizontally aligned and placed on top of one of the plates. These probes consist of 96 single

3
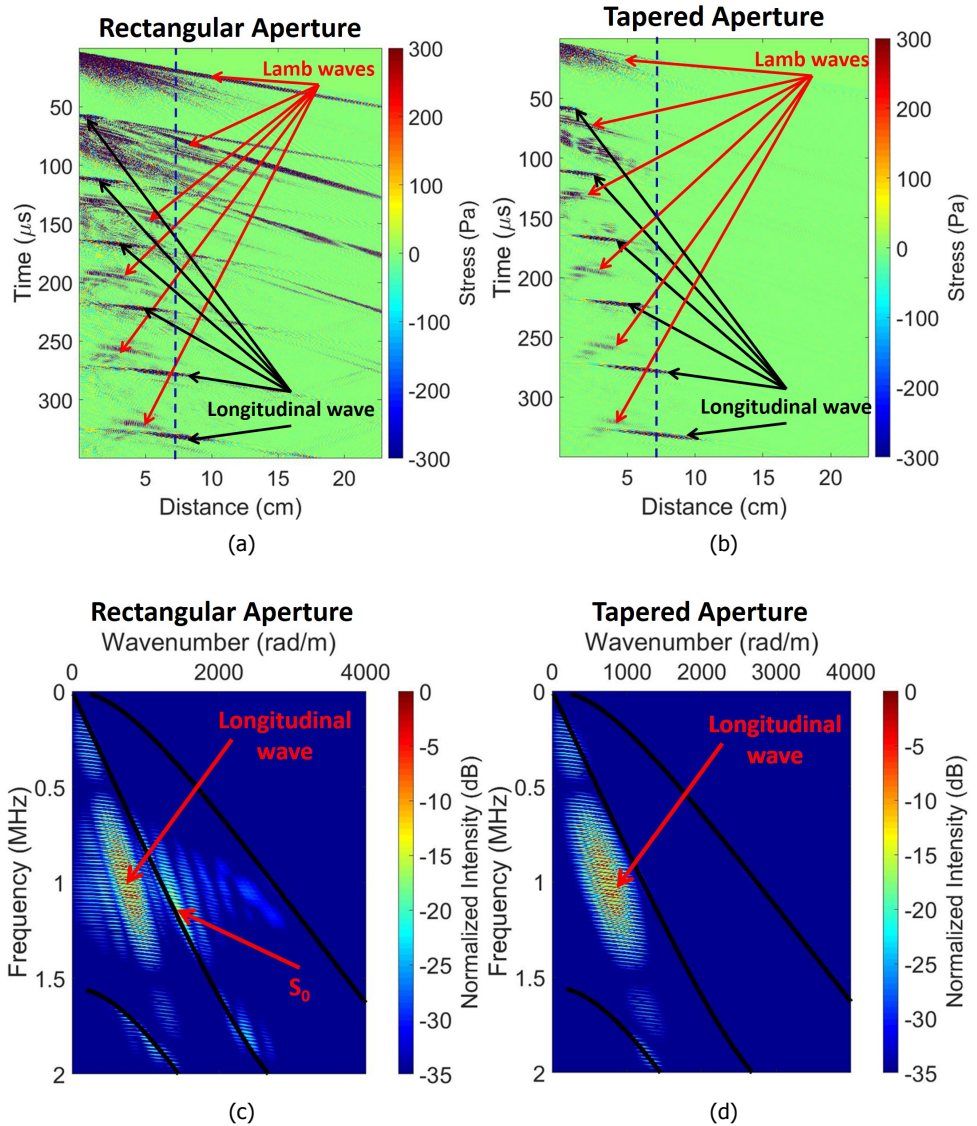
Figure 3.8: Stress (perpendicular component) recorded along the steel-air interface for the two considered simulations with a 37-element transducer array with a center frequency of 1 MHz. (a) Rectangular aperture function (b) Tapered aperture function. The longitudinal wave refracting from water bounced six times within the pipe wall. The blue dashed lines mark the time signal located 7.7 cm away from the source. (c) Normalized 2D FFT of the recorded space-time signals in (a). (d) Normalized 2D FFT of the recorded space-time signals in (b). The black lines represent the theoretical dispersion curves of the Lamb waves that propagate within the steel.
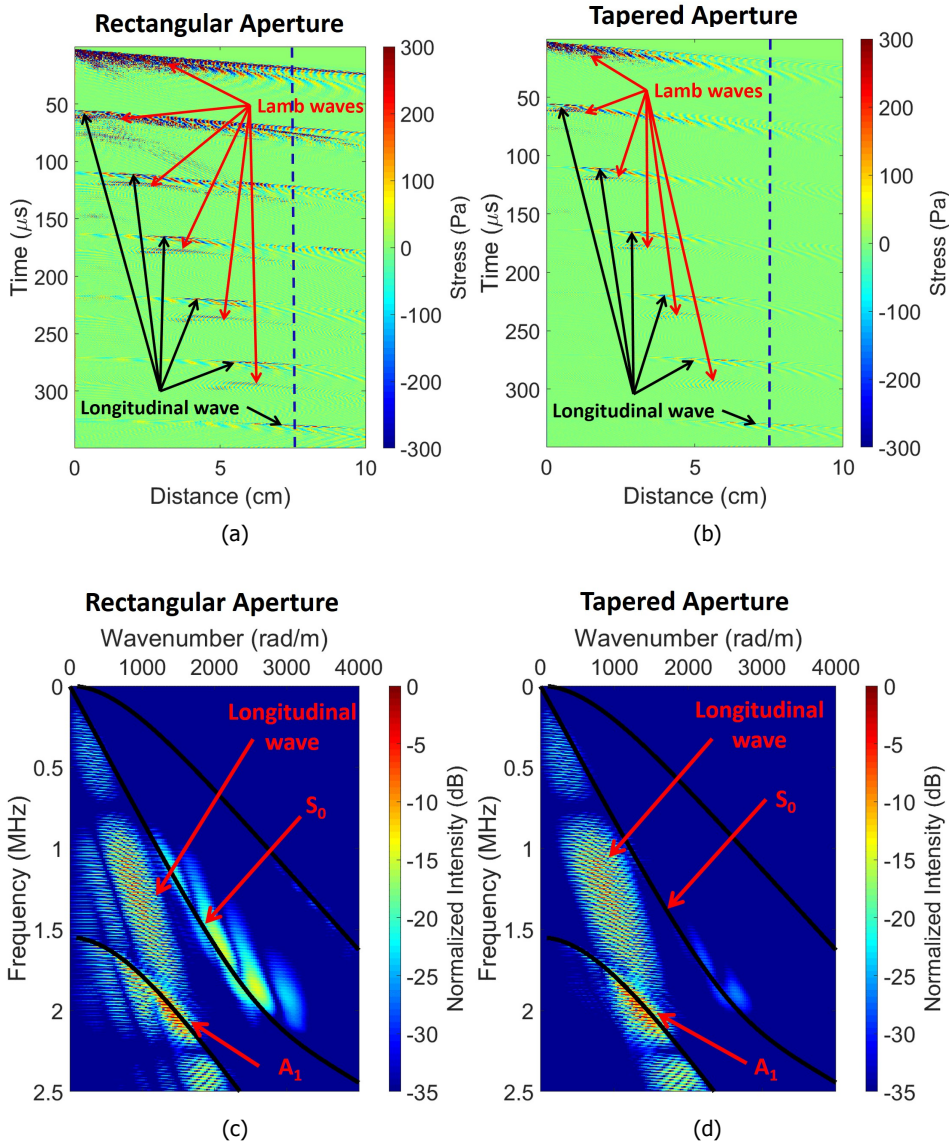
Figure 3.9: Stress (perpendicular component) recorded along the steel-air interface for the two considered simulations with a 25-element transducer array with a center frequency of $1.5\,\mathrm{MHz}$. (a) Rectangular aperture function (b) Tapered aperture function. The longitudinal wave refracting from water bounced six times within the pipe wall. The blue dashed lines mark the time signal located $7.7\,\mathrm{cm}$ away from the source. (c) Normalized 2D FFT of the recorded space-time signals in (a). (d) Normalized 2D FFT of the recorded space-time signals in (b). The black lines represent the theoretical dispersion curves of the Lamb waves that propagate within the steel.
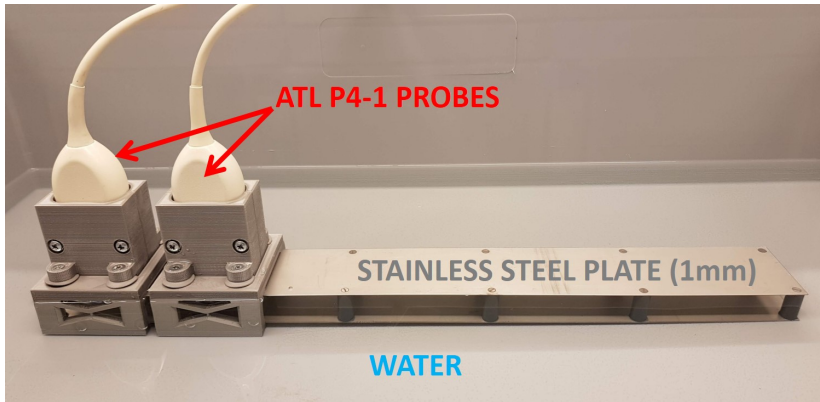
Figure 3.10: Experimental setup. Two ATL P4-1 phased array probes on top of one of the two 1 mm-thick stainless steel plates. The center of the probes were separated by 7.7 cm. The distance between both plates was 40 mm and filled with water. The upper side of the top plate was still loaded by air. Probe holders are made of a material with a similar acoustic impedance as that of water to avoid reflection effects on the recorded data.

elements with a pitch of $295\,\mu m$ and a $-20\,dB$ frequency bandwidth from $1\,MHz$ to $4\,MHz$. A Verasonics Vantage 256 system (Verasonics Inc., Kirkland, WA, USA) was used to drive the probes and record the data.

In transmission, a 16-cycle sine wave with a center frequency of $1.5\,MHz$ was used as a driving signal of one of the probes. Moreover, time delays were applied to its individual elements to excite a longitudinal wave in the steel plate that impinges the steel-water interface under a $45°$ angle. In reception, the second probe was horizontally placed $7.7\,cm$ away from the first one (center to center distance), where according to the simulation results in Fig. 3.8 and Fig. 3.9, it is expected to receive the 5th bounce of the longitudinal wave.

Two experiments were performed. First, a rectangular amplitude weighting function was applied along the elements of the array. Second, a tapered aperture was applied. This aperture was computed using the algorithm previously described.

3.5.2. Results and discussions
Figure 3.11a and Fig. 3.11b show the recorded time signals for each case with all elements of the receiving probe. Five bounces of the beam can be noticed. Due to the bounded spatial region where these signals were recorded ($6.3 - 9.1\,cm$ away from the center of the transmitting probe), it is not as straightforward to identify different propagating wave modes in this domain as it is in Fig. 3.8a, Fig. 3.8b, Fig. 3.9a and Fig. 3.9b.

Several transformations, like the Radon transform, can be used to identify the recorded wave modes [32]. In this case, the magnitude of a 2D FFT of the measured signals was computed for identifying the propagating wave modes. Figure 3.11c and Fig. 3.11d show the independently-normalized magnitudes for each aperture with a dynamic range of $35\,dB$, where the longitudinal wave as well as the S_0 Lamb
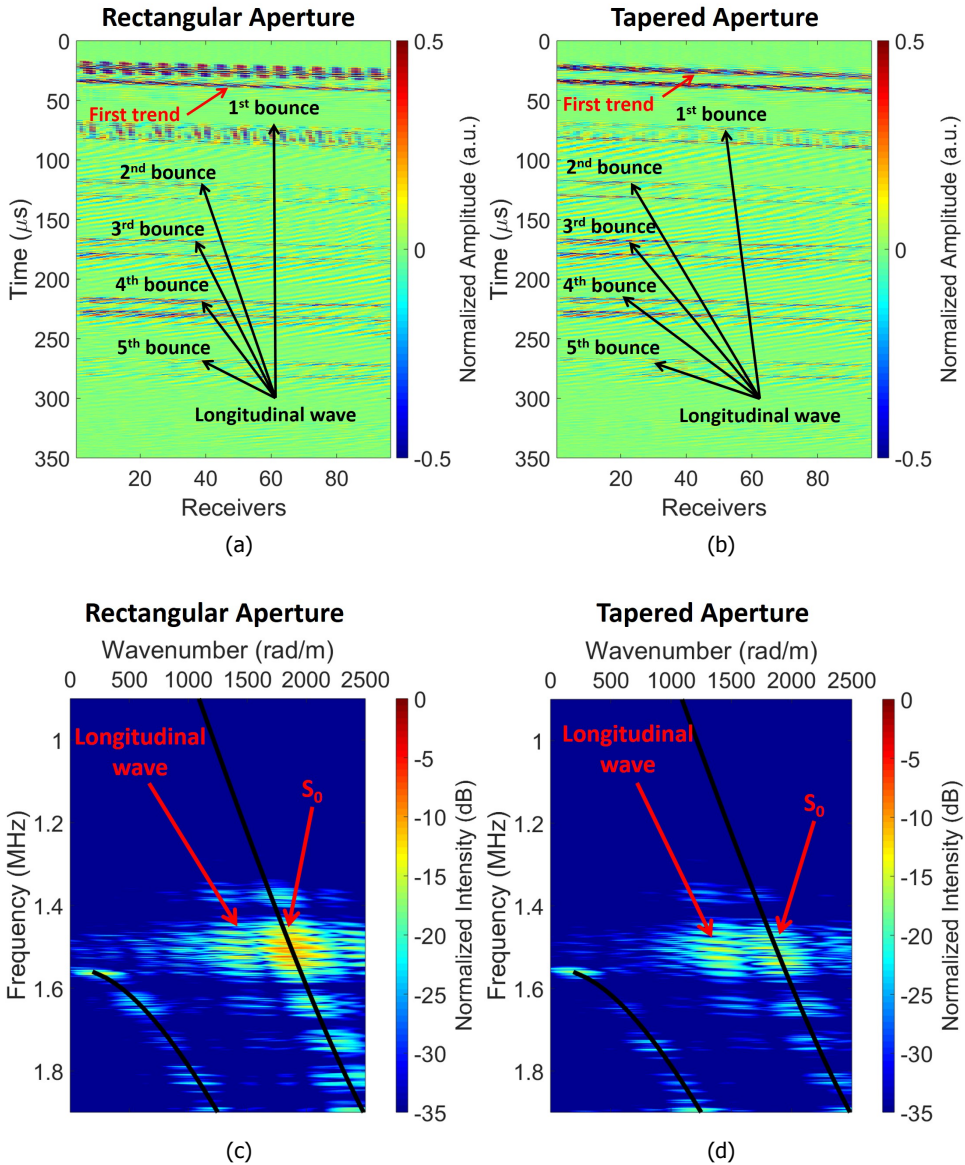
Figure 3.11: Signals recorded with all 96 elements of the receiving probe in the experimental setup. (a) Rectangular aperture function. (b) Tapered aperture function. It becomes challenging to identify the fifth bounce of the longitudinal wave in this domain. (c) Normalized 2D FFT of the measured space-time signals in (a). (d) Normalized 2D FFT of the measured space-time signals in (b). The black lines represent the theoretical dispersion curves of the Lamb waves that propagate in the steel plate.

wave mode can be observed. With a controlled aperture, a suppression of $20\,\mathrm{dB}$ for the S_0 wave mode was achieved. The stripe patterns are due to the implementation of the FFT for the full space-time domain.

The space-limited information of the $2.83\,\mathrm{cm}$ probe aperture gives a less clear suppression effect in Fig. 3.11d relative to Fig. 3.9d. Therefore, a fairer one-to-one comparison was made. The 2D FFTs of the simulated data were computed using the same spatial range as in the experiments. The difference between both aperture schemes was computed and compared to that of the experimental data (see Fig. 3.12). It is observed that the level of suppression of the problematic S_0 Lamb wave mode, within the spatial range of the receiving transducer, is the same for the simulated and measured data, i.e. around $20\,\mathrm{dB}$. Moreover, during suppression, no reduction of the energy of the longitudinal wave took place, as can also be seen in Fig. 3.11b.

3.6. Conclusions

Here, a method has been described to steer an acoustic beam through a pipe wall while suppressing, in transmission, the excitation of spurious Lamb waves. In this way, absolute errors caused by these waves during clamp-on flow metering can be reduced. An algorithm to estimate the transducer array aperture (i.e. the number of elements and their amplitudes) required to achieve a desired performance has been described.
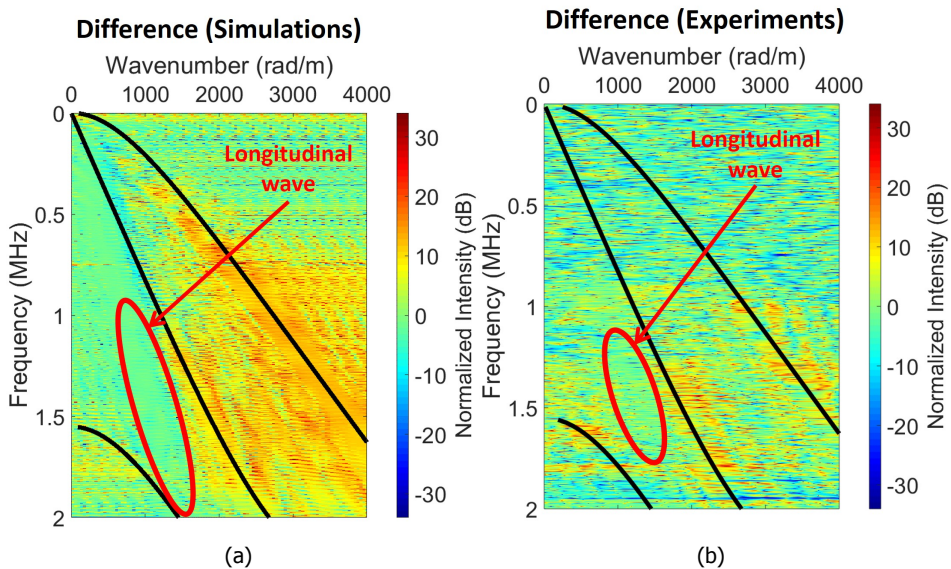
Figure 3.12: Difference between 2D FFTs of space-time signals for a rectangular and a tapered aperture. The spatial domain is located at $6.3 - 9.1\,\mathrm{cm}$ away from the center of the source. (a) Simulations. (b) Experiments. The black lines represent the theoretical dispersion curves.

Due to its particular application for clamp-on flow metering, the method is based on amplitude manipulations of the aperture function of a transducer array, while phase shifts are used to control the shape of the propagating acoustic beam. Simulations and experimental results of an ultrasonic clamp-on flow measurement setting using $1\,\mathrm{mm}$-thick stainless steel plates have been performed as proof and show a good agreement.

References

[1] J. Massaad, P. L. M. J. van Neer, D. M. van Willigen, M. A. P. Pertijs, N. de Jong, and M. D. Verweij, *Suppression of Lamb wave excitation via aperture control of a transducer array for ultrasonic clamp-on flow metering,* J. Acoust. Soc. Am. **147**, 2670 (2020).

[2] J. C. Wendoloski, *On the theory of acoustic flow measurement,* J. Acoust. Soc. Am. **110**, 724 (2001).

[3] W.-S. Cheung, H.-S. Kwon, K.-A. Park, and J.-S. Paik, *Acoustic flowmeter for the measurement of the mean flow velocity in pipes,* J. Acoust. Soc. Am. **110**, 2308 (2001).

[4] R. C. Baker, *Flow measurement handbook: industrial designs, operating principles, performance, and applications* (Cambridge University Press, 2005).

[5] D. Kurniadi and A. Trisnobudi, *A multi-path ultrasonic transit time flow meter using a tomography method for gas flow velocity profile measurement,* Part. Part. Syst. Charact. **23**, 330 (2006).

[6] M. Sanderson and H. Yeung, *Guidelines for the use of ultrasonic non-invasive metering techniques,* Flow. Meas. Instrum. **13**, 125 (2002).

[7] K. Xu, D. Ta, B. Hu, P. Laugier, and W. Wang, *Wideband dispersion reversal of Lamb waves,* IEEE Trans. Ultrason. Ferroelectr. Freq. Control **61**, 997 (2014).

[8] C. Prada and M. Fink, *Separation of interfering acoustic scattered signals using the invariants of the time-reversal operator. Application to Lamb waves characterization,* J. Acoust. Soc. Am. **104**, 801 (1998).

[9] K. G. Sabra, A. Srivastava, F. Lanza di Scalea, I. Bartoli, P. Rizzo, and S. Conti, *Struct. health monit. by extraction of coherent guided waves from diffuse fields,* J. Acoust. Soc. Am. **123**, EL8 (2008).

[10] K. Xu, D. Ta, P. Moilanen, and W. Wang, *Mode separation of Lamb waves based on dispersion compensation method,* J. Acoust. Soc. Am. **131**, 2714 (2012).

[11] G. Dib, O. Karpenko, M. Haq, L. Udpa, and S. Udpa, *Advanced signal processing algorithms in structural integrity monitoring,* Procedia Eng. **86**, 427 (2014).

3

[12] J.-L. Le Calvez and T. M. Brill, *A method to separate flexural and extensional signals from mixed-mode ultrasonic signals,* IEEE Int. Ultrason. Symp. , 1 (2016).

[13] L. Bai, K. Xu, N. Bochud, D. Ta, B. Hu, P. Laugier, and J.-G. Minonzio, *Multichannel wideband mode-selective excitation of ultrasonic guided waves in long cortical bone,* IEEE Int. Ultrason. Symp. , 1 (2016).

[14] H. Li, X. Liu, and L. Bo, *A novel method to analysis strong dispersive overlapping Lamb-wave signatures,* J. Vibroeng (2017).

[15] F. Gao, L. Zeng, J. Lin, and Z. Luo, *Mode separation in frequency–wavenumber domain through compressed sensing of far-field Lamb waves,* Meas. Sci. Technol. **28**, 075004 (2017).

[16] V. Serey, N. Quaegebeur, P. Micheau, P. Masson, M. Castaings, and M. Renier, *Selective generation of ultrasonic guided waves in a bi-dimensional waveguide,* Struct. Health Monit. **18**, 1324 (2019).

[17] W. Zhu and J. L. Rose, *Lamb wave generation and reception with time-delay periodic linear arrays: A BEM simulation and experimental study,* IEEE Trans. Ultrason. Ferroelectr. Freq. Control **46**, 654 (1999).

[18] J. Li and J. L. Rose, *Implementing guided wave mode control by use of a phased transducer array,* IEEE Trans. Ultrason. Ferroelectr. Freq. Control **48**, 761 (2001).

[19] J. L. Rose, *Ultrasonic guided waves in solid media* (Cambridge University Press, 2014).

[20] K.-C. T. Nguyen, L. H. Le, T. N. H. T. Tran, M. D. Sacchi, and E. H. M. Lou, *Excitation of ultrasonic Lamb waves using a phased array system with two array probes: Phantom and in vitro bone studies,* Ultrasonics **54**, 1178 (2014).

[21] C. Adams, S. Harput, D. Cowell, T. M. Carpenter, D. M. Charutz, and S. Freear, *An adaptive array excitation scheme for the unidirectional enhancement of guided waves,* IEEE Trans. Ultrason. Ferroelectr. Freq. Control **64**, 441 (2017).

[22] D. Guyomar and J. Powers, *A Fourier approach to diffraction of pulsed ultrasonic waves in lossless media,* J. Acoust. Soc. Am. **82**, 354 (1987).

[23] R. J. Zemp, J. Tavakkoli, and R. S. Cobbold, *Modeling of nonlinear ultrasound propagation in tissue from array transducers,* J. Acoust. Soc. Am. **113**, 139 (2003).

[24] R. S. Cobbold, *Foundations of Biomedical Ultrasound* (Oxford University Press, 2006).

[25] V. Pagneux, *Revisiting the edge resonance for Lamb waves in a semi-infinite plate,* J. Acoust. Soc. Am. **120**, 649 (2006).

[26] J. D. N. Cheeke, *Fundamentals and Applications of Ultrasonic Waves* (CRC Press, 2016).

[27] I. A. Viktorov, *Rayleigh and Lamb Waves: Physical Theory and Applications. Transl. from Russian. With a Foreword by Warren P. Mason* (Plenum Press, 1967).

[28] R. E. Bunney, R. R. Goodman, and S. W. Marshall, *Rayleigh and Lamb Waves on Cylinders,* J. Acoust. Soc. Am. **46**, 1223 (1969).

[29] A. Velichko and P. D. Wilcox, *Excitation and scattering of guided waves: Relationships between solutions for plates and pipes,* J. Acoust. Soc. Am. **125**, 3623 (2009).

[30] R. M. Levine and J. E. Michaels, *Model-based imaging of damage with Lamb waves via sparse reconstruction,* J. Acoust. Soc. Am. **133**, 1525 (2013).

[31] V. Dayal and V. K. Kinra, *Leaky Lamb waves in an anisotropic plate. I: An exact solution and experiments,* J. Acoust. Soc. Am. **85**, 2268 (1989).

[32] K. Xu, D. Ta, D. Cassereau, B. Hu, W. Wang, P. Laugier, and J.-G. Minonzio, *Multichannel processing for dispersion curves extraction of ultrasonic axial-transmission signals: Comparisons and case studies,* J. Acoust. Soc. Am. **140**, 1758 (2016).

3

4

Measurement of Pipe and Fluid Properties with a Matrix Array-based Ultrasonic Clamp-on Flow Meter

Current ultrasonic clamp-on flow meters consist of a pair of single-element transducers which are carefully positioned before use. This positioning process consists of manually finding the distance between the transducer elements, along the pipe axis, for which maximum SNR is achieved. This distance depends on the sound speed, thickness and diameter of the pipe, and on the sound speed of the liquid. However, these parameters are either known with low accuracy or completely unknown during positioning, making it a manual and troublesome process. Furthermore, even when sensor positioning is done properly, uncertainty about the mentioned parameters, and therefore on the path of the acoustic beams, limits the final accuracy of flow measurements. Here, these issues are addressed using an ultrasonic clamp-on flow meter consisting of two matrix arrays, which enables the measurement of pipe and liquid parameters by the flow meter itself. Automatic parameter extraction, combined with the beam steering capabilities of transducer arrays, yield a sensor capable of compensating for pipe imperfections. Three parameter extraction procedures are presented. First, axial Lamb waves are excited along the pipe wall and recorded with one of the arrays. A dispersion curve-fitting algorithm is used to extract bulk sound speeds and thickness of the pipe wall from the measured dispersion curves.

Second, circumferential Lamb waves are excited, measured and corrected for dispersion to extract the pipe diameter. Third, pulse-echo measurements provide the sound speed of the liquid. The feasibility and effectiveness of these procedures has been tested in simulations and experiments.

4

4.1. Introduction

Ultrasound is widely used to measure flow in industrial environments. There are two major classes of ultrasonic flow meters: in-line and clamp-on. The former typically consists of pairs of single-element transducers positioned inside the pipe and in direct contact with the fluid. The latter generally consists of a single pair of transducers placed on the pipe wall [3] (Fig. 4.1a). In both cases, the flow speed will be obtained by measuring the difference between upstream and downstream transit times of the propagating acoustic waves.

The design of in-line flow meters includes a pipe section with known dimensions, around which the transducers are aligned. This alignment depends on the expected range of flow speeds. For very high flow speeds, the acoustic beams might be deflected by the flow, resulting in lower signal-to-noise ratios (SNRs). Nevertheless, since the dimensions of the pipe are known, the acoustic path is completely characterized, and provided the speed of sound of the liquid contents is known, in-line flow meters do not have to be calibrated.

On the other hand, clamp-on flow meters are commonly placed onto pipes whose wall properties (bulk wave sound speeds, diameter, and thickness) and liquid contents properties (sound speed) are not known with enough accuracy or, less often, are completely unknown [4]. Therefore, this type of flow meter needs to be manually calibrated for each pipe. Apart from measuring the pipe and fluid parameters, this calibration consists of manually aligning the transducers by moving these along the pipe and finding the position for which the transmitted acoustic beams are recorded with the highest amplitude (Fig. 4.1b). The main advantage of these flow meters is that, contrary to their in-line counter-parts, they can be installed without interrupting the flow in the pipeline, which represents a valuable advantage in several industries.

The manual alignment procedure of ultrasonic clamp-on flow meters can be tedious when the pipe properties are not known, and also troublesome when working in confined areas. Moreover, pipe imperfections (i.e. corrosion, thickness and diameter variations, etc.) remain unnoticed and will not be accounted for when calibrating single-element transducers. Furthermore, even when the axial distance between the transducer in Fig. 4.1b is found properly, there still remain uncertain-
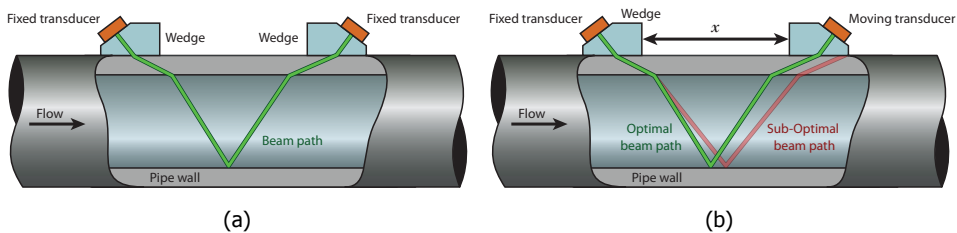
Figure 4.1: (a) Cross-section of a conventional ultrasonic clamp-on flow meter. The beam path depends on pipe and liquid properties. (b) Manual alignment procedure: the transducer separation distance x is varied along the pipe length until a peak amplitude is measured by the moving transducer.

ties on the pipe properties and geometry, as well as on the sound speed of the liquid. This leads to uncertainties in the travel path of the acoustic waves, and thus to errors in the flow estimations. Therefore, it would be very valuable to develop a clamp-on flow meter that is able to characterize the medium and the liquid, find the optimal beam path, and thus automatically calibrate itself prior to metering.

To achieve this, an ultrasonic clamp-on flow meter based on a pair of matrix transducer arrays is proposed. With such arrays, the properties of the pipe (bulk wave sound speeds, diameter, and wall thickness) and the liquid (sound speed) can be measured. From these parameters, and the beam steering capabilities of matrix arrays, the optimal travel path of the acoustic waves can be automatically found without manual displacement of the sensors. Here, the concept of these calibration measurements, as well as simulation and experimental results of their feasibility are presented.

4.2. Guided waves in pipes

The wall of a pipe acts as a waveguide, and when a pipe wall is mechanically excited, dispersive Lamb waves are generated. In a pipe, three types of Lamb wave modes exist: longitudinal, torsional and flexural. The first two modes are axisymmetric, while the last one is not. The mathematical treatment of such waves has been described in [5, 6], and the results are summarized in [7].

Generally, ultrasonic clamp-on flow meters operate in a frequency range from $0.2\,\mathrm{MHz}$ up to $2\,\mathrm{MHz}$ [3], and dispersion curves of guided waves in pipes are very similar to those in plates, except at very low and very high frequency values (Fig. 4.2). Furthermore, if the wavelength λ is much smaller than the pipe circumference, i.e. $\lambda \ll 2\pi R$, with R being the pipe radius, the approximation of a
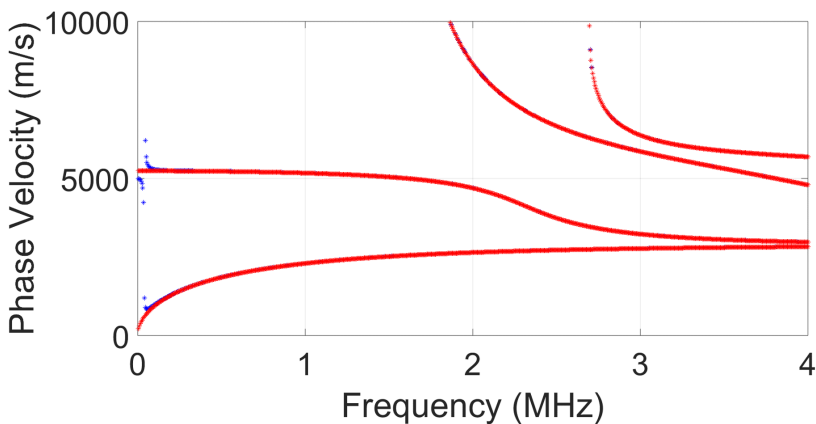
Figure 4.2: Dispersion curves of Lamb waves computed for a stainless steel plate (red), and a $40\,\mathrm{mm}$-inner diameter pipe (blue). Both geometries have a thickness of $h = 1\,\mathrm{mm}$, and sound speeds of $c_L = 5800\,\mathrm{m/s}$ and $c_T = 3100\,\mathrm{m/s}$. The equations that characterize the symmetric and anti-symmetric wave modes of the plate, as well as the longitudinal circumferential wave modes of the pipe, overlap through the whole frequency range, except at very low frequencies.

flat plate can be made [8]. Then, the dispersion behavior of longitudinal Lamb wave modes is given by the Rayleigh-Lamb equation for symmetric and anti-symmetric modes, as described by Eqs. 3.1, 3.2 and 3.3, characterized by the longitudinal and shear bulk wave sound speeds, c_L and c_T respectively, and thickness h of the material.

4.3. Bulk wave sound speeds and wall thickness of the pipe

The procedure for measurement of the bulk wave sound speeds and the wall thickness of the pipe is based on a quantitative fitting of the measured dispersion curves to the relevant dispersion equations. For simplicity, in this section it will be assumed that the transducer array is directly placed on top of the pipe wall i.e., without a coupling piece.

4.3.1. Approach

A cross-section along the axial direction of a clamp-on flow meter with two transducer arrays is shown in Fig. 4.3. To measure the relevant pipe wall parameters, Lamb waves are generated in the pipe wall by exciting one or several elements of one array, and these are recorded by all the elements of the second array. The measured time-distance $(t - x)$ signals can be analyzed in the frequency - horizontal wavenumber (i.e. $f - k_x$) domain, which yields the dispersion curves of the observed symmetric and anti-symmetric modes. The parameters c_L, c_T and h can be found by identifying which combination of these generates the theoretical dispersion curves of Eq. 3.1 and Eq. 3.2 that best match the observed dispersion curves.

The approach of fitting dispersion curves to extract the elastic parameters of materials has been reported for medical [9–11] and industrial [12] applications. However, the fitting process in these cases is performed in a trial-and-error scheme involving the different parameters, and the assessment of the fitting procedure is
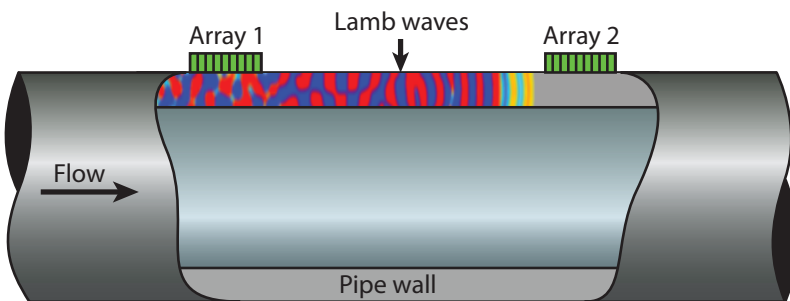
Figure 4.3: Axial cross-section of a clamp-on flow meter with transducer arrays. For measurement of the bulk wave sound speeds and wall thickness of a pipe, one or few elements of one array can be excited, and the propagating guided waves can then be recorded by the other array.

done more qualitatively (i.e. visual comparison of theoretical dispersion curves with experimental ones) rather than quantitatively. Other approaches [13, 14] are more quantitative with respect to extracting and fitting dispersion curves. However, initial guesses of the parameters are needed as inputs for convergence of the optimization algorithms. Furthermore, the approaches have not been tested with ground truth data form simulations, and thus their accuracy has not been verified. Here, dispersion curves from the measured data are directly compared to pre-computed theoretical dispersion curves for a whole score of bulk wave sound speed and thickness values. Initial guesses of parameters may be used to narrow-down the database search, but they are ultimately unnecessary. Since there is no optimization procedure involved, there are no convergence issues.

In principle, this fitting approach could be implemented for dispersion curves of any order. However, for simplicity, the assumption that fitting the A_0 and S_0 wave modes (zero-order anti-symmetric and zero-order symmetric wave modes, respectively) is sufficient to uniquely determine c_L, c_T and h has been taken. Below, a description of the curve extraction and fitting procedure is given, followed by its application to numerical and experimental data.

4.3.2. Curve fitting procedure

To quantitatively compare theoretical dispersion curves to experimental ones, it is first of all necessary to extract the curves from the measured data. In practical terms, converting $t - x$ signals into $f - k_x$ data yields a matrix that associates an amplitude and a phase to each $f - k_x$ coordinate, whereas what is needed is the set of $f - k_x$ coordinates corresponding to a wave mode, i.e. its $f - k_x$ data points. These were identified via the amplitude maxima in the 2D Fourier domain, and their assignment to either wave mode, A_0 or S_0, was performed on the basis of order of appearance along the k_x direction (at every frequency, the horizontal wavenumber k_x belonging to A_0 has a lower value than the one belonging to S_0).

Next, it is necessary to calculate the theoretical dispersion curves corresponding to different sets of the three parameters c_L, c_T and h, i.e. make a look-up table. Each theoretical curve is then compared to the experimental one, and a measure of error (i.e. the mismatch between the two curves) is defined and computed. Finally, the theoretical curve with the smallest error is identified, thus finding which set of parameters describes the recorded dispersion the best.

An alternative way of approaching this problem would be to implement an optimization procedure to identify the theoretical curve corresponding to the smallest error. The disadvantage of such procedures, however, is that they require the computation of a potentially high number of theoretical curves every time that c_L, c_T and h are sought. With the approach implemented here, the fitting procedure is reduced to comparing every new set of experimental curves to the already existing database. Compared to optimization algorithms, the approach described here reduces the computational cost considerably since the database can be computed off-line and once (i.e. before the measurements). A potential drawback of this approach is that the accuracy of the fit is limited by the resolution of the parameter space, which is set at the time of the generation of the database. Moreover,

similarly to optimization algorithms, there is a trade-off between target precision and computation time: the higher the precision, the larger is the database and the longer the computation time, both for database generation and for the fitting procedure.

The comparison between theoretical and experimental curves was performed by computing the magnitude of an error function that quantifies, at each frequency, the deviation of one curve from the other along the k_x direction. The chosen error function represents the root mean square percentile difference (RMS-PD) between a given theoretical curve and the experimental one

$$E = \frac{100}{N} \sum_{i=1}^{N} \sqrt{\left(\frac{k_i^{\text{theo}} - k_i^{\text{exp}}}{k_i^{\text{theo}}}\right)^2}. \qquad (4.1)$$

In Eq. 5.1, E is the RMS-PD error, N is the number of frequencies that are considered, k_i^{exp} is the horizontal wavenumber of the ith frequency for the experimental curve, and k_i^{theo} is the horizontal wavenumber of the same frequency for the theoretical curve.

This error function has several advantages: first of all, normalizing the difference at each frequency by the corresponding horizontal wavenumber (either the theoretical or the experimental one) helps to assign the same weight to all points; without this correction, relatively small deviations at higher frequencies impact the error much more than comparable deviations at lower frequencies (a 10% variation from $k_i = 1000\,\text{rad/m}$ is much larger than a 10% from $k_i = 100\,\text{rad/m}$). Moreover, normalizing the error by the number of points used to compute it allows to compare curves where different values of N are used. Finally, a percentile scale is intuitively easy to interpret, even for very small errors.

One last thing that should be noted is that the dispersion curves of the A_0 and S_0 wave modes are not equally sensitive to all three parameters c_L, c_T and h at all frequencies. From theoretical dispersion curves of Lamb waves for a typical set of metallic pipe properties, it was found that the phase velocity of the A_0 wave mode, for instance, is sensitive to h mainly at low frequencies (i.e. $f \leq 1\,\text{MHz}$), whereas at higher frequencies it is more sensitive to c_T. The S_0 wave mode, on the other hand, shows a stronger sensitivity to h in the range $1.5\,\text{MHz} \leq f \leq 3\,\text{MHz}$, and is especially sensitive to c_L for $f \leq 1\,\text{MHz}$. This means that any fitting procedure could yield more or less accurate for a given property, depending on which wave mode is fitted at which frequency range.

4.3.3. Numerical validation

The procedure described above was first tested on simulated data. A vacuum-loaded stainless steel plate ($c_L = 5800\,\text{m/s}$ and $c_T = 3100\,\text{m/s}$) with a thickness of $h = 1\,\text{mm}$ was simulated using the Finite Element Modelling (FEM) software package PZFlex (Onscale, Redwood City, CA, USA). On one of the surfaces, a small transducer element (HK1HD, TRS Technologies Inc., State College, PA, USA) with a thickness of $0.5\,\text{mm}$ and width of $0.3\,\text{mm}$, was placed and excited with a 1-cycle sine wave with a center frequency of $2.25\,\text{MHz}$. Receivers were placed with a pitch

of $0.02\,\text{mm}$ along a distance of $90\,\text{mm}$ next to the excited transducer and on the same side of the plate to record the propagating Lamb waves.

The recorded $t - x$ signals were then transformed into $f - k_x$ data by means of a 2D FFT, and the A_0 and S_0 wave modes were then extracted following the procedure explained above (see Fig. 4.4). The A_0 wave mode was identified within the frequency range $1.5\,\text{MHz} \le f \le 2.1\,\text{MHz}$, and the S_0 wave mode was observed within the frequency range $1.5\,\text{MHz} \le f \le 2.8\,\text{MHz}$.

Considering the elastic properties of common metals, theoretical dispersion curves were computed for a wide range of fitting parameters: $4500\,\text{m/s} \le c_L \le 7500\,\text{m/s}$, $2000\,\text{m/s} \le c_T \le 4000\,\text{m/s}$ and $0.1\,\text{mm} \le h \le 4\,\text{mm}$, with a sound speed resolution of $50\,\text{m/s}$ and a thickness resolution of $0.1\,\text{mm}$, forming a database of $\approx 10^5$ theoretical curves with a total size of $50\,\text{MB}$. The fitting procedure using this database took $\approx 70\,s$ on a 64-bit Dell laptop (RAM $= 8\,\text{GB}$, Processor: Intel(R) Core(TM) i7-6600U).

Figure 4.5 shows several 2D error maps, computed via Eq. 5.1 from the extracted curves and those in the database. These maps show the distribution of the error as a function of the two bulk wave speeds. Each map corresponds to a fixed thickness value h. Fig. 4.5a and Fig. 4.5b show the error maps for the A_0 and S_0 wave mode, respectively. Fig. 4.6 shows, for the two wave modes, a plot of the minimum RMS-PD error as a function of the thickness h. It can be observed that the final parameters obtained via the fitting algorithm were $c_L = 5850\,\text{m/s}$, $c_T = 3100\,\text{m/s}$ and $h = 1\,\text{mm}$. Compared to the simulation parameters ($c_L = 5800\,\text{m/s}$, $c_T = 3100\,\text{m/s}$ and $h = 1\,\text{mm}$), this implies only a discrepancy of $0.86\,\%$ between the values of c_L. Considering that this discrepancy of $50\,\text{m/s}$ is also the speed resolution of the database, it is possible that a database with higher resolution would yield even more accurate results.
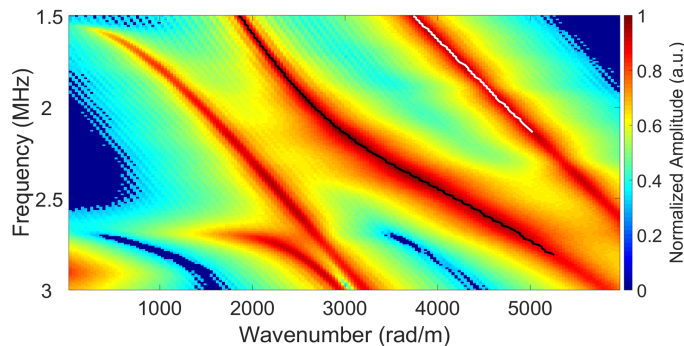
Figure 4.4: Magnitude of a 2D FFT applied on simulated space-time signals of Lamb waves recorded on the surface of a $1\,\text{mm}$-thick stainless steel plate. The black and white lines show the extracted data points of the S_0 and A_0 wave modes, respectively.
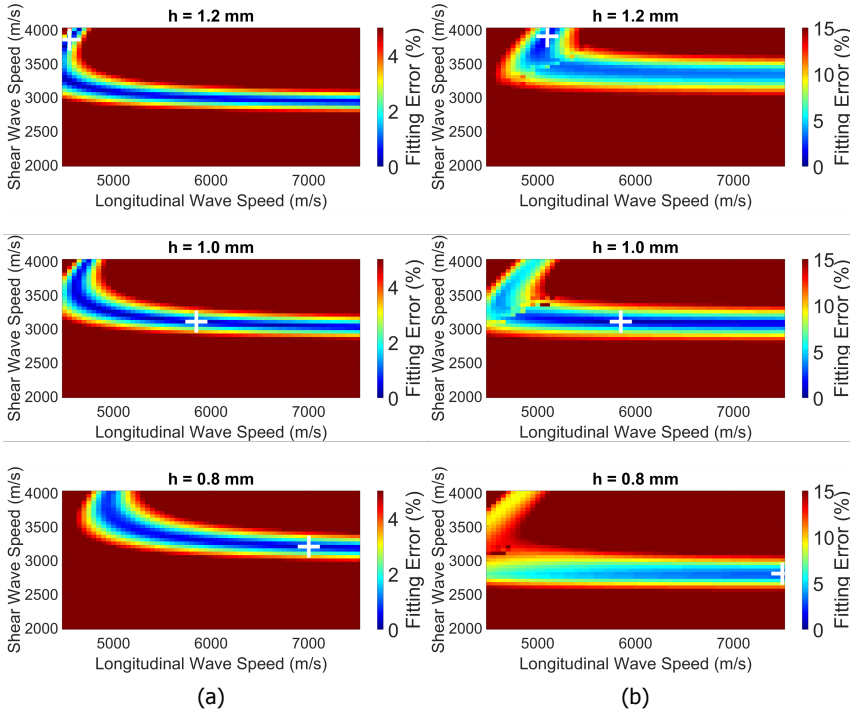
Figure 4.5: Error maps obtained by comparing, respectively, the (a) A_0 and (b) S_0 wave mode dispersion curves extracted from simulated data to the theoretical database, for thickness values of $h = 0.8\,\text{mm}$, $h = 1.0\,\text{mm}$ and $h = 1.2\,\text{mm}$. The white cross in each error map indicates the location of minimum error.
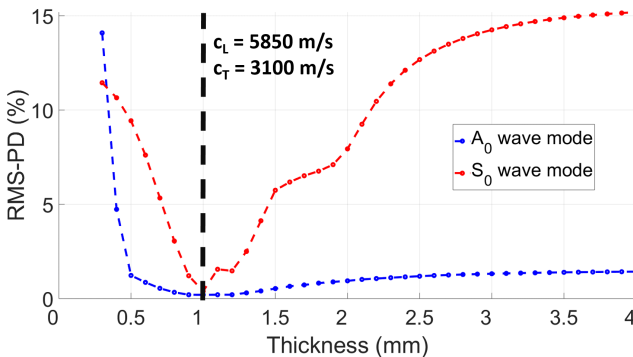
Figure 4.6: Minimum RMS-PD error of the simulated error maps of Fig. 4.5, as a function of thickness h, for the A_0 mode (blue) and the S_0 mode (red). The values of longitudinal and shear wave speeds are shown for the thickness $h = 1\,\text{mm}$, which is the one that reports the minimum error.

4.3.4. Measurements

The fitting procedure was applied to measurements obtained from a $40\,\text{mm}$-inner diameter 304-stainless steel pipe (nominal values [15]: $c_L = 5920\,\text{m/s}$ and $c_T = 3141\,\text{m/s}$) with a wall thickness of $h = 1\,\text{mm}$. The sound speeds of Lamb waves in typical industrial pipe walls are much faster than the sound speed of typical liquids. Therefore, these are very likely to be easily windowed-out in time, and for this reason the air-filled pipe setup of Fig. 4.7a is still representative of a real practical scenario.

As shown in Fig. 4.7a, two ATL P4-1 probes (Philips, Bothell, WA, USA) were placed within a center-to-center distance of $10\,\text{cm}$, and driven with a Verasonics Vantage 256 system (Verasonics Inc., Kirkland, WA, USA). A 1-cycle pulse with a center frequency of $2.25\,\text{MHz}$ was used to excite one element of one probe, and all 96 elements of the other probe were used to record the propagating Lamb waves. A 2D FFT was applied on the measured time signals, and from its magnitude (Fig. 4.7b) the A_0 wave mode was observed within a frequency range of $1.6\,\text{MHz} \leq f \leq 2.8\,\text{MHz}$, whereas the S_0 wave mode was identified within $1.8\,\text{MHz} \leq f \leq 3.2\,\text{MHz}$.

Comparing Fig. 4.4 and Fig. 4.7b, the effect of noise in the mapping of the dispersion curves obtained from experiments was noticed, as well as a difference in spatial resolution of the dispersion curves due to a more limited spatial sampling aperture during experiments. Regardless, the error maps of Fig. 4.8 and Fig. 4.9 show that the thickness of the pipe wall is correctly identified when fitting either wave mode. The S_0 wave mode, as already mentioned above and observed from simulations, appears to be more sensitive to thickness variations. Conversely, the values of c_L and c_T extracted by fitting the A_0 wave mode are closer to the nominal properties of the pipe than those found by fitting the S_0 wave mode. The properties reported in Fig. 4.9 by fitting the A_0 wave mode suggest a discrepancy with nominal values of c_L and c_T of $7.09\,\%$ and $1.27\,\%$, respectively.

The fitting procedure was also applied to measurements obtained from a $62\,\text{mm}$-

(a)   (b)
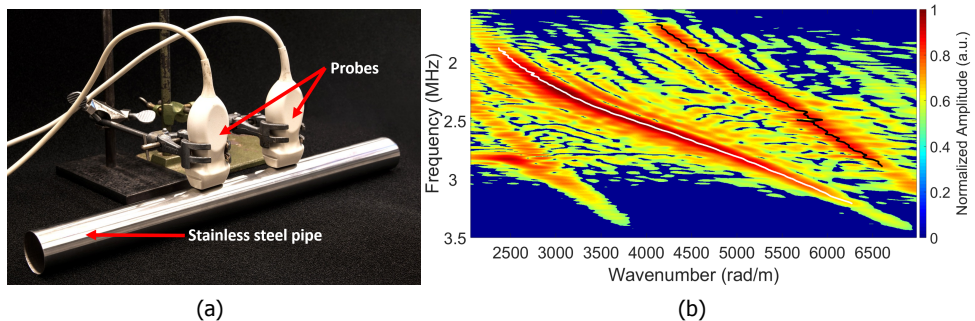
Figure 4.7: (a) Experimental setup used to excite and measure Lamb waves with transducer arrays on a $h = 1\,\text{mm}$-thick 304-stainless steel pipe (nominal values: $c_L = 5920\,\text{m/s}$ and $c_T = 3141\,\text{m/s}$). (b) Magnitude of 2D FFT applied on the measured time signals. The black and white lines show the extracted data points of the A_0 and S_0 wave modes, respectively.
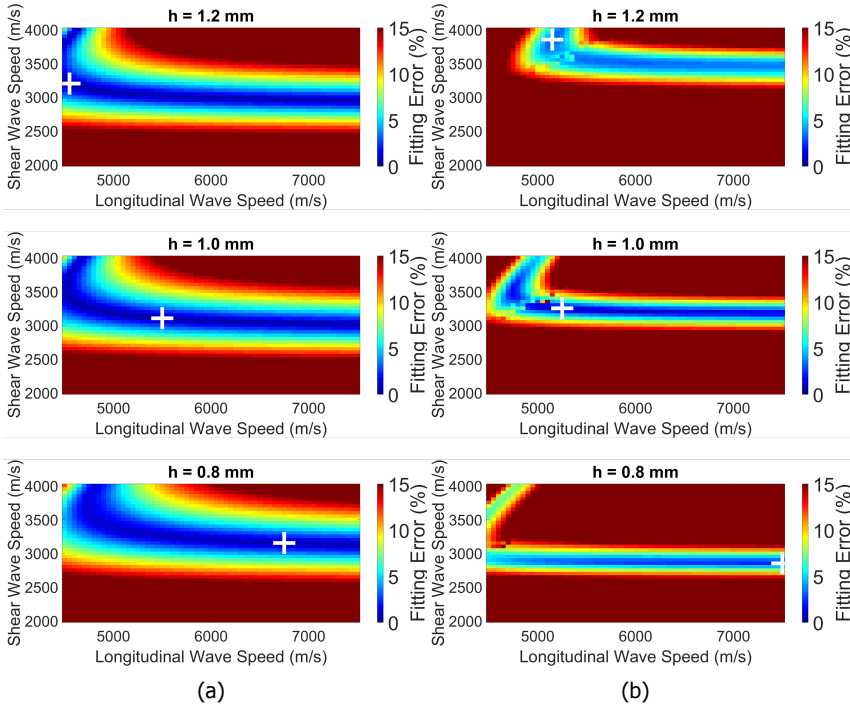
Figure 4.8: Error maps obtained by comparing, respectively, the (a) A_0 and (b) S_0 wave mode dispersion curves extracted from measured data to the theoretical database, for thickness values of $h = 0.8\,\mathrm{mm}$, $h = 1.0\,\mathrm{mm}$ and $h = 1.2\,\mathrm{mm}$. The white cross in each error map indicates the location of minimum error.
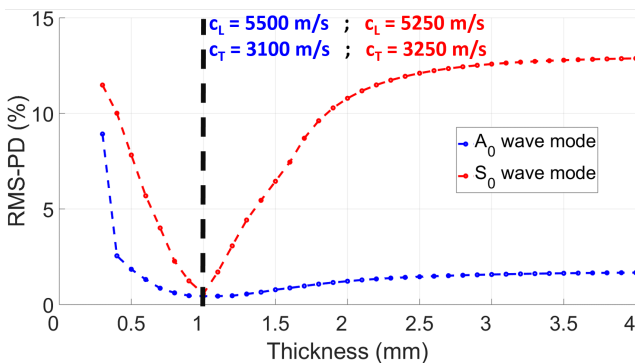
Figure 4.9: Minimum RMS-PD error of measured error maps of Fig. 4.8, as a function of thickness h, for the A_0 mode (blue) and the S_0 mode (red). The values of longitudinal and shear wave speeds are shown for the thickness $h = 1\,\mathrm{mm}$, which is the one that reports the minimum error.
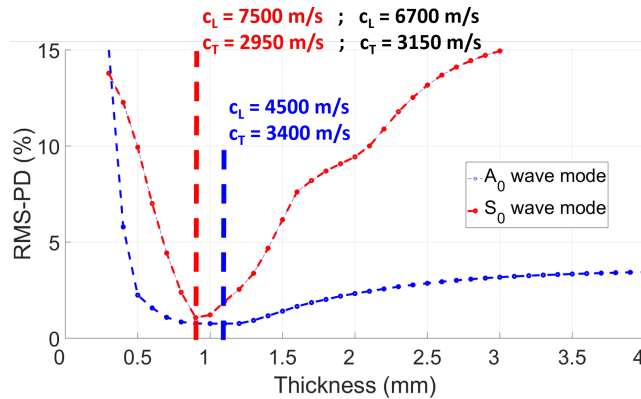
Figure 4.10: Minimum RMS-PD error of measured error maps for an aluminum pipe as a function of thickness h for the A_0 mode (blue) and the mode S_0 (red). The values of longitudinal and shear wave speeds are expressed for thicknesses with lowest error ($h = 0.9$mm for the S_0 wave mode, $h = 1.1$mm for the A_0 wave mode). The wave speeds obtained by fitting the A_0 mode with a plate of thickness $h = 0.9$mm are reported in black.

inner diameter ENAW6063.T66-aluminium pipe (Nedal Aluminium BV, Utrecht, NL; nominal values: $c_L = 6306$ m/s, $c_T = 3114$ m/s), with a wall thickness of $h = 1$ mm. With these measurements it is also shown that the extracted parameters from one dispersion curve may be used as input in the fitting procedure of another curve to obtain more accurate results. For this pipe, $f - k_x$ data points of the A_0 and S_0 wave modes were extracted within the frequency range 1 MHz $\leq f \leq 2.4$ MHz. The properties extracted by fitting each wave mode individually varied considerably from the nominal values. From the A_0 wave mode, values of $c_L = 4600$ m/s, $c_T = 3400$ m/s, $h = 1.1$ mm were obtained, and for the S_0 wave mode, values of $c_L = 7500$ m/s, $c_T = 2950$ m/s, $h = 0.9$ mm were obtained. Because at high frequencies the S_0 wave mode is more sensitive to h than the A_0 wave mode, the value of h obtained by fitting the S_0 wave mode was used as input in the fitting procedure of the A_0 wave mode to obtain a more accurate estimate of the bulk wave sound speeds of the pipe. By implementing this approach, values of $c_L = 6700$ m/s and $c_T = 3150$ m/s were finally obtained (see Fig. 4.10), which represent a discrepancy from nominal values of 8.96 % and 1.49 % respectively, with a thickness estimated at 0.9 mm (a deviation of 10 % from the nominal value).

4.4. Diameter of the pipe

The average diameter of the pipe is determined by measuring the transit time of a particular Lamb wave traveling around the circumference of the pipe. The wave mode is dispersive, therefore, its frequency components will have different transit times $t(\omega)$. Furthermore, since the dispersive group velocity $c_g(\omega)$ of the excited wave mode is known by now, the pipe outer diameter (*OD*) can be computed as

$$OD(\omega) = \frac{c_g(\omega)t(\omega)}{\pi} + h. \tag{4.2}$$

The group velocity $c_g(\omega)$ is associated with the propagation velocity of a group of waves of similar frequency [7]. Within this group, each individual wave propagates with its phase velocity $c_p(\omega) = \omega/k$. Group and phase velocity are related by

$$c_g(\omega) = \frac{d\omega}{dk} = \frac{d(kc_p(\omega))}{dk} = c_p(\omega) + k\frac{dc_p(\omega)}{dk}. \tag{4.3}$$

In practice, however, it becomes challenging (or rather subjective) to identify the transit time of the measured dispersive signal and the corresponding frequency component. A more accurate estimate of the transit time can be made by performing dispersion correction, i.e. correct for the frequency-dependent wave speed.

4.4.1. Lamb wave dispersion correction

Dispersion correction has been applied in non-destructive testing applications at macroscopic [16] and nanoscopic [17] scale. Such correction effectively flattens-out the phase velocity dispersion curve of the measured wave mode ($c_p(\omega) = $ constant). After correction, group and phase velocity are the same (i.e. $c_g(\omega) = c_p(\omega)$ in Eq. 4.3), therefore providing a more accurate estimation of the pipe diameter. Furthermore, since the phase of all frequency components is the same after dispersion correction, a maximum amplitude of the time signal will be achieved at the arrival of the wave, providing the highest possible SNR to estimate the transit time.

Considering a dispersive signal $g(t)$, a frequency component f_0 (associated with phase velocity $c_p(f_0)$) arrives at a time $t(f_0)$. The phase difference between this frequency component and another one is

$$\Delta\Phi = \omega\Delta t = 2\pi[ft(f) - f_0 t(f_0)]. \tag{4.4}$$

Given that all frequency components travel the same path length p, it follows that

$$p = t(f_0)c_p(f_0) = t(f)c_p(f). \tag{4.5}$$

$c_p(f)$ represents the phase velocity of the measured wave mode. Solving for $t(f)$ in Eq. 4.5, and substituting the result in Eq. 4.4 results in

$$\Delta\Phi = \omega\Delta t = 2\pi t(f_0)\left[\frac{c_p(f_0)}{c_p(f)} - \frac{f_0}{f}\right]. \tag{4.6}$$

Given the Fourier Transform of the measured signal $g(f)$, the corrected signal can be computed as

$$g_{\mathrm{corr}}(t) = \mathfrak{F}^{-1}\left\{g(f)\exp\left[2\pi ft(f_0)\left(\frac{c_p(f_0)}{c_p(f)} - \frac{f_0}{f}\right)\right]\right\}, \tag{4.7}$$

where $\mathfrak{F}^{-1}$ represents the inverse Fourier transformation. In Eq. 4.7 it is observed that only the phase of the signal is being manipulated.

Given a phase velocity $c_p(f_0)$ towards which the dispersion curve is being flattened-out, Eq. 4.7 is repeated for a given range of transit times $t(f_0)$. For each trial $t(f_0)$, the envelope of the compressed signal is computed and its peak value monitored. The final dispersion-corrected signal would be the one with the highest peak amplitude of its envelope, and the transit time associated to that peak, together with $c_p(f_0)$, would be the parameters to use in Eq. 4.2 to finally compute pipe diameter.

4.4.2. Simulations

Finite Element simulations of Lamb wave propagation were performed with PZFlex to obtain data that allows to validate the dispersion correction algorithm explained above, as well as Eq. 4.2.

The same transducer element as considered in the previous section was simulated on top of an aluminum pipe ($OD = 60\,\text{mm}$, $h = 1\,\text{mm}$), as seen in Fig. 4.11a. The element was excited with a 2-cycle sine wave with a center frequency of $2.25\,\text{MHz}$. According to the dispersion curves for the pipe, see Fig. 4.11b, the $L(0,1)$, $L(0,2)$ and $L(0,3)$ wave modes are expected to be excited. Lamb waves
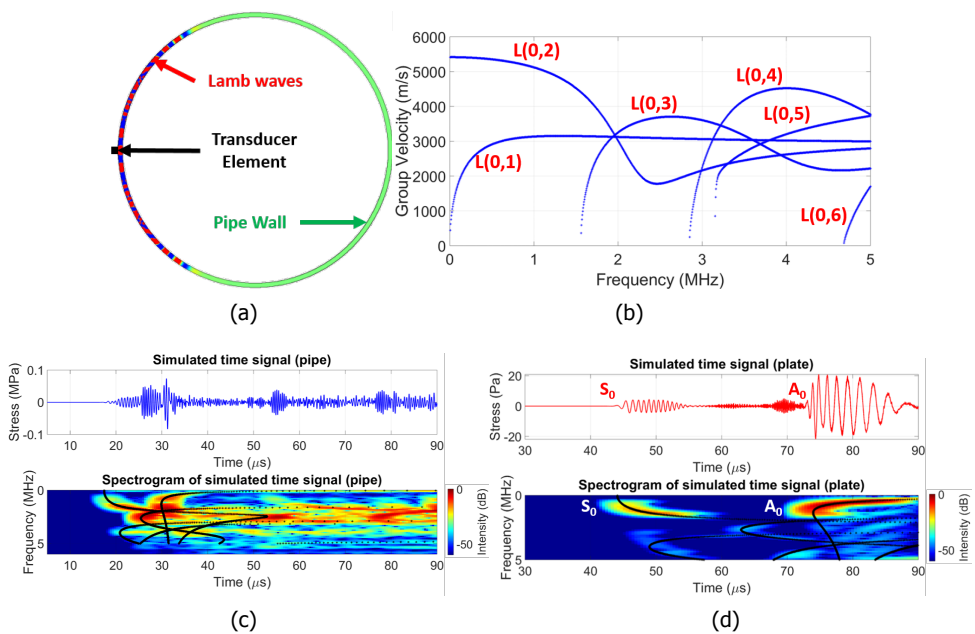
Figure 4.11: (a) Finite Element simulation of an aluminium pipe ($OD = 60\,\text{mm}$, $h = 1\,\text{mm}$). The transducer element was excited with a 2-cycle sine wave with a center frequency of $2.25\,\text{MHz}$, and receivers were placed around the outer surface of the pipe wall. Transducer element dimensions (0.5x0.3 mm) are exaggerated for visualization purposes. (b) Group velocity dispersion curves of Lamb waves for the pipe. Around $2.25\,\text{MHz}$, at least three different wave modes are expected to be excited. (c) Simulated stress signal on the opposite side of the pipe and its spectrogram. The black dotted lines are computed from the group velocities. (d) Simulated stress signal on a flat stainless steel plate, and its spectrogram. The black dotted lines are computed from the group velocities, and overlap with the theoretical curves.
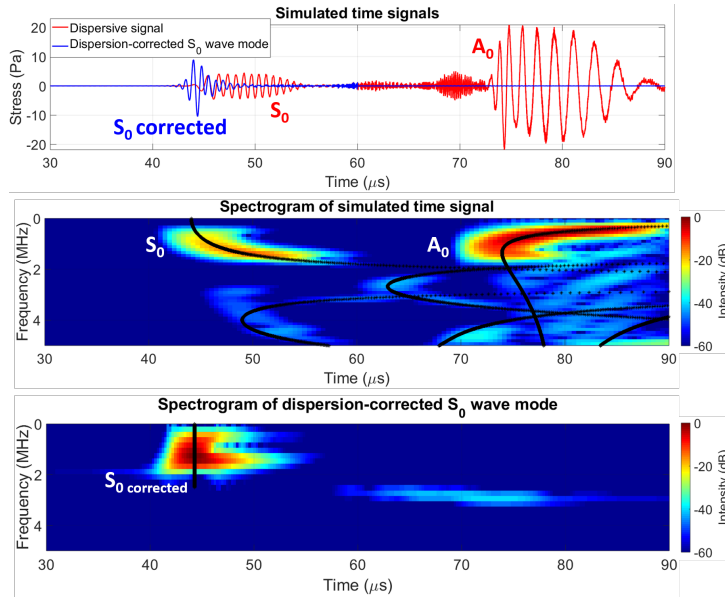
Figure 4.12: Dispersion correction of the S_0 wave mode computed in a Finite Element simulation involving a stainless steel plate with a thickness $h = 1\,\mathrm{mm}$. The black curves in the spectrograms follow from the theoretical group velocities.

were recorded by receivers placed around the outer surface of the pipe wall. From the recorded time signals, a spectrogram was computed considering a moving Hanning window with a time length of $9.5\,\mu\mathrm{s}$. The different wave modes could be identified in Fig. 4.11c.

To assess the accuracy of the proposed method, a simple flat plate geometry was considered as a valid approximation of a cylindrical pipe wall [8]. Lamb waves were computed $23\,\mathrm{cm}$ away from the source. In the process of validating Eq. 4.7, the S_0 wave mode in Fig. 4.11d was considered. After the implementation of the dispersion correction (Fig. 4.12), the computed travel path was $22.82\,\mathrm{cm}$, which represents a discrepancy of $0.8\,\%$ relative to the true value.

4.4.3. Measurements

The proposed procedure for measurement of the pipe diameter was tested on the aluminium pipe described previously. For this purpose, a single ATL P4-1 phase array probe was placed onto the pipe wall in the circumferential direction (Fig. 4.13). Even though most of the piezo-elements were not in mechanical contact with the pipe wall, the one in the middle of the probe was. This element was then excited with a short broadband pulse. The time signal recorded by this element, as well as its spectrogram, are shown in Fig. 4.14, in which several round trips of wave modes, such as the $L(0, 3)$, are observed. Based on the pipe parameters measured in the previous section, group velocity dispersion curves were computed and theoretical curves for the maxima in the spectrogram were derived and plotted in the
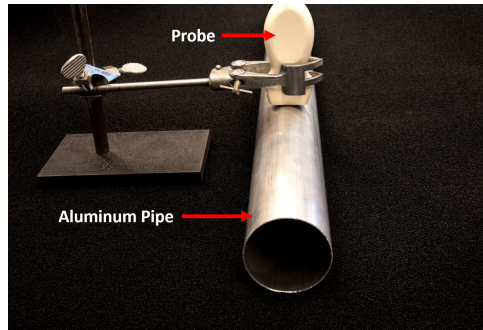
Figure 4.13: Experimental setup to test the proposed procedure for measurement of the pipe diameter, consisting of an aluminum pipe ($OD = 60\,\text{mm}$, $h = 1\,\text{mm}$), and a P4-1 phased array probe placed on top, perpendicular to the pipe axis. A foam layer was placed below the pipe to avoid mechanical coupling and vibrations of the table on which the setup was placed.

spectrogram. These curves show a very good agreement with the locations of the maxima in the measured spectrogram.

Furthermore, the spectrogram of Fig. 4.14 shows that the first wave mode to arrive after propagating a full circumference is the $L(0,2)$. Therefore, this wave mode was windowed-out from the measured time signal and corrected for dispersion. The reference frequency at which the phase velocity dispersion curve of this wave mode was flattened-out was $f_0 = 2\,\text{MHz}$. The proposed dispersion correction algorithm was applied with a sound speed of $c(f_0) = 4294\,\text{m/s}$, and the spectrograms of the measured $L(0,2)$ wave mode before and after dispersion correction are shown in Fig. 4.15.

After correction, a transit time of $45.4\,\mu s$ was obtained. When used in Eq. 4.2, this gives a pipe outer diameter of $OD = 63.05\,\text{mm}$, which implies $5.09\,\%$ discrep-
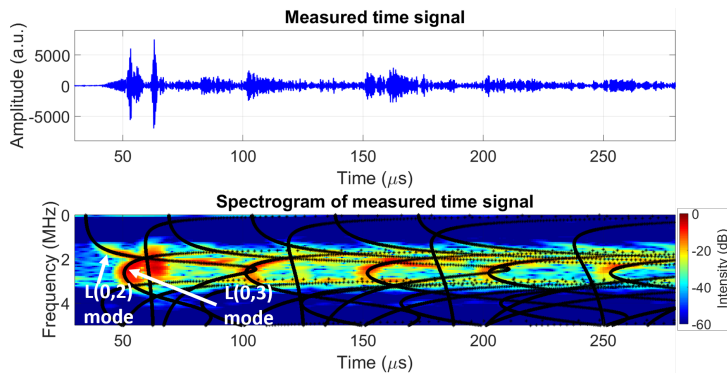
Figure 4.14: Time signal (above) recorded by one piezo-element of the probe in contact with the aluminum pipe, as shown in Fig. 4.13, and its spectrogram (below). The black curves in the spectrogram follow from the theoretical group velocity computed for the pipe parameters measured in the previous section.
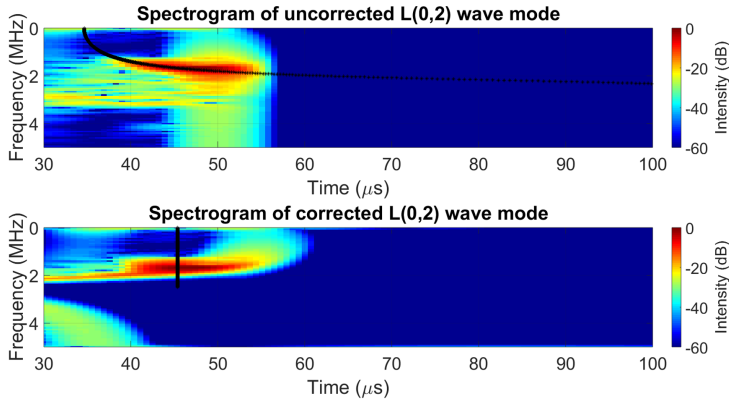
Figure 4.15: Spectrogram, before and after dispersion correction, of a measured $L(0,2)$ wave mode on the aluminium pipe shown in Fig. 4.13. The black curves in the spectrograms follow from the theoretical group velocities.

ancy with the real value. Similarly, measurements were performed for a stainless steel pipe ($OD = 42\,\text{mm}$, $h = 1\,\text{mm}$), and an outer diameter of $OD = 42.83\,\text{mm}$ was obtained, which means a discrepancy of $1.98\,\%$ with the real value.

Two sources of error were identified. First, it is assumed in Eq. 4.2 that the piezo-elements are in direct contact with the pipe wall. Since a commercial probe was used to perform the experiments, there is actually a lens between the piezo-elements and the pipe wall, which was not accounted for in Eq. 4.2. Thus, an effectively longer travel path, and therefore a larger pipe diameter, was obtained. Second, the array probe might have not been placed perfectly perpendicular to the pipe axis. If this was the case, the propagating Lamb wave modes could have travelled around the pipe wall with an angle different from $90°$ relative to the pipe axis, and the travel path of the wave modes might have been longer than the circumference of the pipe. Both errors can be minimized in the future with custom-made transducer arrays designs, such as the one proposed in [18], in which additional path lengths due to the acoustic stack are known and the Lamb waves may be steered to propagate perfectly perpendicular to the pipe axis.

4.5. Sound speed of the liquid

Once the mechanical properties (c_L and c_T) and geometry (h and OD) of the pipe have been characterized, the liquid inside the pipe can also be characterized by measuring its sound speed via pulse-echo measurements. Beam reflections from curved surfaces, such as pipe walls, can modify the waveform and the wave front [7]. To show this effect, a perpendicular cross-section of the measurement setup is considered. Fig. 4.16 shows the proposed geometry, where a lead coupling piece is placed in between a 16-element transducer array and a liquid-filled stainless steel pipe.

Excitation of all transducer elements produces an initial plane wave that refracts

4
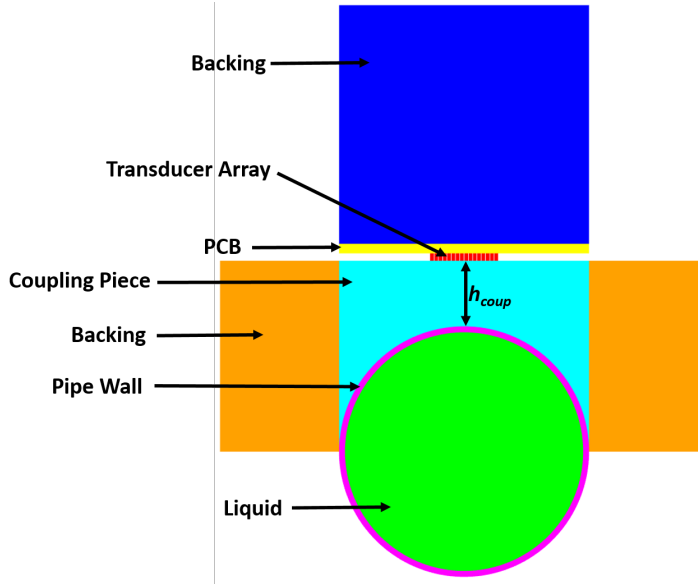
Figure 4.16: Geometry for measurement of the sound speed of the liquid. A 16-element transducer array is placed on top of a lead coupling piece ($c_L = 2200\,\text{m/s}$, $h_{coup} = 11\,\text{mm}$) on top of a stainless steel pipe ($OD = 42\,\text{mm}$, $h = 1\,\text{mm}$). The acoustic stack of the array is based on the design described in [18].

into the pipe. After reflecting from the pipe bottom, the acoustic beam refocuses during propagation in the liquid, refracts back to the coupling piece, and finally impinges the transducer array as a plane wave.

Certainly, the recorded time signals would show all possible echoes: those from other interfaces, open ends, and also the Lamb waves traveling around the pipe wall. All these echoes impinge on the array at different angles. Nevertheless, due to the geometry, the echo containing information about the liquid would be the only one impinging completely perpendicular on the array surface. Therefore, in the $f - k_x$ domain, it would show-up as an echo with nearly infinite phase velocity (i.e. $k_x \cong 0\,\text{rad/m}$), which could be filtered-out to obtain a cleaner and sharper echo, from which a transit time t_a could be finally determined. From this transit time, the sound speed of the liquid c_{liquid} is computed as

$$c_{\text{liquid}} = \frac{OD - 2h}{\frac{t_a}{2} - \frac{h}{c_L} - \frac{h_{\text{coup}}}{c_{L_{\text{coup}}}}}, \tag{4.8}$$

where $c_{L_{\text{coup}}}$ represents the longitudinal bulk wave sound speed of the coupling piece, and h_{coup} its center thickness.

Wave propagation in fluids is assumed to be non-dispersive, therefore, no correction needs to be done on the measured echo from the liquid to estimate the transit time t_a.

4.5.1. Simulations

A Finite Element simulation of the waves occurring in the geometry shown in Fig. 4.16 was performed using PZFlex. The set-up involves a water-filled stainless steel pipe ($OD = 42\,\text{mm}$, $h = 1\,\text{mm}$) and a lead coupling piece ($c_L = 2200\,\text{m/s}$, $h_{\text{coup}} = 11\,\text{mm}$). The transducer array elements were excited with a 1-cycle sine wave with a center frequency of $1\,\text{MHz}$, and the received voltage of each transducer element was recorded up to $80\,\mu\text{s}$. To suppress reflections from the open ends of the coupling piece, an attenuating material is placed around it. In simulations, a $20\,\text{mm}$-thick heavy backing (acoustic impedance $Z = 20\,\text{MRayl}$ and attenuation coefficient $\alpha = 20\,\text{dB/MHz.cm}$) was placed around the lead coupling piece. Furthermore, to achieve a real-case scenario, free boundary conditions were implemented at the edges of the simulation geometry. Time snapshots are shown in Fig. 4.17, where refraction into the pipe wall, as well as refocusing of the acoustic beam after echoing from the bottom of the pipe wall are observed.

The simulated receive voltages from the transducer elements are shown in Fig. 4.18a, from which it is possible to recognize the characteristic plane wave feature of the water echo, arriving at approximately $63\,\mu\text{s}$. Moreover, it is possible to observe that all the other recorded echoes have a curved shape, which means they arrived at the transducer array under varying angles. The average receive voltage is shown in the blue curve of Fig. 4.19, and shows a longer duration than the length of
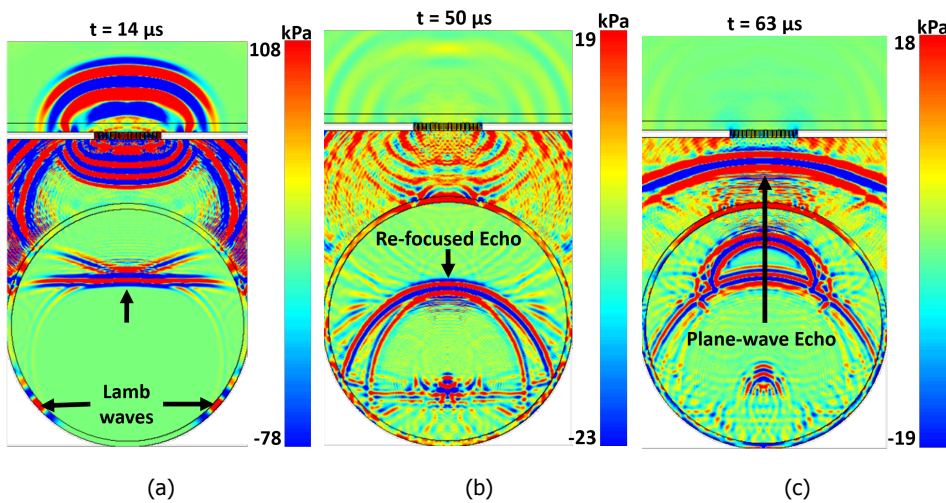
Figure 4.17: Snapshots of a Finite Element simulation of the waves occurring in the measurement of the sound speed of the liquid. The simulated set-up contains the array geometry shown in Fig. 4.16, including a heavy backing material around the coupling piece (not shown here). The pipe was filled with water. (a) At $14\,\mu\text{s}$, the acoustic wave is propagating downwards. (b) At $50\,\mu\text{s}$, the wave refocuses after reflecting from the bottom water - steel interface, and propagates upwards. (c) At $63\,\mu\text{s}$, the wave is about to arrive within the aperture of the array as a plane wave, as expected. The color scale of each snapshot has been clipped to enhance the events indicated with the black arrows.

the 1-cycle excitation pulse due to the reverberations of the signal in the pipe wall. This means that a cross-correlation operation between these two signals would not be suitable to estimate the transit time of the water echo because the peak value of the cross-correlation, would be located somewhere along the length of the pulse, and not at its actual start. Therefore, a zero-crossings tracking algorithm would be more suitable to detect the transit time of the echo from the liquid.

However, detecting the first zero-crossing associated to the start of the acoustic signal may be a bit subjective due to the bandwidth-limited nature of the system, as also suggested by the blue curve in Fig. 4.19. Moreover, other wave modes may overlap in time with the desired echo from the liquid. Furthermore, Eq. 4.8 is very sensitive to the transit time being used. Therefore, it would be very useful to apply some filtering to obtain a final signal with a sharper start of the echo and from which to determine the transit time more accurately.

To achieve this, the data between $60\,\mu s$ and $70\,\mu s$ in Fig 4.18a was taken, tapered in both time and space domain using a Hamming window, and a 2D FFT was applied. The result is shown in Fig. 4.18b, in which the main lobe centered around $k = 0\,\text{rad/m}$ and $f = 1\,\text{MHz}$ corresponds to the plane wave water echo. Within a practical dynamic range of $30\,\text{dB}$, no significant side lobes were present, implying that the implemented tapering is sufficient. By filtering out all the information outside the white rectangles in Fig. 4.18b and applying an Inverse Fast Fourier Transform (IFFT), filtered time domain signals were obtained. These were

(a)   (b)
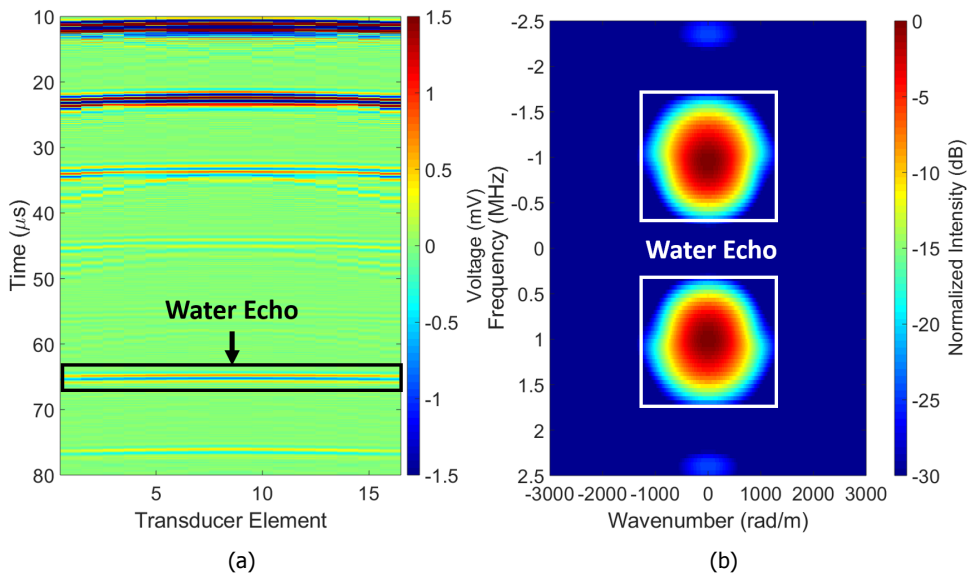
Figure 4.18: (a) Simulated receive voltages from the 16-element transducer array shown in Fig. 4.16. The black rectangle encloses the plane wave water echo. (b) Magnitude of a 2D FFT applied to the tapered data in the time window highlighted in (a). The white rectangles show the band-pass filter applied on the data to dismiss remnant information and achieve a sharper water echo.
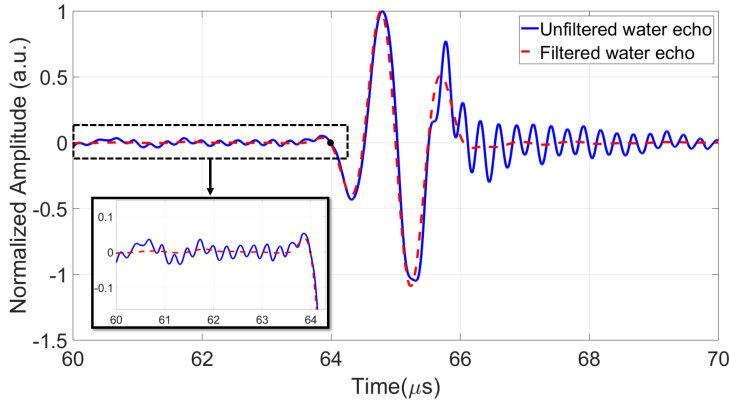
Figure 4.19: Simulated average and normalized water echo voltages, before and after filtering of the echoes impinging under an angle onto the transducer array surface. After filtering, a smoother echo is observed. The black dot located at $63.99\,\mu s$ represents the zero-crossing point that marks the transit time of the filtered water echo signal.

ultimately averaged to achieve an echo with a sharper start (see red curved in Fig. 4.19), from which the transit time can be determined more accurately than the unfiltered version.

An objective method to identify the transit time of the filtered (but still bandwidth-limited) echo may be to scan the time signal from smaller to higher transit times, detect the first amplitude point higher than the noise level, and identify its nearest zero-crossing. The transit time associated to this zero-crossing point may finally be regarded as the transit time of the echo. From the filtered water echo shown in Fig. 4.19, a transit time of $63.99\,\mu s$ was obtained, which according to Eq. 4.8 resulted in a sound speed of the liquid of $c_{\text{liquid}} = 1491.3\,\text{m/s}$. This value has a discrepancy of $0.31\,\%$ with the simulated sound speed value of $1496\,\text{m/s}$ for water.

For measurement of the sound speed of the liquid, it is very important to align the transducer array perfectly perpendicular to the pipe axis. Otherwise, the liquid-related echo might also be recorded under an angle relative to the array surface, and it will be more difficult to differentiate it from all the other echoes. On the other hand, since the matrix array proposed in [18] was still not available at the moment, and given the unknown nature of the acoustic stack of commercial probes, it was not yet possible to test this method experimentally.

4.6. Discussion

The results obtained from simulated data show that the proposed fitting approach is capable of retrieving simultaneously the bulk wave sound speeds (c_L, c_T) and thickness (h) of the pipe wall from a single measurement, without the need for initial guess values. The time required to compare the simulated data to a database of $\approx 10^5$ curves was approximately $70\,\text{s}$, showing great promise for in-situ implementation. Furthermore, the accuracy of this method appeared to be determined by

the resolution of the database, implying that the computational cost can be tailored to the accuracy requirements of specific applications. Preliminary results on a steel and an aluminum pipe confirmed experimentally the validity of the approach proposed here. By comparing the retrieved material properties with the nominal values of the samples, it was found that the accuracy of the obtained values was lower in experiments than in simulations, especially for the longitudinal bulk wave sound speed. This discrepancy could be imputed, in part, to experimental limitations (e.g. spatial and temporal resolution) that affect measured data. However, as would appear from Fig. 4.8, the A_0 and S_0 wave modes are less sensitive to variations of c_L than to variations in c_T and h, potentially impacting the efficacy of the fitting procedure. Moreover, it turned out that the accuracy of the curve-fitting approach increases proportionally to the amount of data points from the wave modes (i.e. $f - k_x$ points) that are available. This means that, to optimize accuracy in practice, it is best to excite the pipe wall with the most broadband signal (i.e. time pulse) possible.

On the other hand, the dispersion effect of Lamb wave modes plays a detrimental role in estimating the outer diameter of the pipe (*OD*), especially if the wave mode is highly dispersive within the operational frequency range of the transducers. For this reason, two approaches are recommended to estimate *OD*: to excite, within the bandwidth of the transducers, a wave mode with a relatively low dispersive behavior or, if this is not possible, to excite the pipe wall with a relatively narrow-band pulse and thereby limit the excitation of many of the highly dispersive frequency components.

Another method that might improve the estimation of the pipe diameter would be to cross-correlate consecutive round-trip arrivals of the same wave mode, like those of the $L(0,3)$ wave mode shown in Fig. 4.14. Certainly, each arrival of the wave mode needs to be corrected for dispersion before cross-correlating them.

The matrix arrays can also be used to monitor the quality of their alignment relative to the pipe axis. During sensor alignment, pulse-echo measurements, like those shown in Fig. 4.18a, can be performed and monitored in real-time. Misalignment of the matrix array(s) would reflect an asymmetric pattern of the $f - k_x$ plots because the echo from the liquid would impinge on the transducer array under an angle relative to the normal of the aperture.

4.7. Conclusion

Here, procedures for the measurement of parameters that will enable auto-calibration of ultrasonic clamp-on flow meters based on a pair of matrix transducer arrays have been presented. With such arrays, pipe properties like wall thickness, bulk wave sound speeds, diameter, and the sound speed of the liquid can be extracted from simulated and measured data. In this way, calibration of ultrasonic clamp-on flow meters by manual displacement of the sensors could be rendered unnecessary.

References

[1] J. Massaad, P. L. M. J. van Neer, D. M. van Willigen, A. Sabbadini, N. de Jong, M. A. P. Pertijs, and M. D. Verweij, *Measurement of pipe and fluid properties with a matrix array-based ultrasonic clamp-on flow meter,* IEEE Trans. Ultrason. Ferroelectr. Freq. Control (submitted).

[2] J. Massaad, P. L. M. J. van Neer, D. M. van Willigen, M. A. P. Pertijs, N. de Jong, and M. D. Verweij, *Towards a calibration-free ultrasonic clamp-on flow meter: Pipe geometry measurements using matrix arrays,* Proc. Meet. Acoust. **39**, 1 (2019).

[3] R. C. Baker, *Flow measurement handbook: industrial designs, operating principles, performance, and applications* (Cambridge University Press, 2005).

[4] D. V. Mahadeva, R. C. Baker, and J. Woodhouse, *Further studies of the accuracy of clamp-on transit-time ultrasonic flowmeters for liquids,* IEEE Trans. Instrum. Meas. **58**, 1602 (2009).

[5] D. C. Gazis, *Three-dimensional investigation of the propagation of waves in hollow circular cylinders. I. Analytical foundation,* J. Acoust. Soc. Am. **31**, 568 (1959).

[6] D. C. Gazis, *Three-dimensional investigation of the propagation of waves in hollow circular cylinders. II. Numerical results,* J. Acoust. Soc. Am. **31**, 573 (1959).

[7] J. L. Rose, *Ultrasonic guided waves in solid media* (Cambridge University Press, 2014).

[8] A. Velichko and P. D. Wilcox, *Excitation and scattering of guided waves: Relationships between solutions for plates and pipes,* J. Acoust. Soc. Am. **125**, 3623 (2009).

[9] K. Heller, L. Jacobs, and J. Qu, *Characterization of adhesive bond properties using Lamb waves,* NDT E. Int. **33**, 555 (2000).

[10] K. Lee and S. W. Yoon, *Feasibility of bone assessment with leaky Lamb waves in bone phantoms and a bovine tibia,* J. Acoust. Soc. Am. **115**, 3210 (2004).

[11] K.-C. T. Nguyen, L. H. Le, T. N. H. T. Tran, M. D. Sacchi, and E. H. M. Lou, *Excitation of ultrasonic Lamb waves using a phased array system with two array probes: Phantom and in vitro bone studies,* Ultrasonics **54**, 1178 (2014).

[12] Y.-C. Lee and S.-W. Cheng, *Measuring Lamb wave dispersion curves of a bi-layered plate and its application on material characterization of coating,* IEEE Trans. Ultrason. Ferroelectr. Freq. Control **48**, 830 (2001).

[13] M. Bernal, I. Nenadic, M. W. Urban, and J. F. Greenleaf, *Material property estimation for tubes and arteries using ultrasound radiation force and analysis of propagating modes,* J. Acoust. Soc. Am. **129**, 1344 (2011).

[14] J. Foiret, J.-G. Minonzio, C. Chappard, M. Talmant, and P. Laugier, *Combined estimation of thickness and velocities using ultrasound guided waves: A pioneering study on in vitro cortical bone samples,* IEEE Trans. Ultrason. Ferroelectr. Freq. Control **61**, 1478 (2014).

[15] P. O. Moore, G. L. Workman, and D. Kishoni, *Nondestructive Testing Handbook, vol. 7: Ultrasonic Testing* (1991).

[16] R. Sicard, J. Goyette, and D. Zellouf, *A numerical dispersion compensation technique for time recompression of Lamb wave signals,* Ultrasonics **40**, 727 (2002).

[17] P. L. M. J. van Neer, B. Quesson, M. H. van Es, M. C. J. M. van Riel, K. Hatakeyama, A. Mohtashami, D. Piras, T. Duivenoorde, M. Lans, and H. Sadeghian, *Optimization of acoustic coupling for bottom actuated scattering based subsurface scanning probe microscopy,* Rev. Sci. Instrum. **90**, 073705 (2019).

[18] J. Massaad, D. van Willigen, P. van Neer, N. de Jong, M. Pertijs, and M. Verweij, *Acoustic design of a transducer array for ultrasonic clamp-on flow metering,* IEEE Int. Ultrason. Symp. , 1133 (2019).

5

An algorithm to minimize the zero-flow error in transit-time ultrasonic flow meters

Transit-time ultrasonic flow meters are widely used in industry to measure fluid flow. In practice ultrasonic flow meters either show a zero-flow error or suffer from a significant random error due to a limited signal-to-noise ratio, requiring a significant amount of averaging to achieve good precision. This work presents a method that minimizes the zero-flow error whilst keeping the random error low, independent of the hardware used. The proposed algorithm can adjust to changing zero-flow errors while a flow is present. The technique combines the benefits of two common methods of determining the transit-time difference between the upstream and downstream ultrasonic waves: cross-correlation and zero-crossing detection. The algorithm is verified experimentally using a flow-loop. It is shown that the zero-flow error can be greatly reduced without compromising the random error or increasing circuit complexity.

5.1. Introduction

Transit-time ultrasonic flow meters are used to measure fluid flow in a large range of industrial applications where the temperature and type of liquid often vary considerably. The transit time difference (TTD) between the upstream and downstream signals is a measure of the flow velocity. The fundamental idea behind ultrasonic flow meters is that the only non-reciprocal effect in the system is the flow itself [2–4]. However, in practical flow meters, an offset in zero-flow conditions is often found, causing a flow velocity to be measured, even in the absence of flow. This offset error is often referred to as the zero-flow error. The offset error can originate from a slight non-reciprocity in the circuit, caused by an impedance mismatch between the transmit and receive circuit. Other sources of offset error are temperature changes [5] (and the associated changes in material properties of the components), temperature differentials across the flow meter and variations in material properties or the liquid over the flow meter geometry. Due to process changes (e.g. variations in temperature or the liquid properties) the offset error can change in operation. Hence, it is important to minimize the magnitude of the error.

Minimizing the offset error is commonly done by matching the impedance of the receive circuit to the impedance of the transmit circuit, in order to maximize the reciprocity of the measurement system [4, 6, 7]. This method is good at reducing the offset error, but a residual offset usually remains.

Industrial flow meters are usually specified for a range of flow velocities, where the accuracy of the lowest flow speed determines the minimum time-difference that has to be detected. For example, in a flow meter that spans a range from $0.1\,\text{m/s}$ to $100\,\text{m/s}$ with a $5\,\%$ accuracy, an error below $5\,\%$ of $0.1\,\text{m/s}$ is required, corresponding to a time difference of $0.18\,\text{ns}$ in water for a $40\,\text{mm}$ inner diameter pipe (with the transducer at a $45°$ angle). For a transmit signal with a center frequency of $2\,\text{MHz}$ this results in a very small phase difference of $360\,\text{ppm}$ of the wavelength. Detecting phase differences that are that small imposes stringent requirements on the electronics and algorithm that are used to calculate the flow. Small errors in the measurements can therefore quickly have a significant influence on the calculated flow velocity.

Two methods that are often used to calculate the phase difference or transit-time difference are zero-crossing detection and cross-correlation. As mentioned in [6], zero-crossing based detection often results in a lower offset error, whereas cross-correlation based methods produce results with lower random error. The latter is caused by the fact that cross-correlation uses information contained in the complete waveform of the received signal rather than just one point. An alternative approach was presented in [8], where the transducers were excited with a fixed frequency until a steady state was reached. The excitation frequency was tuned to calibrate the offset error. Although an interesting approach, its practical applicability is limited as calibration must be performed in zero-flow conditions and the transducers have to be separated by a significant distance to prevent interference of reflected waves. Similar to cross-correlation, an algorithm that uses time and phase domain signals was proposed in [9], with the main objective to be less sensitive to changes in the waveform shape.

Cross-correlating the upstream and downstream signal with their averages has been proposed to increase the measurement precision, because the average has a better resemblance to the waveform than the upstream and downstream signals mutually, because they might differ in amplitude and frequency [10]. Unfortunately, also this method requires recalibration in zero-flow conditions. Other work proposes to compare the measurement to the analytical solution of an oscillator model [11] or reconstructing the signal based on a signal model [12], mitigating the drawbacks of averaging. This method, however, still faces the drawback of the higher offset error commonly seen in cross-correlation measurements.

Thus, an algorithm that minimizes the offset error without compromising on the random error, that does not require calibration measurements, is desirable. This work proposes a method that combines the benefits of zero-crossing and cross-correlation methods to obtain flow measurements with a minimized absolute error in combination with a small random error, while being able to adjust for changes in the offset error over longer term as caused by environmental changes such as changes in temperature and pressure.

5.2. Simulation model

In order to simulate the upstream and downstream signals, the transducers are modeled using the KLM-model [13] in combination with a voltage source V_{in} and a source impedance R_{tx} representing the transmit circuit. The receive circuit impedance is modeled by the load impedance R_{rx}, as shown in Fig. 5.1a. The cable capacitance and piezo capacitance are modeled by C_p and the two resonant branches represent the upstream (A) and downstream (B) transducer, coupled by an acoustic transmission line. Because only the waveform shape and phase difference between the upstream and downstream signal are of interest, the KLM-model can be simplified by removing the acoustic transmission line and replacing it by its characteristic impedance Z_{tl} (Fig. 5.1b). The current in the transmit branch, I_{pulse}, is proportional to particle velocity in the acoustic domain. The acoustic pressure at the receive side of the transmission line is modeled as a voltage source, V_{pulse}, with a source impedance equal to the transmission line impedance Z_{tl}. The transformers and transmission line impedances can be replaced by an inductor when I_{PZT} and V_{pulse} are moved to the other side of the transformer and the values of the RLC-branch are adjusted accordingly. The adjusted component values are denoted $R_{A'}$, $L_{A'}$ and $C_{A'}$. Similarly the receive side can be simplified as well. The resulting circuit model consists of two Butterworth-van-Dyke models [14], where the voltage source at the receive side is proportional to the current through the transmit transducer. The resulting simulation model is shown in Fig. 5.1c.

The component values of the Butterworth-van-Dyke model were determined by analyzing the impedance of a $10\,\mathrm{mm}$ PZT disc, and curve fitting the model parameters. The resulting parameters are shown in Table 5.1. Transducer B is assumed to be equal to transducer A except for a $5\,\%$ mismatch in C_B. To simulate the upstream and downstream waveforms the parameters of the two transducers A and B are interchanged.

(a)

(b)

(c)
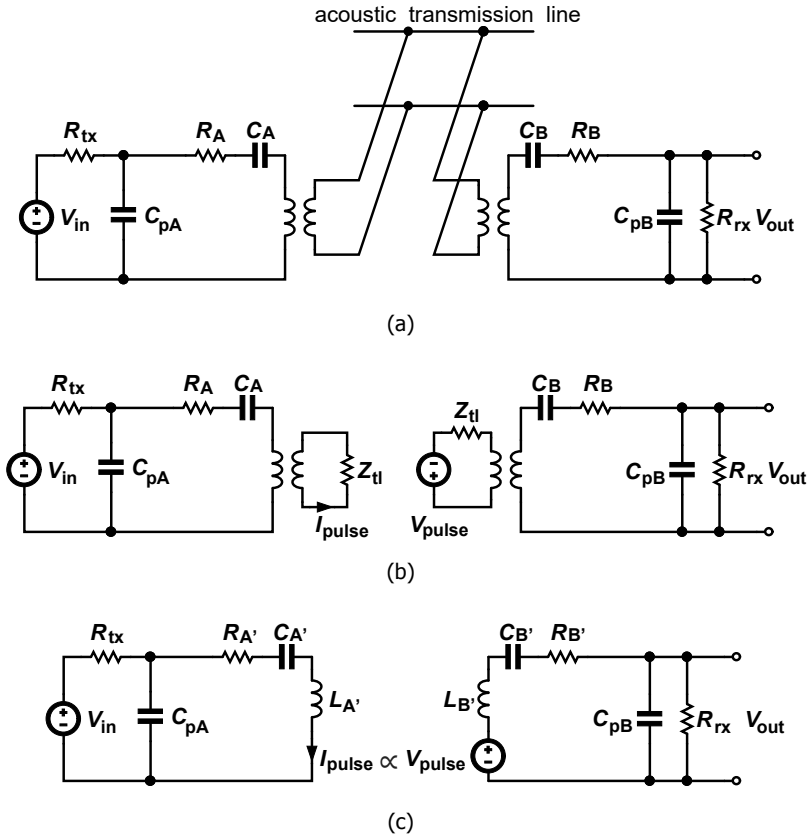
Figure 5.1: Simulation model based on simplified KLM-model. (a) KLM-model with signal source and load impedance. (b) KLM-model without acoustic transmission line. (c) Simplified KLM-model.

5.3. Error sources

In transit-time ultrasonic flow meters two main error sources that are affecting the flow measurements can be distinguished: The offset error, which appears as an offset to the measured flow, and the random error which influences the precision of the measurement and shows as a randomly distributed deviation from the actual flow velocity.

Table 5.1: Fitted model parameters for Butterworth-van-Dyke model.

R	L	C	C_p
$20\,\Omega$	$46\,\mu H$	$139\,pF$	$0.55\,nF$

5.3.1. Offset error

It is well known that the offset error is minimized by making the system as recip-
rocal as possible [15]. When the transducers or the circuit impedances are equal,
the system is fully reciprocal and no offset error is present [4]. In a practical sys-
tem a mismatch between the transducers will always be present. To minimize the
offset error, one thus has to make the impedance of the transmit circuit and the
impedance of the receive circuit equal and preferably both significantly lower or
both significantly higher than that of the transducer [4, 6]. In practice it is not
always trivial to make the circuit impedances equal, especially in mass-produced
devices where batch variations have a significant impact on the performance. In
those cases, often an offset error still exists. The offset error is simulated by intro-
ducing a mismatch between the transmit circuit impedance (R_{tx}) and receive circuit
impedance (R_{rx}), as well as introducing a mismatch between the two transducers.

The offset error can be considered as a systematic error on the measurement:
even with averaging, this error can not be reduced. Using the simplified KLM-
model, an example upstream and downstream waveform are simulated, as shown in
Fig. 5.2a. For illustration purposes, a large mismatch between R_{tx} and R_{rx} was used.
As evident from Fig. 5.2, the upstream and downstream transient waveforms differ
slightly in amplitude and shape. Although the difference looks small, it introduces a
significant error in the flow measurement. This error becomes evident when looking
at the instantaneous phase difference, or more practical, at the zero-crossings of
the two waveforms. Figure 5.2b shows the transit-time difference calculated using
zero-crossings detection. Note how the transit-time difference increases over time,
eventually converging to a linear increase with time associated with the resonance-
frequency difference between the transducers. The best estimate of zero flow can
therefore be found early in the waveform, where the signal's amplitude is low. This
is contradicting with the requirement of a high signal-to-noise ratio (SNR), as the
best SNR can be obtained when a high signal amplitude is available. Therefore
in practical systems that use zero-crossing detection, a trade-off is made between
taking an early zero-crossing and having a good SNR.

The commonly used alternative to detect the phase difference between the up-
stream and downstream signal is by cross-correlating the signals. Cross correlation
between two discrete signals f and g is defined as

$$(f \star g)(\tau) = \int_{-\infty}^{\infty} \overline{f(t)} g(t + \tau) \, dt, \tag{5.1}$$

where $\overline{f(t)}$ denotes the complex conjugate of $f(t)$. In essence cross correlation
delays one of the waveforms (waveform g in Eq. 5.1) and results in the highest
magnitude when both waveforms resemble each other best. The delay τ that results
in the maximum value is assumed to be the phase difference of the two waveforms.
With a phase shift that increases over time, as seen in Fig. 5.2b, the delay τ that
results in the best resemblance between the waveforms f and g will be at a point in
time where significant phase shift is present between the waveforms (as indicated
in Fig. 5.2b by a dashed line). This effect will generally cause the cross-correlation

5
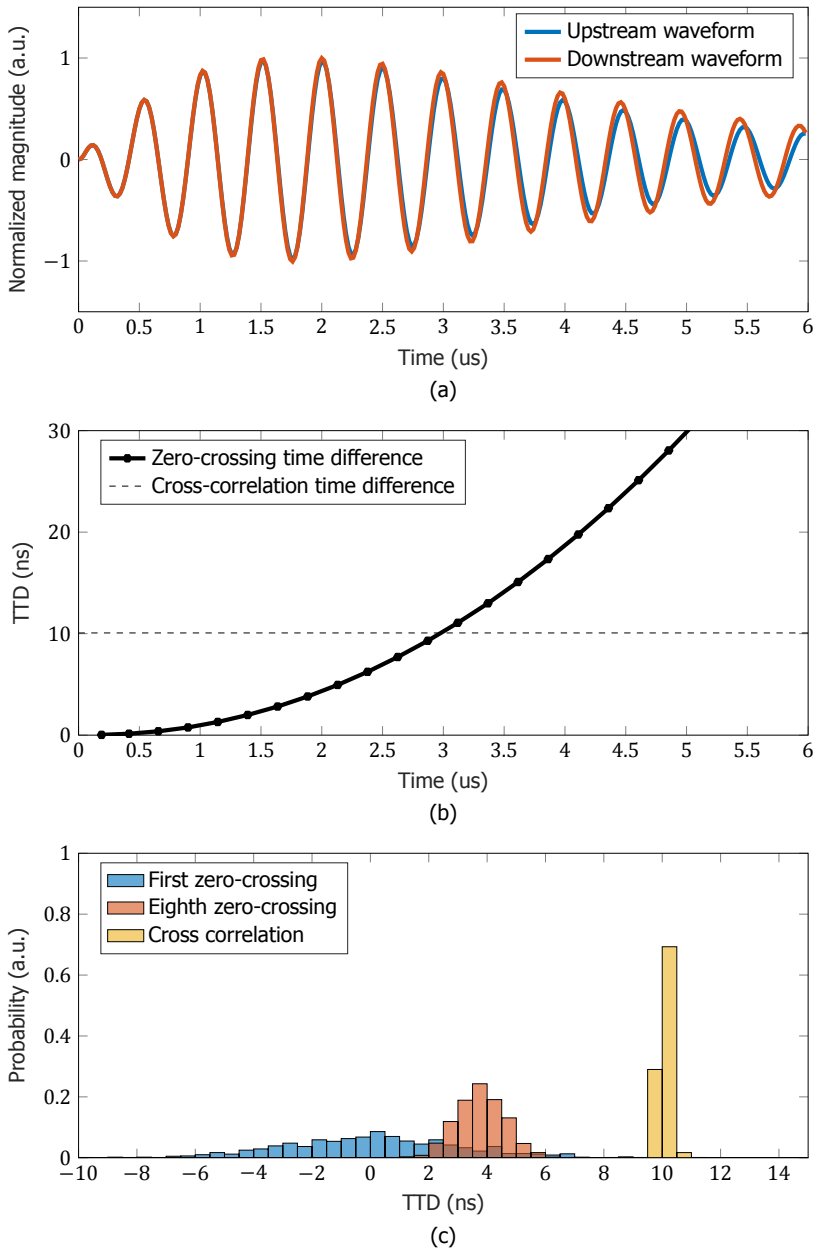
Figure 5.2: Simulated upstream and downstream signals for $R_{tx} = 50\,\Omega$ and $R_{rx} = 20\,\Omega$, excited with a single square pulse: (a) Transient waveforms. (b) Upstream-downstream time-difference (markers represent zero-crossings) and (c) Probability distribution of the transit-time difference obtained using the zero-crossing and cross-correlation based algorithms for 2000 simulated waveforms with $30\,\mathrm{dB}$ SNR.

to result in a higher offset error than the zero-crossing detection result.

5.3.2. Random error

In Fig. 5.2c the probability distribution of 2000 simulated transit-time differences is shown for the first zero-crossing, for the eighth zero-crossing and for cross-correlation, based on a signal with $30\,\mathrm{dB}$ SNR. Clearly visible is the reduction of the random error when using a zero-crossing in the higher-amplitude part of the waveforms (here the eighth zero-crossing) and an even smaller deviation when cross-correlation is used.

Depending on the algorithm used to detect the transit-time difference, the random error varies. Especially in time-domain methods like zero-crossing detection, a low SNR can significantly degrade the precision of the measurement. The SNR can be improved by applying averaging, however the improvement when taking the average of N measurements is only $\sqrt{N}$ [16], so a starting point with a better SNR is beneficial.

Minimizing the random error is important to get a good measurement precision. The random error can be dominated by many sources ranging from thermal noise and clock jitter to turbulence in the flow. To guarantee a good SNR one would like to use a high amplitude transmit signal, however industrial meters are often limited in voltage to guarantee intrinsic safety. Moreover, short well-defined transmit waveforms are commonly chosen. Common transmit waveforms are a single square pulse [17] or a single-cycle sine. Although it is possible to obtain reasonable results with these methods, they suffer from low SNR because the transmit signal contains limited energy [18]. As an alternative, significantly longer transmit waveforms have been proposed, to be able to measure in a steady state [19], but with the drawback that the transducers must be far apart to not be affected by interference of reflected waves. Ideally one would like to use a transmit waveform that contains a significant amount of energy and is easy to cross-correlate to achieve a low random error on the transit-time measurements. From imaging physics, it is well known that the waveform can be optimized to improve the SNR when using cross-correlation [20].

To further improve the cross-correlation result, the receive waveform can be compared with a high SNR version of the signal [10, 11], such as an averaged waveform.

5.4. Algorithm

Processing the measurement data in such a way that the offset error is calculated using zero-crossings, while the flow measurement is based on cross-correlation, combines the benefits of both techniques. An algorithm can thus be designed that removes the offset error caused by the cross-correlation operation. Because changes in the offset error are generally slow (e.g. due to temperature change), the zero-crossing calculation can be performed on an averaged signal, reducing the noise on the offset correction signal.

A diagram showing the steps of the proposed algorithm is shown in Fig. 5.3. By means of a moving average, high SNR versions of the upstream and downstream
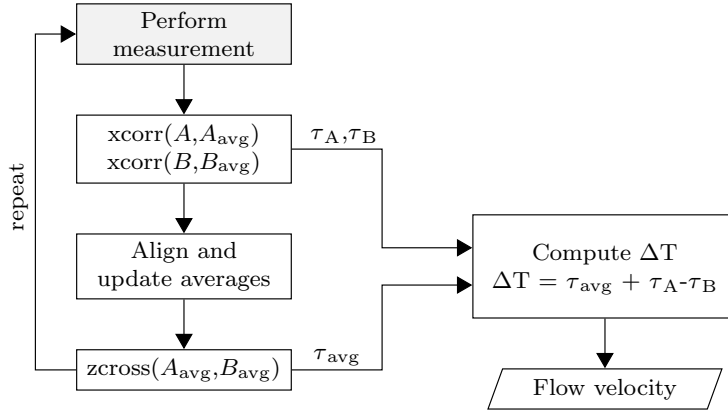
Figure 5.3: Diagram showing the steps of the algorithm.

waveforms are collected: A_{avg} and B_{avg}. Since the flow velocity can change over time, waveforms A and B have to be time shifted before they can be included in the moving averages. The required time shift can be determined by means of a cross-correlation between those waveforms and their respective moving averages

$$\tau_A = \text{xcorr}(A, A_{\text{avg}}), \tag{5.2}$$
$$\tau_B = \text{xcorr}(B, B_{\text{avg}}), \tag{5.3}$$

where the xcorr() operation represents the time delay τ corresponding to the peak of the cross-correlation. The resulting average waveforms will have an unknown time difference τ_{avg} due to the flow. This time-difference is calculated using zero-crossing detection, to obtain the lowest offset-error possible

$$\tau_{\text{avg}} = \text{zcross}(A_{\text{avg}}, B_{\text{avg}}), \tag{5.4}$$

where the zcross() operation represents the time difference between the first zero-crossing of each waveform, after the amplitude of the signal reaches a threshold value (in this work the threshold was set to $10\,\%$ of the peak amplitude). With this time difference, the flow speed associated with the moving average can be determined. The difference between this average flow speed and the instantaneous flow speed can be determined by the earlier calculated time shifts τ_A and τ_B, assuming that only the flow speed has changed. Thus a low-offset version of the time difference representing the instantaneous flow is obtained

$$\Delta T = \tau_{\text{avg}} + \tau_A - \tau_B. \tag{5.5}$$

The random error on the resulting flow value is comparable to that on the cross-correlation, assuming the noise level on the averaged signals is sufficiently small to be negligible. In addition to reducing the offset error, the algorithm also reduces the random error compared to cross-correlation between the upstream and downstream signal. By calculating the cross-correlation between the two signals and their averages separately, the random error is reduced. The same cross-correlation results can also be used to align the signal and update the average without the flow influencing the averaged waveform.

5.5. Measurement setup

A pair of transducers was built with $10\,\mathrm{mm}$ diameter PZ27 piezo-ceramic discs (Meggit A/S, Kvistgård, DK), with a thickness of $1\,\mathrm{mm}$ and a resonance frequency of $2\,\mathrm{MHz}$. The piezo-discs were glued onto a PVC cylinder to create air-backed transducers, as shown in Fig. 5.4. The transducers were then placed at a $45°$ angle in a pipe section with an inner diameter of a $40\,\mathrm{mm}$ (Fig. 5.5) mounted in a flow-loop filled with water. A reference flow meter (Optosonics 3400, KROHNE Nederland B.V., Dordrecht, NL) with an accuracy of $\pm 0.3\,\%\,+\,2\,\mathrm{mm/s}$, placed downstream, was used to validate the measured flow rate.

A measurement setup was built to first test several transmit waveform shapes in zero-flow condition and then measure a varying flow using the proposed algorithm. An Agilent 33522A (Agilent, Santa Clara, USA) arbitrary waveform generator was used to create a single square pulse, Gaussian-apodized sine and chirp signal. A printed circuit board (PCB), schematically shown in Fig. 5.6, was produced. An amplifier (OPA847, Texas Instruments, Dallas, USA) mounted on the PCB was used to buffer the transmit waveform and create a low impedance output to drive the transducers. A trans-impedance amplifier (TIA) constructed using a THS3001 (Texas Instruments, Dallas, USA) amplifier was used to amplify the received acoustic signals with a low input impedance. The upstream (A) and downstream (B) transducer were alternately switched between the transmit and receive circuit using reed relays. Received signals were digitized using a Spectrum M3i.4121 (Spectrum In-

(a)   (b)
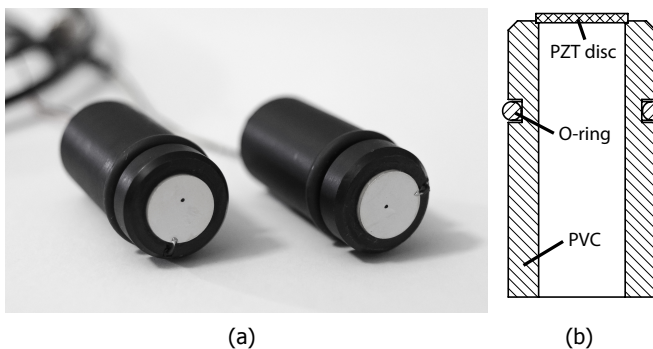
Figure 5.4: Pair of transducers made of an air-backed piezo-ceramic disc mounted onto a PVC cylinder.
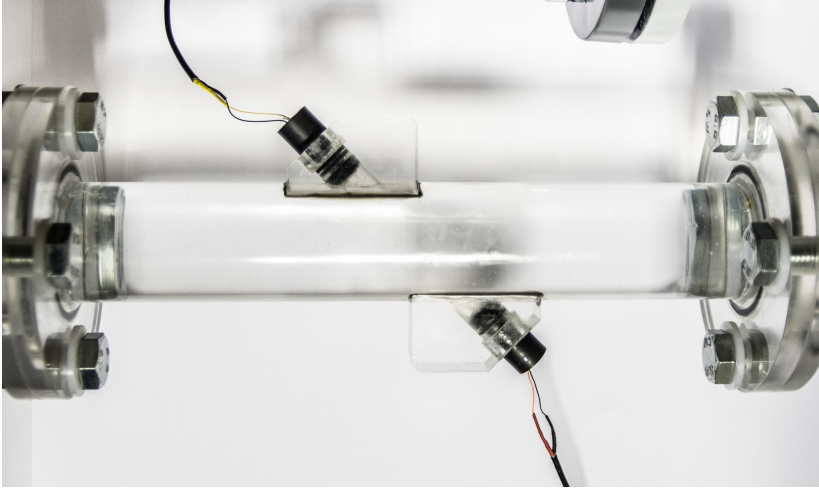
Figure 5.5: Transducers placed co-axially at a $45°$ angle in a $40\,mm$ inner-diameter pipe section of the flow-loop.
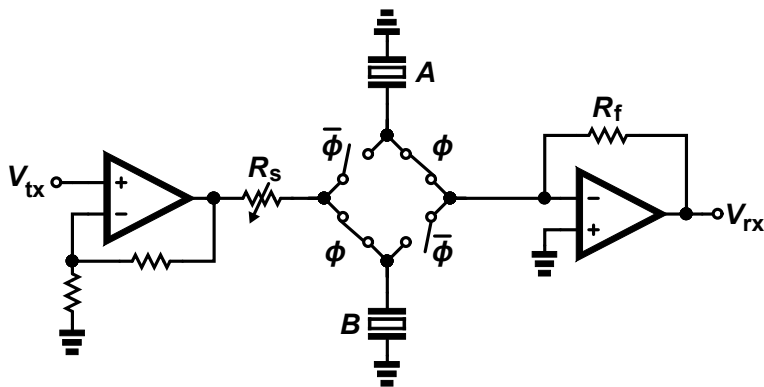
Figure 5.6: Circuit used in the measurements.

strumentation GMbH, Groβhansdorf, DE) acquisition card, with a sampling rate of $250\,MS/s$.

5.6. Experimental results

In zero-flow conditions, measurements were performed with several transmit wave-forms with equal peak-to-peak transmit voltage. In Fig. 5.7 the measurements with three common transmit waveforms are compared; a square pulse, a Gaussian-apodized sine wave ($2\,MHz$) and a chirp ($1.5 - 2.5\,MHz$). As can be seen in the second row, the signal amplitude of the received waveform is highly dependent on the energy contained in the transmitted signal. When the zero-crossing time differ-
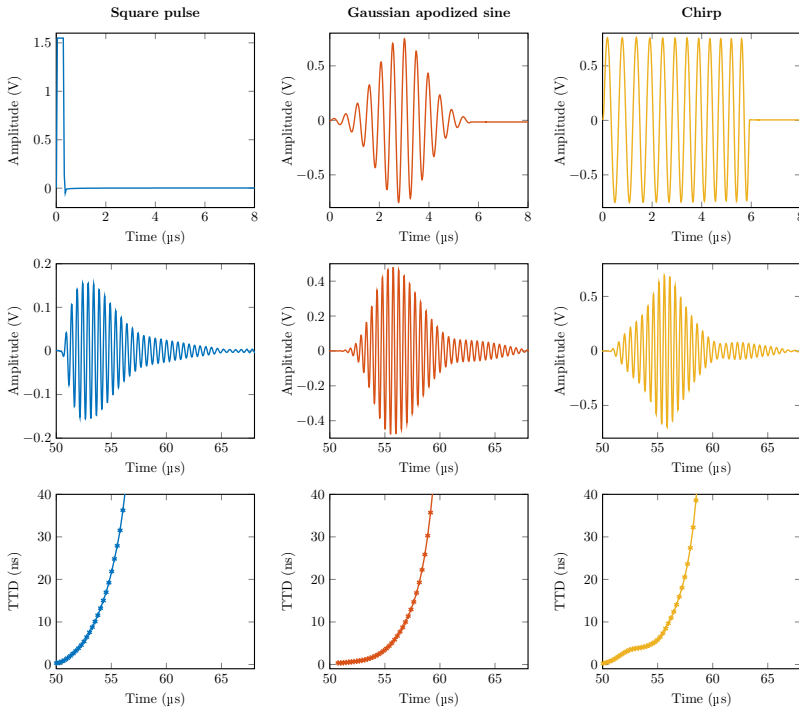
Figure 5.7: Measured transmit waveform (top), receive waveform (middle) and zero-crossing transit time-difference (bottom), for 3 different transmit waveforms with similar peak-to-peak amplitude: square pulse (left), Gaussian-apodized sine (middle) and chirp (right).

ence (Fig 5.7, bottom row) is plotted, it is noticed that, for each type of waveform, the first detected zero-crossing has the lowest transit-time difference, confirming that the first zero-crossing is the best estimate of the zero-flow value. The cross-correlation results always show a relatively large offset error as shown in Table 5.2.

Moreover, these examples show the benefit that can be obtained by choosing the right transmit waveform, because they result in very different random errors with the same transmit amplitude. Table 5.2 also shows that the random error is larger for the zero-crossing method than for cross-correlation, as expected.

Table 5.2: Measured offset error and random error (std.) calculated using zero-crossing detection and cross-correlation for three types of transmit waveforms.

Waveform	zero-crossing		cross-correlation	
	offset	std.	offset	std.
Square pulse	0.35 ns	2.8 ns	8.7 ns	1.49 ns
Gaussian-apodized sine	0.36 ns	1.7 ns	8.6 ns	0.29 ns
Chirp	0.17 ns	1.8 ns	7.2 ns	0.20 ns

Another measurement was performed at zero-flow conditions, this time to compare the proposed algorithm with the cross-correlation and zero-crossing method to see its effect on the offset error. The inset in Fig, 5.8 shows the transit-time differences for the first 400 consecutive measurements, calculated using cross-correlation, zero-crossing detection and the algorithm presented in this work with a moving average of 400 samples. In this measurement, averaging the signal starts at sample 1, causing the offset error to be poorly estimated for the first few samples, where the average still has a low SNR, converging towards a steadier offset estimate when the SNR of the average signal improves. It is evident from the measurement that the random error significantly improves compared to the zero-crossing detection algorithm. The offset is reduced compared to the cross-correlated data by the correction that the zero-crossing detection on the averaged signals provides. As the average waveform is based on 400 measurements only, it is not yet possible to detect the earliest zero-crossing, resulting in a residual offset. By averaging more, this offset can be reduced further because an earlier zero-crossing can be detected.

After 600 measurements, the reciprocity of the circuit was gradually reduced by changing the impedance of the transmit circuit (R_s in Fig. 5.6). This measurement emulates changing environmental conditions. Fig. 5.8 shows how the offset error increases when the mismatch between the impedances of the transmit and receive circuit is larger. The algorithm is still dependent on the reciprocity of the system, but the offset error is significantly lower compared to cross-correlation. In this measurement the offset error is reduced by more than a factor of 7. Moreover, the random error of the algorithm is, with a standard deviation of $17\,\mathrm{ps}$, a factor of 10 lower than with zero-crossing detection, which has a standard deviation of $182\,\mathrm{ps}$ in the measurement. The figure also shows that abrupt changes temporarily cause an increased offset error compared to zero-crossing detection, this is caused by the low-pass behavior of averaging.
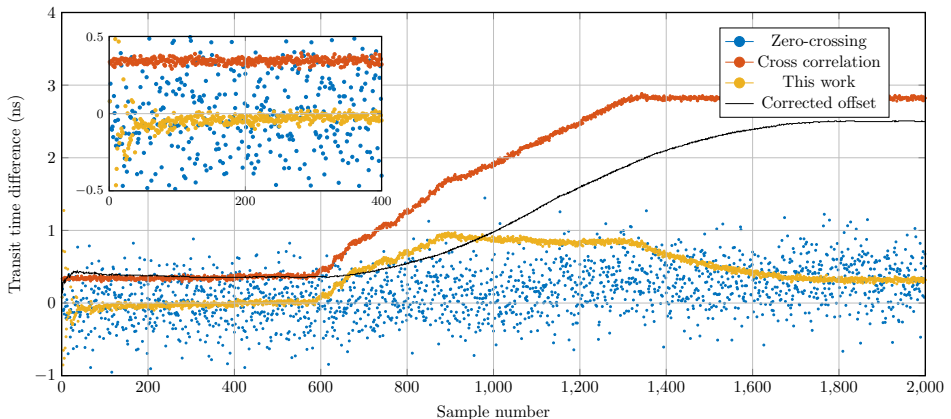
Figure 5.8: Zero flow measurement with varying reciprocity, by introducing a mismatch between the transmit and receive circuit impedance. The corrected offset shows the absolute difference between the cross-correlation algorithm and this work.

A large benefit of the algorithm is that the average signals can be updated in the presence of flow. To show the performance with varying flow velocities, measurements were performed in a flow loop. The flow velocity was varied from $0\,\mathrm{m/s}$ to $0.6\,\mathrm{m/s}$. The measurement results shown in Fig. 5.9 confirm that the algorithm is able to calculate the flow velocity with a significantly lower offset error than obtained using cross-correlation. The random error is also significantly lower than it is for the samples based on the zero-crossings (blue markers). At low flow velocities ($v < 0.2\,\mathrm{m/s}$) the random error of the cross-correlation result is noticeably lower. This difference is likely due to the transition from turbulent to laminar flow condition.

To test the effect of temperature changes on the algorithm, a measurement over a few hours was performed, starting with hot water of 75^oC in the setup and allowing it to cool down towards ambient temperature. Fig. 5.10 shows the measurements for the different algorithms. Also here the proposed algorithm is able to reduce the offset significantly. The figure includes, for comparison, a curve representing the cross-correlation results corrected based on a calibration for the offset error at the start of the measurements. This results in a significant offset error at the end of the measurement, in contrast with the proposed algorithm, that effectively nulls the offset.

5.7. Discussion

The algorithm presented in this work is most effective in transit-time flow meters in which the electronics suffer from non-reciprocity. In applications with quickly changing environments, such as fluctuating temperatures, it might not always be optimal because a smaller number of averages must be used, reducing the measurement accuracy. In the more common environments that have slowly changing environmental parameters, for example changing over the course of minutes, a
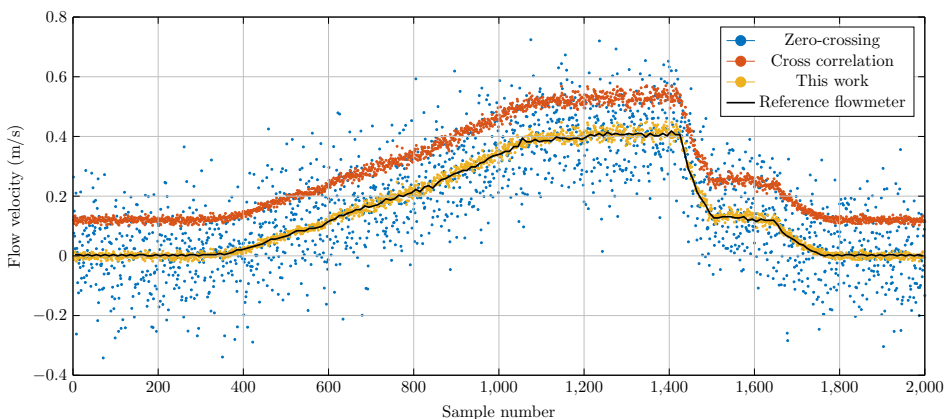
Figure 5.9: Measured flow velocity in the flow-loop with varying flow, showing the effectiveness of zero-crossing detection, cross-correlation and the method described in this work.
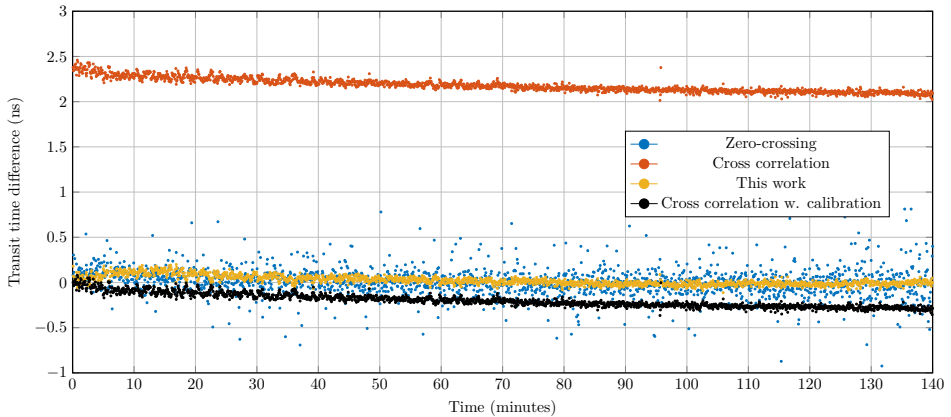
Figure 5.10: Measured transit time difference in zero-flow condition with water temperature decreasing from 75°C to 30°C.

5

large number of averages in the order of tens of thousands of samples can be used to make the zero-crossing detection used in the algorithm as insensitive as possible to noise on the receive signal and thus making the algorithm very robust. The flow measurements shown in this work (Fig. 5.9) only use an average of 2000 waveforms, which can be recorded in a few seconds.

Naturally, averaging is only effective at reducing noise. Periodic interference, such as reflections of the acoustic wave, can still interfere with the measurement and alter the phase of the waveform. Moreover, zero-crossing detection inherently results in a residual offset, because physically the received signal cannot start with a zero-crossing, and thus the phase difference developed at a half-period will remain. Improvements can likely be made by predicting the actual start of the signal, or extrapolating the zero-crossing points.

It is important to note the distinct difference in the way averaging is implemented compared to prior work. By time-shifting the samples to align them before averaging, the average is not affected by a change in flow velocity, in fact, even instantaneous flow changes can be tolerated. The algorithm discussed here is, unlike prior work, not limited to specific waveforms with the benefit that the waveform can be optimized for maximum SNR.

In a practical implementation, the sample rate can be significantly lower than that of the acquisition card used in this work. Moreover, cross-correlation can take place during the transit-time, which is in the order of $50\,\mu s$, relaxing the hardware requirements.

Several implementation variants on the algorithm are conceivable, with differing hardware complexity. For example, cross-correlation with an averaged waveform can be left out when a slight adjustment is made to the algorithm, at the cost of an increase in random error.

5.8. Conclusion

An algorithm for transit-time ultrasonic flow measurements that calculates the flow velocity with a low offset error and with high precision has been designed. It was shown that zero-crossing detection yields the lowest offset error while cross-correlation results in the lowest random error. The algorithm combines those benefits by detecting the zero-crossings of a long-term average. Cross-correlation with the same average was used to achieve the best precision. The described algorithm improved the flow measurements significantly with a 7 times reduction of the offset error compared to cross-correlation. The random error was comparable to cross-correlation and in the measurements 10 times lower compared to zero-crossing detection.

The algorithm was able to adjust to simulated environmental changes, proving it does not require calibration in zero-flow conditions. Moreover, it can be implemented on existing transit-time ultrasonic flow meters that already employ cross-correlation, by updating the software only, potentially improving the specifications with just a firmware update.

5

References

[1] D. M. Van Willigen, P. L. M. J. Van Neer, J. Massaad, N. De Jong, M. D. Verweij, and M. A. P. Pertijs, *An algorithm to minimize the zero-flow error in transit-time ultrasonic flow meters,* IEEE Trans. Instrum. Meas. **70**, 1 (2020).

[2] J. Hemp, *Theory of transit time ultrasonic flowmeters,* J. Sound Vib. **84**, 133 (1982).

[3] P. Lunde, M. Vestrheim, R. Bo, S. Smorgrav, and A. K. Abrahamsen, *Reciprocal operation of ultrasonic flow meters: Criteria and applications,* IEEE Int. Ultrason. Symp. , 381 (2007).

[4] P. Lunde, M. Vestrheim, R. Bø, S. Smørgrav, and A. K. Abrahamsen, *Reciprocity and its utilization in ultrasonic flow meters,* 23rd International North Sea Flow Measurement Workshop Tønsberg, Norway , 18 (2005).

[5] M. Takamoto, H. Ishikawa, K. Shimizu, H. Monji, and G. Matsui, *New measurement method for very low liquid flow rates using ultrasound,* Flow Meas. Instrum. **12**, 267 (2001).

[6] D. van Willigen, P. van Neer, J. Massaad, M. Verweij, N. De Jong, and M. Pertijs, *Minimizing the zero-flow error in transit-time ultrasonic flow meters,* IEEE Int. Ultrason. Symp. , 1 (2018).

[7] J. Borg, J. Johansson, J. Van Deventer, and J. Delsing, *Reciprocal operation of ultrasonic transducers: Experimental results,* IEEE Int. Ultrason. Symp. , 1013 (2006).

[8] A. Hamouda, O. Manck, M. Hafiane, and N.-E. Bouguechal, *An enhanced technique for ultrasonic flow metering featuring very low jitter and offset,* Sensors **16**, 1008 (2016).

[9] M. Kupnik, E. Krasser, and M. Groschl, *Absolute transit time detection for ultrasonic gas flowmeters based on time and phase domain characteristics,* IEEE Int. Ultrason. Symp. , 142 (2007).

[10] H. Zhou, T. Ji, R. Wang, X. Ge, X. Tang, and S. Tang, *Multipath ultrasonic gas flow-meter based on multiple reference waves,* Ultrasonics **82**, 145 (2018).

[11] F. Suñol, D. A. Ochoa, and J. E. Garcia, *High-precision time-of-flight determination algorithm for ultrasonic flow measurement,* IEEE Trans. Instrum. Meas. (2018), 10.1109/TIM.2018.2869263.

[12] Z. Fang, L. Hu, L. Qin, K. Mao, W. Chen, and X. Fu, *Estimation of ultrasonic signal onset for flow measurement,* Flow Meas. Instrum. **55**, 1 (2017).

[13] R. Krimholtz, D. A. Leedom, and G. L. Matthaei, *New equivalent circuits for elementary piezoelectric transducers,* Electron. Lett. **6**, 398 (1970).

[14] K. S. Van Dyke, *The piezo-electric resonator and its equivalent network,* Proc. Inst. Radio Eng. **16**, 742 (1928).

[15] J. Hemp, *Flowmeters and reciprocity,* Q. J. Mech. Appl. Math. **41**, 503 (1988).

[16] S. Grzelak, J. Czoków, M. Kowalski, and M. Zieliński, *Ultrasonic flow measurement with high resolution,* Metrol. Meas. Syst. **21** (2014), 10.2478/mms-2014-0026.

[17] Y. Bo and C. Li, *Electronic circuit design for reciprocal operation of transit-time ultrasonic flow meters,* Flow Meas. Instrum. **32**, 5 (2013).

[18] L. Svilainis, P. Kabisius, A. Aleksandrovas, and A. Chaziachmetovas, *Excitation signal's influence on ultrasonic transit time flow meter's performance,* IOP Conf. Mater. Sci. Eng. **42**, 1 (2012).

[19] Y. Bo, C. Li, and L. Yupin, *Forced oscillation to reduce zero flow error and thermal drift for non-reciprocal operating liquid ultrasonic flow meters,* Flow Meas. Instrum. **22**, 257 (2011).

[20] T. Misaridis and J. A. Jensen, *Use of modulated excitation signals in medical ultrasound. part i: Basic concepts and expected benefits,* IEEE Trans. Ultrason. Ferroelectr. Freq. Control **52**, 177 (2005).

5

6

Flow measurements with a prototype pair of linear transducer arrays

An ultrasonic clamp-on flow meter prototype consisting of two 36-element linear arrays was fabricated based on the matrix transducer design proposed in Chapter 2. Flow speed measurements of water were performed in a custom-made flow loop and in two scenarios: using compressional and shear waves in the pipe wall. The built flow metering system reported a very high level of reciprocity: at zero-flow conditions, transit time differences < 1 ns were measured. Furthermore, it was shown that several recorded travel paths could be combined to estimate a more precise flow speed.

6.1. Introduction

In Chapter 2, it was described in detail the design of a matrix transducer array for ultrasonic clamp-on flow metering in a wide range of situations, i.e. liquids and pipe sizes. Such design inspired the fabrication of a 36-element linear transducer array, whose acoustic characterization reported a very good agreement with the simulations. These results inspired the fabrication of an ultrasonic clamp-on flow meter prototype consisting of two of these linear arrays.

Here it is shown how this custom-built device was used to measure flow, and how new tools and techniques were used within this context to achieve more precise flow measurements compared to common ultrasonic clamp-on flow meters.

6.2. Experimental setup

A custom-made flow loop was built (see Fig. 6.1). It mainly consisted of PVC pipes with a constant inner diameter of $40\,\mathrm{mm}$, and a reference in-line ultrasonic flow meter (Optosonics 3400, KROHNE Nederland B.V., Dordrecht, NL). The liquid used was water. The flow rate was manually controlled with a valve. With this setup it was possible to achieve flow speeds of water up to $0.6\,\mathrm{m/s}$ for relatively long periods of time. A flow speed of $0.6\,\mathrm{m/s}$ could be kept constant for up to $15\,\mathrm{min}$.

A $30\,\mathrm{cm}$ long section consisted of a 304 stainless steel pipe ($c_L = 5920\,\mathrm{m/s}$, $c_T = 3141\,\mathrm{m/s}$), with a wall thickness of $h = 1\,\mathrm{mm}$ and an inner diameter of $D = 40\,\mathrm{mm}$. Both fabricated linear arrays were centrally clamped on this pipe section via custom-made 3D-printed frames to ensure proper mechanical coupling with the pipe. As can also be seen in Fig. 6.1, the arrays were not clamped on the top of the pipe but rather at a sideway location to avoid the potential non-reciprocal effects of bubbles on the measurements.

The axial transducer separation was $80\,\mathrm{mm}$ (see Fig. 2.4c), and flow speed was measured in both scenarios. For compressional waves in the pipe wall, the required steering angle was $12.85\,^\circ$, and the desired wave mode (see Fig. 2.4a)
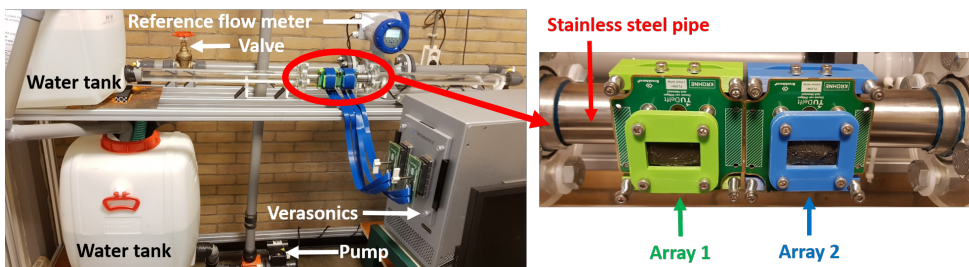
Figure 6.1: Custom-made flow loop to perform ultrasonic clamp-on flow measurements with the fabricated prototype arrays. The red oval indicates the location of the flow sensor with the two linear arrays. Gravity was used to drive flow from left to right through the stainless steel pipe section on which the arrays were installed. The custom-made 3D-printed green and blue frames were designed with a system of screws and springs to achieve good mechanical coupling of the backing with the PCB (front screws), and of the lead coupling piece (not visible here) with the pipe wall (back screws).

was expected to arrive at $\approx 350\,\mu s$. For shear waves in the pipe wall, the steering angle of the acoustic beam within the lead piece was $32.75\,°$, and the desired wave mode (Fig. 2.4b) was expected to arrive at $\approx 130\,\mu s$. These transit times were also cross-checked with FEM simulations.

6.3. Data acquisition

Two custom-made PCBs were designed to wire-out each piezo-element of both linear arrays to a Verasonics Vantage 256 system. This machine was used to excite the piezo-elements with a 1-cycle square pulse with a center frequency of $f_c = 1\,MHz$ and a peak voltage of $5\,V$. Time delays in transmission were also implemented with this machine to produce steered acoustic beams.

Measurements with different pairs of piezo-elements confirmed that the Verasonics machine kept the timing of the signals stable enough to perform flow measurements. The time jitter of the machine was reported to be $\approx 4\,ps$, which was an acceptable value given the few tens of nanoseconds of the expected transit time differences to be measured with the setup.

Upstream and downstream measurements were performed in an interleaved fashion to minimize the effects of temperature change on the sound speed of the liquid, and therefore on the flow speed estimates. One thousand measurements were performed in each direction, with a pulse repetition frequency (PRF) of $\approx 87\,Hz$. This allowed to record all measurements in $23\,s$. Element signals were recorded with a sampling frequency of $62.5\,MHz$. Finally, all signals were exported for further processing.

6.4. Data processing sequence

For each flow speed, the signals were processed as shown in the flowchart of Fig. 6.2. The bandpass filter applied to the raw signals consisted of a $5\,^{th}$-order Butterworth filter. The measured time signals were interpolated with a sampling frequency of $250\,MHz$, i.e. $4\,ns$, which was considered enough to estimate the expected few tens of nanoseconds of transit time differences. Lastly, the signals corresponding to each individual receiving element are delayed to align the signals for a given beam direction, and these are subsequently summed altogether. Two final signals obtained from an upstream and a downstream measurement are subsequently cross-correlated to obtain their transit time difference. This was finally used as input, together with the properties of the pipe and the liquid, to estimate the flow speed.

6.5. Measurements

6.5.1. Time signals

Raw time signals for the two considered acoustic paths, i.e. Fig. 2.4a and Fig. 2.4b, were recorded. Fig. 6.3 shows the measured signals at zero flow conditions. In both scenarios, the desired wave mode of interest was recorded within the expected transit time. Furthermore, other wave modes, including guided waves and

Start

Load signals

Band-pass filter (0.2 - 2 MHz)

Time-windowing around wave mode of interest

Remove signals from dead elements

Narrower time-windowing of wave mode of interest

Interpolate time signals with a sampling frequency of 250 MHz

f-kx filtering of wave modes propagating opposite to the expected direction

Delay and sum

Cross-correlation

Interpolate cross-correlation function

Estimate transit time difference

Estimate flow speed

End

6

Figure 6.2: Signal processing sequence applied to the measured signals from the flow sensor of Fig. 6.1.

reflections from flanges were also recorded. Moreover, as expected, the amplitude of the wave mode of interest was recorded with a higher SNR relative to the amplitudes of the other acoustic paths, which also aided towards its identification within the time domain signals.

The upstream array (Array 1 in Fig. 6.1) had 9 broken elements. The signals corresponding to these elements were removed from the analysis, as well as the

(a)

(b)
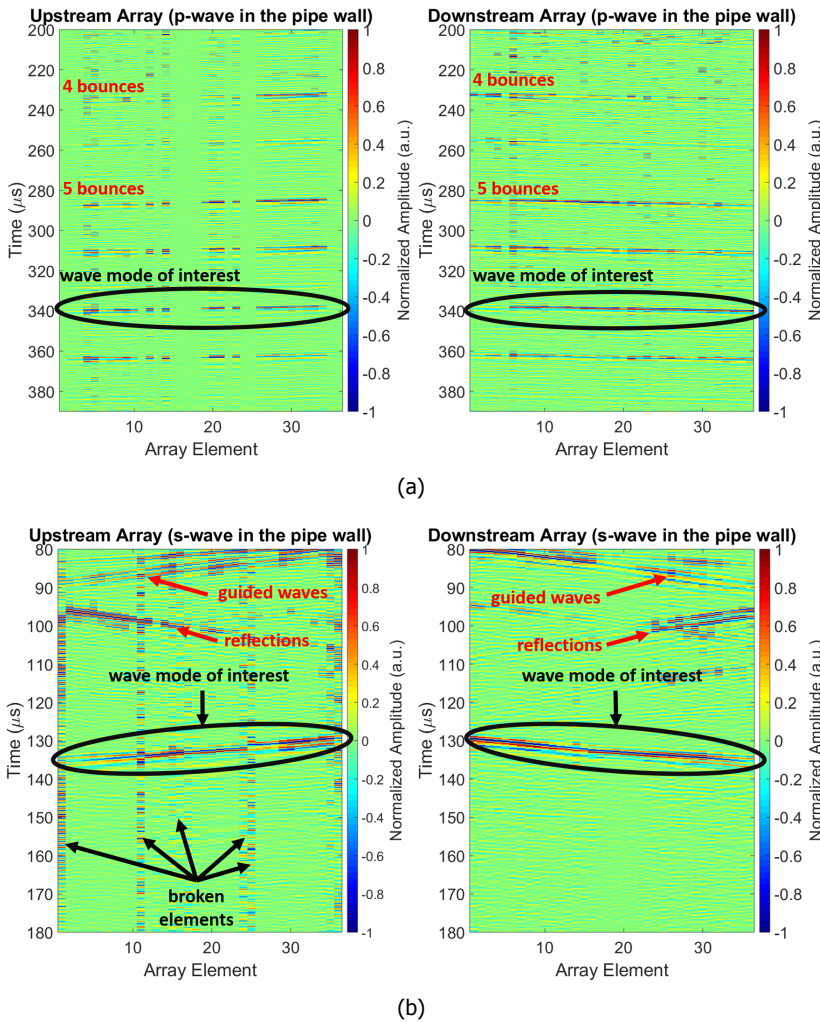
Figure 6.3: Time signals measured at zero-flow conditions with the custom-built ultrasonic clamp-on flow meter based on two linear arrays as shown in Fig. 6.1 for (a) compressional waves in the pipe wall and 6 bounces of the acoustic beam within the pipe (see Fig. 2.4a), and (b) shear waves in the pipe wall and 2 bounces of the acoustic beam within the pipe (see Fig. 2.4b).

signals corresponding to their mirror counter-parts from the downstream array (Array 2 in Fig. 6.1). This way, system reciprocity was kept.

6.5.2. $f - k_x$ filtering

A particularly powerful new tool that linear arrays bring into ultrasonic flow metering is the possibility to filter out undesired spurious wave modes. Given the recorded signals of several transducer elements, it is possible to visualize the propagating

wave modes, both in the time domain (see Fig. 6.4a) and, after applying a 2D Fourier transformation, in the f-k_x domain (see Fig. 6.4b). Although the wave modes could be identified in the time domain, it may not always be possible to easily window out the desired wave mode because it may overlap with the undesired ones. The probability of this overlap increases when the transducers are installed closer to each other, and also when the sensor is installed nearby other features of the pipeline, such as flanges and/or valves. However, the direction (i.e. steering angle) of the transmitted beam is always known during ultrasonic flow metering. Therefore, the expected direction from which it should arrive is also known, and will correspond with a specific straight line in the f-k_x domain. Thus, with linear arrays it is possible to identify this wave mode in the f-k_x domain and filter-out all other undesired wave modes, including guided waves and reflections, to finally obtain cleaner time signals to estimate the flow speed (see Fig. 6.4c).

In principle, to properly implement $f - k_x$ filtering, all piezo-elements of the array should output a coherent signal, so as to achieve uniform sampling in both time and space. Otherwise, the $f - k_x$ spectrum of non-uniformly sampled signals would be distorted, i.e. the wave modes would be located at the wrong positions, and the technique would be sub-optimal. Therefore, in the future, it would be very useful to develop an interpolation-based method that aids towards the inevitable practical malfunctioning of the piezo-elements, so that filtering techniques could still be implemented. Nevertheless, in the particular case of the measurements taken with the setup of Fig. 6.1, it was possible to window-out the wave mode of interest in the time domain and still estimate flow speed.

(a)   (b)   (c)
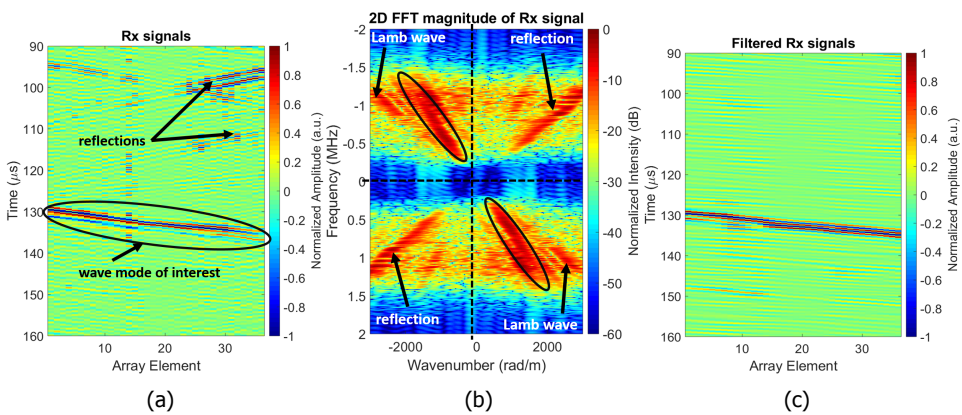
Figure 6.4: (a) Measured raw signals with the 36-element downstream array, i.e. Array 2 of Fig. 6.1, at zero-flow conditions and for the travel path of Fig. 2.4b, where the wave mode of interest is observed at the expected transit time, as well as reflections from the flanges and the open ends of the lead coupling piece. (b) Magnitude of the 2D Fast Fourier Transform (FFT) applied on the time signals of (a), where different wave modes are identified. Based on the location of the desired wave mode of interest (black oval), the 1st and 3rd quadrant may be filtered out, as well as certain regions of the 2nd and 4th quadrant. (c) Time signals after filtering, in the Fourier domain, the undesired spurious wave modes.

6.5.3. Flow speed

Considering a sound speed in water of $c_{liquid} = 1500\,\text{m/s}$, it was possible to compute the theoretical transit time difference Δt between upstream and downstream signals measured for the travel paths in the scenarios of Fig. 2.4a and Fig. 2.4b. At zero-flow conditions, it was expected to measure $\Delta t = 0\,\text{ns}$ for both scenarios. However, in practice, an ultrasonic flow metering system is never completely reciprocal, and a transit time difference is still measured at zero-flow conditions. This value is usually known as the zero-flow error.

With the fabricated pair of linear arrays, and considering the acoustic beam paths of a compressional wave (Fig. 2.4a) and a shear wave (Fig. 2.4b) in the pipe wall, values of $\Delta t = 0.55\,\text{ns}$ and $\Delta t = 0.19\,\text{ns}$ respectively, were measured at zero-flow conditions. These values are significantly lower than the usual few nanoseconds of zero-flow error reported by common single-element ultrasonic clamp-on flow meters. Furthermore, these values reported a median absolute deviation (mad) of $\text{mad} = 2.19\,\text{ns}$ and $\text{mad} = 1.06\,\text{ns}$, respectively. Measured time signals are shown in Fig. 6.5a and Fig. 6.5b.

For the highest possible reference flow speed, i.e. $v_{ref} = 0.6\,\text{m/s}$, theoretical transit time differences of $\Delta t = 39.27\,\text{ns}$ and $\Delta t = 33.86\,\text{ns}$, respectively, were computed. The measured values for this flow speed were $\Delta t = 38.46\,\text{ns}$ and $\Delta t = 33.80\,\text{ns}$, with median absolute deviation of $\text{mad} = 4.05\,\text{ns}$ and $\text{mad} = 2.39\,\text{ns}$, respectively. Measured time signals are shown in Fig. 6.5c and Fig. 6.5d. The reported median absolute deviations, like those shown in Fig. 6.6, apply to a single measurement. The slight discrepancies between measured and theoretical values are probably due to the chosen theoretical sound speed of the water. Also, when considering compressional waves in the pipe wall, the transit time of the acoustic waves is higher than with shear waves, which is the reason for the higher transit time differences in the former scenario relative to the latter.

The flow speed v_f can be obtained from the acoustic beam path of Fig. 2.4a and Fig. 2.4b, the properties of the pipe, the sound speed of the liquid, and the measured transit time differences between upstream and downstream measurements. This requires computing the positive root of the following second-order equation

$$[\Delta t \sin^2(\theta_{liquid})]v_f^2 + [4bD\tan(\theta_{liquid})]v_f - \Delta t c_{liquid}^2 = 0, \tag{6.1}$$

where θ_{liquid} represents the steering angle of the acoustic beam in the liquid, and b represents the number of bounces (v-shapes) of the acoustic beam within the pipe wall before arriving at the receiving transducer.

For the measurement scenarios of Fig. 2.4a and Fig. 2.4b, the flow speed was obtained and compared with the reference measurement. At zero-flow conditions, flow speeds of $v_f = 0.008\,\text{m/s}$ and $v_f = 0.003\,\text{m/s}$, were estimated, with a median absolute deviation of $\text{mad} = 0.03\,\text{m/s}$ and $\text{mad} = 0.02\,\text{m/s}$, respectively. Furthermore, at a reference flow speed of $v_{ref} = 0.6\,\text{m/s}$, the measured flow speeds with the prototype were $v_f = 0.59\,\text{m/s}$ and $v_f = 0.60\,\text{m/s}$, with a median absolute deviation of $\text{mad} = 0.06\,\text{m/s}$ and $\text{mad} = 0.04\,\text{m/s}$, respectively.

A linear fit between the reference flow speeds and those measured with the fabricated prototype was performed. The slopes of the linear fits shown in Fig. 6.7

6
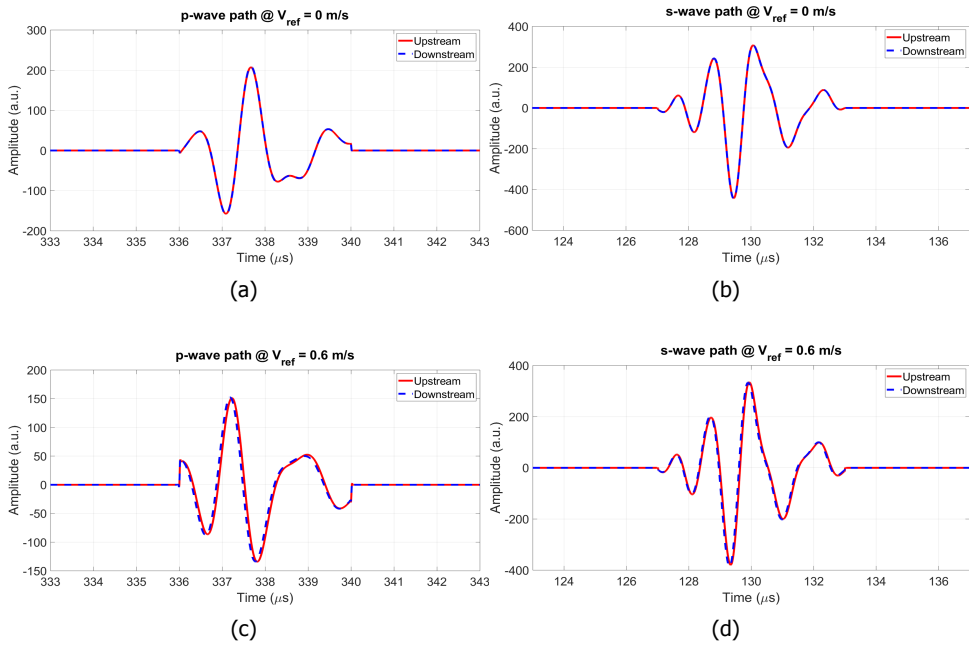
Figure 6.5: Processed upstream (red) and downstream (blue) time signals with the fabricated linear arrays of Fig. 6.1 at (a,b) zero-flow conditions and (c,d) a reference flow speed of $v_{ref} = 0.6\,\text{m/s}$, considering a compressional wave in the pipe wall (travel path of Fig. 2.4a) and a shear wave in the pipe wall (travel path of Fig. 2.4b).
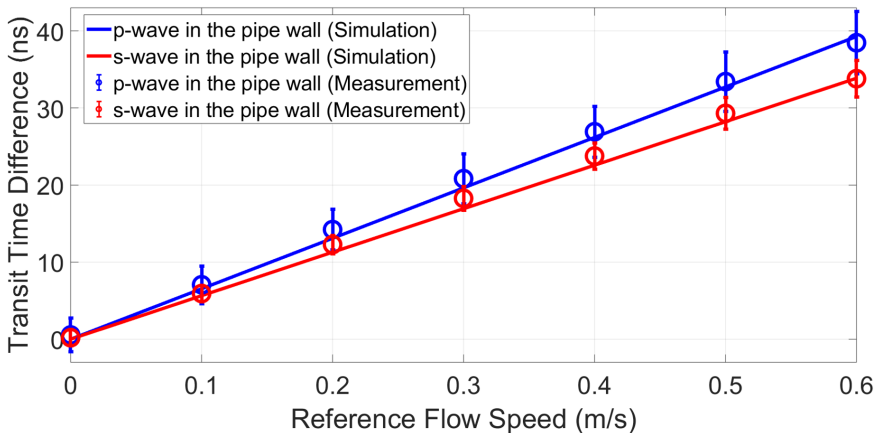
Figure 6.6: Theoretical transit time difference (solid lines) and measured transit time difference (circles) between upstream and downstream signals, versus flow speed, for the scenarios of Fig. 2.4a (blue) and Fig. 2.4b (red). Vertical bars indicate median absolute deviations.
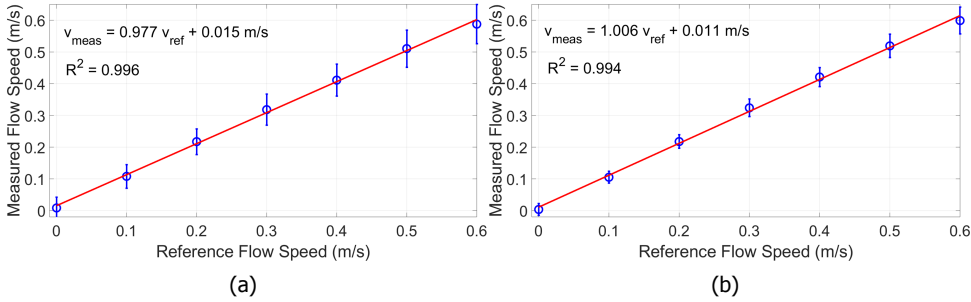
Figure 6.7: Measured vs. reference flow speed of water for the acoustic beam paths considering a compressional wave in the pipe wall (travel path of Fig. 2.4a) and (b) a shear wave in the pipe wall (travel path of Fig. 2.4b). Vertical bars indicate median absolute deviations.

were 0.977 and 1.006, respectively, which suggest a good correspondence between reference and measurements.

6.6. Considering more acoustic paths

In principle, other travel paths relative to those depicted in Fig. 2.4a and Fig. 2.4b are also sensitive to the flow (e.g. those in which the acoustic beam bounces 4, 5, 6 and 7 times within the pipe, see Fig. 6.3a). The information from these other travel paths (which are similar to those also shown in [2]) could also be used to extract more estimates of the flow speed, and in that sense reduce the measurement uncertainty. However, their refraction angle into the liquid (θ_{liquid}) is different and needs to be adjusted in Eq. 6.1 before computing the flow speed.

Considering the measurement scenario where a compressional wave in the pipe wall was excited, Fig. 6.8 shows the relation between measured and reference flow speed for the different travel paths (bounces) recorded and shown in Fig. 6.3a, where it was possible to realize that, besides the travel path considered so far (i.e. the one recorded after 6 bounce within the liquid, see Fig. 2.4a), other travel paths also report sensitivity to the flow speed.

However, due to the limited aperture that a finite-sized array has, it was expected that some travel paths were more useful than others for estimating flow speed. From the linear fits shown in Fig. 6.8 it was possible to conclude that the measurements related to the travel paths with 5 and 6 bounces within the pipe wall were the most appropriate to combine for improving the precision of the flow estimates. Moreover, the same conclusion was drawn when SNR (amplitude) levels were compared for all travel paths (see Fig. 6.9).

The combination of the travel paths related to 5 and 6 bounces reported flow speeds that correlated even better with the reference values (see Fig. 6.10a and compare to Fig. 6.7a).

Another way to represent the uncertainty of flow meters is by computing the relative error e_r, defined as
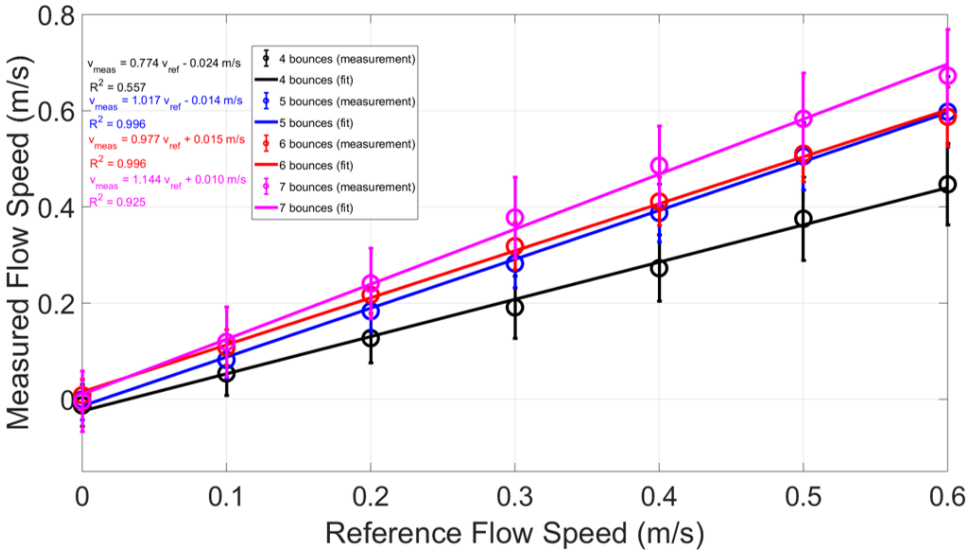
Figure 6.8: Measured vs. reference flow speed of water considering compressional waves in the pipe wall and the travel paths for 4, 5, 6 and 7 bounces of the beam within the pipe wall.

6

$$e_r = 100 \frac{v_{\text{meas}} - v_{\text{ref}}}{v_{\text{ref}}}, \qquad (6.2)$$

as a function of the Reynolds number (Re), defined as
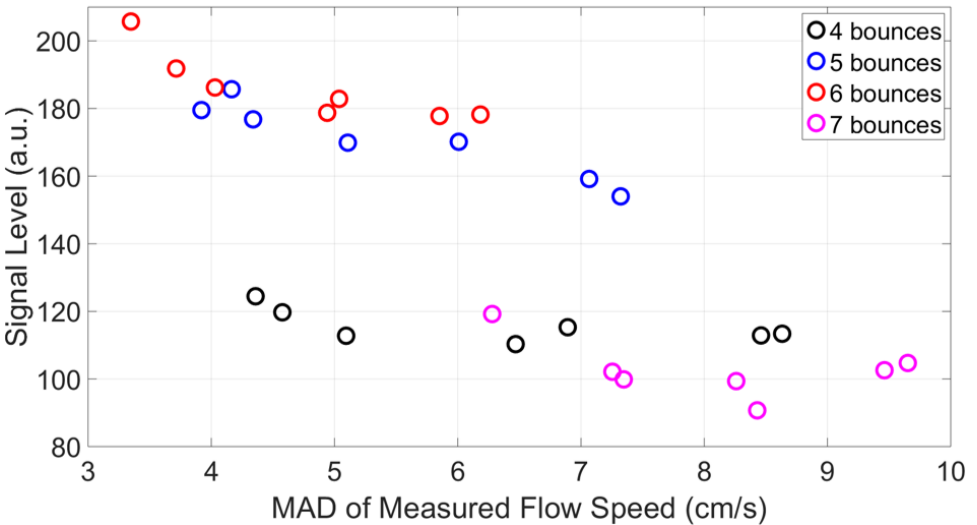
Figure 6.9: Measured SNR levels as a function of the median absolute deviations for the different travel paths shown in Fig. 6.3a. Each travel path reports the values for the seven measured flow speeds.
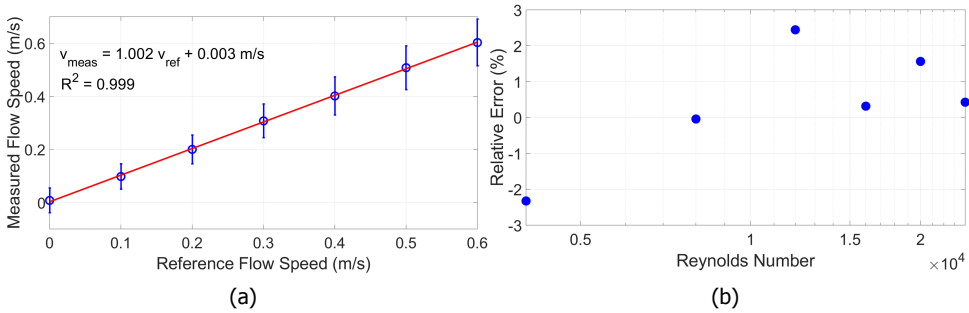
Figure 6.10: (a) Measured vs. reference flow speed of water considering compressional waves in the pipe wall and the combined information of the travel paths indicated in Fig. 6.3a and associated to 5 and 6 bounces within the pipe wall before being recorded by the linear arrays. (b) Relative error as a function of the Reynolds number reported by flow speeds estimated with the combination of the previously mentioned travel paths.

$$Re = \frac{\rho v_{meas} D}{\mu},\tag{6.3}$$

where v_{meas} represents the measured flow speed, v_{ref} represents the reference flow speed value, ρ is the density of the fluid ($1000\,kg/m^3$ for water), D is the inner diameter of the pipe, and μ is the dynamic viscosity of the liquid ($1\,mPa.s$ for water).

This relation is shown in Fig. 6.10b, and reported relative flow speed errors below $2\,\%$.

6.7. Monitoring the zero-flow error

It is always important to study the stability of a flow metering system through time because there are different factors that may dynamically affect reciprocity, such as temperature changes of the surrounding environment or the flowing medium and/or the nonlinear behavior of transducers and the electronic components of the sensor. Therefore, to realize whether these factors have a significant effect on the flow speeds measured with the fabricated sensor shown in Fig. 6.1, the same sensor was used to measure flow speed at zero-flow reference conditions for a relatively long period of time.

6.7.1. At room temperature

A 24h-monitoring of the flow speed was performed using both measurement modes: a compressional wave (see Fig. 6.11) and a shear wave in the pipe wall (see Fig. 6.12). Each flow speed measurement, i.e. upstream-downstream signal pair, together with a reference measurement, was taken every second in intervals of $30\,min$ during a $24\,h$ period. Between each measurement interval there was a gap of $\approx 10\,min$ due to buffer memory limits and re-initialization of the acquisition machine.

The spread of the measured data points considering a compressional wave (Fig. 6.11) was wider compared to those obtained considering a shear wave (Fig. 6.12), which was expected from the measured uncertainties shown in Fig. 6.7. Nevertheless, for both scenarios, a moving median of these measurements was computed taking into account 300 data points, i.e. corresponding to a $5\,\mathrm{min}$ measurement interval, to visualize in a more practical way any potential drifts of the zero-flow error through time. From these, no significant drift of the flow measurements was observed, and the recorded variations were within the same order as those recorded with the reference flow meter. These measurements lead to conclude that the fabricated ultrasonic clamp-on flow meter system of Fig. 6.1 was fairly stable.

Some quantitative analysis also explained these measurements and lead to the same conclusion. Considering the scenarios of Fig. 6.11 and Fig. 6.12, the recorded temperature drifted by $\approx 0.4\,{}^{\circ}\mathrm{C}/24\mathrm{h}$ and $\approx 0.3\,{}^{\circ}\mathrm{C}/24\mathrm{h}$, respectively. The temperature change between an upstream and a downstream signal, sampled with a PRF of $87\,\mathrm{Hz}$ ($t = 11.5\,\mathrm{ms}$), was of $\approx 5.32\mathrm{x}10^{-8}\,{}^{\circ}\mathrm{C}$ and $\approx 3.99\mathrm{x}10^{-8}\,{}^{\circ}\mathrm{C}$, respectively. A typical temperature gradient of the sound speed of water [3] reports that, around the measured temperatures, the sound speed of water changes with a rate of $\approx 3\,\mathrm{m/s/{}^{\circ}C}$, which combined with the previous estimations of temperature change translates into a change of the sound speed of $\approx 15.97x10^{-8}\,\mathrm{m/s}$ and $\approx 11.98x10^{-8}\,\mathrm{m/s}$, respectively. These changes of the sound speed are insignificantly small to produce a visible effect in the change of the zero-flow error.

6
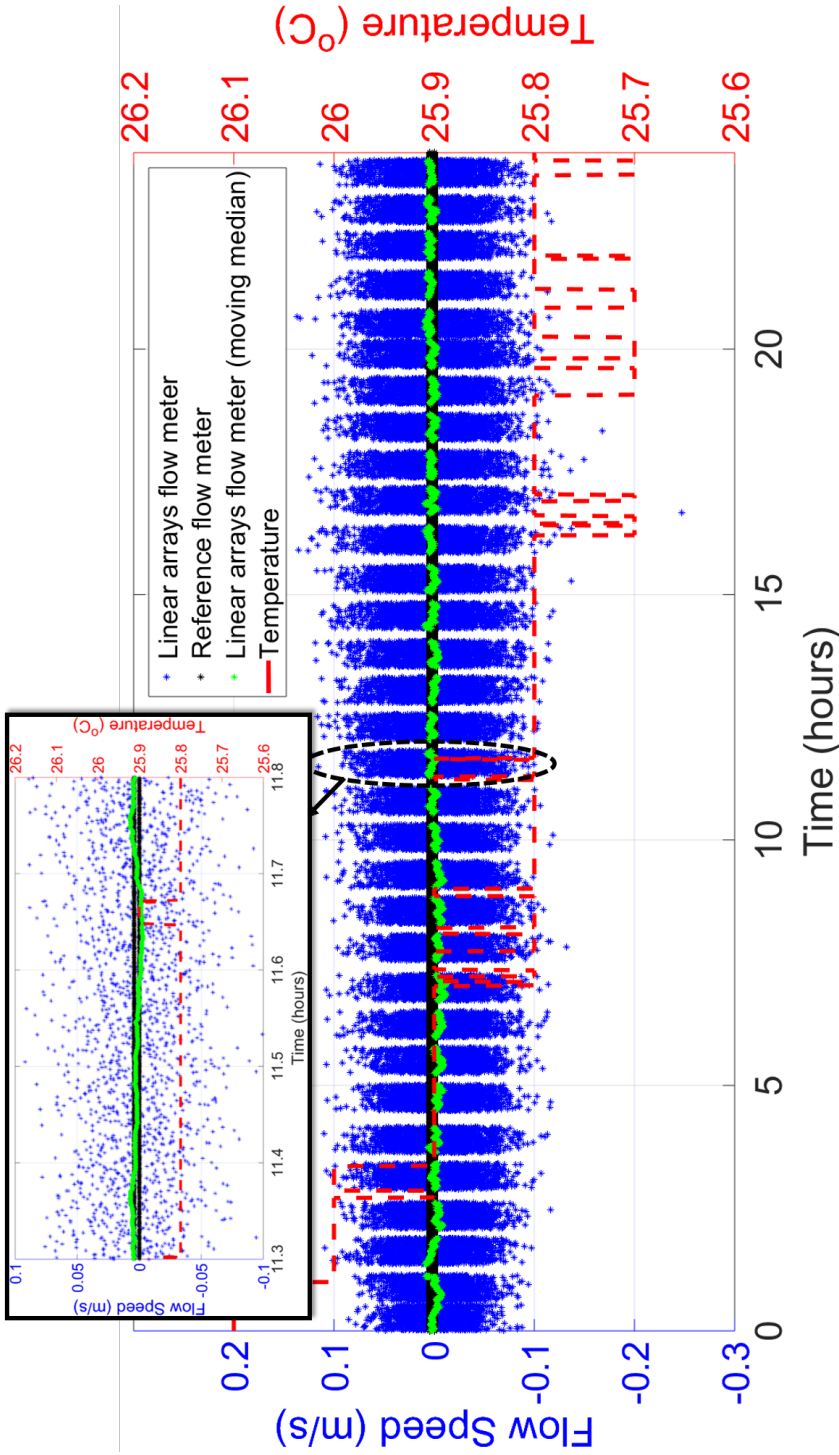
Figure 6.11: 24 h-monitoring of the flow speed at zero-flow conditions, measured with the fabricated sensor shown in Fig. 6.1 (blue) considering a compressional wave in the pipe wall (travel path of Fig. 2.4a), and with a reference flow meter (black). In green is shown a moving median of the measured flow speeds with the fabricated sensor considering a time window of 300 points (i.e. 5 min). A temperature log of the water is shown in red.

6
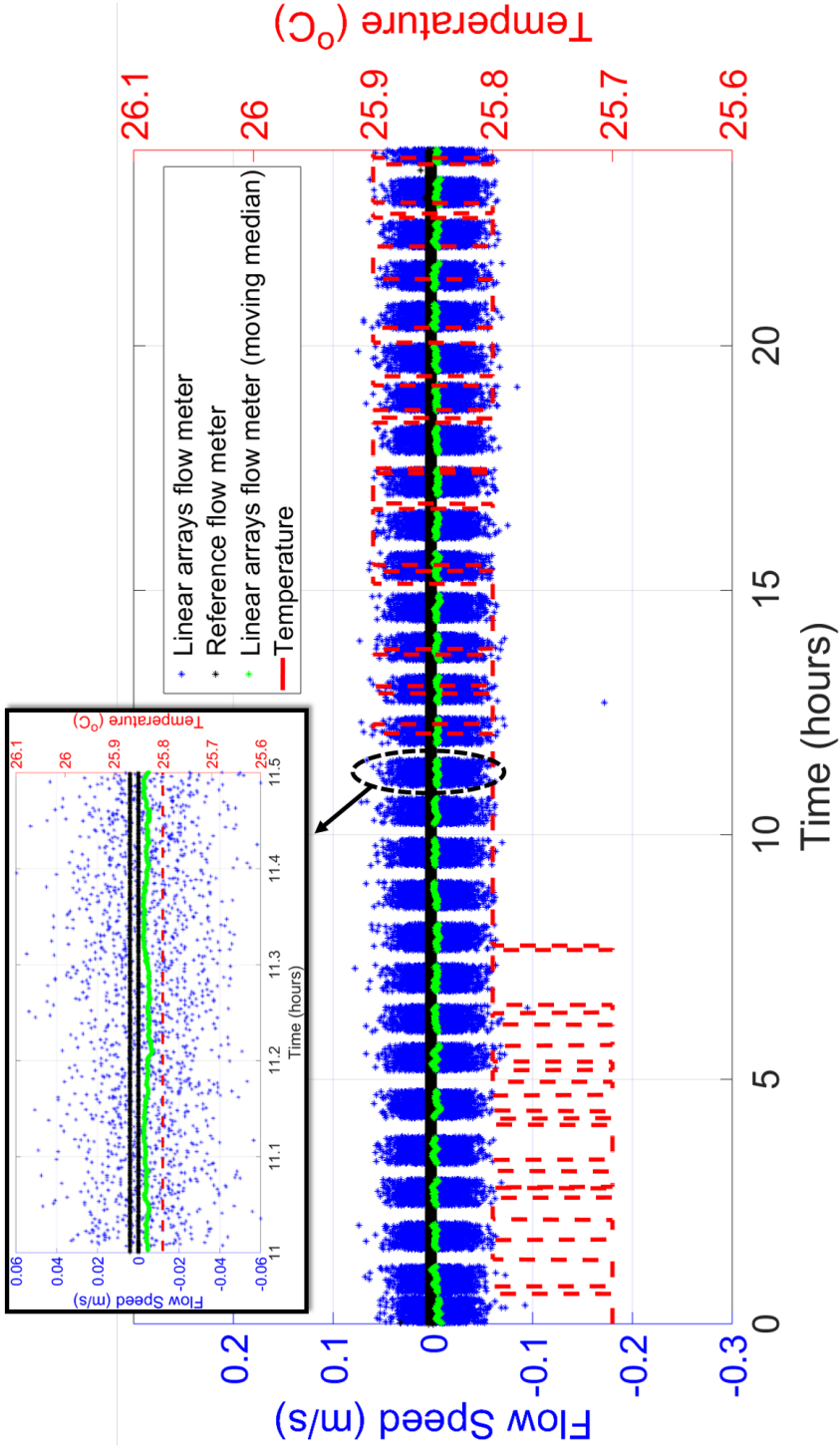
Figure 6.12: 24 h-monitoring of the flow speed at zero-flow conditions, measured with the fabricated sensor shown in Fig. 6.1 (blue) considering a shear wave in the pipe wall (travel path of Fig. 2.4b), and with a reference flow meter (black). In green is shown a moving median of the measured flow speeds with the fabricated sensor considering a time window of 300 points (i.e. 5 min). A temperature log of the water is shown in red.

6.7.2. Heating the liquid

The stability of the built ultrasonic clamp-on flow metering system shown in Fig. 6.1 was tested even further by directly heating the water in the flow loop. In this way it could be assessed whether the flow speeds, measured at zero-flow reference conditions, report a dynamic drift due to changes in the sound speed of the liquid.

To perform this measurement, a heater was placed on the top water tank of Fig. 6.1, and a low flow speed of $v_f = 0.1\,\mathrm{m/s}$ was induced to transfer the heat more easily to the flow loop. This process increased the temperature of the water from $\approx 32\,^\circ\mathrm{C}$ to $\approx 46\,^\circ\mathrm{C}$ (see Fig. 6.13). Some pipe sections of the flow loop consisted of acrylic and PVC, therefore, for safety purposes, the heater was turned-off and temperature was not increased further. This heating process lasted $\approx 3\,\mathrm{h}$. At this point, the valve of the flow loop was closed, the water temperature started to decrease, and flow speed continued to be measured at zero-flow reference conditions for $\approx 3.5\,\mathrm{h}$ more.

From the recorded temperature log in Fig. 6.13, it could be observed that water was being heated at a rate of $\approx 4.67\,^\circ\mathrm{C/h}$. Considering the $11.5\,\mathrm{ms}$ of sampling time between an upstream and a downstream signal, the temperature change of the water between these measurements was estimated to be $\approx 1.49\mathrm{x}10^{-5}\,^\circ\mathrm{C}$, and given that its sound speed gradient is $\approx 3\,\mathrm{m/s/^\circ c}$, this translates into a change in the sound speed of only $\approx 4.48x10^{-5}\,\mathrm{m/s}$ which, as also reported in the previous section, is an extremely low value for temperature changes in the liquid to play a significant role in the stability of the flow speeds recorded with the fabricated sensor.

6.8. Discussion

Flow speeds measured considering compressional waves in the pipe wall (Fig. 6.10a) were comparable, in terms of uncertainty, to those considering shear waves in the pipe wall (Fig. 6.10b). In terms of SNR, the amplitudes of the time signals measured in the first scenario were $\approx 1.7\,\mathrm{dB}$ lower than the amplitudes of the time signals measured in the second scenario. This value is reasonably close to the $\approx 3.3\,\mathrm{dB}$ expected SNR difference from the theoretical calculations for water ($\alpha = 0.002\,\mathrm{dB/MHz.cm}$) shown in Fig. 2.7. Moreover, the proof that both measurement scenarios are possible opens the door to the possibility of deciding whether to operate the flow sensor by using either compressional or shear waves in the pipe wall. Since the travel paths for the former are usually much longer than for the latter, this last one would be more preferable for measuring the flow speed of highly attenuating liquids or gases. On the other hand, compressional waves in the pipe wall could be used when the length of the pipe section in which the sensor would need to be installed is very limited and only relatively small beam steering angles are possible.
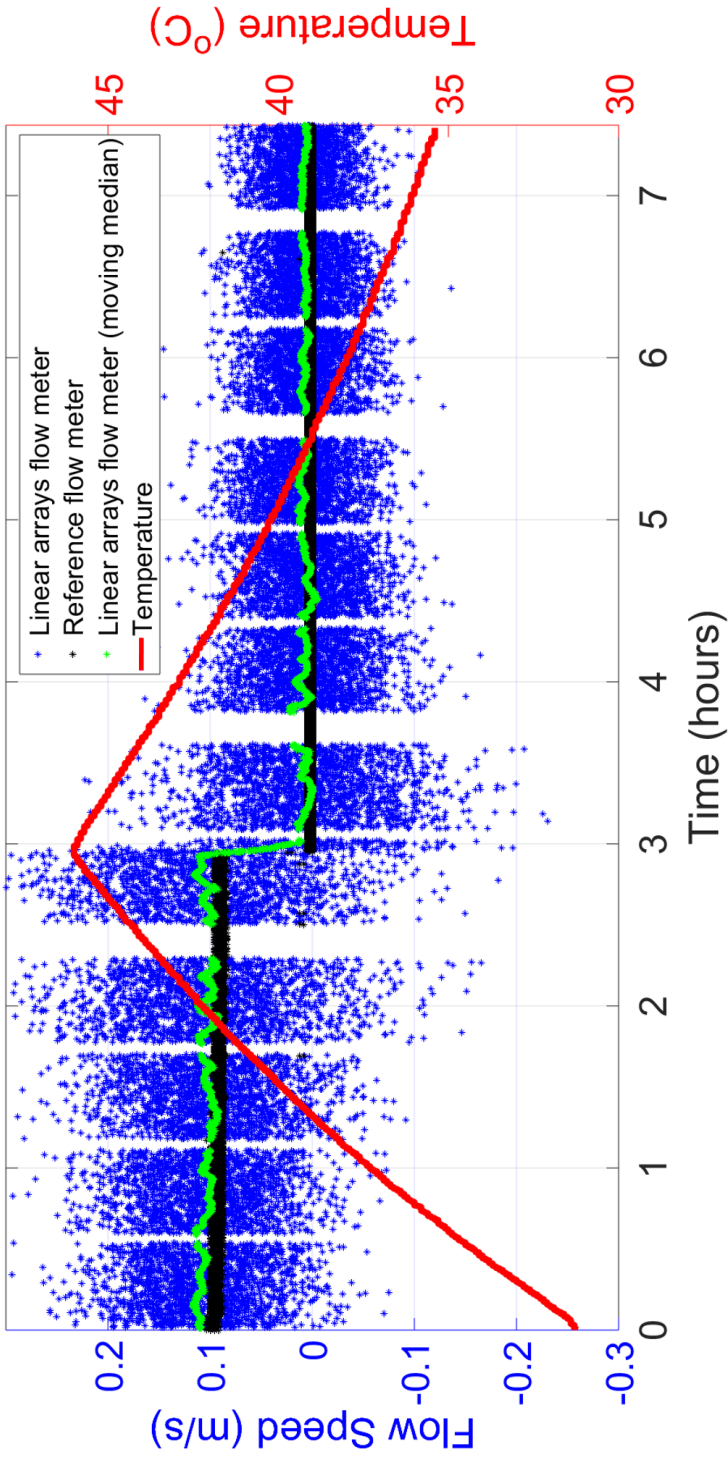
Figure 6.13: 7.5 h-monitoring of the flow speed measured with the fabricated sensor shown in Fig. 6.1 (blue) while heating the water. A shear wave in the pipe wall was considered (travel path of Fig. 2.4b). Reference flow speed measurements are shown in black, and a temperature log of the water is shown in red. In green is shown a moving median of the measured flow speeds with the fabricated sensor considering a time window of 300 points (i.e. 5 min).

Although the transducer array was designed to measure flow speed using an optimized acoustic beam that propagates through a specific travel path (see Fig. 2.4a), the finite-sized aperture of the array also allows for other travel paths which are also sensitive to the flow. Even though the SNR of these other travel paths is lower compared to that of the optimized beam (see Fig. 6.9), it was found that if their SNR is not too low, they can still be used in combination with the optimal travel path to achieve a more precise estimate of the flow speed.

6.9. Conclusion

Here, flow measurements with a fabricated ultrasonic clamp-on flow meter consisting of two linear arrays based on the matrix transducer design described in Chapter 2 were presented. A high degree of reciprocity of the built system was obtained: zero-flow transit time differences $< 1\,\mathrm{ns}$ were measured. Moreover, the correlation factor between measured and reference flow speed was > 0.99. Also, flow measurements were achieved using both compressional and shear waves in the pipe wall.

The potential of $f - k_x$ filtering of undesired wave modes was shown, which is a unique operation for array-based flow meters. Furthermore, it was demonstrated that different recorded travel paths could be combined to improve even further the flow speed estimations and decrease measurement uncertainty.

Finally, the proven beam steering capabilities and advanced processing demonstrated with linear arrays point towards matrix array-based flow meters being highly suitable for automated calibration procedures.

References

[1] J. Massaad, P. L. M. J. van Neer, D. M. van Willigen, E. C. Noothout, N. de Jong, M. A. P. Pertijs, and M. D. Verweij, *Design of a matrix transducer array for self-calibrated ultrasonic clamp-on flow measurements,* IEEE Trans. Ultrason. Ferroelectr. Freq. Control (submitted).

[2] M. Aanes, R. A. Kippersund, K. D. Lohne, K.-E. Frøysa, and P. Lunde, *Time-of-flight dependency on transducer separation distance in a reflective-path guided-wave ultrasonic flow meter at zero flow conditions,* J. Acoust. Soc. Am. **142**, 825 (2017).

[3] W. D. Wilson, *Speed of sound in distilled water as a function of temperature and pressure,* J. Acoust. Soc. Am. **31**, 1067 (1959).

6

7

Exploiting nonlinear wave propagation to improve the precision of ultrasonic flow meters

Acoustic wave propagation in ultrasonic flow measurements is typically assumed to be linear and reciprocal. However, if the transmitting transducer generates a sufficiently high pressure, nonlinear wave propagation effects become significant. In flow measurements, this would translate into more information to estimate the flow and therefore a higher precision relative to the linear case. Here, it is investigated how the generated harmonics can be used to measure flow. Measurements in a custom-made flow loop and simulations using the Khokhlov-Zabolotskaya-Kuznetsov (KZK) equation will show that the second harmonic component provides similar transit time differences to those obtained from the fundamental component, their linear combination results in more precise flow measurements compared to the estimations with the fundamental component alone.

7.1. Introduction

Ultrasound is a common modality to measure flow in an industrial setting. There are two types of ultrasonic flow sensors: in-line sensors and clamp-on sensors. The first configuration usually consists of a perforated pipe section with aligned pairs of transducers in direct contact with the flow (Fig. 7.1a), and the second configuration typically consists of a pair of single element transducers that are fixed on the outside of the pipe wall (Fig. 7.1b). In either configuration, the propagation direction of the acoustic waves generated by the transducers has a component parallel to the pipe axis, which makes the travel time of the waves sensitive to the flow [3]. As a result, the acoustic wave with a propagation component in the direction of the flow (downstream) travels faster than the one that propagates with a propagation component in the opposite direction of the flow (upstream). The ultrasonic flow meter system (including acoustic waves, transducers, and electronics) is assumed to be reciprocal, which means that, in the absence of flow, the system response remains unchanged when the role of transducers A and B are interchanged. Moreover, linear flow theory is assumed, i.e. the transit time difference or phase difference between upstream and downstream waves is directly proportional to the flow speed [4].

Provided that both upstream and downstream time pulses $s_u(t)$ and $s_d(t)$ have a the same shape but show a relative time difference, their cross-correlation will have a peak at a time instant that corresponds to the delay between both signals. The cross-correlation algorithm is often implemented to measure flow speed [5–8] because it has a low sensitivity to the random (thermal) noise occurring in the flow, the electrical components, and the transducers in typical ultrasonic flow meter systems [8, 9].

However, the precision of cross-correlation algorithms in estimating transit time differences is limited by factors such as the total available bandwidth of the system, and the length and signal-to-noise ratio (SNR) of the applied time pulses [11]. In practice, the bandwidth of the system cannot be increased since it depends on the properties of the installed transducers. Also, the frequency dependent amplitude

(a)   (b)
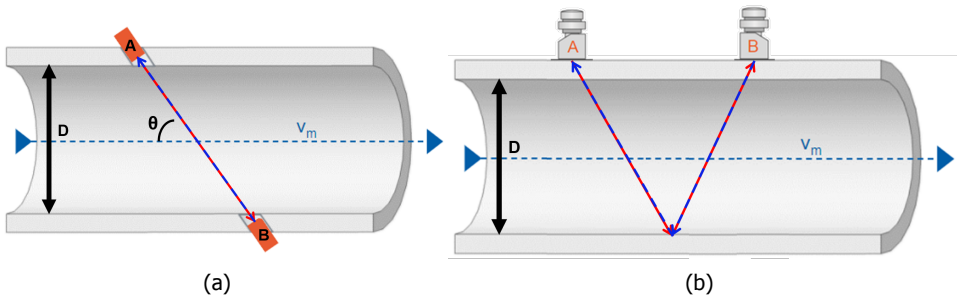
Figure 7.1: Ultrasonic (a) in-line and (b) clamp-on flow meter configuration. A liquid moves from left to right with a flow speed v_m within a pipe with an inner diameter D. The solid red and dashed blue arrows indicate the downstream and upstream travel paths of the acoustic beams generated by transducers A and B, respectively. Modified from [10].

behavior of the system causes challenges in generating long coded excitations that perform favorable with cross-correlation algorithms, e.g. chirps.

It is often implicitly assumed that during ultrasonic flow measurements acoustic wave propagation is linear (this should not to be confused with linearity of the flow speed metering). However, it is well known from the acoustic literature that wave propagation is actually a nonlinear phenomenon [12]. At sufficiently high pressures, nonlinear wave propagation effects become significant and the resulting harmonics may be recorded when these fall within the bandwidth of the system. In practice, from each recorded time signal two versions can be extracted by filtering: one with a frequency band centered around the fundamental (transmitted) frequency, and another one with a frequency band centered around the second harmonic (twice the transmitted) frequency. To the best of the authors' knowledge, the extra frequency band generated by nonlinear wave propagation is not used in current ultrasonic flow meter designs.

Here, it will be shown that in a realistic flow metering system a higher pressure in the fundamental frequency band will lead to nonlinear wave propagation. Furthermore, it is also tested the hypotheses that the second harmonic frequency band may also be used to estimate the flow speed, and that this increases the total number of flow estimates, which improves flow measurement precision. Also, some challenges that are imposed by applying nonlinear wave propagation will be discussed.

7.2. Theory

In this section, linear ultrasonic flow metering theory is presented. Moreover, the KZK equation for modeling nonlinear acoustic wave propagation is described. In ultrasonic flow metering, acoustic waves propagate under an angle relative to the flow direction (see Fig. 7.1). In contrast, the KZK equation provides the acoustic wavefield parallel to the propagation axis of the wave. Therefore, the assumptions and approximations that make it possible to use the KZK equation to model nonlinear wave propagation in an ultrasonic flow metering scenario are also presented.

7.2.1. Linear ultrasonic flow metering

A typical configuration of a flow metering system is shown in Fig. 7.1a. Two single-element transducers, in direct contact with the flow and facing each other under a certain angle θ relative to the direction of the flow, i.e. the pipe axis, are excited and the transit time of the respective upstream (t_u) and downstream (t_d) acoustic waves is given by [4]

$$t_u = \frac{D}{\sin\theta}\frac{1}{c_0 - v_m\cos\theta},$$
$$t_d = \frac{D}{\sin\theta}\frac{1}{c_0 + v_m\cos\theta},$$

(7.1)

where D represents the inner diameter of the pipe, c_0 represents the small-signal sound speed of the fluid, and v_m represents the flow speed. Combining the

expressions of Eq. 7.1, a linear relation between the flow speed, and the transit time difference Δt is obtained

$$v_m = \frac{D}{\sin 2\theta} \frac{t_u - t_d}{t_u t_d} = \frac{c_0^2 \tan \theta \, \Delta t}{2D}. \tag{7.2}$$

In the last step a quadratic term in v_m has been neglected because it can be assumed that $v_m \ll c_0$ (see Appendix A).

7.2.2. Nonlinear acoustic wave propagation

Diffraction, absorption and nonlinearity effects of a beam-like wave generated by a transducer can be simulated using the parabolic approximation of the wave equation provided by the Khokhlov-Zabolotskaya-Kuznetsov (KZK) equation. In Cartesian coordinates, the 3D-KZK equation can be expressed as

$$\frac{\partial p}{\partial z} = \frac{c_0}{2} \int_{-\infty}^{t'} \left(\frac{\partial^2 p}{\partial x^2} + \frac{\partial^2 p}{\partial y^2} \right) dt'' + \frac{\delta}{2c_0^3} \frac{\partial^2 p}{\partial t'^2} + \frac{\beta}{2\rho_0 c_0^3} \frac{\partial p^2}{\partial t'}. \tag{7.3}$$

In Eq. 7.3, $p = p(x, y, z, t')$ represents the acoustic pressure in the medium, z the axial coordinate (perpendicular to the transducer surface), x and y the lateral coordinates (parallel to the transducer surface), $t' = t - \frac{z}{c_0}$ the retarded time with t begin the actual time, δ the diffusivity of sound of the medium, ρ_0 the density of mass of the medium, and β the coefficient of nonlinearity of the medium, defined as

$$\beta = 1 + \frac{B}{2A}, \tag{7.4}$$

where B/A is known as the parameter of nonlinearity.

Different methods to solve Eq. 7.3 have been proposed [13–17]. Usually, a transformation of Eq. 7.3 is performed [16]

$$P = p/p_0, \quad \chi = x/r, \quad \psi = y/r, \quad \sigma = z/d, \quad \tau = \omega_0 t', \tag{7.5}$$

where p_0 is the maximum pressure at the surface of the transducer, d is the characteristic range length (for which $d = 1\,\text{m}$ was taken), r is the characteristic transverse length (for which we have taken the transducer aperture), and ω_0 is the central angular frequency of the transmitted pressure pulse. Substituting the expressions of Eq. 7.5 into Eq. 7.3 yields

$$\frac{\partial P}{\partial \sigma} = \frac{1}{4G} \int_{-\infty}^{\tau} \left(\frac{\partial^2 P}{\partial \chi^2} + \frac{\partial^2 P}{\partial \psi^2} \right) d\tau' + A \frac{\partial^2 P}{\partial \tau^2} + NP \frac{\partial P}{\partial \tau}, \tag{7.6}$$

where the dimensionless coefficients G, A and N follow as

$$G = z_0/d, \quad A = \alpha_0 d, \quad N = d/\bar{z}, \tag{7.7}$$

where $z_0 = \omega_0 r^2 / 2c_0$ represents the Rayleigh distance, $\alpha_0 = \delta \omega_0^2 / 2c_0^3$ is the attenuation coefficient of the medium and $\bar{z} = \rho_0 c_0^3 / \beta \omega_0 p_0$ is the plane wave shock

formation distance. The first term at the right-hand side of Eq. 7.6 accounts for diffraction, the second term for absorption, and the third term for nonlinear behavior of the acoustic wave.

Here, the time-domain numerical approach developed by [16] to solve Eq. 7.6 was implemented.

Modeling assumptions and approximations

The propagation speed of a progressive nonlinear wave, propagating in the z-direction in a medium without flow is given by [12] as

$$\frac{dz}{dt} = c_0 + \beta u, \tag{7.8}$$

where u is the particle velocity, i.e. the velocity of the medium due to the acoustic wave. Substituting Eq. 7.4 into Eq. 7.8, it is possible to get

$$\frac{dz}{dt} = c_0 + \left(1 + \frac{B}{2A}\right)u = \left(c_0 + \frac{B}{2A}u\right) + u. \tag{7.9}$$

As reported in [12], assuming an isentropic (i.e. adiabatic) fluid, the term in parenthesis at the right-hand side of Eq. 7.9 is the large-signal sound speed of the medium, c, so

$$\frac{dz}{dt} = c + u. \tag{7.10}$$

Here it is seen that the propagation speed of the nonlinear wave is the sum of the large-signal sound speed and the motion of the medium induced by the acoustic wave. The latter can be compared to the 'wind effect' in outdoor sound propagation. In this work, it is assumed that the flow speed v_m adds linearly to the 'wind effect' term, so the total propagation speed of the wave is given by

$$\frac{dz}{dt} = c + u + v_m \cos\theta = (c_0 + v_m \cos\theta) + \beta u, \tag{7.11}$$

where θ represents the angle of propagation of the acoustic beam relative to the direction of the flow (i.e. the pipe axis). Comparison of the Eqs. 7.8 and 7.11 shows that the flow of the medium can be accounted for by adding a correction term to the small-signal sound speed of the medium.

Simulation settings

The following medium parameters were considered for the simulation of nonlinear wave propagation in water: $\rho_0 = 1000\,\mathrm{kg/m^3}$, $\alpha_0 = 0.002\,\mathrm{dB/MHz.cm}$, and $\beta = 3.5$. To account for the flow of the medium, the small-signal wave speed of the medium was taken as to be

$$c_0' = 1500\,\mathrm{m/s} \mp v_m \cos\theta, \tag{7.12}$$

with $\theta = 45°$ being the angle of the transducer axis relative to the flow direction. Furthermore, upstream and downstream wave propagation was considered by either taking the $-$ or the $+$ sign, respectively, in Eq. 7.12.

As source signature, a 5-cycle Gaussian-modulated sine wave, with a center frequency of $f_0 = 2.3\,\text{MHz}$, was used. Moreover, a spatial discretization of $\Delta\sigma = 0.06$ (equivalent to ≈ 10 points per wavelength) was defined and found to be sufficient to discard potential numerical dispersion effects in the solution of the KZK equation.

Considering a rectangular transducer aperture, the range of validity of the implemented solution of the KZK equation was reported in [18]

$$z > \sqrt{\frac{a^2 + b^2}{2}} \left(k \sqrt{\frac{a^2 + b^2}{2}} \right)^{1/3}, \tag{7.13}$$

where $2a$ and $2b$ are the dimensions of the rectangular aperture, and k represents the wavenumber. Here it has been chosen a transducer aperture of $12\,\text{mm}\times16\,\text{mm}$, which is equal to our design of a transducer for generating nonlinear waves in an ultrasonic flow meter. In this case, the range of validity of the KZK equation starts at a depth of $z > 29.8\,\text{mm}$. For a pipe with an inner diameter of $D = 40\,\text{mm}$, the implementation of [16] for solving the KZK equation is valid for simulating the ultrasonic flow measurement in the setting of Fig. 7.2.

7.3. Experimental study

7.3.1. Flow setup

A custom-made flow loop was built and filled with water (Fig. 7.2). Moreover, a custom flow sensor was built. It consisted of two single-element transducers
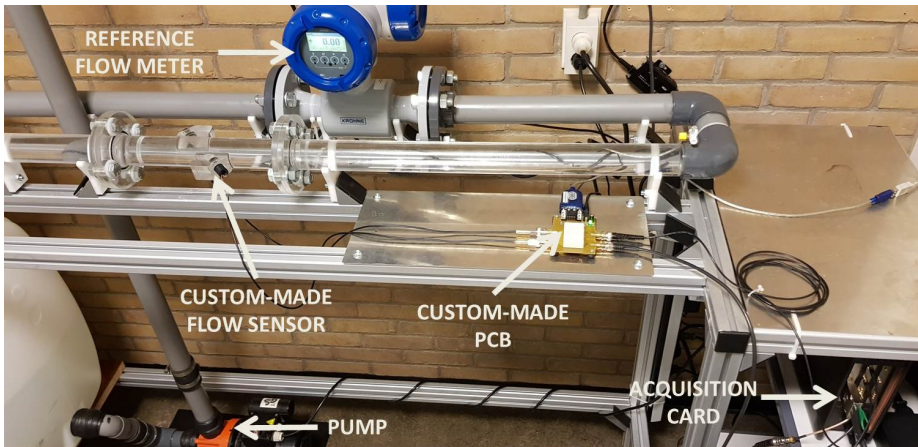
Figure 7.2: Custom-made flow loop for ultrasonic flow measurements. The custom-made flow sensor is installed in an acrylic pipe with an inner diameter of $40\,\text{mm}$. Flow moves through the sensor from left to right.

(V382, Olympus, Tokyo, JP) with a diameter of $12.7\,\mathrm{mm}$, a center frequency of $f_c = 3.5\,\mathrm{MHz}$, and a $-6\,\mathrm{dB}$ bandwidth between $2.24 - 4.42\,\mathrm{MHz}$. The transducers were placed $45°$ relative to the axis of a pipe with an inner diameter of $D = 40\,\mathrm{mm}$. Furthermore, a gear pump was used to hold-off air bubbles within the loop during flow measurements, because bubbles would have an adverse scattering effect on the ultrasound waves. With this configuration, it was possible to achieve flow speeds up to $v_m = 0.5\,\mathrm{m/s}$. Flow speed was also measured by a reference ultrasonic flow meter (Optosonic 3400, KROHNE Nederland B.V., Dordrecht, NL).

7.3.2. Data acquisition

A 5-cycle Gaussian-modulated sine wave with a center frequency of $f_c = 2.3\,\mathrm{MHz}$ and a peak-to-peak voltage of $0.6\,\mathrm{V}$ was generated using an arbitrary waveform generator (AWG; Agilent 33521A, Keysight Technologies, Santa Rosa, CA, USA), and amplified by a $50\,\mathrm{dB}$ amplifier (2100L RF Amplifier, Electronic Navigation Industries, Rochester, NY, USA), to achieve a signal with a peak-to-peak voltage of $180\,\mathrm{V}$. For larger voltages, nonlinearities of the electronic equipment were no longer negligible. The amplified signal was directed to a custom printed circuit board (PCB) that was built to perform a fast $50\,\mathrm{ms}$ switching between upstream and downstream flow measurements. The same amplified signal was also directed to an attenuator (Bench Top Attenuator, JFW Industries Inc., IN, USA) and then recorded simultaneously with the received signal by an acquisition card (M3i.4142 Spectrum Instrumentation GMbH, Großhansdorf, DE).

Five flow speeds were measured, and 1000 upstream and downstream signal pairs were recorded for each considered speed.

7.3.3. Signal processing

A flowchart of the signal processing algorithm developed to extract transit time differences is shown in Fig. 7.3, which includes the filtering of the bandwidth around the fundamental ($f_1 = 2.3\,\mathrm{MHz}$) and second harmonic ($f_2 = 4.6\,\mathrm{MHz}$) of the recorded signals. This processing scheme was implemented on the 1000 upstream-downstream signal pairs recorded for each flow speed. Finally, an average transit time difference was estimated from the fundamental frequency band ($1000\,\Delta t_{f1}$ values), the second harmonic frequency band ($1000\,\Delta t_{f2}$ values), and the combined fundamental and second harmonic bands ($1000\,\Delta t_{f1}$ and $1000\,\Delta t_{f2}$, i.e. 2000 values).

7.3.4. Results and discussion

A typical measured signal is shown in Fig. 7.4a. Furthermore, the magnitude of its Fast Fourier Transform (FFT) in Fig. 7.4b clearly shows a second harmonic component centered at $4.6\,\mathrm{MHz}$ generated by nonlinear wave propagation, with an amplitude approximately $24\,\mathrm{dB}$ below that of the fundamental component. If the fundamental frequency is chosen in the lower part of the frequency band of the transducer, the second harmonic frequency could be recorded in the upper part of the frequency band of the same transducer. This approach has been followed for the measurements. Moreover, SNR was limited by random noise and not by spurious acoustic signals (e.g. guided waves propagating in the pipe wall) that introduce
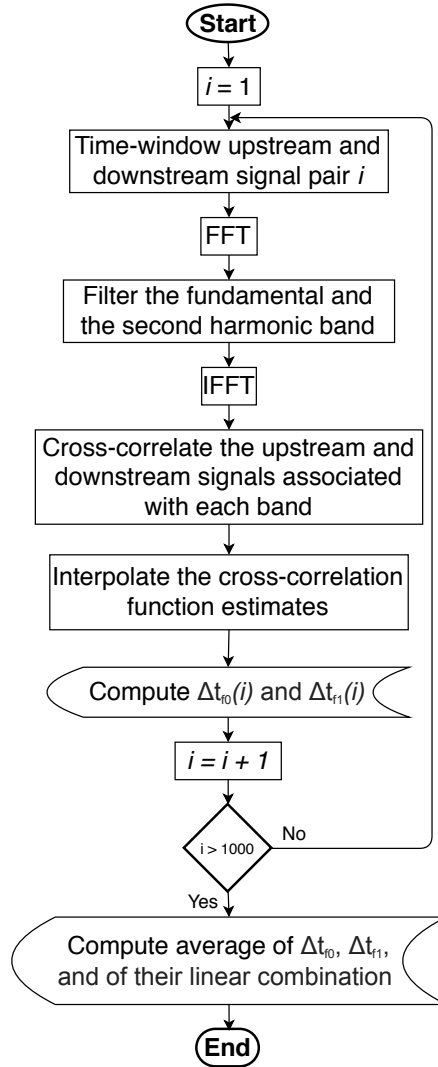
Figure 7.3: Signal processing scheme implemented to extract transit time difference from the 1000 upstream-downstream measured time signal pairs recorded for each considered flow speed.

offset errors and cannot be averaged out in the measurements.

For upstream and downstream time signals related to the second harmonic, the only non-reciprocal factor was the flow speed. Thus, regardless of their difference in amplitude and in transit time of the second harmonic components relative to the unfiltered time signals, it was expected for their relative transit time difference (Δt_{f2}) to be similar to that associated with the fundamental components (Δt_{f1}). This approach has been followed for the measurements. Results in Fig. 7.5a show
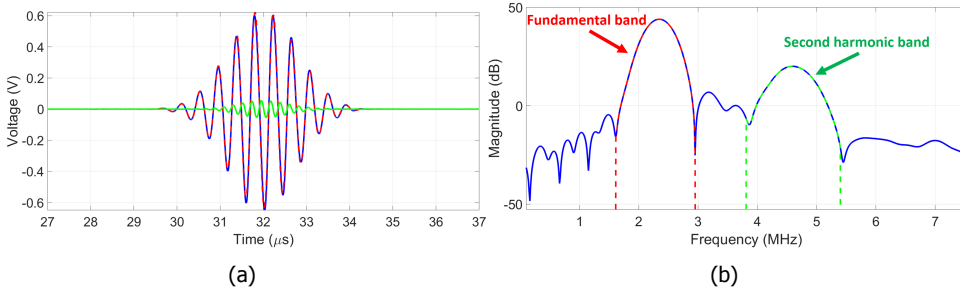
Figure 7.4: (a) A measured nonlinear time signal during flow measurements (blue), as well as its fundamental (red) and second harmonic (green) components. (b) Magnitude of the Fast Fourier Transform (FFT) applied on the time signal shown in (a).

that the transit time differences computed from the second harmonic are indeed similar to those of the fundamental. Therefore, when both estimates are used, the standard deviation of the flow estimate becomes lower than the one obtained using only the fundamental or the second harmonic, as confirmed by Fig. 7.5b. The linear fit on the measured data reported a coefficient of determination of $R^2 = 0.9999$.

In ultrasonic flow metering of very high flow speeds, i.e. when v_m is comparable to c, the upstream and downstream effective wave speeds are very different, as seen from Eq. 7.11. Therefore, it is expected that each signal would distort very differently relative to the other. Moreover, the quadratic term discarded in Eq. 7.2 may no longer be omitted (see Appendix A), and the transit time difference estimations would not follow the expected linear trend with flow speed observed in Fig. 7.5a. Since it was not possible to achieve higher flow speeds in the flow loop, nonlinear wave propagation simulations were performed to cross-check the linear results of Fig. 7.5a, and to study the effect of very high flow speeds on transit time difference estimations.
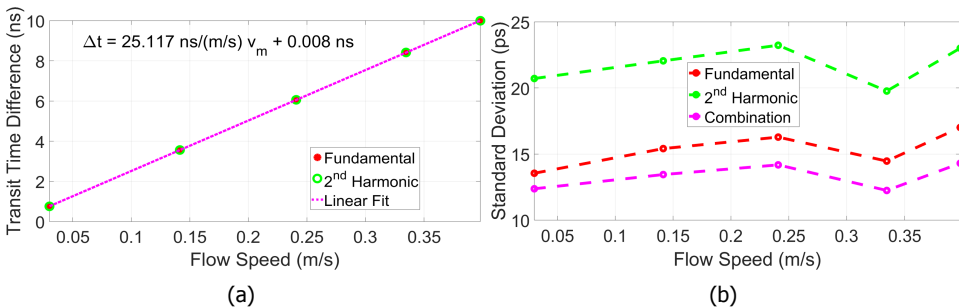
Figure 7.5: (a) Measured linear relation between transit time difference and flow speed, for both the fundamental and the second harmonic of the time signals. (b) Standard deviations of the computed transit time differences for the fundamental, the second harmonic, and their combination.
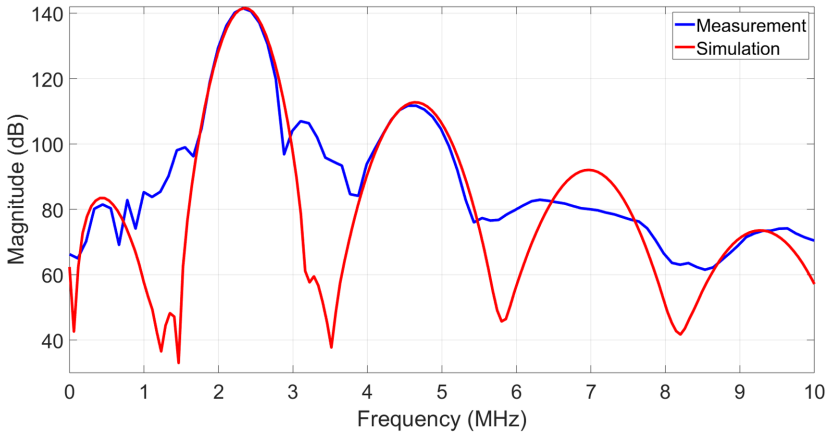
Figure 7.6: Magnitude of the FFT performed on received signals for the measured (blue) and simulated (red) waveforms, for the simulation parameter $p_0 = 0.2\,\mathrm{MPa}$ that gives the best overlap.

7.4. Simulation study

In the simulations, the parameter p_0 had to be chosen properly to achieve a good correspondence between the measured and simulated pressures. The value of this parameter was determined by comparing the magnitude of the FFT of a measured time signal with that of a simulated one. The best possible overlap of both spectra was achieved with a value of $p_0 = 0.2\,\mathrm{MPa}$ (Fig. 7.6).

Using this value and the previously defined simulation parameters, low and high flow speed scenarios were simulated. In view of the considered pipe diameter, values of $v_m > 0.5\,\mathrm{m/s}$ were labeled as high flow speeds.

7.4.1. Low flow speeds

Five flow speeds between $v_m = 0.1\,\mathrm{m/s}$ and $v_m = 0.5\,\mathrm{m/s}$ were considered, which covers the range of the measurements in Fig. 7.5a. After applying the same signal processing scheme as for the measurements, similar results were obtained (see Fig. 7.7). The transit time differences estimated using cross-correlation, and the flow speeds computed via Eq. A.7 reported deviations (relative errors) from the theoretically expected values of less than $0.04\,\%$ (see Fig. 7.8).

7.4.2. High flow speeds

Equation 7.2 suggests that the transit time difference increases with flow speed in a linear manner. However, if the flow speed becomes comparable to the small-signal sound speed, the approximation used in the last part of Eq. 7.2 will no longer be valid and the linearity between Δt and v_m will no longer hold. Thus, Eq. A.7 should be the one to be considered. In addition, Eq. 7.12 shows that the speed c'_0 of the upstream and downstream waves will differ significantly if the flow speed is of the same order as the small-signal sound speed. As a result of this, the upstream and downstream waves will undergo a different amount of nonlinear deformation. To
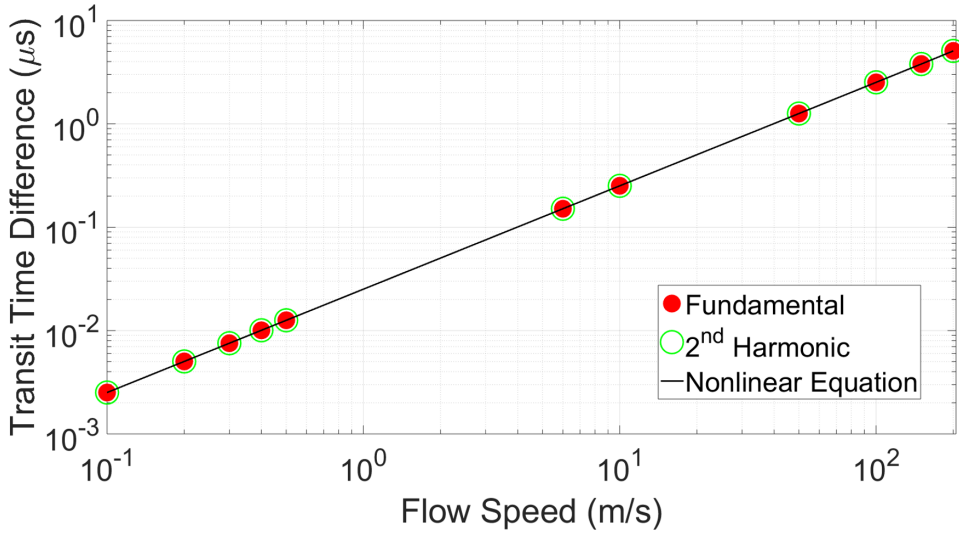
Figure 7.7: Simulation results of transit time difference as a function of flow speed, as obtained from the fundamental (dots) and the second harmonic (circles). The black line represents the theoretical nonlinear relation between both quantities, given by Eq. A.7.

simulate this scenario, flow speeds of $6\,\mathrm{m/s}$, $10\,\mathrm{m/s}$, $50\,\mathrm{m/s}$, $100\,\mathrm{m/s}$, $150\,\mathrm{m/s}$ and $200\,\mathrm{m/s}$ were considered.

Similarly to the scenario of low flow speeds, the transit time differences estimated via cross-correlation and the computed flow speeds using Eq. A.7 reported comparable deviations, which were also below $0.04\,\%$ (see Fig. 7.8). Due to the nonlinear relation between Δt and v_m, the error in the flow speed for the highest considered value (i.e. $v_m = 200\,\mathrm{m/s}$) is slightly lower than the error in the transit time difference.
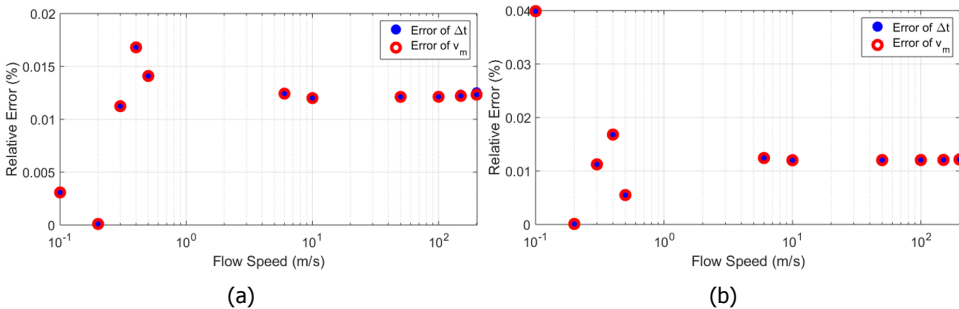
Figure 7.8: Relative error between theoretically expected values and those extracted from (a) the fundamental and (b) the second harmonic band of the time signals obtained from KZK simulations. Blue bullet points and red circles represent the errors of the transit time difference and the flow speed, respectively.

Furthermore, it was also observed that for increasing flow speed, the nonlinear distortion increases for the upstream wave and decreases for the downstream wave (see Fig. 7.9, particularly the increase (decrease) in the magnitude of the Fourier spectra associated to the upstream (downstream) time signals obtained when considering $v_m = 200\,\mathrm{m/s}$, relative to their spectra when considering low flow speeds). We thus see that this effect is non-reciprocal for upstream and downstream signals.

7.4.3. The effect of nonlinear wave propagation

Already from Fig. 7.8 it may be interpreted that the nonlinearity due to wave propagation has an insignificant contribution in the discrepancy of Δt and v_m with the ground truth. Nevertheless, we performed KZK simulations considering the same range of flow speeds, an initial pressure of $p_0 = 0.2\,\mathrm{kPa}$ (i.e. 1000x smaller than in previous simulations), and did not consider the nonlinear term of Eq. 7.3. As expected, the obtained errors in Δt and v_m were comparable to those shown in Fig. 7.8a.
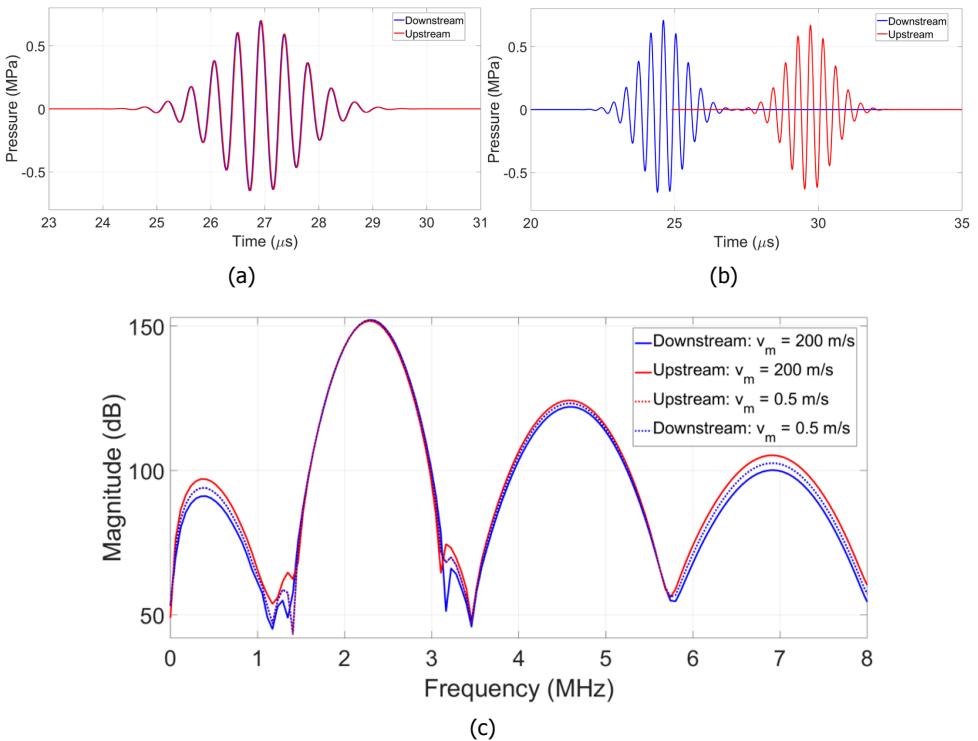
Figure 7.9: Simulated upstream and downstream nonlinear time signals considering flow speeds of (a) $v_m = 0.5\,\mathrm{m/s}$ and (b) $v_m = 200\,\mathrm{m/s}$. (c) Magnitude of the Fourier spectra of the signals shown in (a) and (b).

7.5. Discussion

Nonlinear wave propagation applied to ultrasonic flow measurements is beneficial because the second harmonic upstream and downstream signals provide additional flow speed estimations that can increase the precision of the measurement. However, nonlinear propagation is non-reciprocal for upstream and downstream waves at nonzero flow because these experience a different wave speed. This becomes manifest when the flow speed cannot be considered small relative to the small-signal sound speed. Moreover, for these higher flow speeds linear flow theory, i.e. the linear relation between transit time difference Δt and flow speed v_m given in Eq. 7.2, no longer holds.

Next, it is further elaborated on the limitations of the method presented here, and also discussed how it could be implemented in practice.

7.5.1. Transit time difference between non-reciprocally distorted signals

Cross-correlating two signals, e.g. an upstream and a downstream flow measurement, to estimate their transit time difference is performed under the assumption that the shape of the signals is the same. During nonlinear wave propagation, the waveform deforms with distance. For low flow speeds, the signals obtained with simulations and measurements report a very similar degree of distortion, as seen in the overlapping Fourier spectra in Fig. 7.9c when considering $v_m = 0.5\,\mathrm{m/s}$. Therefore, in this case it was reasonable to assume that both signals had the same shape and the determination of the transit time difference was not influenced by the nonlinear propagation. In contrast, the Fourier spectra in Fig. 7.9c when considering high flow speeds ($v_m = 2000\,\mathrm{m/s}$) clearly show that waveform distortion is different for upstream and downstream signals because of the different large-signal wave speed c'_0 in both cases. On the other hand, a zero-crossings approach also reported a nonlinear relation between transit time difference and flow speed, which was also observed by [19] in simulations considering high flow speeds of gas.

7.5.2. SNR and standard deviation

In most acoustic flow measurement systems, the signal-to-noise ratio (SNR) is limited by the thermal noise of the transducers and the electronic components. Because the fundamental and second harmonic frequency bands do not overlap, the noise in these frequency bands can be considered as being uncorrelated. On the other hand, the second harmonic signal is directly related to the fundamental signal, but it has a smaller amplitude, and thus a lower SNR than the fundamental signal. Therefore, it is still up for debate whether addition of measurement points derived from the second harmonic achieves a $\sqrt{2}$ better precision of flow measurements. To answer this question, the trade-off between the SNR of the fundamental and that of the second harmonic should be investigated in more detail to further delineate the conditions under which useful flow measurements may be performed with separate consideration of the second harmonic.

Given that the standard deviation of an acoustic measurement is proportional

7. Exploiting nonlinear wave propagation to improve the precision of
ultrasonic flow meters
138

to the available system bandwidth and the length of the pulse [20], it could be argued that, instead of using the fundamental and second harmonic in a system with nonlinear wave propagation, spikes or chirps could be used in a linear system to achieve the same standard deviation. However, the inherently limited bandwidth of ultrasound transducers and a further bandwidth reduction caused by the frequency content of the flow noise and the attenuation of the medium [21], make it challenging to achieve broadband input signals such as spikes (e.g. a Dirac δ pulse) or chirps in practice. Also, it becomes challenging to produce a chirp with practical amplifiers that always show some degree of nonlinear behavior and a frequency-dependent amplification factor. Furthermore, for such amplifiers the complexity, and therefore the cost, is proportional to the bandwidth.

7.5.3. Practical implementation

Generally, there is a high difference between the acoustic impedance of the transducer and the flowing medium, especially in a gas flow metering setting [22]. Therefore, the main practical measure being taken to achieve the required SNRs, is to increase the input voltage on the transducers [23]. By doing so, the amplitude of the fundamental could increase to such a level that a second harmonic is generated due to nonlinear wave propagation. As a consequence, more information is retrieved with the same transducers, provided these have sufficient bandwidth to record both the fundamental and the second harmonic.

Ultrasonic flow meters are designed for the most attenuating liquid/gas that can be expected in the pipeline. Therefore, in less extreme situations, the electric system of the sensor is actually overdimensioned and, within the typical safety limits, is able to provide increased amplitudes of the fundamental that will induce significant nonlinear wave propagation. Hence, in practice it seems feasible and beneficial to use nonlinear wave propagation to extract more information from the measurements and thus achieve more precise flow estimates than with the fundamental signal alone.

Finally, even though the idea presented here has been implemented with inline flow meters, considering the same assumptions, it could be implemented in clamp-on flow meters as well.

7.6. Conclusion

Here, it has been introduced a method to employ nonlinear wave propagation for measuring flow speed in liquids. Using nonlinear wave propagation, the number of flow estimates per measurement, and thus the measurement precision, can be increased. At low flow speeds, good agreement was obtained between measurements and simulations. At high flow speeds, the simulations showed a deviation from the linear relation between the transit time difference and the flow speed, which was caused by the nonreciprocal behavior of the upstream and downstream nonlinear waves.

References

[1] J. Massaad, P. L. M. J. van Neer, D. M. van Willigen, N. de Jong, M. A. P. Pertijs, and M. D. Verweij, *Exploiting nonlinear wave propagation to improve the precision of ultrasonic flow meters,* Ultrasonics (submitted).

[2] J. Massaad, P. van Neer, D. van Willigen, N. de Jong, M. Pertijs, and M. Verweij, *Feasibility of ultrasonic flow measurements via non-linear wave propagation,* IEEE Int. Ultrason. Symp. , 1 (2018).

[3] R. C. Baker, *Flow measurement handbook: industrial designs, operating principles, performance, and applications* (Cambridge University Press, 2005).

[4] D. Kurniadi and A. Trisnobudi, *A multi-path ultrasonic transit time flow meter using a tomography method for gas flow velocity profile measurement,* Part. Part. Syst. Charact. **23**, 330 (2006).

[5] A. Worch, *A clamp-on ultrasonic cross correlation flow meter for one-phase flow,* Meas. Sci. Technol. **9**, 622 (1998).

[6] V. Skwarek and V. Hans, *Multipath cross-correlation flowmeters,* Proc. IMEKO , 1 (2000).

[7] V. Skwarek, H. Windorfer, and V. Hans, *Measuring pulsating flow with ultrasound,* Measurement **29**, 225 (2001).

[8] P. Brassier, B. Hosten, and F. Vulovic, *High-frequency transducers and correlation method to enhance ultrasonic gas flow metering,* Flow Meas. Instrum **12**, 201 (2001).

[9] H. Zhou, T. Ji, R. Wang, X. Ge, X. Tang, and S. Tang, *Multipath ultrasonic gas flow-meter based on multiple reference waves,* Ultrasonics **82**, 145 (2018).

[10] S. Brauers, *Ultrasonic flow meters - liquids,* KROHNE Academy Online (2012).

[11] E. Mandard, D. Kouame, R. Battault, J.-P. Remenieras, and F. Patat, *Methodology for developing a high-precision ultrasound flow meter and fluid velocity profile reconstruction,* IEEE Trans. Ultrason. Ferroelectr. Freq. Control **55**, 161 (2008).

[12] M. F. Hamilton, D. T. Blackstock, *et al.*, *Nonlinear Acoustics*, Vol. 237 (Academic Press San Diego, 1998).

[13] Y.-S. Lee and M. F. Hamilton, *Time-domain modeling of pulsed finite-amplitude sound beams,* J. Acoust. Soc. Am. **97**, 906 (1995).

[14] R. O. Cleveland, M. F. Hamilton, and D. T. Blackstock, *Time-domain modeling of finite-amplitude sound in relaxing fluids,* J. Acoust. Soc. Am. **99**, 3312 (1996).

7

[15] X. Yang and R. O. Cleveland, *Time domain simulation of nonlinear acoustic beams generated by rectangular pistons with application to harmonic imaging,* J. Acoust. Soc. Am. **117**, 113 (2005).

[16] M. M. M. Voormolen, *3D Harmonic Echocardiography* (2007).

[17] J. Huijssen, *Modeling of Nonlinear Medical Diagnostic Ultrasound* (2008).

[18] A. C. Baker, A. M. Berg, A. Sahin, and J. N. Tjøtta, *The nonlinear pressure field of plane, rectangular apertures: Experimental and theoretical results,* J. Acoust. Soc. Am. **97**, 3510 (1995).

[19] M. Willatzen and H. Kamath, *Nonlinearities in ultrasonic flow measurement,* Flow Meas. Instrum. **19**, 79 (2008).

[20] L. Svilainis, P. Kabisius, A. Aleksandrovas, and A. Chaziachmetovas, *Excitation signal's influence on ultrasonic transit time flow meter's performance,* IOP Conf. Mater. Sci. Eng. **42**, 1 (2012).

[21] T. Folkestad and K. S. Mylvaganam, *Chirp excitation of ultrasonic probes and algorithm for filtering transit times in high-rangeability gas flow metering,* IEEE Trans. Ultrason. Ferroelectr. Freq. Control **40**, 193 (1993).

[22] K. S. Mylvaganam, *High-rangeability ultrasonic gas flowmeter for monitoring flare gas,* IEEE Trans. Ultrason. Ferroelectr. Freq. Control **36**, 144 (1989).

[23] W.-J. Zhu, K.-J. Xu, M. Fang, W. Wang, and Z.-W. Shen, *Mathematical modeling of ultrasonic gas flow meter based on experimental data in three steps,* IEEE Trans. Instrum. Meas. **65**, 1726 (2016).

7

8

On planar wave guide characterization by multi-parameter Lamb wave dispersion curve analysis

In recent years, several fitting techniques have been presented to reconstruct the parameters of a plate from its Lamb wave dispersion curves. Published studies show that these techniques can yield high accuracy results and have the potential of reconstructing several parameters at once. The precision with which parameters can be reconstructed by inverting Lamb wave dispersion curves, however, remains an open question of fundamental importance to many applications. In this work, it is presented an approach that allows both the simultaneous extraction of the thickness of a plate and the shear and longitudinal bulk wave sound speeds, as well as the provision of quantitative information on the precision with which these parameters can be extracted. As opposed to the error minimization algorithms commonly employed in fitting techniques, the approach presented here compares a target curve to a database of theoretical ones that covers a given parameter space. For every point in the parameter space, a measure of dissimilarity, or error, thus showing not only the location of the minimum error, but also the distribution of the error itself. This approach is used to reconstruct the parameters of a plate from Finite Element simulations and experimental measurements of the zero order Lamb wave modes (A_0 and S_0), showing that the precision with which each parameter is reconstructed depends on the wave mode used, as well as the frequency range in which it is considered.

8.1. Introduction

In a variety of fields, from medical research to industrial applications, measurements of the propagation of a mechanical wave through a medium are used to reconstruct its material properties [2–7]. In the simple case of a fluid bulk medium, the propagation speed of a wave is proportional to the inverse square root of the density and the compressibility of the medium. However, when the object under investigation is a solid plate or a plate-like geometry, waves are characterized by sets of symmetric and anti-symmetric dispersive wave modes. The propagation speed of these wave modes depends not only on the elastic properties of the medium, but also on the product of its thickness and the frequency of the wave [8, 9].

Due to the dispersive behaviour of Lamb waves, time-of-flight measurements of wave speed cannot be employed directly to reconstruct the properties of a medium [10–12]. Rather, a common approach consists in assuming that a given combination of longitudinal speed (c_L), shear speed (c_T) and thickness (h) defines uniquely a set of dispersion curves; based on this assumption, these three material properties can be reconstructed by extracting the dispersion curves from a measurement and then finding the parameters that generate the same (or most similar) curves [13–17]. Several techniques have already been developed to extract the dispersion curves from measured data [18–20] and to solve the so-called inverse problem for one or more parameters simultaneously [15–18, 21–24]. In most of these studies, the accuracy of the techniques is then compared with benchmarking methods, such as mechanical testing or pulse-echo measurements. However, little to no information is available on the reliability of the Lamb dispersion curve approach: whether the solution is unique and independent of the inversion algorithm employed, how robust this approach is with respect to noise, how sensitive different wave modes are to the three parameters and whether this sensitivity depends on the frequency range available, and, in general, how precise the results are. This information, however, is crucial to assess whether and when this approach can be used in practical applications. If, for instance, two different sets of material properties generated similar A_0 curves, and if noise would cause these curves to become indistinguishable, the inversion would not necessarily be able to distinguish between the two sets in practice.

In the first part of this work it is presented an approach to simultaneously extract c_L, c_T, and h from measured or simulated dispersion curves. In addition to parameter extraction, this method provides quantitative information on how sensitive a wave mode is to each of the three parameters, as well as an indication of whether a solution is at least locally unique. This method is then employed to show numerically how random noise applied to the dispersion curves in the wavenumber direction can affect the results. Moreover, it is shown how the sensitivity of the zero order wave modes (A_0 and S_0) to c_L, c_T, and h varies between wave modes and how it depends on the frequency range available. Finally, applications of the proposed approach are shown on simulated and experimental data.

8.2. Setup

8.2.1. Numerical simulations

The Finite Element software package PZFlex (Onscale, Redwood City, CA, USA) was used to simulate the acoustic wave propagation of Lamb waves in a $h = 1\,\text{mm}$-thick stainless steel plate, which was simulated using nominal values of $c_L = 5800\,\text{m/s}$ and $c_T = 3100\,\text{m/s}$. Guided waves were excited in the plate by placing a small transducer on one of the surfaces and exciting it with a broadband ultrasound pulse with a center frequency of $2.7\,\text{MHz}$. Considering the lowest sound speed of the geometry, a mesh consisting of square grids with a length of 30 points per wavelength was defined to properly sample the guided waves. Along one of the surfaces of the plate, virtual receivers were placed over a distance of $90\,\text{mm}$ to record the time signals of these waves. Finally, a 2D Fast Fourier Transform (FFT) was applied to visualize the propagating wave modes, i.e. the dispersion curves, in the $f - k_x$ domain .

8.2.2. Experimental setup

The experiments were conducted on a $40\,\text{mm}$ inner diameter 304-stainless steel pipe (nominal values: $c_L = 5920\,\text{m/s}$ and $c_T = 3141\,\text{m/s}$) with a wall thickness of $h = 1\,\text{mm}$. Two ATL P4-1 probes (Philips, Bothell, WA, USA), one functioning as an ultrasound source and the other as a receiver, were placed in line on the pipe wall, with a center-to-center distance of $10\,\text{cm}$, and were driven with a Verasonics Vantage 256 (Verasonics Inc., Kirkland, WA, USA) system. A 1-cycle pulse with a center frequency of $2.25\,\text{MHz}$ was used to excite one element of the source probe, and all 96 elements of the receiver probe were used to record the propagating guided waves (see Fig. 8.1).
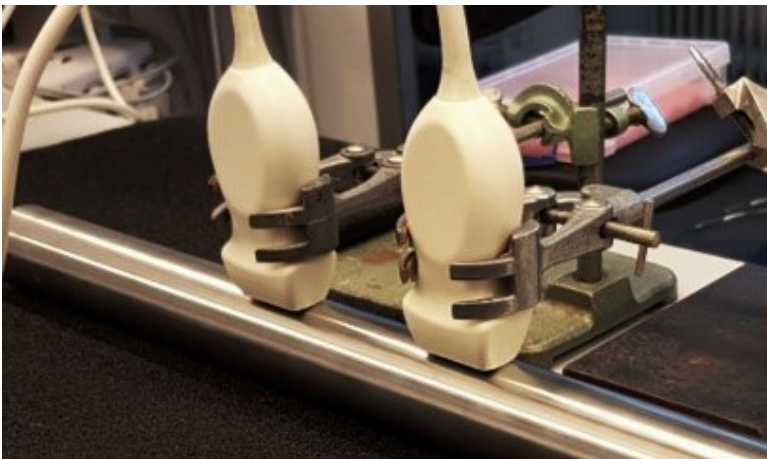
Figure 8.1: Experimental setup, consisting of two ATL P4-1 probes held in contact with a $h = 1\,\text{mm}$-thick stainless steel pipe.

8.3. Methodology

8.3.1. Dispersion curve extraction

Measured data

The following procedure was adapted from [18] to isolate and extract the A_0 and S_0 wave modes (see Fig. 8.2). First, all the local maxima of the $f - k_x$ surface were found and connected by straight lines, so as to generate a new, smoother dataset. This interpolation removes the valleys between consecutive peaks, e.g. turning a sawtooth pattern into a straight line. The new dataset, converted to decibel scale, was then squared (to increase the prominence of the highest peaks) and thresholded (to remove the lower values), thus partially isolating the wave modes and removing noise. The local maxima of the treated data were then extracted again and stored into a database (e.g. $data_A$).

The wave mode identification was then executed as a search for chains of neighbouring maxima: starting from a point in $data_A$, it was determined which (if any) other local maximum was the closest neighbour within a given radius; if such a point was found, the starting point would be moved from $data_A$ into a different database (e.g. $mode_I$), and the neighbour would become the next starting point. Once no neighbour was found within the searching radius, a new starting point was chosen from $data_A$ and a new database (e.g. $mode_2$) was created to store the next chain. Finally, spurious chains were separated from the real wave modes on the basis of chain length because a wave mode, being a set of points ordered along a curve, forms a consistently longer chain than randomly distributed spurious clusters of maxima). The wave modes themselves were identified on the basis of the order
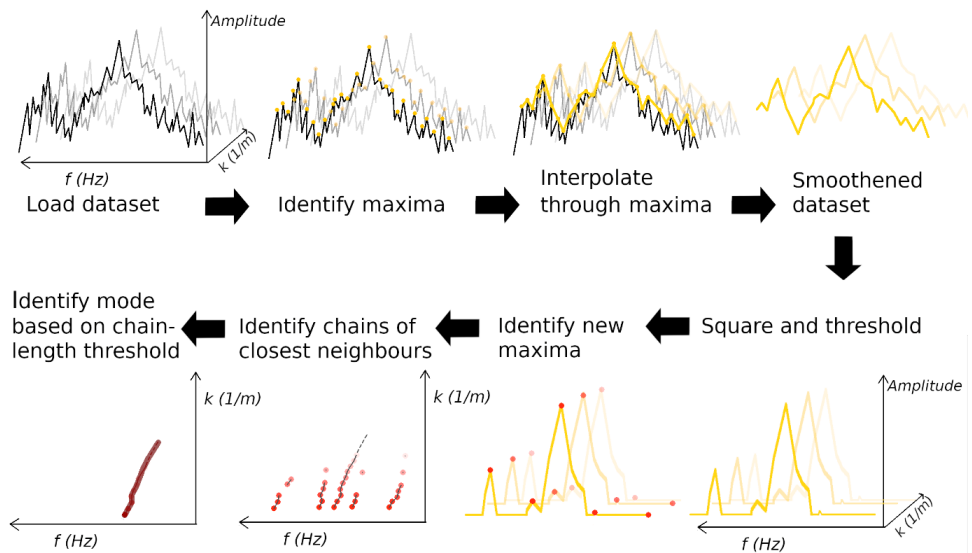
Figure 8.2: Algorithm to extract the dispersion curves from experimental data in the frequency-wavenumber domain.
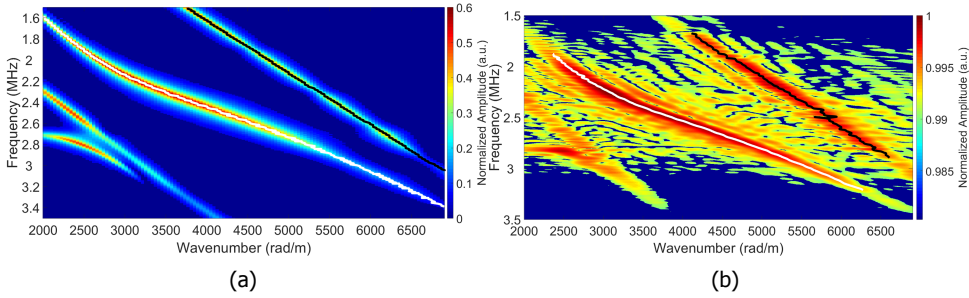
Figure 8.3: Magnitude of a 2D FFT applied to time signals obtained on the surface of a $1\,\text{mm}$-thick simulated stainless steel plate (left) and measured on the surface of a $1\,\text{mm}$-thick stainless steel pipe (right). The white lines show the reconstructed S_0 wave mode, the black lines indicate the reconstructed A_0 wave mode.

of appearance along the k_x direction: at every frequency, the k_x belonging to the A_0 wave mode have a lower value than those belonging to the S_0 wave mode.

Simulated data

The extraction of dispersion curves from the simulated data was more straightforward, thanks to the comparatively low level of noise: the curves were found by extracting directly the local maxima in the untreated $f - k_x$ domain, and were then sorted out according to the last step of the procedure described above. The results of the curve extraction algorithms are shown for both experiment and simulation in Fig. 8.3.

8.3.2. Curve fitting and error volumes

Once an experimental or simulated curve has been extracted, a fitting procedure can be used to identify the set of c_L, c_T and h (longitudinal bulk wave speed, shear bulk wave speed and thickness) that generates a theoretical curve that best matches the extracted ones. Typically, such fitting procedures consist in defining an error function that describes the discrepancy between the target and the model, and then applying an optimization algorithm to minimize this error. For instance, a least squares fitting algorithm can be used [17, 21].

In contrast with other studies, the present work does not make use of an optimization algorithm to find the best fitting curve. Instead, a 3D parameter space of $4500\,\text{m/s} \leq c_L \leq 7500\,\text{m/s}$, $2000\,\text{m/s} \leq c_T \leq 4000\,\text{m/s}$ and $0.1\,\text{mm} \leq h \leq 4\,\text{mm}$ was considered, with speed resolution of $50\,\text{m/s}$ and thickness resolution of $0.1\,\text{mm}$. For each point in this space, the theoretical curves of A_0 and S_0 were computed at frequencies comprised between $50\,\text{kHz}$ and $3.6\,\text{MHz}$, sampled every $50\,\text{kHz}$. Each curve was then stored in a database. Similarly to other fitting procedures, an error function E was then introduced, defined here as a Mean Absolute Percentage Error (MAPE),

$$E = \frac{100}{N} \sum_{i=1}^{N} \left| \frac{k_i^{\text{th}} - k_i}{k_i^{\text{th}}} \right|, \tag{8.1}$$

where N is the number of frequencies considered, the index i runs from 1 to N, k_i is the wavenumber corresponding to the ith frequency of the measured dispersion curve, and k_i^{th} is the wavenumber of the theoretical curve at the same frequency.

The extracted curves were compared to every theoretical curve in the corresponding database, and the MAPE of each comparison was added to a 3D plot. The resulting image shows the volumetric distribution of the MAPE in the entire parameter space. This distribution will be referred to as as "error volume". Once the error volume has been reconstructed, it is possible to identify the best fitting theoretical curve by finding the coordinates of the global minimum of the MAPE. Moreover, this approach allows to observe the distribution of the error in the parameter space.

8.3.3. Fitting reliability

To study how noise can affect the correct identification of c_L, c_T and h, the theoretical dispersion curves corresponding to the A_0 and S_0 wave modes were employed as target curves, with random noise assigned to the wavenumber coordinate of each point on the curves. At each point, the noise applied was drawn from a uniform distribution of values between -0.5% and $+0.5\%$ of the wavenumber value of the point. The boundaries of the noise distribution were chosen so that the minimum MAPE would be between 0.2% and 0.4%, which were the values observed for the global minimum in simulated data of A_0 and S_0, respectively. Repeating the analysis for ten different realizations of the noise, it was observed that the minimum MAPE value could vary by up to approximately 10% of its average value.

Within the resolution of the database, it is possible to determine whether the minimum is global, as well as how sensitive the error is to the different parameters. For instance, if many points along the c_L axis correspond to comparably low values of MAPE, similar curves can be generated by different values of longitudinal speed; the optimal value of c_L may therefore be not reliable.

A traditional sensitivity analysis would be ill suited to describe the reliability of MAPE minimizations, due to its local nature (see Appendix B). Instead, to quantify this concept of reliability based on the error volume analysis, two parameters are introduced: a low error volume (LEV) and a spread around the minimum (SAM). The LEV value indicates the number of theoretical curves whose MAPE is at most 10% greater than the global minimum; this boundary was chosen based on the 10% variation in minimum MAPE that was observed to come from random noise. Notably, the points within the LEV form a curved shape within the 3D space, thus the LEV cannot be described as a rectangular volume (i.e. as the product of three orthogonal coordinates). The SAM values indicate how far the points within the LEV are spread along each axis. The SAM values are computed as a weighted mean absolute percentage deviation from the coordinates with minimum MAPE

$$\text{SAM}_\text{x} = \frac{100}{X_\text{min}} \frac{\sum\limits_{i=1}^{N} \frac{|X_i - X_\text{min}|}{(E_i - E_\text{min})}}{\sum\limits_{i=1}^{N} \frac{1}{(E_i - E_\text{min})}},$$ (8.2)

where X_i is the ith coordinate within the LEV on the X axis (e.g. longitudinal speed), E_i is the corresponding MAPE, and the sum runs over all the coordinates within the LEV on that axis, except from the coordinate of the global minimum. This function was chosen so as to give more relevance to the points whose MAPE is the most similar to the minimum. The percentage term $100/X_\text{min}$ was included to allow the comparison of SAM values of different axes.

8.4. Results

8.4.1. Error volumes

Simulated data

Figure 8.4 shows slices of the error volume computed for an A_0 curve extracted between 1.5 MHz and 3.1 MHz from simulated data. A global minimum exists within the parameter space considered, and corresponds to a MAPE of 0.218 % at coordinates: $c_L = 4800 \pm 25$ m/s, $c_T = 3200 \pm 25$ m/s, and $h = 1.1 \pm 0.05$ mm. The indicated variations are due to the step-sizes of the parameters. The material properties corresponding to the best fitting curve, therefore, are in poor agreement with the actual values ($c_L = 5800$ m/s, $c_T = 3100$ m/s and $h = 1$ mm). As can be seen in the plot, however, there is an extended volume in the parameter space in which the MAPE is within 1 %. In fact, the third-lowest error point corresponds to a MAPE of 0.225 % at coordinates: $c_L = 5850 \pm 25$ m/s, $c_T = 3100 \pm 25$ m/s, and $h = 1.0 \pm 0.05$ mm, which are in much better agreement with the input parameters of the simulation.

The same analysis was performed for the S_0 wave mode extracted from the simulated data, see Fig. 8.5. Once again, there is a global minimum error within the parameter space, corresponding to a MAPE of 0.551 % at coordinates: $c_L = 5850 \pm 25$ m/s, $c_T = 3100 \pm 25$ m/s, and $h = 1.0 \pm 0.05$ mm. As can be seen in Fig. 8.5, the distribution on the $c_L - c_T$ plane is similar to that of the A_0 wave mode, while the distribution on the other planes is clearly different. Interestingly, while the coordinates of the global minimum are much closer to the expected values than those of A_0, overall the MAPE is higher. This result suggests that, at the frequencies considered, variations in the parameter space of material properties cause greater variations in S_0 than in A_0 curves. As a consequence, an extracted S_0 curve that deviates more from the theoretical one may still yield parameters that are closer to the actual ones, as compared to the A_0 case.

Comparing the error volumes for the A_0 and S_0 wave modes, it can be observed that they show a similar trend for the distribution of the low errors along the longitudinal speed axis (almost uniform for $c_L > 5000$ m/s, indicating a low sensitivity to overestimations of this parameter), whereas the distribution in the $c_T - h$ plane

8
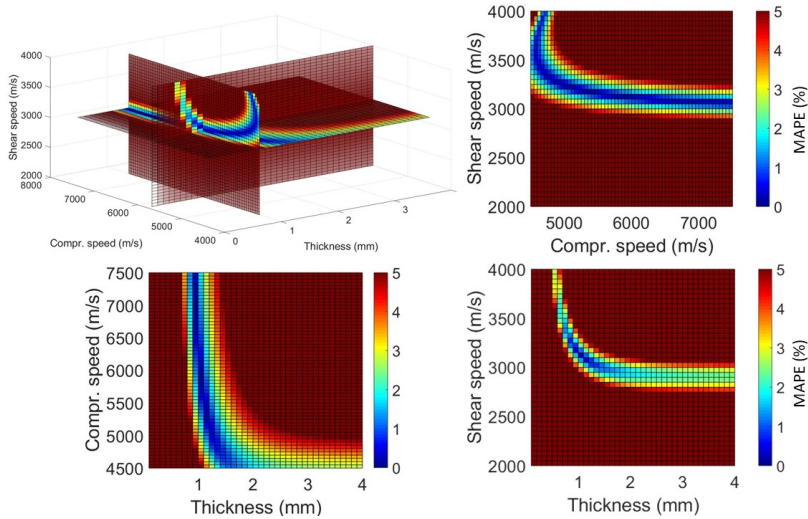
Figure 8.4: The top-left panel shows slices of the error volume for the simulated A_0 wave mode of a stainless steel plate at frequencies between $1.5\,\text{MHz}$ and $3.1\,\text{MHz}$. The slices represent planes at the fixed values $c_L = 5800\,\text{m/s}$, $c_T = 3100\,\text{m/s}$ and $h = 1\,\text{mm}$, which are the actual values of these parameters. Each other panel shows the frontal view of a single plane ($c_L - c_T$, $c_T - h$, $c_L - h$, in clockwise order). Colors represent the value of MAPE at each coordinate in the parameter space.
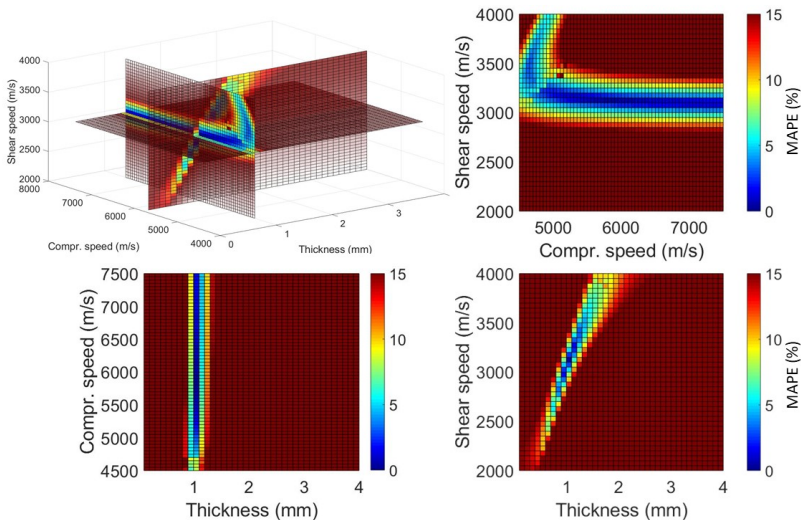
Figure 8.5: The top-left panel shows slices of the error volume for the simulated S_0 wave mode of a stainless steel plate at frequencies between $1.5\,\text{MHz}$ and $3.1\,\text{MHz}$. The slices represent planes at the fixed values $c_L = 5800\,\text{m/s}$, $c_T = 3100\,\text{m/s}$ and $h = 1\,\text{mm}$, which are the actual values of these parameters. Each other panel shows the frontal view of a single plane ($c_L - c_T$, $c_T - h$, $c_L - h$, in clockwise order). Colors represent the value of MAPE at each coordinate in the parameter space.
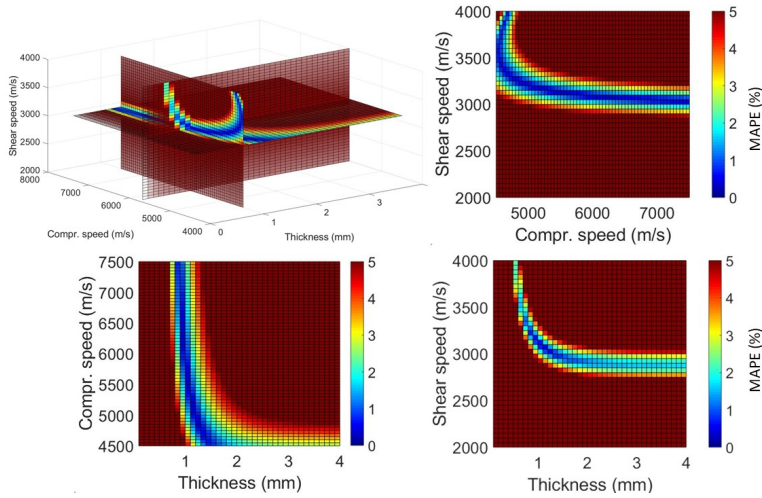
Figure 8.6: The top-left panel shows slices of the error volume for the A_0 wave mode extracted from an experiment on a 1 mm-thick stainless steel pipe at frequencies between 1.5 MHz and 3.1 MHz. The slices represent planes at the fixed values $c_L = 5800$ m/s, $c_L = 3100$ m/s and $h = 1$ mm, which are the actual values of these parameters. Each other panel shows the frontal view of a single plane ($c_L - c_T$, $c_T - h$, $c_L - h$, in clockwise order). Colors represent the value of MAPE at each coordinate in the parameter space.
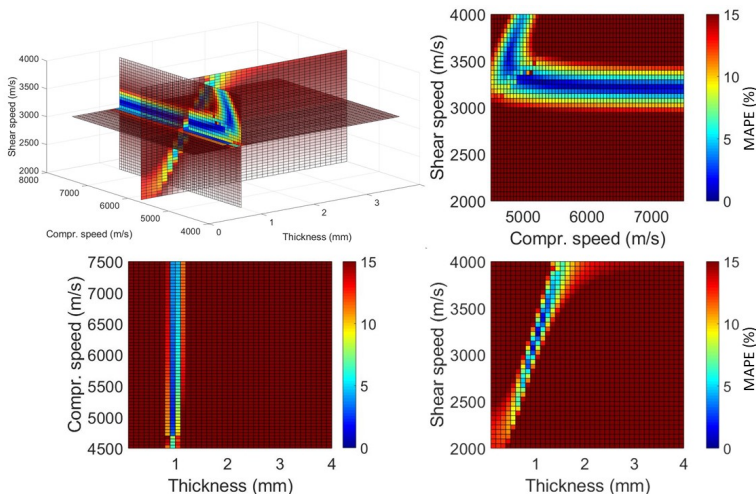
Figure 8.7: The top-left panel shows slices of the error volume for the S_0 wave mode extracted from an experiment on a 1 mm-thick stainless steel pipe at frequencies between 1.5 MHz and 3.1 MHz. The slices represent planes at the fixed values $c_L = 5800$ m/s, $c_L = 3100$ m/s and $h = 1$ mm, which are the actual values of these parameters. Each other panel shows the frontal view of a single plane ($c_L - c_T$, $c_T - h$, $c_L - h$, in clockwise order). Colors represent the value of MAPE at each coordinate in the parameter space.

is different: for the S_0 wave mode, the coordinates of low error points on the c_T axis increase with increasing thickness, while for the A_0 wave mode the distribution along h is similar to that along c_L, indicating low sensitivity to thickness overestimations.

Measured data

Figures 8.6 and 8.7 show the error volumes computed for the A_0 and S_0 curves extracted from the experiment. Qualitatively speaking, the volumes appear very similar to those of the simulated data. The material properties identified by the minimum of the error volume of A_0 are: $c_L = 5500 \pm 25$ m/s, $c_T = 3100 \pm 25$ m/s; those extracted from S_0 are: $c_L = 5250 \pm 25$ m/s, $c_T = 3250 \pm 25$ m/s, and $h = 1.0 \pm 0.05$ mm.

Subsequently, the LEV and SAM values were computed for the two wave modes for both simulated and experimental data, and are reported in Table 8.1. For each dataset, the S_0 wave mode appears more sensitive than the A_0 wave mode: the LEV and all the SAM values are smaller, confirming that variations in the parameter space of material properties lead to greater variations in S_0 than in A_0.

8.4.2. Robustness against noise

The theoretical curves of A_0 and S_0 wave modes were calculated between 50 KHz and 3.5 MHz for a 1 mm-thick stainless steel plate. As described in the previous section, random noise was added to the wavenumber coordinates of both curves. For each curve, the error volume was reconstructed and used to identify the best fitting curve, i.e. the curve with minimum error. This procedure was repeated ten times for each wave mode. Table 8.2 shows the average and highest minimum MAPE, and the mean absolute error (MAE) and maximum error of c_L, c_T and h, compared to their true values ($c_L = 5800$ m/s, $c_T = 3100$ m/s and $h = 1$ mm), for each wave mode.

Table 8.1: Values of LEV and SAM for the A_0 and S_0 wave modes extracted from a simulated 1 mm-thick stainless steel plate (above) and from an experiment on a 1 mm-thick stainless steel pipe (below) at frequencies between 1.5 MHz and 3.1 MHz.

Simulated Data

Wave Mode	LEV (a.u.)	SAM c_L (%)	SAM c_T (%)	SAM h (%)
A_0	50	20.8	3.2	10.0
S_0	14	0.8	0.0	0.0

Experimental Data

Wave Mode	LEV (a.u.)	SAM c_L (%)	SAM c_T (%)	SAM h (%)
A_0	209	13.0	2.1	7.0
S_0	7	3.8	0.4	0.0

Table 8.2: Results of generating ten A_0 and ten S_0 dispersion curves affected by uniformly distributed random noise applied to the wavenumber coordinates. Entries in the table show, from left to right: the average minimum MAPE (Av. E), the highest value of minimum MAPE (Max. E), the mean and maximum absolute error of c_L compared to the true value (MAE c_L and Max. Δc_L), the mean and maximum absolute error of c_T compared to the true value (MAE c_T and Max. Δc_T), and the mean and maximum absolute error of h compared to the true value (MAE h and Max. Δh).

	Av. E (%)	Max. E (%)	MAE c_L (m/s)	Max. Δc_L (m/s)
A_0	0.25	0.27	95	1000
	MAE c_T (m/s)	**Max. Δc_T (m/s)**	**MAE h (mm)**	**Max. Δh (mm)**
	10	100	0.01	0.1

	Av. E (%)	Max. E (%)	MAE c_L (m/s)	Max. Δc_L (m/s)
S_0	0.24	0.26	5	50
	MAE c_T (m/s)	**Max. Δc_T (m/s)**	**MAE h (mm)**	**Max. Δh (mm)**
	0	0	0.00	0.0

8.4.3. Frequency range analysis

During data analysis, it was observed that theoretical curves generated for different values of one parameter could be more similar to each other at certain frequencies than at others. For example, the MAPE between two S_0 dispersion curves corresponding to thicknesses of $1\,\text{mm}$ and $1.2\,\text{mm}$, for shear and longitudinal speeds fixed at $c_T = 3100\,\text{m/s}$ and $c_L = 5800\,\text{m/s}$ respectively, was less than $1\,\%$ at frequencies between $0\,\text{MHz}$ and $1\,\text{MHz}$, and around $18\,\%$ between $1.5\,\text{MHz}$ and $2.5\,\text{MHz}$.

To investigate how different frequency regions affected the LEV and SAM results, comparison of noiseless theoretical A_0 and S_0 dispersion curves to the database was performed at various frequency ranges. The frequency ranges considered included bands with a width of $0.2\,\text{MHz}$ and $2.9\,\text{MHz}$, within an overall range of $0.1 - 3.1\,\text{MHz}$. For each frequency range, the LEV and SAM values were computed and plotted. For this calculation only, the LEV was defined as all the curves whose MAPE was within $110\,\%$ of the second-lowest error, instead of the lowest error. This choice was made because the lowest error was always zero, since theoretical curves were considered and the database contained the theoretical curves themselves.

Figures 8.8 and 8.9 show the values of LEV and SAM at different frequency ranges for the noiseless theoretical A_0 and S_0 dispersion curves, respectively, of a $1\,\text{mm}$-thick stainless steel plate. The vertical axis represents the starting frequency for each of the ranges considered, while the horizontal axis represents the bandwidth of each range. Since only frequencies between $0.1\,\text{MHz}$ and $3.1\,\text{MHz}$ were considered in this analysis, the maximum bandwidth of the frequency ranges decreases with the increase of the starting frequency. Each point in the plots shown in Fig. 8.8 and Fig. 8.9 thus corresponds to an analysis performed at a different frequency range, determined as the combination of a starting frequency and a bandwidth.

For the A_0 wave mode, considering only higher frequencies introduces a greater

8

Figure 8.8: (a) LEV, (b) SAM c_L, (c) SAM h, (d) SAM c_T for a theoretical A_0 dispersion curve considering different frequency ranges. The color scales represent the amplitude of each variable. Each point corresponds to a different combination of starting frequency (ordinate axis) and frequency bandwidth (abscissa axis).
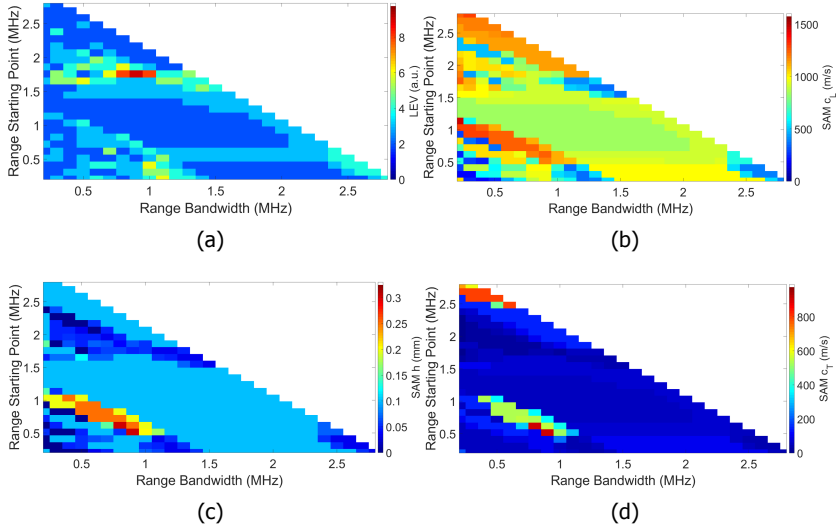
8

Figure 8.9: (a) LEV, (b) SAM c_L, (c) SAM h, (d) SAM c_T for a theoretical S_0 dispersion curve considering different frequency ranges. The color scales represent the amplitude of each variable. Each point corresponds to a different combination of starting frequency (ordinate axis) and frequency bandwidth (abscissa axis).
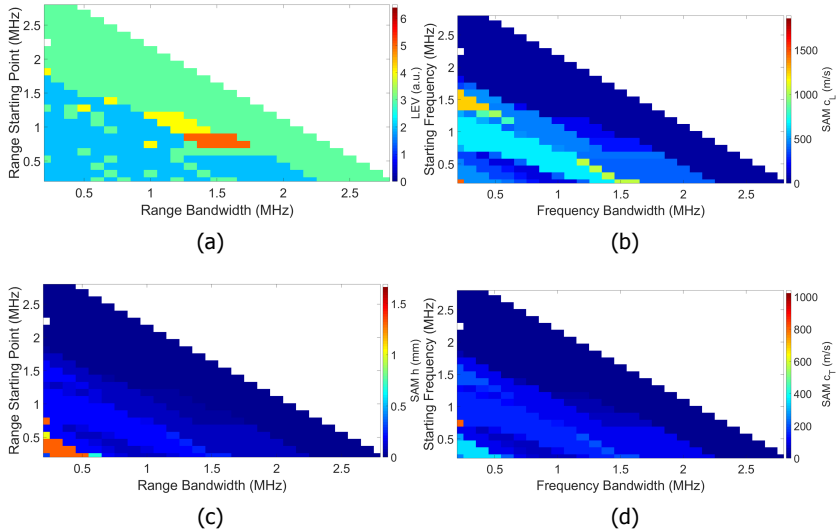
variability of longitudinal speeds within the LEV, while the highest precision seems to be achievable for all three parameters within the first MHz; the value of SAM of the shear speed appears to be relatively low (within $50\,\mathrm{m/s}$) at most frequencies. The LEV itself can vary considerably depending on the frequency band considered. In contrast, the SAM values for the S_0 wave mode are almost uniformly low at the higher frequencies, while there is a region of frequencies around $0.5\,\mathrm{MHz}$ in which they increase, especially for the thickness.

8.5. Discussion

Several studies can be found in literature detailing techniques to extract Lamb dispersion curves and inversion methods to reconstruct material properties [13–24]. However, these studies rely on minimization techniques that only yield information about the (possibly) global minimum of a given error function. When employing such an approach, therefore, all information about how the error is distributed over the parameter space is lost. One of the advantages of the comparison approach presented in this paper is that information about the matching error of the dispersion curves (the MAPE defined in Eq. 8.1) is extracted along with the coordinates of the global minimum, at the cost of having to initially compute and store dispersion curves for the entire parameter space. This additional information is necessary to assess how reliable the results of the inversion are, both in a general sense (i.e. how precise can a multi- or single-parameter inversion be) and for a specific measurement (e.g. how reliable a measurement is performed with a given setup under specific experimental conditions and corresponding experimental noise). Moreover, the results identify which zero order wave mode is the most sensitive to what material property at what frequencies, and the approach presented here could also be employed to extend these results to higher order wave modes and higher frequencies, providing a toolset to maximise the precision of the results of inversion.

To better understand how information on the MAPE is connected to the precision of the inversion, let us consider the following: if, along a given axis (e.g. longitudinal wave speed), there are multiple coordinates at which the MAPE is comparable to the global minimum, then many curves corresponding to different material properties are comparably similar to the target one (e.g. the one extracted from experiments). Small variations in the target curve, for instance due to experimental noise or poor reconstruction of the wave mode, could then greatly shift the location of the global minimum and therefore the values of the reconstructed properties. Knowing the distribution of the MAPE, then, allows one to know how much the material properties can vary with small variations of this error. Intuitively, the larger the range of parameters with a low error, the less reliable are the properties corresponding to the global minimum.

To provide a quantitative measure of the sensitivity described above, the values of Low Error Volume (LEV) and Spread Around Minimum (SAM) have been introduced. The LEV value represents how many different curves have a MAPE comparable to the minimum one. Here, "comparable" is defined as a threshold of up to $10\,\%$ higher than the minimum MAPE. By itself, however, the LEV is not sufficient to tell whether a result is reliable: if there were 100 curves represented

within the LEV, but all located at similar coordinates, even if the global minimum was shifted to another point (e.g. due to noise), the result would not be affected greatly. The SAM values represent how the error spreads along each parameter axis: a lower spread along one axis means a higher precision with respect to the corresponding parameter. This is different from a standard sensitivity analysis, in that the SAM values consider all the points within the LEV to determine how much a coordinate could vary, whereas the sensitivity analysis only looks at the derivatives in the neighbourhood of the minimum, fixing two coordinates out of three at a time. A more detailed explanation of why this local information is not sufficient is given in Appendix B.

Practical observations guided the choices made for the LEV and SAM thresholds: the LEV boundary (110% of the minimal MAPE) was established based on the observed variability in minimal MAPE when the target curve was a theoretical curve with uniformly distributed random noise on the wavenumber coordinates; the SAM values were computed as an average weighted by the inverse of the MAPE, to reflect that lower error curves are more likely to be mixed up with the curve of the global minimum. As long as LEV and SAM are defined consistently, they allow to compare different curves of the same wave mode, different wave modes and frequency ranges, and even different experiments.

By employing the LEV and SAM parameters, it was also possible to analyse how the sensitivity of the A_0 and S_0 wave modes varies with the frequency range over which the curves are compared. In particular, Figures 8.8 and 8.9 show that the A_0 wave mode can be more reliable than the S_0 wave mode in estimating the longitudinal wave speed and the thickness when only low frequencies are available, i.e. up to $1\,\text{MHz}$ for a $1\,\text{mm}$-thick plate. At higher frequencies, the S_0 wave mode appears to provide more precise information about all three parameters. Notably, in this study it has been kept a focus on zero order wave modes, and these two wave modes were only analysed separately. As mentioned above, however, the approach presented here can be used also to analyse higher order wave modes. It would be interesting to investigate, then, if combining multiple wave modes at their "best" frequency ranges, e.g. by combining their error volumes by sum or multiplication, could improve precision or accuracy.

Low values of LEV and SAM, however, don't guarantee that the minimum error curve corresponds to the true values of the properties of the medium; they should be interpreted as a measure of precision, rather than accuracy. In fact, when comparing the A_0 and S_0 wave modes in the experimental data, the SAM and LEV values are lower for S_0, but the parameters identified by the minimum of the error volume of A_0 are more accurate compared to the expected nominal properties of the pipe. This result means that, in this one measurement, the curves extracted from the experiment yield a more accurate result for A_0 than for S_0; however, given the higher values of SAM and LEV, it is reasonable to expect that repeated experiments would show a greater variation in results for A_0 than for S_0. It is also worth mentioning here that the central assumption, i.e. that the Lamb characteristic equations to describe the measurements can be used, is verified only in an approximate sense: the equations, in fact, are defined for infinite plates with perfectly parallel, smooth

surfaces and elastic, homogeneous and isotropic materials, while a real metal plate necessarily presents surface roughness and imperfections, warping, and anisotropic behaviours due to sheet fabrication process. For finite element simulation, moreover, the applied discretization scheme (size and shape of the elements, interpolation between nodes) can alter the accuracy with which results are calculated. All of these factors are likely to cause deviations from the theoretical curves, and it is reasonable to expect that different wave modes will be affected differently, due to their different particle motion patterns and wave velocities.

Besides providing information on the distribution of the matching error, the approach employed in this study has several other advantages over traditional optimization algorithms. For one, its results don't depend on initial guesses. Moreover, most of the computational cost lies in the generation of the database of theoretical curves that is used for the comparisons with the target curve; once the database exists, it can be used any number of times on any number of different experimental or simulated curves. In contrast, every time an optimization algorithm runs, it has to re-compute each theoretical curve it uses. While the number of curves thus computed is usually lower than that necessary to create a database, the cost for the database is paid only once, whereas that of the optimization is paid every time it is employed. In terms of real-world applications, this approach could benefit greatly the efficiency of in-situ non-destructive tests, such as pipe inspections, where the database could be computed during the fabrication of the testing instrument, ready to be used at every subsequent test.

A drawback of the database approach, however, is that it only provides results within its parameter space, which is defined at the moment of the creation of the database. Moreover, there is a trade-off between accuracy (limited by the resolution of the database), range of parameters explored (defined by the boundaries of the database) and size of the database itself (for reference, the database used in the present work has a size of $55\,\mathrm{MB}$). This problem can be circumvented by preparing various application-specific databases, in which resolution and boundaries of a database are tailored to the use it has to serve, e.g. analysing a steel pipe with nominal thickness of $1\,\mathrm{mm}$.

Finally, the results presented in Table 8.2 highlight a potential general weakness in the approach of inverting dispersion curves to reconstruct material properties. In fact, while the S_0 curve showed less sensitivity to the random noise, one out of ten noise-affected A_0 curves yielded a longitudinal speed 1000 m/s lower than the true value. Repeating the same analysis with noise randomly distributed across a wider range (between $-1\,\%$ and $1\,\%$ of each wavenumber coordinate), comparable to the average variations observed in the experiment, yielded three cases out of ten in which the longitudinal speed extracted from the A_0 curve was between $800\,\mathrm{m/s}$ and $1000\,\mathrm{m/s}$ lower than the true value. These results would suggest that the properties found by inverting the A_0 curve can be considerably affected by noise, undermining their reliability in practical applications. Moreover, here all three parameters (transverse and longitudinal wave speeds, and thickness) were extracted simultaneously, but it would also be reasonable to investigate whether prior knowledge on some of the parameters would improve the results. Indeed, for

a noise-affected theoretical A_0 curve in which three-parameters estimation yielded $c_L = 4800\,\text{m/s}$, it was observed that fixing the thickness at $1\,\text{mm}$ corresponded to a minimum error curve generated by $c_L = 5500\,\text{m/s}$; fixing both the thickness at $1\,\text{mm}$ and the shear speed at $c_T = 3100\,\text{m/s}$ yielded an estimated $c_L = 5850\,\text{m/s}$, suggesting that a priori knowledge of some parameters can increase the robustness of results against noise. In principle, using these results, it could even be possible to extract a single property using the most precise combination of wave mode and frequency range, then use that property as input fixed value and extract the second property, again based on its corresponding best wave mode and frequency range, and iterate until all properties are extracted. This boot-strapping approach could be very useful in applications where a priori knowledge is not available; however, it remains to be proven whether it would have the same effect, which likely depends on the accuracy with which the first property is extracted. In any case, it would be interesting to perform a more extensive analysis, both on noise-affected theoretical curves as well as on repeated experiments, to determine what percentage of cases leads to significant over- or underestimations of material properties.

8.6. Conclusions

Here, a new approach for the extraction of parameter values from Lamb wave dispersion curves has been presented. This approach yields simultaneously three parameters of the wave guide (thickness, longitudinal speed and shear speed), as well as quantitative information on the precision with which the information is extracted. It was observed observed that low amplitude random noise can affect the results of Lamb wave dispersion curve inversion, with few A_0 dispersion curves yielding longitudinal speeds far off their true value, thus highlighting the importance of having such a measure of precision. Moreover, using the proposed method, it was shown that the S_0 wave mode is more sensitive than the A_0 wave mode to all three properties at higher frequencies, and that both wave modes are more sensitive to shear speed and thickness than to longitudinal speed. These results could therefore be employed to increase the precision with which the material properties are reconstructed, by identifying the optimal combination of wave mode and frequency range for each.

References

[1] A. Sabbadini, J. Massaad, P. L. M. J. van Neer, N. de Jong, and M. D. Verweij, *On waveguide characterization by multi-parameter Lamb wave dispersion curve analysis,* Ultrasonics (submitted).

[2] P. Song, X. Bi, D. C. Mellema, A. Manduca, M. W. Urban, J. F. Greenleaf, and S. Chen, *Quantitative assessment of left ventricular diastolic stiffness using cardiac shear wave elastography: a pilot study,* J. Ultrasound Med. **35**, 1419 (2016).

[3] S. Otsuka, X. Shan, K. Yoshida, T. Yakura, M. Naito, and Y. Kawakami, *Site*

8

dependent elastic property of human iliotibial band and the effect of hip and knee joint angle configuration, J Biomech. , 1 (2020).

[4] M. A. Fakih, S. Mustapha, J. Tarraf, G. Ayoub, and R. Hamade, *Detection and assessment of flaws in friction stir welded metallic plates,* Proc. SPIE **10168**, 1 (2017).

[5] G. Rizzuti and A. Gisolf, *2-D wavefield inversion for high-resolution elastic property estimation,* 76th $EAGE$ $Conference$ and $Exhibition$ **2014**, 1(2014).

[6] K. Heller, L. Jacobs, and J. Qu, *Characterization of adhesive bond properties using Lamb waves,* NDT E. Int. **33**, 555 (2000).

[7] K. Lee and S. W. Yoon, *Feasibility of bone assessment with leaky Lamb waves in bone phantoms and a bovine tibia,* J. Acoust. Soc. Am. **115**, 3210 (2004).

[8] H. Lamb, *On waves in an elastic plate,* P. Roy. Soc. A-Math. Phy. **93**, 114 (1917).

[9] J. L. Rose, *Ultrasonic guided waves in solid media* (Cambridge University Press, 2014).

[10] A. Sabbadini, A. Caenen, L. B. H. Keijzer, P. L. M. J. van Neer, N. de Jong, H. J. Vos, and M. D. Verweij, *Tapering of the interventricular septum can affect ultrasound shear wave elastography: an in vitro and in silico study,* J. Acoust. Soc. Am. (submitted).

[11] E. Maksuti, F. Bini, S. Fiorentini, G. Blasi, M. W. Urban, F. Marinozzi, and M. Larsson, *Influence of wall thickness and diameter on arterial shear wave elastography: a phantom and finite element study,* Phys. Med. Biol. **62**, 2694 (2017).

[12] A. Caenen, M. Pernot, D. A. Shcherbakova, L. Mertens, M. Kersemans, P. Segers, and A. Swillens, *Investigating shear wave physics in a generic pediatric left ventricular model via in vitro experiments and finite element simulations,* IEEE Trans. Ultrason. Ferroelectr. Freq. Control **64**, 349 (2016).

[13] I. Z. Nenadic, M. W. Urban, S. A. Mitchell, and J. F. Greenleaf, *Lamb wave dispersion ultrasound vibrometry (LDUV) method for quantifying mechanical properties of viscoelastic solids,* Phys. Med. Biol. **56**, 2245 (2011).

[14] T. N. H. T. Tran, M. D. Sacchi, D. Ta, V.-H. Nguyen, E. Lou, and L. H. Le, *Nonlinear inversion of ultrasonic dispersion curves for cortical bone thickness and elastic velocities,* Ann. Biomed. Eng. **47**, 2178 (2019).

[15] L. Zhu, X. Duan, and Z. Yu, *On the identification of elastic moduli of in-service rail by ultrasonic guided waves,* Sensors **20**, 1769 (2020).

[16] C. Grünsteidl, T. Berer, M. Hettich, and I. Veres, *Using zero-group-velocity Lamb waves to determine thickness and bulk sound velocities of isotropic plates,* AIP Conf. Proc. **2102**, 1 (2019).

8

[17] M. Bernal, I. Nenadic, M. W. Urban, and J. F. Greenleaf, *Material property estimation for tubes and arteries using ultrasound radiation force and analysis of propagating modes,* J. Acoust. Soc. Am. **129**, 1344 (2011).

[18] M. Ponschab, D. A. Kiefer, and S. J. Rupitsch, *Simulation-based characterization of mechanical parameters and thickness of homogeneous plates using guided waves,* IEEE Trans. Ultrason. Ferroelectr. Freq. Control **66**, 1898 (2019).

[19] C. Y. Chang and F. G. Yuan, *Dispersion curve extraction of Lamb waves in metallic plates by matrix pencil method,* Proc. SPIE **10168**, 1 (2017).

[20] P. Zabbal, G. Ribay, B. Chapuis, and J. Jumel, *Multichannel multiple signal classification for dispersion curves extraction of ultrasonic guided waves,* J. Acoust. Soc. Am. **143**, EL87 (2018).

[21] J. L. Deán, C. Trillo, Á. F. Doval, and J. L. Fernández, *Determination of thickness and elastic constants of aluminum plates from full-field wavelength measurements of single-mode narrowband Lamb waves,* J. Acoust. Soc. Am. **124**, 1477 (2008).

[22] M. Sale, P. Rizzo, and A. Marzani, *Semi-analytical formulation for the guided waves-based reconstruction of elastic moduli,* Mech. Syst. Signal Process. **25**, 2241 (2011).

[23] Y.-C. Lee and S.-W. Cheng, *Measuring Lamb wave dispersion curves of a bilayered plate and its application on material characterization of coating,* IEEE Trans. Ultrason. Ferroelectr. Freq. Control **48**, 830 (2001).

[24] J. Foiret, J.-G. Minonzio, C. Chappard, M. Talmant, and P. Laugier, *Combined estimation of thickness and velocities using ultrasound guided waves: A pioneering study on in vitro cortical bone samples,* IEEE Trans. Ultrason. Ferroelectr. Freq. Control **61**, 1478 (2014).

8

9

Conclusions

The work presented in this thesis paves the way towards self-calibrated high-precision ultrasonic clamp-on flow measurements using matrix transducer arrays. This sensor will minimize human operation error by estimating the properties of the pipe and the liquid needed to achieve self-calibration, rendering manual calibration unnecessary anymore, which will simplify installation procedures and enhance safety. Furthermore, this state-of-the-art will expand the toolkit of techniques to perform more stable, accurate and repeatable measurements in a wide range of situations, independent of pipe size, mechanical properties, or changes in temperature, density and/or composition of the flow. Moreover, it would be possible to perform measurements during laminar and turbulent flow regimes, expanding the range of linearity of the sensor to a very wide range of Reynolds numbers. Also, multi-path measurements will be able to reconstruct flow profiles. These features will expand the areas of application of ultrasonic clamp-on flow meters, and contribute in making industrial processes such as product monitoring distribution, and custody transfer much more automated and accurate.

9.1. Matrix array design and performance of first linear array prototype

9.1.1. Design

A matrix transducer array for ultrasonic clamp-on flow measurements in a wide range of liquids and pipe sizes was designed in Chapter 2. To achieve this, three requirements were defined for the flow meter:

1. Measurement accuracy $\leq 1\%$ for flow speeds $\geq 1\,\mathrm{m/s}$.

2. Liquid sound speed range between $1000 - 2000\,\mathrm{m/s}$, with attenuation coefficients up to $1\,\mathrm{dB/MHz.cm}$.

3. Able to achieve auto-calibration.

To achieve these, the following array requirements were derived:

1. Operational bandwidth between $0.2 - 2\,\mathrm{MHz}$.

2. Center frequency of $1\,\mathrm{MHz}$.

3. Array pitch of $0.72\,\mathrm{mm}$.

4. SNR $\geq 20\,\mathrm{dB}$.

Guided waves propagating in the pipe wall introduce absolute errors in the flow measurements. Therefore, it was necessary to estimate how much suppression of these guided waves was needed to achieve the desired measurement accuracy. This was achieved by estimating how much phase shift do spurious guided waves, with different amplitude and phase shift levels, introduce on "clean" upstream and downstream flow measurement signals. It was shown in Chapter 2 that, for inter-array distances $\geq 5\,\mathrm{cm}$, the amplitudes of guided waves should be below $55\,\mathrm{dB}$

relative to the longitudinal wave mode refracting from the liquid and containing information about the flow speed.

With Finite Element simulations, it was found that guided waves have amplitudes which are already $20\,\mathrm{dB}$ below the desired wave mode. Therefore, it was only necessary to achieve the suppression of the remaining $35\,\mathrm{dB}$. The method described in Chapter 3 was used to achieve this, which basically consists in using a transducer array to implement, in transmission, a filter in the frequency - horizontal wavenumber (i.e. $f - k_x$) domain. Simultaneously, with this method, it was possible to estimate the amount of transducer array elements needed to suppress the guided waves by the desired amount and which would also produce an incidence acoustic wave with a beam width upon reception similar to the receiving array aperture, which would optimize the SNR of the flow measurements. With this analysis it was found that the matrix array should have 37 elements along the axial direction of the pipe, and 17 along the circumferential direction, which resulted in a total amount of 629 transducer array elements.

When an acoustic wavefield impinges a solid, wave mode conversion occurs, i.e. longitudinal and shear waves are excited. In a solid-liquid interface, the angle of refraction of the shear wave in the solid into the liquid is usually higher than the angle of refraction of the longitudinal wave in the solid into the liquid. Common ultrasonic clamp-on flow meters make use of this fact, and place angled wedges between the single-element transducer and the pipe wall. The angle of these wedges is large-enough to excite only shear waves in the pipe wall. Usually, plastic wedges are used, with angles ranging between $20 - 30\,^\circ$. However, these wedges also have a relatively low acoustic impedance ($Z \approx 2.5\,\mathrm{MRayl}$) compared to that of typical metal pipe walls ($Z \approx 46\,\mathrm{MRayl}$), which results in most of the acoustic energy being reflected back at the wedge - pipe wall interface. To improve this, lead was chosen as coupling piece between the transducer array and the pipe wall. There were two main reasons for this. First, due to their higher impedance ($Z \approx 24.6\,\mathrm{MRayl}$) relative to commonly used plastic wedges, they offer the possibility to proportionally increase SNR by a factor of ≈ 10. Second, the longitudinal bulk wave sound speed of lead ($c = 2200\,\mathrm{m/s}$) is very similar to that of plastic ($c = 2290\,\mathrm{m/s}$), which would allow to achieve wave mode conversion in the pipe wall under the same range of incidence angles.

The design of the acoustic stack of the array was performed using the Finite Element simulation software PZFlex, where the material properties and dimensions of each layer, including the PZT, the backing and the lead coupling piece, were optimized to achieve a thickness resonance frequency centered at $1\,\mathrm{MHz}$, and without any lateral resonance modes within the bandwidth of interest, i.e. $0.2 - 2\,\mathrm{MHz}$, as desired. To maximize SNR, it was necessary to choose a piezo-material able to be sub-diced, and with a high dielectric constant (ϵ_{33}^S) and coupling factor (k_{33}). For this reason, PZT was used, specifically HK1HD ($\epsilon_{33}^S = 6800$, $k_{33} = 0.72$). Furthermore, to minimize guided wave propagation within the PCB layer, a backing material was designed and fabricated. This material was designed with an acoustic impedance equal to the of the PCB. i.e. $Z = 6.7\,\mathrm{MRayl}$, and and attenuation coefficient, at $1\,\mathrm{MHz}$, of $5\,\mathrm{dB/MHz.cm}$. In practice, with a mix of epoxy and tungsten

9

particles, it was possible to fabricate a backing with the desired acoustic impedance and with an attenuation coefficient, at $1\,MHz$, of $15\,dB/MHz.cm$, which was enough for the application.

Before computing the expected SNR levels, it was necessary to estimate the noise level. Using the Johnson-Nyquist equation, it was estimated that a single piezo-element would produce, at room temperature, a noise of approximately $1.1\,\mu V_{RMS}$. With this reference value, it was possible to use the sonar equation - which took into account transducer efficiency, acoustic wave propagation, diffraction and attenuation - and compute the expected SNR levels for two measurement paths: longitudinal waves in the pipe wall and shear waves in the pipe wall. For the first one, six bounces (v-shapes) of the longitudinal wave in the liquid were considered before being recorded, and for the second one, only two bounces of the same wave mode were considered. The reported values, at the center frequency of $1\,MHz$, showed SNR levels above the required $20\,dB$ for all considered liquids (i.e. $\alpha \leq 1\,dB/MHz.cm$).

With the possibility of choosing either travel path for performing ultrasonic clamp-on flow measurements, the practical scenarios on which the designed matrix array could be used is expanded. For instance, longitudinal waves in the pipe wall could be used whenever the pipeline has very limited dimensions and only small incidence angles are possible, and shear waves in the pipe wall could be used when measuring high attenuating liquids and shorter travel paths of the acoustic beams are required.

9.1.2. Prototype sensor and flow measurements

Based on the proposed matrix transducer design, a 36-element linear array prototype was built and acoustically characterized. A plate of PZ26 was sub-diced to produce the piezo elements. The array was acoustically coupled to a PCB and backing layer on the back side, and to a flat $11\,mm$-thick lead piece on the front side. The fabricated acoustic stack was placed on a $1\,mm$-thick stainless steel plate and finally on water, where hydrophone measurements were taken to estimate its transmit transfer function. At a resonance frequency of $\approx 1.12\,MHz$, an efficiency of $\approx 0.82\,kPa/V$ was measured in water, which corresponded reasonably well with the $\approx 0.88\,kPa/V$ expected from simulations. Furthermore, a $-20\,dB$ bandwidth between $1.38 - 1.70\,MHz$ was measured. On the other hand, two differences were observed relative to the simulations, but these were due to some practical limitations during the measurements. First, the resonance peaks seemed to be shifted by approximately $10\,\%$, which may be explained by a few factors. The thin layers of glue may vary slightly in thickness along the array. Also, the nominal values of the PZT parameters used in simulations may report, in practice, uncertainties up to $10\,\%$. Moreover, the backing and lead layers are not standardized materials, and their simulated properties probably also varied slightly from those used in simulations. Second, the measured bandwidth was a bit narrower than expected because, due to space limitations in the water tank, the measurements were performed near the natural focus of the array, which affected the diffraction correction term, producing a a spike-like shape around the resonance frequency.

Furthermore, with this same setup, time delays were applied on the piezo-elements to asses the beam steering capabilities of the fabricated linear array, including wave mode conversion in the steel layer. Acoustic beams were steered under angles up to $40°$. Along the azimuth of the fabricated array, linear scans of the acoustic wavefield in water were measured. The location of the peak pressures on these profiles showed very good agreement with the theory, and also proved the ability to induce only shear waves in the metal.

An ultrasonic clamp-on flow meter was built with two of these fabricated linear arrays, as shown in Chapter 6. The arrays were place on the center of a $30\,cm$-long stainless steel pipe with an inner diameter of $40\,mm$. This pipe section was placed on a custom-built flow loop filed with water, where it was possible to measure flow speeds up to $0.6\,m/s$. The built system reported a high level of reciprocity. At zero flow conditions, for each measurement scenario, i.e. longitudinal and shear waves in the pipe wall, flow speeds of $\Delta t \leq 0.008\,m/s$ and $\Delta t \leq 0.003\,m/s$ were measured, respectively, with median absolute deviations of $mad = 0.03\,m/s$ and $mad = 0.02\,m/s$, respectively. On the other hand, for the highest possible reference flow speed, i.e. $V_{ref} = 0.6\,m/s$, the measured flow speeds with the fabricated prototype were $V_f = 0.59\,m/s$ and $V_f = 0.60\,m/s$, respectively, with a median absolute deviation of $mad = 0.06\,m/s$ and $mad = 0.04\,m/s$, respectively. Finally, a linear fit between the measured and reference flow speeds showed very good correlation, reporting slopes of ≈ 0.977 and ≈ 1.006, respectively.

9.2. Suppression of guided waves in transmission

As mentioned before, guided waves in the pipe wall represent a serious problem during ultrasonic clamp-on flow metering since they introduce absolute errors in the measurements. To overcome this, common sensors place absorbing layers around the pipe wall with the purpose of attenuating the guided waves. Also, the inter-transducer distance may be adjusted to achieve proper time-windowing of the desired longitudinal wave mode refracting from the liquid. However, it was discussed in Chapter 3 that these solutions are not always doable or practical. The installation of absorbing layers around a pipe wall is difficult and sometimes not possible due to other layers already in place (e.g. for thermal isolation). On the other hand, the amount of dispersive guided wave modes grows proportionally with frequency and pipe wall thickness, increasing the probability of overlap of the guided waves with the wave mode of interest, making proper time-windowing no longer possible.

Transducer arrays may be used to suppress guided waves while performing ultrasonic clamp-on flow metering without the need to use absorbing layers or conveniently moving the transducers along the pipe wall. The method to achieve this was described in Chapter 3. It consists of cleverly manipulating the aperture of a transducer array to suppress the excitation of guided waves: the phase of the elements is used to steer a well-defined flat wavefront, and the amplitude is used to suppress the excitation of the guided waves.

The proposed method consists in finding the amount of array elements that produce an acoustic beam with side lobe levels below the desired amount of sup-

9

pression of guided waves, but that also has a beam width, upon reception, equal or very similar to the receiving aperture, which would optimize SNR. Then, considering the most problematic guided wave mode, proper beam steering may be carried-out to avoid its excitation above the required level after each bounce of the acoustic beam within the pipe.

From Chapter 2 it was known that $35\,\mathrm{dB}$ of suppression of the guided waves from the pipe wall were needed to achieved the required flow measurement accuracy of $1\,\%$. With the method proposed in Chapter 3, the matrix array apertures needed to achieve these levels of guided wave suppression along the axial (37 elements) and circumferential (17 elements) direction of the pipe, were estimated.

Finite Element simulations were performed to test the proposed method. A $40\,\mathrm{mm}$-thick water column layer was simulated between two $1\,\mathrm{mm}$-thick stainless steel plates. On the vacuum-loaded side of one of the plates, a 37-element linear array with a center frequency of $1\,\mathrm{MHz}$ was placed. The amplitudes and phases of the linear array were manipulated according to the method described in Chapter 3 to steer an acoustic beam through the steel plate and into the water. The time - space (i.e. $t - x$) and $f - k_x$ information showed the suppression of guided waves by the desired amount of $35\,\mathrm{dB}$ after each reflection of the acoustic beam at the water-steel interface. This was replicated experimentally, where two commercial ATL linear array probes were used, and the measurements showed very good agreement with the simulations.

9.3. Sensor auto-calibration

Before metering, ultrasonic clamp-on flow meters are calibrated, i.e. the correct position between the transducers along the pipe wall is found. As shown in Chapter 2, this position depends on the sound speeds of the pipe wall, the pipe diameter, and the sound speed of the liquid. In practice, during installation, the operator does not have accurate information on these parameters. Therefore, the calibration process of the sensor consists in manually moving one of the transducers relative to the other one along the pipe wall until a peak amplitude is recorded. This manual calibration process is cumbersome and time consuming, especially in confined areas. For this reason, it was shown in Chapter 4 how to make use of two transducer arrays to measure the necessary parameters of the pipe and the liquid that would characterize the travel paths of the acoustic beams, which combined with beam steering capabilities of such arrays would make possible the automatic calibration of the sensor without having to manually move the transducers.

Three measurement procedures were proposed in Chapter 4. The first method consists in estimating the pipe wall thickness (h) and bulk wave sound speeds (i.e. longitudinal and shear wave speed, c_L and c_T, respectively), and it consisted in exciting and measuring guided waves in the pipe wall and along the axis of the pipe because it is known that the dispersive behavior of such wave modes depends on these three parameters. The measured $t - x$ information was visualized in the $f - k_x$ domain, where the dispersion curves were identified, and the $f - k_x$ coordinates of the wave modes were extracted. Then, a quantitative comparison between measured and theoretical dispersion was implemented: the difference

between the measured and theoretical coordinates were considered and reported a certain fitting error. Finally, the desired pipe parameters (h, c_L and c_T) would be related to the theoretical dispersion curve that reports the lowest fitting error relative to the measured dispersion curve.

From these measurements, it was found that symmetric and anti-symmetric guided wave modes are not equally sensitive to the same pipe wall parameter. The zero-order symmetric wave mode (A_0) was found to be more sensitive to c_L and h, while the zero-order anti-symmetric wave mode (S_0) was more sensitive to c_T. Therefore, in practice, and depending on the available system bandwidth, this sensitivity to the parameters should be taken into account.

The second measurement proposed in Chapter 4 consisted in estimating the pipe diameters (inner and outer, OD and ID, respectively) by exciting and measuring the transit time of a circumferential guided wave around the pipe wall after propagating a full circumference. To optimize the accuracy in the estimation of the transit time of the recorded wave mode, its associated time signal was corrected for dispersion (i.e. the dispersion curve gets effectively flattened-out).

Lastly, the proposed measurement to estimate the sound speed of the liquid (c_{liquid}) consisted in performing a pulse echo measurement using the matrix transducer array elements located along the circumferential direction of the pipe. As discussed in Chapter 4, this measurement may also be used to monitor the alignment of the matrix arrays on the pipe wall.

The first two measurements proposed in Chapter 4 were performed with simulated and measured data. Experiments were performed on stainless steel ($h = 1, \text{mm}$, $OD = 42, \text{mm}$) and aluminium pipes ($h = 1, \text{mm}$, $OD = 60, \text{mm}$) using commercial ATL probes. In practice, deviations from nominal values ranged around a few %. However, these are not definitive about the accuracy of the methods due to the bandwidth (i.e. transducer)-dependent sensitivity of the measured dispersion curves to the different pipe wall parameters. Simulation results for the third calibration procedure showed $< 0.4, \%$ discrepancies with the ground truth.

9.4. Decreasing flow measurement uncertainty with nonlinear wave propagation

It is known that the nonlinear nature of wave propagation becomes significant when the input amplitudes of the signals is high enough. During propagation, the time signal associated to the acoustic wave, which has an initial frequency component of f_0, distorts in such a way that generates harmonic frequency components, i.e. $n.f_0$, where $n = 2, 3....$ In Chapter 7 it was shown and discussed how this phenomenon may be exploited to improve the uncertainty of ultrasonic flow meters.

The precision of most ultrasonic flow measurement systems is limited by random noise (e.g. the flow, the electrical components, the transducers themselves). Therefore, the harmonics generated during nonlinear wave propagation may be treated independently from the fundamental.

Chapter 7 described in-line ultrasonic flow measurements performed in water by inducing nonlinear wave propagation. A fundamental and a 2nd harmonic frequency

component were generated during wave propagation in the liquid, and recorded by the receiving transducers. The upstream and downstream signals related to the bandwidth centered around the 2nd harmonic frequency component showed a similar transit time difference to the one reported by the time signals associated to the bandwidth centered around the fundamental frequency component. Therefore, for each measured flow speed, the amount of flow estimates doubled within the same system bandwidth, which decreased the overall uncertainty. The measurement results were corroborated with simulations using the Khokhlov-Zabolotskaya-Kuznetsov (KZK) equation, which accounted for diffraction, attenuation and nonlinearity of the acoustic wave during wave propagation, and where the flow speed V_f was added linearly to the small-signal sound speed of the medium c_0.

Simulations and measurements reported a linear relation between the flow speed V_f and the transit time difference Δt. They were performed for relatively low flow speeds, in which wave distortion was generally similar for upstream and downstream time signals. However, simulations considering much higher flow speeds showed that the relation between V_f and Δt is no longer linear. Part of the explanation for this was that commonly used cross-correlation (or zero-crossing) algorithms implemented to estimate Δt intrinsically assume that both functions have the same shape, which does not hold within the context of high flows because the equivalent sound speeds between both upstream and downstream time signals may differ very much.

Regardless of these extreme (high flow speed) scenarios, it was also discussed in Chapter 7 how nonlinear wave propagation could already be implemented in practical, not extreme, ultrasonic flow metering situations. Usually, flow meters are designed taking into account the most attenuating liquid, therefore, in not so extreme conditions, the sensors should be equipped with enough power to subject the transducers to high-enough voltages, which would excite acoustic waves that would distort non-linearly during propagation and generate a 2nd harmonic frequency component. On the other hand, current ultrasonic flow meters of gases already implement very large voltages ($+100\,\text{V}$) to overcome the acoustic impedance mismatch between the transducer and the gas. Therefore, nonlinear wave propagation may already be occurring, and it would be a matter of using the extra information provided by the 2nd harmonic to increase the precision of the flow estimate.

9.5. Final remarks and future recommendations

Flow measurement results with the fabricated linear arrays presented in Chapter 6 motivate, as a next step, the fabrication of the full matrix array designed in Chapter 2. With two matrix arrays it will be possible to also estimate the properties of the pipe and the liquid necessary to achieve sensor self-calibration by performing the measurements proposed in Chapter 4. These measurements should also be further investigated. Although their feasibility was clearly demonstrated, a more extensive study would provide more knowledge about their precision and robustness.

The work presented in this thesis also leads the path towards other research directions. For instance, a matrix transducer array that also exploits nonlinear wave

propagation during ultrasonic flow metering could be designed. With such sensor it could be possible to exploit the beam steering capabilities of arrays, as shown in Chapter 2 and Chapter 6, and the extra information of the harmonic frequency component(s), as shown in Chapter 7. Literature about inter-leaved transducers arrays for medical imaging applications is already available, which could be used as a starting point to design this matrix array.

On the other hand, some materials engineering could be implemented to fabricate a safer custom-made material that could be used as coupling piece between the transducer arrays and the pipe wall. However, this material should have, in principle, a similar density and longitudinal bulk wave sound speed as the currently used lead.

Finally, with matrix arrays as flow sensors, it would be possible to investigate the potential to perform flow profile measurements by steering the acoustic beam both in the axial and circumferential direction of the pipe. Next to this, the effect of flow turbulence could be studied in more detail. Furthermore, flow measurements under the condition of partially filled pipes or multi-phase fluids could start to be considered.

9

A

Derivation of the equation for the flow speed – linear and nonlinear Version

In an in-line flow meter, the upstream and downstream transit times are

$$
\begin{aligned}
t_u &= \frac{D}{\sin\theta} \frac{1}{c_0 - v_m \cos\theta}, \\
t_d &= \frac{D}{\sin\theta} \frac{1}{c_0 + v_m \cos\theta}.
\end{aligned}
\tag{A.1}
$$

These expressions can be combined into

$$
\begin{aligned}
\frac{1}{t_d} - \frac{1}{t_u} &= \frac{t_u - t_d}{t_u t_d} \\
&= \frac{\sin\theta}{D}(c_0 + v_m \cos\theta - c_0 + v_m \cos\theta) \\
&= 2\sin\theta\cos\theta \frac{v_m}{D} \\
&= \sin 2\theta \frac{v_m}{D},
\end{aligned}
\tag{A.2}
$$

from which it follows that

$$
v_m = \frac{D}{\sin 2\theta} \frac{t_u - t_d}{t_u t_d} = \frac{D}{\sin 2\theta} \frac{\Delta t}{t_u t_d}.
\tag{A.3}
$$

However, this does not yet give a linear relation between the flow speed v_m and the transit time difference Δt, because $t_u t_d$ still depends on v_m

$$t_u t_d = \left(\frac{D}{\sin\theta}\right)^2 \frac{1}{(c_0 - v_m \cos\theta)(c_0 + v_m \cos\theta)}$$
$$= \left(\frac{D}{\sin\theta}\right)^2 \frac{1}{c_0^2 - v_m^2 \cos^2\theta}. \tag{A.4}$$

A.1. Low flow speed

If $v_m \ll c_0$, we can neglect the $v_m^2 \cos^2\theta$ term in the denominator of Eq. A.4, and substitution into Eq. A.3 then yields

$$v_m = \frac{D}{\sin 2\theta}\left(\frac{\sin\theta}{D}\right)^2 c_0^2 \Delta t = \frac{c_0^2 \tan\theta}{2D}\Delta t, \tag{A.5}$$

which is the linear relation between v_m and Δt.

A.2. Large flow speed

If $v_m \ll c_0$ no longer holds, Eq. A.4 can directly be substituted into Eq. A.3 to obtain

$$v_m = \frac{D}{\sin 2\theta}\left(\frac{\sin\theta}{D}\right)^2 \Delta t(c_0^2 - v_m^2 \cos^2\theta)$$
$$= \frac{\tan\theta}{2D}\Delta t(c_0^2 - v_m^2 \cos^2\theta). \tag{A.6}$$

The inverse of this relation is

$$\Delta t = \frac{2D}{\tan\theta}\frac{v_m}{c_0^2 - v_m^2 \cos^2\theta}. \tag{A.7}$$

Eqs. A.6 and A.7 are nonlinear relationships between v_m and Δt. The solutions for v_m are

$$v_m = A(-1 \pm \sqrt{1 + B}), \tag{A.8}$$

with:

$$A = \frac{2D}{\sin 2\theta \Delta t}, \tag{A.9}$$

$$B = \left(\frac{c_0 \Delta t \sin\theta}{D}\right)^2. \tag{A.10}$$

For the physically valid solution, the + sign in Eq. A.8 has been chosen.

B

Sensitivity analysis of Lamb waves

In Chapter 8, we often refer to the reliability extracting parameters by inverting Lamb wave modes, or the sensitivity of such a procedure to each parameter. A well-known approach to quantify this information is to perform a so-called sensitivity analysis. In this case, this would be done by considering the error function E (corresponding to the MAPE values) and computing its first derivatives around the minimum. For example, the sensitivity of E with respect to variations on the longitudinal speed axis can be calculated as

$$S(c_L, P) = \left.\frac{\partial E}{\partial c_L}\right|_P, \tag{B.1}$$

where S is the sensitivity, c_L is the longitudinal speed, and |P indicates that the derivative is evaluated at the coordinates (c_L^P, c_T^P, h^P) of the point P, which corresponds to the minimum MAPE value.

This value of S expresses how fast the function E grows for small variations of the c_L coordinate. However, it does not provide any information on the existence and location of the local minima of comparable depth that can exist within the MAPE space. As such, the sensitivity analysis does not show that a small variation in MAPE could lead to large variations in e.g. c_L. The SAM and LEV values were introduced to provide this necessary information.

Figure B.1 shows data from the experiment of Fig. 8.6. The left panel is the same as in Fig. 8.6, while the right panel shows all the points within the LEV, projected onto the $h - c_L$ plane. The points highlighted as P1 and P2 in the right panel correspond to the minimum and second-minimum MAPE points, respectively. The coordinates of P1 are: $c_L = 5500$m/s; $c_T = 3100$m/s; $h = 1.0$mm; The coordinates of P2 are: $c_L = 4850$m/s; $c_T = 3150$m/s; $h = 1.1$mm. The MAPE of P1 is 0.439%, the MAPE of P2 is 0.441%. These numbers show that the two curves corresponding

to P1 and P2 are very similar to each other; the smallest alteration of P1 could turn it into P2, resulting in an extracted longitudinal speed of $c_L = 4850\text{m/s}$ instead of $c_L = 5500\text{m/s}$.

The sensitivity analysis E in the c_L direction around P1, $S(c_L, P1) = 0.5\text{ms/m}$ (i.e. the MAPE grows by approximately 6% in a step of $50\,\text{m/s}$ on the c_L axis) is limited to a local description along a single axis, and it does not provide any information to describe the situation shown in Figure B.1. The SAM_{c_L} value of $604\,\text{m/s}$, on the other hand, accounts for the entire LEV (acros all three axes), and it does show that small variations of the MAPE could potentially lead to large variations in longitudinal speed. As such, in this situation the LEV and SAM values are necessary to provide the quantitative description that a standard sensitivity analysis cannot supply.

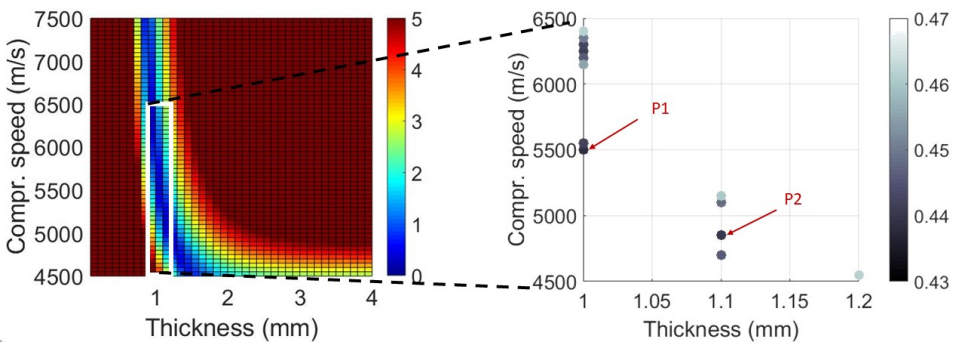Figure B.1: Left panel: the $h - c_L$ slice of the MAPE error for the A_0 wave mode extracted from the experiment on the steel pipe, at fixed $c_T = 3100\text{m/s}$. Right panel: the LEV of this dataset, collapsed onto the $h - c_L$ plane. Highlighted are P1 and P2, the points corresponding to the lowest and second-lowest values of MAPE, respectively. The colors in both panels represent the MAPE.

Summary

Ultrasonic clamp-on flow meters can be installed on pipelines without the need to interrupt the flow or to perforate the pipe wall, which enhances safety, reduces maintenance, and saves costs in many industrial applications. However, their operational stability is limited, their installation requires a-priori knowledge of the properties of the pipe and the liquid to perform a cumbersome manual alignment of the transducers along the pipe wall, and they are unable to measure flow profiles (in contrast to expensive multi-path in-line flow meters), which limits their linearity. An ultrasonic clamp-on flow meter consisting of two matrix transducer arrays has been proposed as a solution to tackle these drawbacks. With matrix arrays, multi-path measurements may be performed. Furthermore, the travel paths of the acoustic beams may be automatically adjusted to account for dynamic temperature, pressure and/or flow composition changes, which may improve the overall stability of the sensor and increase its linearity across a wide range of laminar and turbulent flow regimes. Also, due to its potential for $f - k_x$ filtering of unwanted wave modes, the matrix arrays may also be installed closer to other pipeline features, such as valves and flanges. In addition, prior to flow metering, the matrix arrays may be used to measure the properties of the pipe and the liquid necessary to characterize completely the travel paths of the acoustic beams and enable the auto-calibration of the flow sensor without the need to move the transducers manually. Moreover, during flow metering, transducer arrays may be cleverly excited to suppress problematic guided waves that propagate within the pipe wall and which introduce offset errors in the flow measurements.

In this thesis, the design of such matrix array has been proposed, together with the required measurements to achieve self-calibration and a method to suppress guided waves while performing ultrasonic clamp-on flow measurements. The acoustic design of the matrix array was performed using Finite Element Modeling, where linear isotropic elasticity was assumed, a visco-elastic model was adopted, and the anisotropic piezo-electric constitutive equations were solved for the piezo-materials. The acoustic stack of the designed matrix array consisted of 36 elements along the axial direction and 16 elements along the circumferential direction of the pipe, a light backing layer with an acoustic impedance of $Z = 6.7\,\mathrm{MRayl}$ and an attenuation coefficient of $\alpha = 5\,\mathrm{dB/MHz.cm}$, and a a lead coupling piece between the matrix array and the pipe wall. The resonance frequency of the acoustic stack was $1\,\mathrm{MHz}$ and it reported a $-20\,\mathrm{dB}$ bandwidth between $0.2 - 2\,\mathrm{MHz}$. Moreover, at resonance, a transmit efficiency of $36.4\,\mathrm{kPa/V}$ and a receive sensitivity of $9.2\,\mathrm{\mu V/Pa}$ were obtained, which guaranteed SNR levels $> 20\,\mathrm{dB}$ for liquids with attenuation coefficients between $0 - 1\,\mathrm{dB/MHz.cm}$.

The designed matrix array inspired the fabrication of a first linear array prototype consisting of 36 piezo-elements. The measured performances of this array had

a good agreement with the simulations. Furthermore, the fabricated array was able to steer acoustic beams up to $\approx 46°$ through metal layers, which guaranteed its capability to excite shear waves in the pipe wall and to perform ultrasonic clamp-on flow measurements for a wide range of liquids, i.e. with sound speeds between $1000 - 2000 \, \mathrm{m/s}$. Based on these results, an ultrasonic clamp-on flow meter was built using two of these linear arrays and placed on a custom-built flow loop filled with water. At zero-flow conditions, the measurement system (acoustics and electronics) reported a high level of reciprocity, with transit time differences $\Delta t < 1 \, \mathrm{ns}$ between upstream and downstream time signals. Furthermore, flow measurements were performed using an excited longitudinal or shear wave in the pipe wall, and in both scenarios, the measured and reference flow speeds reported a correlation factor > 0.99.

A method to suppress, in transmission, guided waves in the pipe wall, and at the same time perform flow measurements with optimal SNR using a transducer array has been proposed. The method consisted in cleverly manipulating the phase and the amplitude of each individual array element. The phases were used to steer acoustic beams with clear wave fronts, and the amplitudes were used to adjust the level of the side lobes to the desired suppression level of the guided waves. Optimal SNR for flow measurements is achieved with the proposed method because it also reports the necessary array aperture, i.e. number of elements, needed to produce an acoustic beam with an equal (or very similar) width as the receiving array aperture upon reception. Finite Element simulations and experiments using commercial probes were performed to validate the method: the amplitudes of Lamb waves on a $1 \, \mathrm{mm}$-thick stainless steel plate were suppressed by $35 \, \mathrm{dB}$ relative to the amplitude of the longitudinal wave impinging the plate from a water column.

Three measurement procedures were proposed to estimate the properties of the pipe and the liquid needed to achieve sensor auto-calibration. The first procedure consisted in exciting and measuring dispersion curves along the pipe wall, and implementing an algorithm that fitted/compared the measured dispersion curves with theoretical ones and estimate, from the best fit, the bulk wave sound speeds and thickness of the pipe wall. The second procedure consisted in exciting a guided wave around the pipe wall and measuring its transit time after a full circumferential travel path to estimate the diameter of the pipe. For more accuracy in estimating the transit time of this wave, a dispersion correction algorithm was also proposed and implemented. The third procedure consisted in a pulse-echo measurement to estimate the sound speed of the liquid. The feasibility of these procedures was validated in simulations and in experiments using commercial probes and common stainless steel and aluminium pipes, and the obtained parameters of the pipe and the liquid differed only a few percent from nominal values.

On the other hand, it was also proposed that nonlinear wave propagation may be exploited to extract more information about the flow and achieve more precise measurements with the same operational bandwidth of the system. A custom-built in-line flow meter consisting of two single-element commercial transducers was built to test this idea. At low flow speeds, relative to the sound speed of the liquid, the transit time differences between upstream and downstream time signals of the

2nd harmonic (which had $25\,dB$ lower SNR relative to the fundamental) reported a linear relation with flow speed. Furthermore, in combination with the transit time differences of the fundamental, the uncertainties of the estimated flow speeds were lower than those reported by the fundamental alone. These results where confirmed with simulations using the KZK equation. Moreover, it was discussed the feasibility of how this method may be implemented in practical flow metering situations.

The research presented here has shown the great potential of matrix transducer arrays as self-calibrated ultrasonic clamp-on flow meters able to operate in a wide range of situations with minimum operator/user input. Overall, in terms of performance, linearity, accuracy and repeatability, this sensor will bring ultrasonic clamp-on flow meters closer to their in-line counterparts, which will ultimately expand the application space of clamp-on flow meters.

Samenvatting

Opklembare ultrasone stromingsmeters kunnen zonder de stroming te onderbreken of de pijpwand te doorboren worden geïnstalleerd, waardoor in veel industriële toepassingen de veiligheid wordt verbeterd, minder onderhoud nodig is en kosten worden bespaard. Dat komt echter met een beperkte stabiliteit, installatie die voorkennis van de eigenschappen van de pijp en vloeistof vereist en een omslachtige handmatige uitlijning van de transducers op de pijpwand. Daarnaast zijn deze niet in staat stromingsprofielen te meten (in tegenstelling tot dure multi-pad in-lijn stromingsmeters) waardoor hun lineariteit beperkt is. Een opklembare ultrasone stromingsmeter die uit twee matrix transducenten bestaat, wordt als oplossing voorgesteld om deze nadelen aan te pakken. Matrix transducenten kunnen gebruikt worden om multipad metingen uit te voeren. Daarnaast kunnen de paden van de akoestische bundel automatisch worden aangepast om te compenseren voor veranderende temperaturen, drukverschillen en/of veranderingen in de stromingssamenstelling, waardoor de stabiliteit en lineariteit van de sensor kunnen worden verbeterd over een groot bereik aan laminaire en turbulente stromingen.

Doordat de matrix array de mogelijkheid biedt tot $f-k_x$ filteren van ongewenste golfsoorten kan hij dichter bij andere onderdelen van de pijpleiding, zoals kleppen en flenzen, worden geplaatst. Verder kan de matrix worden gebruikt om, voorafgaand aan de stromingsmeting, de eigenschappen van de pijp en de vloeistof te meten die nodig zijn om het volledige pad van de akoestische golven te bepalen. Daarmee wordt het automatisch kalibreren mogelijk gemaakt, zonder dat transducenten handmatig verplaatst dienen te worden. Daarnaast kunnen, tijdens de stromingsmeting, de transducenten op een slimme manier aangestuurd worden, waardoor problematische geleide golven, die zich voortplanten in de pijpwand en offset fouten introduceren, in de stromingsmeting onderdrukt kunnen worden.

In dit proefschrift wordt een dergelijk ontwerp voor een matrix array voorgesteld, samen met de benodigde metingen om zelf-kalibratie te realiseren en een methode om de geleide golven te onderdrukken tijdens het uitvoeren van stromingsmetingen met opgeklemde ultrasone meters. Het akoestisch ontwerp van de matrix array werd uitgevoerd aan de hand van eindige elementen modellen, waarbij van lineaire isotropische elasticiteit werd uitgegaan, een visco-elastisch model werd gebruikt en waarbij anisotropische piëzo-elektrische constitutieve vergelijkingen werden opgelost voor het piëzo-materiaal. Het akoestisch ontwerp van de matrix array bestond uit 36 elementen in de axiale richting en 16 elementen in de omtrek-richting van de pijp, een achterlaag met een akoestische impedantie van $Z = 6.7\,\mathrm{MRayl}$ en een verzwakkings-coëfficiënt van $\alpha = 5\,\mathrm{dB/MHz \cdot cm}$, en een loden koppelstuk tussen de matrix array en de buiswand. De resonantiefrequentie van de transducent was $1\,\mathrm{MHz}$ met een $-20\,\mathrm{dB}$ bandbreedte tussen $0.2 - 2\,\mathrm{MHz}$. Verder werden op de resonantiefrequentie een zendefficiëntie van $36.4\,\mathrm{kPa/V}$ en een ont-

vangstgevoeligheid van $9.2\,\mu V/Pa$ verkregen, waarmee signaal-ruis verhoudingen groter dan $20\,dB$ gehaald kunnen worden in vloeistoffen met een verzwakkingscoëfficiënt tussen $0-1\,dB/MHz \cdot cm$.

De ontworpen matrix array gaf aanleiding tot de fabricage van een eerste lineair prototype bestaande uit 36 piëzo-elementen. De gemeten prestaties van deze array kwamen goed overeen met de simulaties.

Daarnaast was de geproduceerde array in staat om akoestische bundels door metalen lagen te sturen tot hoeken van $\approx 46\,°$, wat het mogelijk maakte om schuifgolven op te wekken in de pijpwand en ultrasone stromingsmetingen uit te voeren voor een groot bereik aan vloeistoffen, dat wil zeggen met geluidssnelheden van $1000-2000\,m/s$.

Op basis van deze resultaten werd een opklembare ultrasone flow meter gebouwd, bestaande uit twee van de genoemd lineaire arrays. Deze stromingsmeter werd op een zelfgebouwde stromingslus geplaatst, die gevuld was met water. Bij stromingsloze condities rapporteerde het meetsysteem (akoestisch en elektronisch) een hoge mate van reciprociteit, met looptijdverschillen tussen de arrays van $\Delta t < 1\,ns$ tussen de stroomopwaartse en stroomafwaartse tijdsignalen.

Bovendien werden stromingsmetingen uitgevoerd met zowel compressiegolven als schuifgolven in de pijpwand. In beide situaties resulteerde dit in een correlatiefactor > 0.99 tussen de gemeten en de referentie stromingssnelheid.

Tevens worden een methode om tijdens het uitzenden geleide golven te onderdrukken en tegelijkertijd stromingsmetingen uit te voeren met een optimale signaalruis verhouding voorgesteld. De methode bestaat uit het slim manipuleren van de fase en de amplitude van de individuele array elementen. De fases worden gebruikt om de akoestische golven te sturen, met een duidelijk golffront terwijl de amplitude gebruikt werd om het niveau van de zijlobben aan te passen aan de gewenste onderdrukking van de geleide golven. Met de genoemde methode werd een optimale signaal-ruis verhouding bereikt omdat het ook de benodigde openingshoek, en daarmee het. aantal elementen, van de array bepaalt die nodig zijn om een akoestische golf met eenzelfde (of vergelijkbare) breedte als de ontvangende array te genereren.

Eindige-elementen simulaties en experimenten met commerciële transducenten werden uitgevoerd om de methode te valideren: de amplitude van de Lamb-golven in een $1\,mm$ dikke roestvrijstalen plaat werden met $35\,dB$ onderdrukt in verhouding tot de amplitude van de compressiegolf die vanuit een waterkolom de plaat binnenvalt.

Ook worden drie meetmethode voorgesteld om de pijp- en vloeistofeigenschappen te kunnen schatten die nodig zijn voor het automatisch kalibreren van de sensor. De eerste methode bestaat uit het opwekken en meten van de dispersiekrommen langs de buiswand en het implementeren van een algoritme dat gemeten dispersiekrommen vergelijkt met de theoretische, en vervolgens de bulk geluidssnelheid en dikte van de pijpwand schat aan de hand van de beste overeenkomst.

De tweede procedure bestaat uit het opwekken van een geleidde golf rondom de pijpwand en het meten van de looptijd na een volledige rondgang, om de diameter van de pijp te schatten. Voor meer nauwkeurigheid werd er ook een dispersie

correctie algoritme voorgesteld en toegepast.

In de derde procedure wordt met een puls-echo meting de geluidssnelheid in de vloeistof bepaald. De haalbaarheid van deze procedures werd gevalideerd met simulaties en experimenten, waarbij commerciële transducenten evenals roestvrij-stalen en aluminium pijpen, gebruikt werden. De verkregen parameters verschilden daarbij maar enkele procenten van de nominale waarden.

Daarentegen wordt er ook voorgesteld dat niet-lineaire golfvoortplanting mogelijk benut kan worden om extra informatie over de stroming af te leiden en zo preciezere metingen te verkrijgen bij onveranderde bandbreedte van het systeem.

Een zelfgebouwde in-lijn stromingsmeter, gemaakt met commerciële transducenten bestaande uit twee losse elementen, werd gebruikt om dit idee te onderzoeken. Bij stromingssnelheden die laag waren ten opzichte van de geluidssnelheid in de vloeistof, werden looptijdverschillen tussen de stroomopwaartse en stroomafwaartse signalen van de 2^e harmonische (die een $25\,\mathrm{dB}$ lagere signaalruisverhouding had ten opzichte van de grondtoon) waargenomen, met een lineaire relatie tot stromingssnelheid. Gecombineerd met de looptijdverschillen van de grondtoon waren de onzekerheden van de geschatte stroomsnelheid kleiner dan die van de grondtoon alleen. Deze resultaten werden bevestigd met simulaties aan de hand van de KZK-vergelijking. Daarnaast werd de toepasbaarheid op stromingsmetingen in de praktijk besproken.

Het hier gepresenteerde onderzoek laat het grote potentieel zien dat matrix transducenten hebben voor zelf-calibrerende, opklembare ultrasone stromingsmeters die in veel verschillende situaties en met minimale handmatige handelingen gebruikt kunnen worden. Al met al zal deze sensor de opklembare ultrasone stromingsmeters dichter bij hun in-lijn tegenhanger brengen in termen van prestatie, lineariteit, nauwkeurigheid en herhaalbaarheid, wat uiteindelijk de toepassingsmogelijkheden van opklembare stromingsmeters zal vergroten.

Propositions

accompanying the dissertation

High-precision Versatile Ultrasonic Flow Meters Based on Matrix Transducer Arrays

by

Jack Mitchell MASSAAD MOUAWAD

1. Matrix arrays make manual calibration of clamp-on flow meters superfluous (this thesis).

2. Compared to existing clamp-on flow meters, and assuming a developed flow profile, flow meters with arrays can operate closer to pipeline obstacles (this thesis).

3. It is a missed opportunity that people do not use nonlinear wave propagation for ultrasonic flow metering (this thesis).

4. When modeling acoustic systems, you have to take into consideration the complex practical nature of the piezo-elements (this thesis).

5. Guided waves in pipe walls during ultrasonic clamp-on flow metering are the equivalent of having toxic family members. You cannot get rid of them, so you just have to figure out how to deal with them.

6. The hardest crises of our time (forced migration, terrorism, famine) are fostered, in large part, by depraved humans. Once this is understood, long-term solutions (instead of naive short-term ones) can be implemented.

7. If things are going well for too long in your scientific research, you have probably stopped doing science.

8. In capitalism, you can control your probability of dying of a heart attack. In socialism, you cannot control your probability of dying of starvation.

9. Statistically, cold weather seems to be correlated to the level of progress of a society.

10. Nothing makes your home country's food taste better than living abroad.

These propositions are regarded as opposable and defendable, and have been approved as such by the promotors Prof. dr. ir. N. de Jong & Dr. ir. M. D. Verweij.

Stellingen

behorende bij het proefschrift

High-precision Versatile Ultrasonic Flow Meters Based on Matrix Transducer Arrays

door

Jack Mitchell MASSAAD MOUAWAD

1. Matrix arrays maken handmatige kalibratie van clamp-on stromingsmeters overbodig (dit proefschrift).

2. Onder aanname van een ontwikkeld stromingsprofiel kunnen stromingsmeters met arrays dichter bij obstakels in de pijpleiding werken dan bestaande clamp-on stromingsmeters (dit proefschrift).

3. Het is een gemiste kans dat men voor ultrasone stromingsmeting geen gebruikmaakt van niet-lineaire golfpropagatie (dit proefschrift).

4. Voor het modelleren van akoestische systemen moet men rekening houden met het in de praktijk complexe karakter van piëzo-elementen (dit proefschrift).

5. Geleide golven in pijpwanden zijn voor ultrasone clamp-on stromingsmetingen hetzelfde als giftige familieleden. Je komt niet van hen af, dus je zult gewoon een manier moeten vinden om met hen om te gaan.

6. De zwaarste crises van onze tijd (gedwongen migratie, terrorisme, hongersnood) worden voornamelijk veroorzaakt door verdorven mensen. Wanneer dit duidelijk is, kunnen langetermijnoplossingen (in plaats van naïeve kortetermijnoplossingen) worden doorvoerd.

7. Als je wetenschappelijk onderzoek te lang goed gaat, ben je waarschijnlijk gestopt met het beoefenen van wetenschap.

8. In het kapitalisme heb je de kans dat jij aan een hartaanval sterft, in eigen hand. In het socialisme heb je de kans dat jij van de honger sterft, niet in eigen hand.

9. Statistisch gezien lijkt koud weer te correleren met de mate van vooruitgang van een samenleving.

10. Niets laat het eten uit je thuisland beter smaken dan wonen in het buitenland.

Deze stellingen worden opponeerbaar en verdedigbaar geacht en zijn als zodanig goedgekeurd door de promotors Prof. dr. ir. N. de Jong & Dr. ir. M. D. Verweij.

List of Publications

11. A. Sabbadini **J. Massaad**, P. L. M. J. van Neer, N. de Jong and M. D. Verweij. *On planar wave guide characterization by multi-parameter Lamb wave dispersion curve analysis*, Ultrasonics (submitted).

10. **J. Massaad**, P. L. M. J. van Neer, D. M. van Willigen, N. de Jong, M. A. P. Pertijs and M. D. Verweij. *Exploiting nonlinear wave propagation to improve the precision of ultrasonic flow meters*, Ultrasonics (submitted).

9. **J. Massaad**, P. L. M. J. van Neer, D. M. van Willigen, E. C. Noothout, N. de Jong, M. A. P. Pertijs and M. D. Verweij. *Design of a Matrix Transducer Array for Self-calibrated Ultrasonic Clamp-on Flow Measurements*, IEEE Trans. Ultrason. Ferroelectr. Freq. Control (submitted).

8. **J. Massaad**, P. L. M. J. van Neer, D. M. van Willigen, A. Sabbadini, N. de Jong, M. A. P. Pertijs and M. D. Verweij. *Measurement of Pipe and Fluid Properties with a Matrix Array-based Ultrasonic Clamp-on Flow Meter*, IEEE Trans. Ultrason. Ferroelectr. Freq. Control (submitted).

7. D. M. van Willigen, P. L. M. J. van Neer, **J. Massaad**, N. de Jong, M. D. Verweij and M. A. P. Pertijs. *An Algorithm to Minimize the Zero-Flow Error in Transit-Time Ultrasonic Flow Meters*, IEEE Trans. Instrum. Meas., Vol. 70, pp. 1-9, (2020).

6. **J. Massaad**, P. L. M. J. van Neer, D. M. van Willigen, M. A. P. Pertijs, N. de Jong and M. D. Verweij. *Suppression of Lamb wave excitation via aperture control of a transducer array for ultrasonic clamp-on flow metering*, J. Acoust. Soc. Am., Vol. 147(4), pp. 2670-2681, (2020).

5. **J. Massaad**, P. L. M. J. van Neer, D. M. van Willigen, M. A. P. Pertijs, N. de Jong and M. D. Verweij. *Towards a calibration-free ultrasonic clamp-on flow meter: Pipe geometry measurements using matrix arrays*, Proc. Meet. Acoust., Vol. 39(1), pp. 1-7, (2020).

4. **J. Massaad**, D. van Willigen, P. van Neer, N. de Jong, M. Pertijs and M. Verweij. *Acoustic Design of a Transducer Array for Ultrasonic Clamp-on Flow Metering*, IEEE Int. Ultrason. Symp., pp. 1133-1136, (2019).

3. D. van Willigen, P. van Neer, **J. Massaad**, M. Verweij, N. de Jong and M. Pertijs. *Minimizing the Zero-Flow Error in Transit-Time Ultrasonic Flow Meters*, IEEE Int. Ultrason. Symp., pp. 1-4, (2018).

2. **J. Massaad**, P. van Neer, D. van Willigen, N. de Jong, M. Pertijs and M. Verweij. *Feasibility of Ultrasonic Flow Measurements via Non-linear Wave Propagation*, IEEE Int. Ultrason. Symp., pp. 1-4, (2018).

1. **J. Massaad**, P. van Neer, D. van Willigen, M. Pertijs, N. de Jong, and M. Verweij. *Clamp-on Ultrasonic Flow-metering via Matrix Transducers*, Ultrasonics Portugal, (2018).

Acknowledgements

How much does life change after an almost 10000 Km journey and four years of PhD. Ups and downs that have made me, exponentially through these years, the best version of myself so far.

Of course, this research work was the result of the combined support from many people. First, I want to thank my supervisors: Nico de Jong and Martin Verweij, for giving me my first job opportunity and for showing genuine interest in my professional and personal life through our project. Their knowledge, attention to detail and powerful feedback always helped me to become a better scientist and improve the quality of my work.

Up next, a great person that supervised me along the way was Paul van Neer. His expertise and acute feedback always helped to better define my research questions and tackle them with the proper answers. Furthermore, as a mentor, during our late meetings, he always supervised my work with the harsh critical view of the world and, at the same time, with the friendly approach of his character that always inspired me to keep going. Thankfully with the years, I got better in anticipating your questions. This smoothed our meetings and shortened them, which I think is something that your family also appreciated :) (It was his fault Suzana, he always arrived 30min late). Finally, I value very much our friendly relation, which helped me understand a lot of things of the Netherlands and of life. Thank you very much for your dedication, I hope to keep learning a lot from you.

I want to especially thank Jankees Hogendoorn, Jeroen van Klooster, Rogier Geerders and Arie Huijzer from KROHNE. They always showed great scientific and logistical support towards the project. I appreciated our meetings along the way since they were very productive, with a dynamic that always made me feel valuable and at the same time challenged and inspired to solve a real problem.

Also, I have to thank the support from Henry den Bok during this project. He always had the most attentive attitude towards helping me achieve experiments by helping me find parts, providing tools, and assisting me in building experimental setups. I don't think anyone else has biked through all the corners of the Netherlands more than you.

Spoiler alert: The Netherlands is a very bureaucratic country! To deal with it during four years, I have to thank Angela van der Sande. Her continuous help and support with all the bureaucracy of the university always made my life much easier. Also, during my time as a PhD candidate, we established a friendly relation, in which she showed me and part of my family, the kindness of Dutch people.

A key person in the realization of this project was Emile Noothout. His technical experience, work precision and attention to detail was always the needed ingredient in fabricating the best possible devices and experimental setups.

During this journey I have to thank our team members from EWI: Douwe van Willigen and Michiel Pertijs. Their constant input and practical approach always contributed to progress. I felt very lucky to establish a good professional relationship with Douwe along the journey, as well as our personal conversations about the weather, woodwork and the Dutch language while enjoying great food from our friends of The Greek Olive :).

Finally, I want to thank the friendship of my colleagues: Albe, Elango, Ulas, Fabian, Boudewine, Moein, Maysam, Verya and Rik. It has been a great journey, thanks to all.

Curriculum Vitæ

Jack Mitchell MASSAAD MOUAWAD

12-07-1992   Born in Caracas, Venezuela.

Education

2017–2020   PhD. Applied Physics
Technische Universiteit Delft, Delft, the Netherlands
Thesis: High-precision Versatile Ultrasonic Flow Meters Based on Matrix Transducer Arrays
Promotors: Prof. dr. ir. N. de Jong & Dr. ir. M. D. Verweij

2014–2016   MSc. Petroleum Geophysics
Norges Teknisk-naturvitenskapelige Universitet, Trondheim, Norway

2009–2014   BSc. Geophysics Engineering
Universidad Simón Bolívar, Caracas, Venezuela

Experience

2017–2020   PhD. Candidate
Technische Universiteit Delft, Delft, the Netherlands

2016   Summer Student
SINTEF Petroleum Research, Trondheim, Norway

2015–2016   Teaching Assistant
Norges Teknisk-naturvitenskapelige Universitet, Trondheim, Norway

2013   Intern: QC of 3D multi-component reflection seismic data
PDVSA, El Tigre, Venezuela